The Southern Ocean carbon cycle 1985-2018: Mean, seasonal cycle, trends and storage

Judith Hauck[1], Luke Gregor[2], Cara Nissen[3], Lavinia Patara[4], Mark Hague[5], Precious Mongwe[6], Seth M Bushinsky[7], Scott C. Doney[8], Nicolas Gruber[9], Corinne Le Quéré[10], Manfredi Manizza[11], Matthew R. Mazloff[12], Pedro M. S. Monteiro[13], and Jens Terhaar[14]

[1]Alfred Wegener Institute Helmholtz Centre for Polar and Marine Research
[2]ETH Zurich
[3]University of Colorado Boulder
[4]GEOMAR Helmholtz-Zentrum für Ozeanforschung Kiel
[5]Environmental Physics, Institute of Biogeochemistry and Pollutant Dynamics, ETH Zuric
[6]Council for Scientific and Industrial Research (CSIR)
[7]University of Hawaii at Mānoa
[8]University of Virginia
[9]ETH Zürich
[10]School of Environmental Sciences, University of East Anglia, UK
[11]Scripps Institution of Oceanography
[12]UCSD
[13]CSIR
[14]Climate and Environmental Physics - University of Bern

May 25, 2023

Abstract

We assess the Southern Ocean CO2 uptake (1985-2018) using data sets gathered in the REgional Carbon Cycle Assessment and Processes Project phase 2 (RECCAP2). The Southern Ocean acted as a sink for CO2 with close agreement between simulation results from global ocean biogeochemistry models (GOBMs, 0.75±0.28 PgCyr-1) and pCO2-observation-based products (0.73±0.07 PgCyr-1). This sink is only half that reported by RECCAP1. The present-day net uptake is to first order a response to rising atmospheric CO2, driving large amounts of anthropogenic CO2 (Cant) into the ocean, thereby overcompensating the loss of natural CO2 to the atmosphere. An apparent knowledge gap is the increase of the sink since 2000, with pCO2-products suggesting a growth that is more than twice as strong and uncertain as that of GOBMs (0.26±0.06 and 0.11±0.03 PgCyr-1 decade-1 respectively). This is despite nearly identical pCO2 trends in GOBMs and pCO2-products when both products are compared only at the locations where pCO2 was measured. Seasonal analyses revealed agreement in driving processes in winter with uncertainty in the magnitude of outgassing, whereas discrepancies are more fundamental in summer, when GOBMs exhibit difficulties in simulating the effects of the non-thermal processes of biology and mixing/circulation. Ocean interior accumulation of Cant points to an underestimate of Cant uptake and storage in GOBMs. Future work needs to link surface fluxes and interior ocean transport, build long overdue systematic observation networks and push towards better process understanding of drivers of the carbon cycle.

The Southern Ocean carbon cycle 1985-2018: Mean, seasonal cycle, trends and storage

Judith Hauck[1], Luke Gregor[2],Cara Nissen[1,3], Lavinia Patara[4], Mark Hague[2], N. Precious Mongwe[5], Seth Bushinsky[6], Scott C. Doney[7], Nicolas Gruber[2], Corinne Le Quéré[8], Manfredi Manizza[9], Matthew Mazloff[9], Pedro M. S. Monteiro[5,10], Jens Terhaar[11,12,13]

[1]Alfred-Wegener-Institut, Helmholtz-Zentrum für Polar- und Meeresforschung, Bremerhaven, Germany
[2]Environmental Physics, Institute of Biogeochemistry and Pollutant Dynamics, ETH Zurich, Zürich, Switzerland
[3]Department of Atmospheric and Oceanic Sciences and Institute of Arctic and Alpine Research, University of Colorado, Boulder, Colorado, USA
[4]GEOMAR Helmholtz Centre for Ocean Research Kiel, Kiel, Germany
[5]Southern Ocean Carbon-Climate Observatory, CSIR, South Africa
[6]University of Hawai'i Mānoa
[7]Dept. of Environmental Sciences, University of Virginia, Charlottesville, VA, USA
[8]School of Environmental Sciences, University of East Anglia
[9]Scripps Institution of Oceanography, University of California - San Diego, La Jolla, CA
[10]School for Climate Studies, Stellenbosch University, South Africa
[11]Climate and Environmental Physics, Physics Institute, University of Bern, Switzerland
[12]Oeschger Centre for Climate Change Research, University of Bern, Switzerland
[13]Department of Marine Chemistry and Geochemistry, Woods Hole Oceanographic Institution, 360 Woods Hole Road, Woods Hole, 02543, Massachusetts, USA

Key Points:

- Ocean models and machine learning estimates agree on the mean Southern Ocean CO_2 sink, but the trend since 2000 differs by a factor of two.
- Compared with RECCAP1, the updated estimate for the Southern Ocean CO_2 uptake is 50% smaller.
- Large model spread in summer and winter indicates that sustained efforts are required to understand driving processes in all seasons.

Corresponding author: Judith Hauck, `judith.hauck@awi.de`

Abstract

We assess the Southern Ocean CO_2 uptake (1985-2018) using data sets gathered in the REgional Carbon Cycle Assessment and Processes Project phase 2 (RECCAP2). The Southern Ocean acted as a sink for CO_2 with close agreement between simulation results from global ocean biogeochemistry models (GOBMs, 0.75±0.28 PgC yr^{-1}) and pCO_2-observation-based products (0.73±0.07 PgC yr^{-1}). This sink is only half that reported by RECCAP1. The present-day net uptake is to first order a response to rising atmospheric CO_2, driving large amounts of anthropogenic CO_2 (C_{ant}) into the ocean, thereby overcompensating the loss of natural CO_2 to the atmosphere. An apparent knowledge gap is the increase of the sink since 2000, with pCO_2-products suggesting a growth that is more than twice as strong and uncertain as that of GOBMs (0.26±0.06 and 0.11± 0.03 Pg C yr−1 $decade^{-1}$ respectively). This is despite nearly identical pCO_2 trends in GOBMs and pCO_2-products when both products are compared only at the locations where pCO_2 was measured. Seasonal analyses revealed agreement in driving processes in winter with uncertainty in the magnitude of outgassing, whereas discrepancies are more fundamental in summer, when GOBMs exhibit difficulties in simulating the effects of the non-thermal processes of biology and mixing/circulation. Ocean interior accumulation of C_{ant} points to an underestimate of C_{ant} uptake and storage in GOBMs. Future work needs to link surface fluxes and interior ocean transport, build long overdue systematic observation networks and push towards better process understanding of drivers of the carbon cycle.

Plain Language Summary

The ocean takes up CO_2 from the atmosphere and thus slows climate change. The Southern Ocean has been long known to be an important region for ocean CO_2 uptake. Here, we bring together all available data sets that estimate the Southern Ocean CO_2 uptake, from models that simulate ocean circulation and physical and biological processes that affect the ocean carbon cycle, from surface ocean observation-based estimates, from atmospheric transport models that ingest atmospheric CO_2 observations, and from interior ocean biogeochemical observations. With these data sets, we find good agreement on the mean Southern Ocean CO_2 uptake 1985-2018, which is 50% smaller than previous estimates when recalculated for the time period and spatial extent used in the previous estimate. However, the estimates of the temporal change of the Southern Ocean CO_2 uptake differ by a factor of two and thus are not in agreement. We further highlight that knowledge gaps exist not only in winter when observations are typically rare, but equally in summer when biology plays a larger role, which is typically represented in a too simplistic fashion in the dynamic models.

1 Introduction

The Southern Ocean (Figure 1) is the primary conduit between the surface and the deep ocean (Talley, 2013; Morrison et al., 2022) making it a key region for the global carbon cycle and the climate system across time-scales from paleo to present day and into the future (Canadell et al., 2021). Firstly, water mass formation of Antarctic surface water occurs during large-scale upwelling of deep, old and carbon-rich water masses due to strong westerly winds (Russell et al., 2006; Marshall & Speer, 2012). Part of this water moves northwards by Ekman transport and contributes to the formation of Southern mode and intermediate waters (Ito et al., 2010; Sallée et al., 2012; Morrison et al., 2022) together with subtropical water masses (Iudicone et al., 2016). Another part moves southward and circulates in the large gyres of the Weddell and Ross Seas (Klatt et al., 2005). A fraction of these Antarctic surface waters densify on the Antarctic shelves through cooling and brine rejection during sea-ice formation on the Antarctic shelves to then flow down the Antarctic slope and form Antarctic Bottom Water (Orsi et al., 1999; Jacobs, 2004).

Historically, in pre-industrial times, the Southern Ocean was a net source of CO_2 to the atmosphere due to upwelling of carbon-rich deep waters (Mikaloff Fletcher et al., 2007). Importantly, the large-scale upwelling that drove the natural outgassing fluxes in the polar and subpolar Southern Ocean still occurs today. However, since industrialisation, increasing atmospheric levels of CO_2 have shifted the thermodynamic equilibrium of CO_2 partial pressure between the ocean and the atmosphere in the favor of the latter, thus overcompensating the natural outgassing(e.g., Hoppema, 2004). The contemporary net flux in the Southern Ocean can thus be understood as the sum of the outgassing of natural CO_2 and uptake of anthropogenic CO_2 (Gruber et al., 2009; Gruber, Landschützer, & Lovenduski, 2019). Importantly, the Southern Ocean has acted as the primary region of uptake for anthropogenic CO_2 in the industrialized era (Sarmiento et al., 1992; Orr et al., 2001; Caldeira & Duffy, 2000; Khatiwala et al., 2009; Frölicher et al., 2015; Mikaloff Fletcher et al., 2006), which is attributed to upwelling of old water masses (with low anthropogenic carbon) in a region of high wind speeds, as well as subsequent transport of excess carbon from the surface into the ocean interior through the formation of Subantarctic Mode and Antarctic Intermediate Water (Waugh et al., 2006; Mikaloff Fletcher et al., 2006; Bopp et al., 2015; Langlais et al., 2017; Sallée et al., 2012). In the absence of evidence of substantial changes in the biological carbon pump over the past decades, the role of biology for anthropogenic carbon uptake is thought to be small (Murnane et al., 1999; Holzer & DeVries, 2022). However, the biological carbon pump can have a strong imprint on the net fluxes during the summer when primary production draws down natural CO_2 at the surface (e.g., E. Jones et al., 2012, 2015).

While the general importance of the Southern Ocean for the ocean carbon sink is recognised, it is also the region with the largest uncertainty in the mean and trend of the sink (Hauck et al., 2020; Friedlingstein et al., 2022). This is partly because the observation-based estimates and model-based estimates measure different components of the ocean carbon sink, and assumptions on fluxes associated with river discharge need to made, which carry high uncertainty themselves (Aumont et al., 2001; Lacroix et al., 2020). Further, the decadal variability of the Southern Ocean and the underlying mechanisms thereof are a key contributor to the uncertainty and are a topic of continued discussion (Le Quéré et al., 2007; Landschützer et al., 2015; Gruber, Landschützer, & Lovenduski, 2019; Hauck et al., 2020; McKinley et al., 2020; Canadell et al., 2021). A stagnation in the growth of the Southern Ocean carbon sink in the 1990s is commonly attributed to a strengthening of the westerly winds and associated intensified upwelling of carbon- and nutrient-rich deep water (Le Quéré et al., 2007; Lovenduski et al., 2007; Hauck et al., 2013). Indeed, evidence for this stronger upwelling is indirectly observed by enhanced surface nutrient concentrations in all Southern Ocean basins (Hoppema et al., 2015; Panassa et al., 2018; T. Iida et al., 2013; Ayers & Strutton, 2013; Pardo et al., 2017). The early 2000's marked the start of the so-called reinvigoration of the Southern Ocean carbon sink (Landschützer et al., 2015). The strength of the reinvigoration is uncertain due to the observation-based products potentially overestimating the trends owing to data sparsity (Landschützer et al., 2015; Gloege et al., 2021; Hauck et al., 2023), while further analysis on the trends in the models is needed. Furthermore, the drivers of the reinvigoration are less well understood than for the stagnation, but it may be linked to changes in the atmospheric forcing (Gruber, Landschützer, & Lovenduski, 2019) and/or changes in the overturning circulation (DeVries et al., 2017). There is also evidence that both the stagnation and the reinvigoration are part of a global response to variations in atmospheric CO_2 growth rate, ocean temperature and circulation induced by the 1992 eruption of Mount Pinatubo (McKinley et al., 2020; Eddebbar et al., 2019).

The Southern Ocean carbon sink is projected to continue to play an important role in the future carbon cycle as shown by Earth System Model simulations (Hauck et al., 2015; Kessler & Tjiputra, 2016; Canadell et al., 2021; Terhaar et al., 2021). However, there are indications that system changes may occur, such as a shift to a larger proportion of the CO_2 uptake occurring in the polar Southern Ocean (Hauck et al., 2015), and a strong sensitivity of Southern Ocean carbon storage to physical ventilation and warming (Katavouta & Williams, 2021; Terhaar et al., 2021; Bourgeois et al., 2022).

In this study, we aim to synthesize and assess information on the Southern Ocean carbon sink over the period 1985 to 2018 in the framework of the REgional Carbon Cycle Assessment and Processes project, phase 2 (RECCAP2). This work builds on a previous assessment, RECCAP phase 1 (referred to as RECCAP1 for clarity), for the period 1990 to 2009 (Lenton et al., 2013). In RECCAP1, the Southern Ocean was defined as the ocean south of 44°S (building on earlier classification in the atmospheric inversion community), which, however, cut through the major anthropogenic CO_2 uptake region at the northern edge of the Southern Ocean. The assessment was based on five global ocean biogeochemical models, eleven atmospheric inversions, ten ocean inversions and a single pCO_2 observation-based data set, the climatology of Takahashi et al. (2009). RECCAP1 resulted in a best estimate of the net Southern Ocean CO_2 uptake (1990-2009) of 0.42±0.07 PgC yr^{-1} based on all models (including inversions), with a surface pCO_2-based climatology (Takahashi et al., 2009) suggesting a lower number of 0.27±0.13 PgC yr^{-1} Lenton et al. (2013). The interannual variability was estimated to be ±25% around this mean value. The largest proportion of the mean flux occurred in the region 44-58°S which spans large parts of the Subantarctic Zone and of the Polar Frontal Zone with similar contributions from the Atlantic, Pacific and Indian Ocean sectors. In the Antarctic Zone (south of 58°S), individual estimates did not agree on the sign of the net CO_2 flux.

A major advance since RECCAP1 is the release and continued updating of the Surface Ocean CO_2 Atlas (SOCAT Bakker et al., 2016), which currently provides 33.7 million quality-controlled and curated surface ocean pCO_2 measurements with an accuracy of <5 μatm in the 2022 release (Bakker et al., 2022). The release of SOCAT allowed for the development of the surface ocean pCO_2 observation-based products (pCO_2-products) that interpolate and extrapolate sparse ship-based observations from SOCAT to global coverage. Based on these maps of surface pCO_2, the air-sea CO_2 flux is then calculated using gas-exchange parameterizations and input data fields such as sea surface temperature and wind fields (R. H. Wanninkhof, 2014). Since RECCAP1, a diverse set of statistical and machine-learning approaches have been developed (e.g., Landschützer et al., 2014; Rödenbeck et al., 2014; Gregor et al., 2019; Chau et al., 2022). The pCO_2-products allowed for observation-based investigation of interannual and decadal variability. They confirmed the reported stagnation of the Southern Ocean carbon sink in the 1990s (Le Quéré et al., 2007), and identified the aforementioned reinvigoration in the 2000s (Landschützer et al., 2015; Ritter et al., 2017). However, these pCO_2-products have made the Southern Ocean's long-standing issue of sparse observations even more evident. Observation system simulation experiments (OSSEs) have shown that these methods are prone to regional and temporal biases (Denvil-Sommer et al., 2021) and some pCO_2-products may overestimate the decadal variability by 30% (Gloege et al., 2021). In fact, a recent study showed that the SOM-FFN pCO_2-product used in the reinvigoration study of Landschützer et al. (2015) overestimates the model-based decadal trend 2000-2018 by 130% in an ocean model subsampling experiment (Hauck et al., 2023). However, these OSSEs have also shown that augmenting ship-based observations with well-placed, high accuracy pCO_2 observations from autonomous platforms can reduce these biases (Denvil-Sommer et al., 2021; Djeutchouang et al., 2022; Hauck et al., 2023).

The gap in ship-based pCO_2 observations is slowly being addressed by a second major advance, that is autonomous measurement devices. Among these are pH-equipped biogeochemical Argo floats (BGC-floats) (Williams et al., 2016; Johnson et al., 2017). With this approach, float pH measurements are combined with multi-linear regression-derived alkalinity (Williams et al., 2016; Carter et al., 2016, 2018, 2021), to calculate estimates of pCO_2. Although uncertainties of the BGC-float based estimates of pCO_2 are, to date, higher (theoretical uncertainty of 11 μatm, Williams et al., 2017) than for direct pCO_2 measurements (2μatm, Bakker et al., 2016), some of these indirect pCO_2 estimates fill critical gaps in the sparsely sampled winter months. These novel data, either on their own (Gray et al., 2018) or as additional input for pCO_2-products (Bushinsky et al., 2019), reported a strong winter outgassing of CO_2 in the subpolar Southern Ocean for the years 2015 through 2017 that also led to a substantially smaller estimate of the annual Southern Ocean CO_2 uptake for these years. However, these larger-than-expected winter outgassing estimates were challenged by airborne flux estimates and direct pCO_2 measurements from a circumpolar navigation by an uncrewed sailing drone (Long et al., 2021; Sutton et al., 2021). The sailing drone observations were in agreement with ship-based pCO_2-product estimates throughout all seasons (Sutton et al., 2021). The authors attributed the discrepancy between BGC-floats and other estimates to either a bias of the float measurement devices or interannual variability. In support of the latter argument, the BGC-Argo-based air-sea CO_2 flux in the years 2017-2019 also did not reveal the strong winter outgassing signal of the years 2015 and 2016 (Sutton et al., 2021).

Another advance since RECCAP1 is that more global ocean biogeochemical models (GOBMs) have become available with improvements in resolution and physical and biogeochemical process representation (R. H. Wanninkhof et al., 2013; Friedlingstein et al., 2022). While the ability of the GOBMs to capture interannual variability of air-sea CO_2 fluxes (FCO_2) was questioned by the larger variability of pCO_2-product estimates (Le Quéré et al., 2018), the lower interannual variability of GOBMs now falls within the range of the larger ensemble of pCO_2-products (McKinley et al., 2020; Hauck et al., 2020). For the decadal variability of FCO_2, there is a moderate agreement between GOBMs and pCO_2-products on a stagnation of the sink in the 1990s and an increase of the sink in 2002-2011 but with a larger amplitude of the multi-year/decadal variability in the pCO_2-products (McKinley et al., 2020; Hauck et al., 2020; Gruber et al., 2023). Although the GOBMs compare reasonably well to global and Southern Ocean observations of surface ocean pCO_2 (Hauck et al., 2020), their estimates of the global ocean carbon sink remain below those of interior ocean anthropogenic carbon accumulation estimates from 1994 to 2007 (Gruber, Clement, et al., 2019), atmospheric inversions, observed O_2/N_2 ratios (Friedlingstein et al., 2022; Tohjima et al., 2019), and a similar underestimation was found in Earth System Models (Terhaar et al., 2022).

The final major advance in the last decade are regional and global data-assimilating global ocean biogeochemistry models (Verdy & Mazloff, 2017; Carroll et al., 2020). These models bring together the process-based knowledge from GOBMs, but use data assimilation schemes to minimize mismatches between simulated fields, and physical and biogeochemical observations.

Despite these recent advances in observations and models, the Southern Ocean is still the region with the largest discrepancy in mean CO_2 flux (although within the uncertainty of the fluxes associated with river discharge which are implicitly included in the observation-based estimates, but not in the models, see sections 2.2.1 and 2.3.1) and variability, as well as largest model spread (Friedlingstein et al., 2022; Canadell et al., 2021). In this study, we aim to quantify the Southern Ocean (following the RECCAP2 biome shown in Figure 1) surface CO_2 fluxes and interior storage of anthropogenic carbon over the period 1985-2018 from different classes of models and observations, and to identify knowledge gaps and ways forward.

This study is organized in the following way. In our methods, we describe the region (section 2.1), the datasets that we use throughout this synthesis (section 2.2), and how the data were processed (section 2.3). Our results contain first the estimates of the mean fluxes 1985-2018 and their decomposition into anthropogenic and natural fluxes, and atmospheric CO_2 versus climate effects (section 3.1). This is followed by an analysis of summer and winter fluxes and the full seasonal cycle, where we also decompose

pCO_2 into seasonal thermal and non-thermal contributions (section 3.2). We then analyse the regionally averaged temporal trends of CO_2 flux and also of pCO_2 in comparison with in situ pCO_2 observations, as well as atmospheric CO_2 and climate effects as drivers of the trends (section 3.3). In the final part of the results, the study then evaluates the GOBM simulation results with observation-based estimates of ocean interior storage of anthropogenic carbon in the Southern Ocean (section 3.4). The discussion first summarizes the results with a comparison of the RECCAP1 and RECCAP2 results (section 4.1). We also discuss the drivers of the seasonal cycle (section 4.2), the interannual and decadal variability (section 4.3), and the zonal asymmetry of the fluxes in the Southern Ocean (section 4.4). Lastly, we discuss how our study links with and can inform observational programs (section 4.5), before presenting a conceptual characterization of the Southern Ocean carbon cycle in the conclusions (section 5).

2 Methods

2.1 Regions

We use the RECCAP2 regions (DeVries, 2022) to define the Southern Ocean and its northern boundary (Figure 1). This definition of the Southern Ocean covers the subtropical seasonally stratified biome (STSS), the subpolar seasonally stratified biome (SPSS), and the ice biome (ICE) and is based on the global open ocean biome classification of Fay and McKinley (2014). This covers a larger area than the definition used in RECCAP1 (44-58°S, 58-75°S Lenton et al., 2013) and has the advantage that it does not cut through the subtropical region with its large CO_2 flux into the ocean. The northernmost extent of the Southern Ocean in this definition is 35°S. For parts of our analysis, we further separate the Atlantic, Indian, and Pacific Ocean sectors along longitudes of 20°E, 147°E, and 290°E (Figure 1).

2.2 Data sets

Here, we introduce data sets across four different data classes that are used for the assessment of the Southern Ocean CO_2 fluxes and storage, namely: ocean biogeochemistry models (14), surface pCO_2-based data-products (11), data assimilated and ocean inverse models (3), and atmospheric inversion models (6).

2.2.1 Ocean biogeochemistry models

We used 13 global ocean biogeochemistry models (GOBMs) and 1 regional ocean biogeochemistry model (Table 1). These models simulate ocean circulation and biogeochemical fluxes caused by physics (advection, mixing, gas-exchange) and by biological processes. They are forced with atmospheric fields from reanalysis products, e.g., by either heat and freshwater fluxes directly or by air temperature, wind speed, precipitation and humidity, which are converted to heat and freshwater fluxes using bulk formulae (see references in Table 1; Large et al., 1994). From these 14 models, eleven models are global ocean models with roughly 1°×1° resolution, and two global models (FESOM_REcoM_HR and ORCA025-GEOMAR) and the regional model (ROMS-SouthernOcean-ETHZ) are available in ca. 0.25°×0.25° resolution. Details of global model set-ups are given in (DeVries et al., 2023). The ROMS-based regional Southern Ocean model has a northern boundary at 24°S.

For the ocean-models listed above, up to four different simulations were provided (see also Table S1 and DeVries et al., 2023). These differ in whether atmospheric CO_2 and all other atmospheric forcing variables vary on interannual time scales, are repeated for a single year, or follow a multi-year climatology. In simulation A, the historical run, both atmospheric CO_2 and all other physical forcing variables vary on interannual time scales. In simulation B, the preindustrial control run, a repeated year or climatological

Table 1. Overview of data sets used in this paper. Sorted by data class, here: Global Ocean Biogeochemistry Models (GOBMs), Regional Ocean Biogeochemistry Model, and data assimilated models.

Data set	Time period	Specific information	Reference
Global Ocean Biogeochemistry Models		**Simulations**	
CCSM-WHOI	1985-2017	A, B, C, D	Doney et al. (2009)
CESM-ETHZ	1985-2018	A, B, C, D	Lindsay et al. (2014); S. Yang and Gruber (2016)
CNRM-ESM2-1	1985-2018	A, B, C, D	Séférian et al. (2019); Berthet et al. (2019); Séférian et al. (2020)
EC-Earth3	1985-2018	A, B, C, D	Döscher et al. (2022)
FESOM_REcoM_HR	1985-2018	A, B	Hauck et al. (2013); Schourup-Kristensen et al. (2014, 2018)
FESOM_REcoM_LR	1985-2018	A, B, C, D	Hauck et al. (2013); Schourup-Kristensen et al. (2014); Hauck et al. (2020)
MOM6-Princeton	1985-2018	A, B	Liao et al. (2020); Stock et al. (2020)
MPIOM-HAMOCC	1985-2018	A, B, C, D	Ilyina et al. (2013); Paulsen et al. (2017); Mauritsen et al. (2019)
MRI-ESM2-1	1985-2018	A, B, C, D	Urakawa et al. (2020)
NorESM-OC1.2	1985-2018	A, B, C, D	Schwinger et al. (2016)
ORCA025-GEOMAR	1985-2018	A, B, C, D	Madec and the NEMO team (2016); Kriest and Oschlies (2015); Chien et al. (2022)
ORCA1-LIM3-PISCES (IPSL-NEMO-PISCES)	1985-2018	A, B, C, D	Aumont et al. (2015)
PlankTOM12	1985-2018	A, B, C, D	Le Quéré et al. (2016); Buitenhuis et al. (2019); Wright et al. (2021)
Regional Ocean Biogeochemical Models		**Simulations**	
ROMS-SouthernOcean-ETHZ	1985-2018	A, B, D	A. Haumann (2016); Nissen et al. (2018)
Data-assimilated models			
B-SOSE	2013-2018		Verdy and Mazloff (2017)
ECCO-Darwin	1992-2017		Carroll et al. (2020, 2022)
OCIMv2021	1780-2018	A, B, C	DeVries (2022)

Table 2. Overview of data sets used in this paper (continued). Sorted by data class, here: pCO_2-products and atmospheric inversions. The atmospheric inversions were provided only since 1990.

Data set	Time period	Specific information	Reference
pCO_2-products			
AOML_EXTRAT	1998-2018		R. Wanninkhof (2023)
CMEMS-LSCE-FFNN	1985-2018		Chau et al. (2022)
CSIR-ML6	1985-2018		Gregor et al. (2019)
Jena-CarboScope (Mixed Layer Scheme)	1985-2018		Rödenbeck et al. (2013, 2022)
JMA-MLR	1985-2018		Y. Iida et al. (2021)
LDEO-HPD	1985-2018		Gloege et al. (2022)
NIES-ML3	1985-2018		Zeng et al. (2022)
OceanSODA-ETHZ	1985-2018		Gregor and Gruber (2021)
MPI-SOM-FFN	1985-2018		Landschützer et al. (2016, 2020)
Jena-CarboScope (SOCCOM)	2015-2018		Bushinsky et al. (2019) updated
MPI-SOM-FFN (SOCCOM)	2015-2018		Bushinsky et al. (2019) updated
Watson2020	1988-2018		Watson et al. (2020)
LDEO_climatology (Takahashi legacy)	climatology		Takahashi et al. (2009)
Atmospheric inversions		**Ocean prior**	
Jena CarboScope	1957-2020 (1990-2020)	CarboScope pCO_2-product	Rödenbeck et al. (2018)
CAMS	1979-2020 (1990-2020)	CMEMS-LSCE-FFNN pCO_2-product	Chevallier et al. (2005)
NISMON-CO2	1990-2020	JMA-MLR pCO_2-product	Niwa et al. (2017)
CarbonTrackerEurope (CTE)	2001-2020	CarboScope pCO_2-product	van der Laan-Luijkx et al. (2017)
UoE	2001-2020	Takahashi climatology	Feng et al. (2016)
CMS-Flux	2010-2020	MOM6 GOBM	Liu et al. (2021)

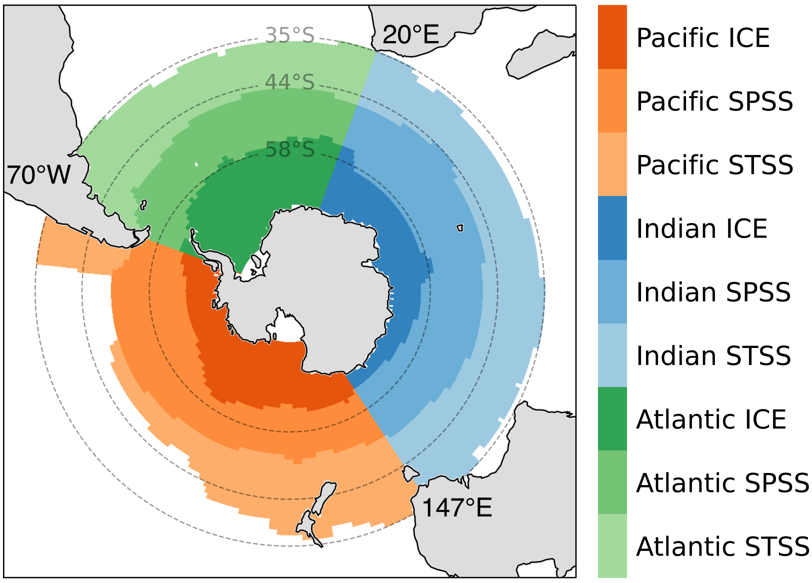

Figure 1. Study region. The Southern Ocean covers three biomes: The subtropical seasonally stratified (STSS), the subpolar seasonally stratified (SPSS), and the ice (ICE) biome. The biomes are defined following Fay and McKinley (2014). We further consider the Atlantic, Pacific, and Indian Ocean sectors separately in parts of the analysis. The dashed lines show the RECCAP2 Southern Ocean northernmost extent (35°S), the RECCAP1 Southern Ocean northernmost extent (44°S), and RECCAP1's boundary for the circumpolar region (58°S).

physical atmospheric forcing is used, and the atmospheric CO_2 levels are held constant at pre-industrial levels. In simulation C, the atmospheric CO_2 varies interannually and only the physical atmospheric forcing is climatological. In simulation D, the atmospheric CO_2 levels are held constant at pre-industrial levels, whereas the physical atmospheric forcing varies interannually. These simulations allow for the separation of the effects of the increase in atmospheric CO_2 and climate change and variability on air-sea CO_2 fluxes: the steady-state and non-steady state components of both natural and anthropogenic carbon. Here *anthropogenic* refers to the direct effect of increasing atmospheric CO_2 and *non-steady state* encompasses the effects of climate change and variability. For a detailed explanation, please see DeVries et al. (2023) and further explanation in Le Quéré et al. (2010); McNeil and Matear (2013); Hauck et al. (2020); Crisp et al. (2022); Gruber et al. (2023). Simulation A includes all components of the carbon fluxes. In the control simulation B, only the steady-state component of natural carbon is considered. In simulation C, only the steady-state components of both natural and anthropogenic carbon are accounted for. Lastly, in simulation D, only the steady state and non-steady state components of natural carbon are represented.

The majority of models do not account for the river-induced outgassing of carbon (DeVries et al., 2023; Terhaar et al., 2023), hence the air-sea CO_2 flux in simulation A corresponds to the S_{OCEAN} definition used in the Global Carbon Budget (Friedlingstein et al., 2022), which differs from pCO_2-product estimates by the river-induced term. Note that the river-induced term will be discussed in greater detail in section 4.1. In addition, simulation A may include a model bias (mean offset) and drift (temporally changing offset). We assess the model drift of the air-sea CO_2 flux by calculating the linear trend of the integrated CO_2 flux time series for the period 1985-2018 in simulation B for each model and each biome. The time series plots and the linear trends reported in Figure

8 are drift corrected by subtracting the trend from simulation B. We note that this drift-correction only marginally impacts the reported trends in the result section, as the trends in simulation B are small compared to the mean fluxes for all models (see supplementary material: Text S1 and Figure S1). In contrast to a global bias (any deviation of the global mean CO_2 flux from 0 in simulation B, see Hauck et al., 2020), the regional bias in the simulated flux cannot be assessed by the set of simulations as it cannot be separated from the natural steady-state air-sea CO_2 flux (Terhaar et al., 2023), which is non zero on a regional level.

We use the full suite of models in all analyses, with two exceptions. Firstly, we excluded the MPIOM-HAMOCC model in all seasonal analyses (Fig. 4-7) because its amplitude of the seasonal cycle is a factor 3-6 larger than in the other models in the three main Southern Ocean biomes (Figure S2), and including this outlier would skew the ensemble mean disproportionately. The exaggerated seasonal cycle in the MPIOM-HAMOCC model was found in earlier studies and is attributed to excessive net primary production in the Southern Ocean (Mongwe et al., 2018). Secondly, the decomposition into natural and anthropogenic CO_2 fluxes was not possible with GOBMs that only provided simulations A and B (MOM6-Princeton and FESOM-REcoM-HR). See section 2.3.4 for further restrictions on GOBM use and interpretation for the interior ocean anthropogenic carbon accumulation.

2.2.2 Surface pCO_2-based data-products

As a second data class, we use surface ocean pCO_2 observation-based data products (pCO_2-products) (Table 2, for more details see DeVries et al., 2023). These pCO_2-products extrapolate or interpolate sparse ship-based measurements of pCO_2 using statistical modeling approaches. All pCO_2-based data-products use SOCAT as the target dataset. The majority of pCO_2-products use similar gridded prediction datasets to fill the gaps, including sea surface temperature, sea surface salinity, mixed-layer depth, and chlorophyll-a estimates for the open ocean. We use 8 such pCO_2-products that all cover the full time-series 1985-2018 for the ensemble mean of pCO_2-products. AOML_EXTRAT covers a shorter period, and is thus not included in the ensemble mean 1985-2018, but is included in the ensemble mean 2015-2018. The largest methodological difference between the pCO_2-products stems from the algorithm choice. The majority of the methods use regression approaches (a.k.a. machine learning) such as artificial neural networks (e.g, MPI-SOM-FFN) and gradient boosted decision trees (e.g., CSIR-ML6) to capture the relationship between the ship-based measurements and the predictor variables. The Jena-CarboScope product includes a mechanistic understanding of mixing, entrainment, and fluxes of CO_2 into and out of the mixed layer (Rödenbeck et al., 2014). The HPD-LDEO method adjusts global ocean biogeochemistry model estimates of pCO_2 to be closer to observed ship-based measurements and is thus an observation-based posterior correction to the GOBM estimates (Gloege et al., 2022).

Further, two additional variants of MPI-SOM-FFN and Jena-CarboScope by Bushinsky et al. (2019, ship+float estimates are used here) include additional BGC-float-derived pCO_2 for the Southern Ocean (referred to as BGC-float pCO_2-products, 2015-2018). We also use the Watson2020 product, which is a neural network approach (based on MPI-SOM-FFN) but applies an adjustment to SOCAT pCO_2 that accounts for the difference between ship intake temperature and satellite sea surface temperature (Watson et al., 2020). The BGC-float pCO_2-products (2015-2018) and Watson2020 (1988-2018) are not included in the pCO_2-product ensemble averages, as they are based on fundamentally different pCO_2 values. We also use a monthly climatology product (LDEO-clim) that is centered on the year 2010 (Takahashi et al., 2009).The LDEO-clim product fills the gaps using a combination of inverse distance weighted interpolation and a diffusive-advective interpolation scheme (Takahashi et al., 2009). Note that this product is only used in representations of the seasonal cycle, and not for trend analyses. All these pCO_2-products estimate the bulk air-sea CO_2 flux with:

$$FCO_2 = K_0 \cdot k_w \cdot (\mathrm{pCO_2}^{\mathrm{sea}} - \mathrm{pCO_2}^{\mathrm{atm}}) \cdot (1 - \mathrm{ice}) \tag{1}$$

where K_0 is the solubility of CO_2 in seawater, k_w is the gas transfer velocity, $\mathrm{pCO}_2^{\mathrm{sea}}$ is the oceanic estimate of pCO_2 from the pCO_2-product, pCO_2atm is the atmospheric pCO_2, and ice is the sea-ice fraction, with the majority of the open ocean having a fraction of 0. Other than pCO_2^{sea}, k_w is the largest source of uncertainty in the calculation of bulk air-sea CO_2 fluxes R. H. Wanninkhof (2014); Fay et al. (2021). However, most of the pCO_2-products use a quadratic formulation of k_w as described by R. Wanninkhof et al. (1993) meaning that the product spread is reduced due to similar choices – details are shown in Global chapter's Table S2 (DeVries et al., 2023). An exception is the Watson2020 product (Watson et al., 2020) that calculates air sea CO_2 fluxes using the formulation described in Woolf et al. (2016) where a cool and salty skin adjustment is applied.

2.2.3 Data-assimilated models

We use three data-assimilating models (Table 1). The Biogeochemical Southern Ocean State Estimate (B-SOSE Verdy & Mazloff, 2017) is an eddy-permitting 1/6-degree resolution data-assimilating model, which assimilates the data from Southern Ocean Carbon and Climate Observations and Modelling (SOCCOM) BGC-Argo floats as well as shipborne and other autonomous observations (i.e., GLODAP and SOCAT) over the period 2013-2018. In situ and satellite observations of the physical state are also assimilated. B-SOSE is based on the MIT general circulation model (MITgcm Campin et al., 2011) and uses software developed by the consortium for Estimating the Circulation and Climate of the Ocean (ECCO Stammer et al., 2002; Wunsch & Heimbach, 2013) to build on the SOSE physical model framework by adding the Nitrogen version of the Biogeochemistry with Light, Iron, Nutrients, and Gases (N-BLING; evolved from Galbraith et al., 2010) biogeochemical model. Consistency with the data is achieved by systematically adjusting the model initial conditions and the atmospheric state through the 4D-Var assimilation methodology. This B-SOSE assimilation methodology does not break the model biogeochemical or physical budgets. The budgets are closed, which allows one to understand signal attribution, though limits the control we have over the solution. For this reason B-SOSE is only consistent with the data on the timescales longer than approximately 90 days; the mesoscale eddies are reproduced statistically and not deterministically. Even with this assimilation methodology some seasonal biases still exist, and B-SOSE is still a work in progress.

The ECCO-Darwin data-assimilation model (Carroll et al., 2020) is based on a global ocean and sea ice configuration (about 1/3 degree) of the MIT general circulation model and is available from January 1992 to December 2017. Besides being global and covering a longer duration than B-SOSE, this product also uses a different biogeochemical model and assimilation technique. The ECCO circulation estimates used in this version are coupled online with the Darwin ecosystem model (Dutkiewicz et al., 2009), which represents the planktonic ecosystem dynamics coupled with biogeochemical cycles in the ocean. The R. Wanninkhof (1992) parameterization of gas transfer velocity is used and $\mathrm{pCO}_2^{\mathrm{atm}}$ is the National Oceanic and Atmospheric Administration Marine Boundary Layer Reference product (Dlugokencky et al., 2021). The biogeochemical observations used to evaluate and adjust ECCO-Darwin include (1) surface ocean fugacity (fCO_2) from the monthly gridded Surface Ocean CO_2 Atlas (SOCATv5 Bakker et al., 2016), (2) GLODAPv2 ship-based profiles of NO_3, PO_4, SiO_2, O_2, dissolved inorganic carbon (DIC), and alkalinity (Olsen et al., 2016), and (3) BGC-Argo float profiles of NO_3 and O_2 (Drucker & Riser, 2016; Riser et al., 2018). To adjust the model's fit to the global biogeochemical observations, the Green's function approach is used to adjust biogeochemical initial conditions and model parameters.

OCIMv2021 is an inverse model that assimilates observations of temperature, salinity, CFCs and radiocarbon to achieve an estimate of the climatological mean ocean circulation (DeVries, 2022). This steady-state circulation model is used together with an abiotic carbon cycle model and atmospheric CO_2 forcing to simulate anthropogenic carbon uptake and its redistribution within the ocean. It uses a monthly time-step and simulates the period 1780 to 2018. No assimilation takes place during this period.

2.2.4 Atmospheric inversions

Six atmospheric inversions are available for our analysis (Table 2). Atmospheric inversions make use of the worldwide network of atmospheric CO_2 observations. They ingest a dataset of fossil fuel emissions, which are assumed to be well known, into an atmospheric transport model and then solve for the spatio-temporal distribution of land and ocean CO_2 fluxes while minimizing the mismatch with atmospheric CO_2 observations (Friedlingstein et al., 2022). Thus, the resulting land and ocean carbon fluxes are bound to the atmospheric CO_2 growth rate, but the estimated regional fluxes depend on the number of stations in the observational network. The inversions also start from prior estimates of land and ocean fluxes. For four inversion data sets that we use here, the ocean prior is taken from pCO_2 -products that are used in this analysis as well (Table 2). One inversion (UoE) uses the Takahashi climatology as a prior and one (CMS-Flux) an ocean biogeochemical model. The atmospheric inversions are thus not independent from the other data classes (Friedlingstein et al., 2022, their Table A4). The atmospheric inversion data were submitted for RECCAP in the same version as in the Global Carbon Budget 2021 (Friedlingstein et al., 2022), but only since 1990. The three inversions starting later (2001 or 2010) are only included in averages reported for 2015-2018 (Figures 4 and 5), and as individual lines in the time-series figure (Figure 8).

2.3 Processing

Throughout this study, we report the air-sea CO_2 exchange as the net flux (FCO_2), which is the sum of natural, anthropogenic and river-induced air-sea CO_2 flux (see e.g., DeVries et al., 2023; Hauck et al., 2020; Crisp et al., 2022). As the GOBMs vary widely in their choices on river carbon and nutrient input into the ocean and burial at the seafloor (see DeVries et al., 2023; Terhaar et al., 2023), an adjustment is applied to make all data classes comparable.

2.3.1 River flux adjustment

Globally, the majority of GOBMs produce a small imbalance of riverine carbon inflow and burial globally (<0.14 PgC yr^{-1}), which is smaller than the current best estimate of river-induced CO_2 ocean outgassing of 0.65 PgC yr^{-1} (Regnier et al., 2022). The imbalances are due to manifold choices and illustrate the lack of a closed land-ocean carbon loop in the GOBMs. As the GOBMs do not adequately account for the river discharge and its fate within the ocean, and thus for river-derived ocean CO_2 outgassing (Terhaar et al., 2023), we account for this outgassing by using the spatial patterns of river-induced air-sea CO_2 fluxes from Lacroix et al. (2020) that are scaled to the global value of 0.65 PgC yr^{-1} (Regnier et al., 2022). Southern Ocean outgassing from rivers amounts to 0.04 PgC yr^{-1}, i.e., around 6% of the global river flux. It is distributed over the Southern Ocean biomes as follows (positive outgassing): 0.00036 PgC yr^{-1} in the ICE biome, 0.053 PgC yr^{-1} (SPSS biome), -0.014 (STSS biome). The estimated riverine CO_2 fluxes were added to biome-integrated fluxes in simulation A for all GOBMs, so that these are comparable to the pCO_2-products. They are not added to spatial maps of CO_2 fluxes due to large uncertainties in the regional attribution by Lacroix et al. (2020). The riverine fluxes are one (ICE) to multiple (SPSS, STSS) orders of magnitude smaller than the mean fluxes quantified in this study. The uncertainty associated with the river flux adjustment is discussed in section 4.1.

2.3.2 Treatment of different area coverage

Air-sea CO_2 fluxes in all data classes were integrated over the area available for each GOBM, pCO_2-product etc., i.e., fluxes were not scaled to the same ocean area here. Relative to the ocean area in the RECCAP mask, the covered ocean areas in the GOBMs and data-assimilating models corresponds to 96.2-100% (minimum for CCSM-WHOI) and to 95.6-100% in the pCO_2-products (minimum for JMA-MLR). These differences mainly stem from the ICE biome. We assume that the discrepancy arising from differences in covered area are smaller than the uncertainty arising from any extrapolation to the same area.

2.3.3 pCO_2 decomposition

To separate temperature driven changes in pCO_2 from biological processes and mixing-driven entrainment, pCO_2 is decomposed into thermal and non-thermal components (Takahashi et al., 1993). The thermal component (pCO_2^T) is calculated as

$$pCO_2^T = \overline{pCO_2} \cdot e^{(0.0423 \cdot \Delta T)} \tag{2}$$

where $\overline{pCO_2}$ is the annual mean of pCO_2 and ΔT difference of the monthly mean temperature from the annual mean temperature. The non-thermal contribution (pCO_2^{nonT}) is estimated as the difference of the thermal contribution (pCO_2^T) from the monthly-averaged pCO_2. The first derivatives of these two components are subtracted from each other to create the pCO_2 seasonal driver metric, denoted as λpCO_2:

$$\lambda pCO_2 = \left| \frac{pCO_2^T}{\delta t} \right| - \left| \frac{pCO_2^{nonT}}{\delta t} \right| \tag{3}$$

Here, positive values indicate periods when the thermal component is a larger contributor to pCO_2, and negative values show where the DIC processes (non-thermal) play a dominant role in surface pCO_2 changes. We also denote the first derivatives as $pCO_2^{T'}$ and $pCO_2^{nonT'}$ for brevity.

2.3.4 Anthropogenic carbon inventories

Anthropogenic CO_2 (C_{ant}) is defined as the change in ocean dissolved inorganic carbon (DIC) since preindustrial times due to the direct effect of increasing CO_2 concentration in the atmosphere. It is computed as the DIC difference between experiments A and D. The accumulation of C_{ant} can be separated into a steady-state component (C_{ant}^{ss}, DIC difference between experiments C and B), that is influenced only by the increased atmospheric CO_2, and a non-steady-state component (C_{ant}^{ns}), which considers the effect of climate variability and change on C_{ant} (and which is maximally 10-20% of C_{ant}, Text S2 and Figures S3-S4). Here we focus mainly on the change in C_{ant} that has occurred over the period 1994-2007 (hereafter ΔC_{ant}), to correspond to the years covered by the eMLR(C*) observation-based estimate (Gruber, Clement, et al., 2019). The eMLR(C*) method (Clement & Gruber, 2018) uses ocean measurements of DIC from GLODAP2 (Olsen et al., 2016) over more than 30 years as the foundation to determine ΔC_{ant} between nominal years 1994 and 2007. The method has been shown to be accurate at global and basin scales, but is more uncertain at sub-basin scales and should not be used below 3000 m depth. The (2 sigma) uncertainty of the eMLR(C*) product is estimated to be around 19% for the Southern Hemisphere (Gruber, Clement, et al., 2019). The eMLR(C*) method differs fundamentally from past indirect or model-based methods used to estimate C_{ant} accumulated since pre-industrial times (Gruber et al., 1996; Sabine et al., 2004; Waugh et al., 2006; DeVries, 2014). Of these, we used the 1800-1994 cumulative C_{ant}

estimate based on (Sabine et al., 2004), which is characterized by an uncertainty of about 20% globally (Sabine et al., 2004; Matsumoto & Gruber, 2005). In terms of GOBMs, we used all those listed in Table 1, with the exception of FESOM-REcoM-HR and MOM6-Princeton who provided only experiments A and B. For most GOBMs, we analyze C_{ant}^{tot}, to allow for a more accurate comparison with the observation-based data set (eMLR(C*)). However, for MPIOM-HAMOCC and CNRM-ESM2-1 it was only possible to compute C_{ant}^{ss}, because of physical forcing inconsistencies between experiments A and D. We believe that the advantage of including all GOBMs in the analysis outweighs the disadvantages of having an incoherent definition of C_{ant} among GOBMs. It should be noted that the spin-up procedure of ROMS-SouthernOcean-ETHZ, which uses atmospheric CO_2 from 1969 to 1978 (for a ten year spin-up of the biogeochemical component), makes it suitable only for the analysis of ΔC_{ant} between 1994 and 2007, and not of cumulative C_{ant} until 1994 nor of air-sea C_{ant} fluxes in specific years. As explained in the RECCAP2 model evaluation chapter (Terhaar et al., 2023), all GOBMs are forced with a very similar atmospheric CO_2 mixing ratio (xCO_2) over the historical period. However, the atmospheric xCO_2 in the pre-industrial control simulations across the GOBM ensemble varies between 278 ppm and 287.4 ppm, leading to an underestimate of the C_{ant} storage for those models with a late starting date (Terhaar et al., 2023).

3 Results

3.1 Mean air-sea CO_2 fluxes 1985-2018

We start with a comparison of the average air-sea CO_2 flux in the two data classes (GOBMs, pCO_2-products) that cover the full period 1985-2018. We exclude data classes with fewer products for the sake of robustness, and show the comparison between all data classes in sections 3.2 and 3.3. The mean net Southern Ocean air-sea CO_2 flux 1985-2018 by the GOBM ensemble is -0.75± 0.28 PgC yr^{-1} and -0.73 ±0.07 PgC yr^{-1} (flux into the ocean) for the pCO_2-product ensemble mean (Figure 2a). While both ensemble means result in an almost identical ocean uptake of CO_2, the GOBM ensemble spread is four times larger.

All Southern Ocean regions are sinks of CO_2 based on the ensemble averages of the GOBMs and pCO_2-products (Figure 2). The subtropical seasonally stratified biome (STSS), which is a subduction area with deep winter mixed layer depth and intermediate chlorophyll concentration (Fay & McKinley, 2014), is the largest sink according to all data sets (GOBMs: -0.53±-0.17 PgC yr^{-1}, pCO_2-based products:-0.62±0.06 PgC yr $^{-1}$, Figure 2a). Second is the subpolar seasonally stratified biome (SPSS) (GOBMs: -0.13± 0.14 PgC yr^{-1}, pCO_2-products: -0.07± 0.02 PgC yr^{-1}), which is characterized by upwelling of old water, rich in natural carbon but with low anthropogenic carbon content. The upwelled water is also rich in nutrients, and thus a region with important biological activity. Note that three GOBMs simulate the SPSS to be a source of CO_2 to the atmosphere. The marginal sea ice (ICE) biome is the weakest CO_2 sink (GOBMs: -0.09±0.13 PgC yr^{-1}; pCO_2-products: -0.05±0.02 PgC yr^{-1}) due to sea ice acting as a lid that prevents carbon outgassing in winter, and is the smallest of all three biomes covering an area of about 60% the size of STSS or SPSS (Fay & McKinley, 2014). Four individual models suggest that the ICE biome is a weak outgassing region, but no other data set supports this.

In a zonal mean view (Figure 2b), the smallest uptake occurs between 62 and 55°S and the largest uptake around 40°S. However, the amplitude differs between data classes, with the pCO_2-products having a larger difference between minima and maxima (1.96 mol C m^{-2} yr^{-1}), than the GOBM ensemble mean (1.19 mol C m^{-2} yr^{-1}). Some of the individual GOBMs deviate from this pattern (see supplementary figure S5a for zonal means of individual models).

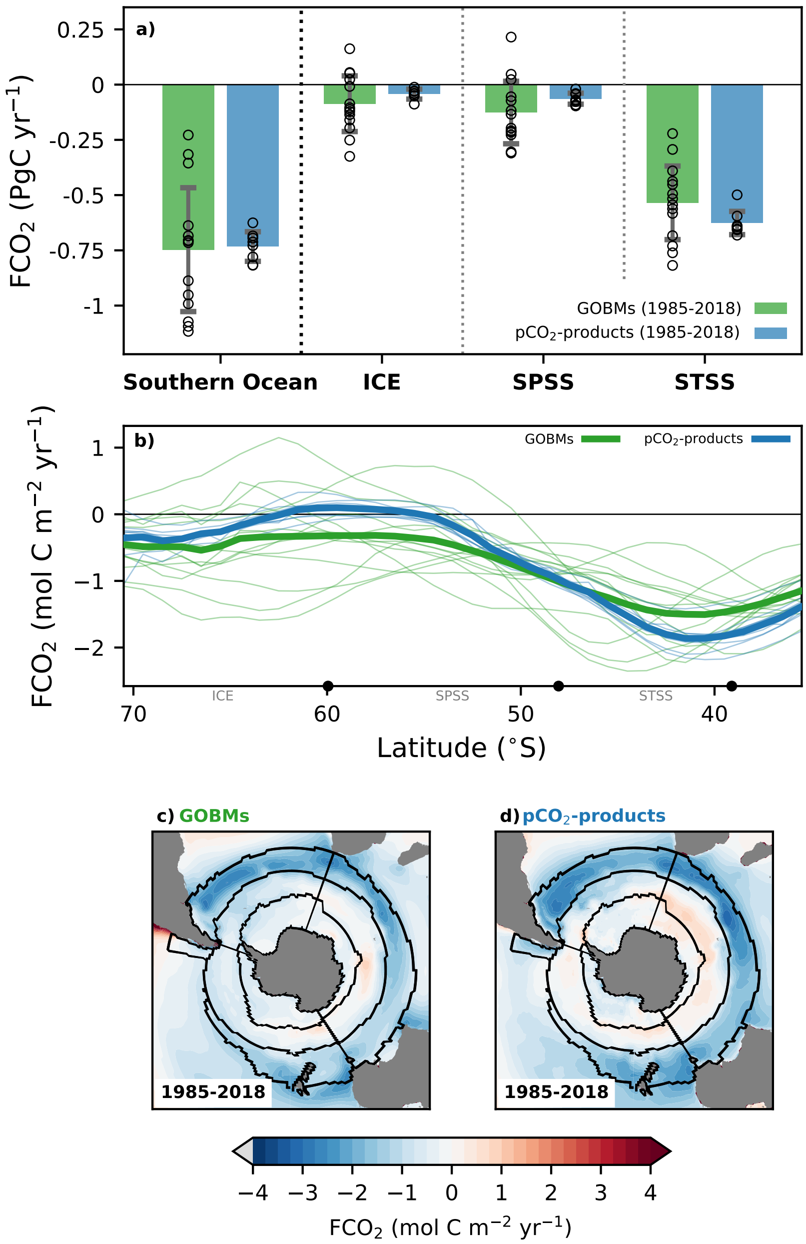

Figure 2. Temporal average of the Southern Ocean CO_2 net flux (FCO_2). A positive flux denotes outgassing from ocean to atmosphere. The temporal average is calculated over the period 1985 to 2018 for the global ocean biogeochemistry models (GOBMs) and pCO_2-products (Table 1). (a) The green and blue bar plots show the ensemble mean of the GOBMs and pCO_2-based data-products, and open circles indicate the individual GOBMs and pCO_2-products. The ensemble standard deviation (1σ) is shown by the error bars. The river flux adjustment added to the GOBMs is small (0.04 PgC yr^{-1}), its distribution over the biomes is described in section 2.3.1. (b) zonal mean flux density of the different data sets. Thick green and blue lines show the ensemble means, and thin green and blue lines show the individual GOBMs and pCO_2-products. Approximate boundaries for biomes are marked with black points on the x-axis. (c-d) maps of spatial distribution of net CO_2 flux for ensemble means of GOBMs, and pCO_2-products.

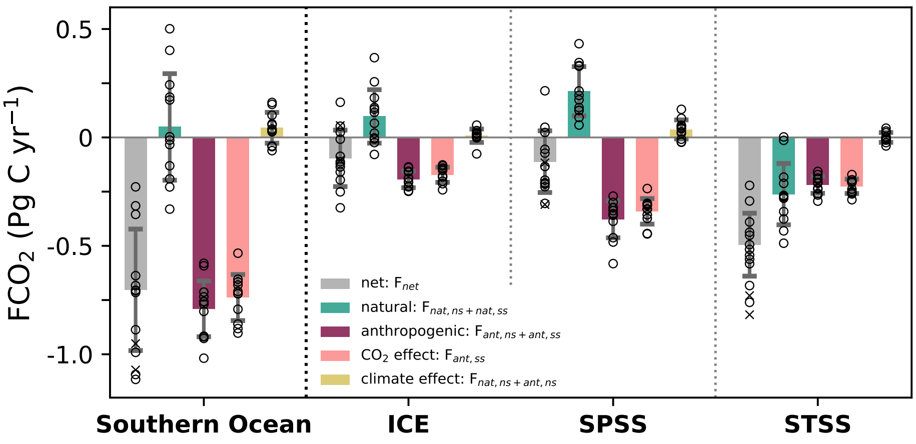

Figure 3. Decomposition of the modeled net air-sea CO_2 flux 1985-2018 into natural and anthropogenic CO_2 fluxes; as well as into CO_2 and climate effects. See method section 2.2.1 for explanation on this decomposition. The separation into natural and anthropogenic CO_2 fluxes is not possible for FESOM-REcoM-HR and MOM6-Princeton models as only simulations A and B are available. These models are only shown as crosses for net FCO_2 but not used for averaging. Hence, separation within this figure is coherent, but the net FCO_2 is slightly different from the net FCO_2 in Figure 2.

Regionally, significant differences emerge between the Atlantic, Indian and Pacific sectors of the Southern Ocean (Figure 2c-d). Within the STSS, large CO_2 fluxes into the ocean occur in the Atlantic and Indian sector across all data classes (Figure 2b-c, mean flux density: -1.93 mol C m^{-2} yr^{-1} and -2.05 mol C m^{-2} yr^{-1} for GOBMs and pCO_2-products, respectively, in the Atlantic sector, -1.44 mol C m^{-2} yr^{-1} and -1.89 mol C m^{-2} yr^{-1} in the Indian sector, and -1.22 mol C m^{-2} yr^{-1} and -1.54 mol C m^{-2} yr^{-1} in the Pacific sector). CO_2 outgassing locations differ across the data classes. In the GOBM ensemble mean, the outgassing is mainly confined to the Indian sector of the SPSS, whereas it is more widely spread in the pCO_2-product ensemble mean covering the Pacific and Indian Ocean sectors of the SPSS and the Indian sector in the ICE biome. The smooth appearance of the outgassing signal in the GOBM and pCO_2-product ensemble means may be partly attributable to averaging over multiple data sets and months and years.

3.1.1 Decomposition into anthropogenic and natural carbon fluxes and climate versus atmospheric CO_2 effects on the mean CO_2 flux

With the aid of the additional model simulations, we can decompose the net Southern Ocean air-sea CO_2 flux into natural and anthropogenic components, and separate the indirect effects of physical climate change and the direct geochemical effect of increasing atmospheric CO_2 mixing ratios. The GOBM ensemble mean indicates that the *natural* Southern Ocean carbon cycle without anthropogenic perturbation would be a small CO_2 source to the atmosphere of 0.05 PgC yr^{-1}, although with a large model spread as indicated by the standard deviation of 0.25 PgC yr^{-1} (Figure 3). In fact, six GOBMs simulate negative natural CO_2 fluxes, i.e., into the ocean, and six GOBMs simulate positive natural fluxes, i.e., out of the ocean. This also illustrates that the GOBM spread of net fluxes (standard deviation: 0.28 PgC yr^{-1}) is, to the first order, dominated by the model differences of natural fluxes (standard deviation: 0.25 PgC yr^{-1}), which may contain artifacts from model biases and drift (Terhaar et al., 2023). The spread of anthropogenic fluxes is smaller (0.13 PgC yr^{-1}). The small *natural* outgassing signal in the ensemble mean is a balance of natural CO_2 uptake in the STSS (-0.26±0.14 PgC yr^{-1}) and outgassing in the SPSS (0.21±0.11 PgC yr^{-1}) and ICE (0.10± 0.12 PgC yr^{-1}) biomes. This is in qualitative agreement with the patterns of natural CO_2 fluxes by Mikaloff Fletcher et al. (2007).

The *anthropogenic* perturbation (-0.79±0.13 PgC yr^{-1}) has turned the SPSS and ICE biomes, and possibly the entire Southern Ocean, from source to sink. The large anthropogenic flux contribution in the SPSS (-0.38±0.08 PgC yr^{-1}) suppresses the natural CO_2 outgassing flux. The STSS is a sink for both natural and anthropogenic flux components. The *direct effect of increasing atmospheric CO_2* enhances the Southern Ocean sink by -0.74±0.11 PgC yr^{-1} and is the largest signal in the anthropogenic perturbation. A smaller component stems from the climate change effect on this steady state CO_2-induced flux (Figure S6). The direct CO_2 effect is largest in the SPSS (-0.34±0.06 PgC yr^{-1}) where old water masses reach the surface that are undersaturated in anthropogenic carbon, followed by the STSS and ICE biomes (-0.23±0.03 PgC yr^{-1} and -0.17±0.03 PgC yr^{-1}). In the upwelling regions, the primary effect of rising atmospheric CO_2 is thus to suppress the outgassing of natural carbon.

The *effect of physical climate change and variability*, i.e., warming and changes in wind speed patterns and strength that provoke changes in circulation (Le Quéré et al., 2007; Lovenduski et al., 2007; Hauck et al., 2013), reduces the CO_2 flux into the ocean (+0.04±0.07 PgC yr^{-1}), but is overall small in comparison to the direct CO_2 effect. This climate change induced outgassing stems nearly entirely from the SPSS (+0.04±0.04 PgC yr^{-1}), with the largest contribution from the Indian sector followed by the Pacific (Figure S7). Thus, the climate change effect amplifies the natural CO_2 outgassing, which is also the largest in the Indian and Pacific sectors of the SPSS. The climate effect is a combination of climate effects on natural and anthropogenic CO_2 fluxes, which partly oppose each other (Figure S6).

3.2 The seasonal cycle of air-sea CO_2 fluxes in the Southern Ocean

We now shift our focus to seasonal fluxes by separating fluxes into separate winter (Figure 4) and summer (Figure 5) mean CO_2 fluxes. For this, we examine the period 2015-2018, for which all data sets are available (see Figure S8 for an annual mean figure for 2015-2018).

3.2.1 Winter

In winter, all but two data sets (one GOBM and BGC-float pCO_2-products) agree that the Southern Ocean is a sink of CO_2 (GOBMs: -0.83±0.40 PgC yr^{-1}, pCO_2 products: -0.48±0.08 PgC yr^{-1}; Figure 4a). The general pattern of strong uptake towards the north and a reduction towards the south is common to all data classes, though exceptions for individual GOBMs do exist (Figure 4a,b). Expounding on this, the strong uptake in the STSS is shown by all data sets, but further south the coherence disintegrates. Within the SPSS, there is considerable variation in position and magnitude of maximum outgassing with some GOBMs being a sink along the entire zonal mean (Figure 4a,b). Towards the southern reaches of the ICE biome, fluxes are more coherent as they are constrained by sea-ice cover in winter (Figure 4b). For the zonal means of individual GOBMs, see Figure S5.

The divergence between data class average flux estimates for the Southern Ocean are explained nearly entirely by differences in the SPSS (GOBMs: -0.15±0.32 PgC yr^{-1} and pCO_2 products: 0.15±0.09 PgC yr^{-1}, in Figure 4a). Note also that the spread of the individual GOBMs is the largest in the SPSS (0.32 PgC yr^{-1}), although it is also substantial in the other biomes (STSS: 0.29 PgC yr^{-1}, ICE: 0.13 PgC yr^{-1}) (Figure 5a).

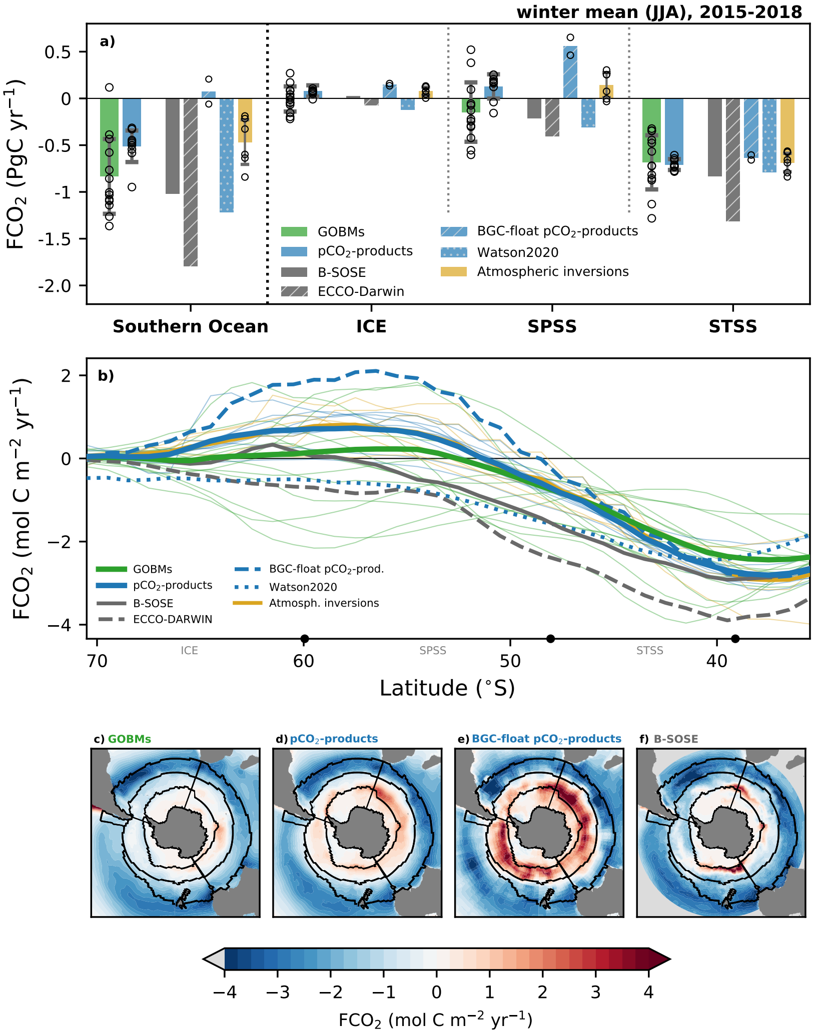

Figure 4. Average winter (June-August) air-sea CO_2 fluxes (FCO_2) in the period 2015-2018, (a) averaged over biomes, (b) zonal mean flux density, (c-f) maps of flux density. Same as Figure 2, but including also data sets with shorter coverage, and a map of the CO_2 flux from the BGC-float pCO_2-products (panel e), and B-SOSE (f), and hence focussing on the period 2015-2018 for all data sets for comparability. Note that the MPI model is excluded here. The zonal mean of individual models are presented in Figure S5c.

The SPSS is also where we see the largest impact of the inclusion of floats in the BGC-float pCO_2-products (Figure 4d,e), with the mean outgassing flux more than doubling that of the regular pCO_2-product ensemble.

The zonal differences and features of fluxes between data classes are also most distinct in the SPSS (Figures 4c-f). In short, the Atlantic sector of the SPSS has the lowest flux (weak source or even sink), while the Indian and Pacific sectors dominate the outgassing. The data-assimilated model B-SOSE has stronger localized outgassing compared with the other data classes but bear in mind that B-SOSE is only one data sets (Figure 4f), while the other data classes (Figures 4c-e) represent up to 13, thus potentially averaging out local signals. The outgassing hotspot at the boundary between the Atlantic and Indian sectors of the SPSS can also be recognized in the pCO_2-products (Figure 4d). The second hotspot in the western Pacific SPSS is not distinguishable in the other data sets.

3.2.2 Summer

In summer, GOBMs, pCO_2-products and inversions largely show CO_2 uptake within the three Southern Ocean biomes, and outgassing north of the STSS (Figure 5a-b). In contrast to winter, the GOBM ensemble mean for summer 2015-2018 (-1.04±0.77 PgC yr^{-1}) underestimates the CO_2 uptake relative to the pCO_2-product ensemble mean (-1.46±0.18 PgC yr^{-1}, Figure 5a). This also holds true for the data-assimilated models, where B-SOSE even simulates outgassing in the SPSS (Figure 5a,b,f). Otherwise, the data-assimilated models, B-SOSE and ECCO-Darwin, deviate substantially from the other data classes. The differences between pCO_2-products with and without BGC-float data are hardly apparent in summer (Figure 5a, compared to 4a). This could be due to a smaller discrepancy between float and ship-data in summer, and/or a dominance of SOCAT data in summer for the ship+float estimate. For context, for the period 2015 through 2018, BGC-float data account for up to 70% of winter pCO_2 monthly by 1°×1° measurements in the Southern Ocean (SOCAT + floats), while in summer the floats represent only 20% (Bakker et al., 2016; Bushinsky et al., 2019).

While the STSS was a region of coherence between data classes in winter (Figure 4), it is the main source of the discrepancy between the GOBM and pCO_2-product ensemble means in summer (GOBMs: -0.40±0.28 PgC yr^{-1}, pCO_2-products: -0.73±0.08 PgC yr^{-1}). The discrepancy is comparatively smaller in the SPSS (GOBMs: -0.33±0.34 PgC yr^{-1}, pCO_2-products: -0.42±0.06 PgC yr^{-1}). We note that CO_2 fluxes for both GOBMs and pCO_2-products show less variation from ICE to STSS in summer compared to winter (Figure 4b vs 5b, respectively). There is, nevertheless, an offset with lower GOBM CO_2 uptake than in pCO_2-products north of 55°S, and vice versa to the south. Also, the GOBM spread in the represented magnitude of the fluxes is large. In absolute terms, the GOBM ensemble spread of fluxes in summer (from -2.03 to +0.28 PgC yr^{-1}) is larger than in winter (from -1.36 to 0.12 PgC yr^{-1}) or than the spread in the annual mean (from -1.30 to -0.38 PgC yr^{-1}; see Figure S5b for zonal means of individual GOBMs). This mirrors the difficulty in representing the balance between physical and biological processes in summer, which is further assessed in the next two sections 3.2.3 and 3.2.4.

3.2.3 The full seasonal cycle

We diagnose distinctly different seasonal cycles in the three biomes. The ICE biome has a rather clear maximum uptake in summer in the GOBM and pCO_2-product ensemble means, as well as most individual data sets (Figure 6a). In the STSS, the pCO_2-products suggest a weak seasonal cycle with a maximum uptake in autumn (Figure 6c), while the majority of GOBMs simulate a maximum CO_2 uptake in winter and a substantially smaller flux in summer. The largest disagreement occurs in the SPSS, where the seasonal cycle transitions from winter outgassing in the ICE biome to summer outgassing in the STSS

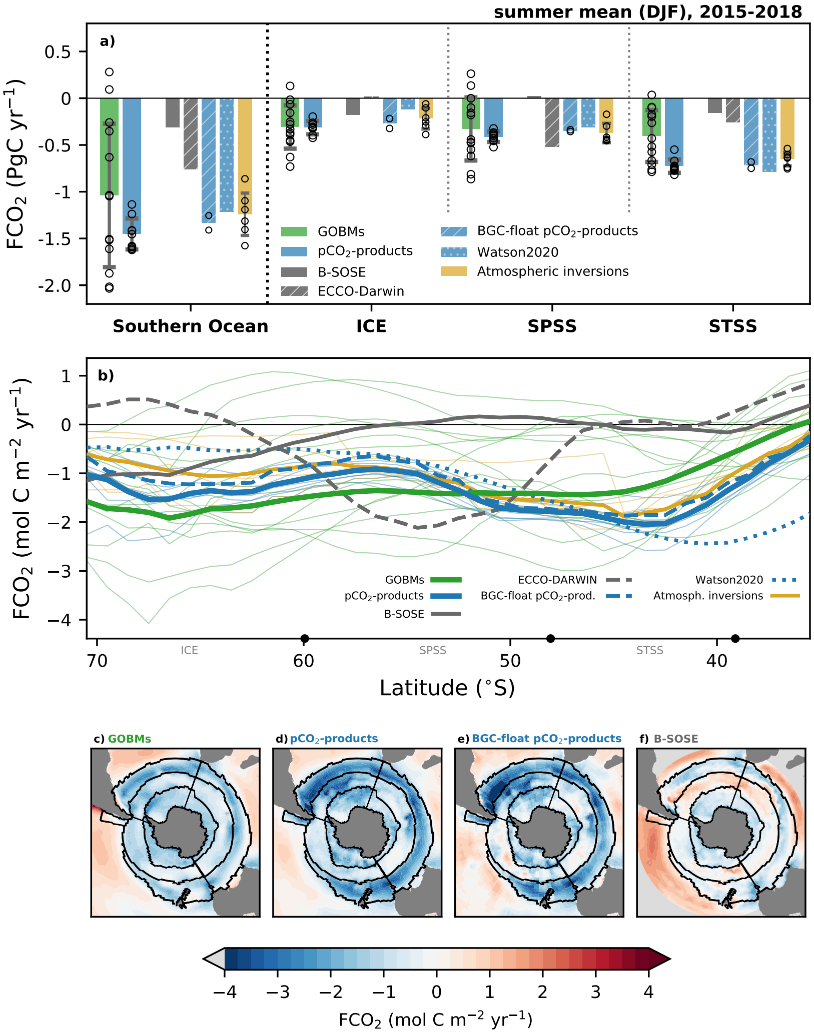

Figure 5. Average summer (December-February) air-sea CO_2 fluxes (FCO_2) in the period 2015-2018. Same as Figure 4, but for summer. The zonal mean of individual models are presented in Figure S5b.

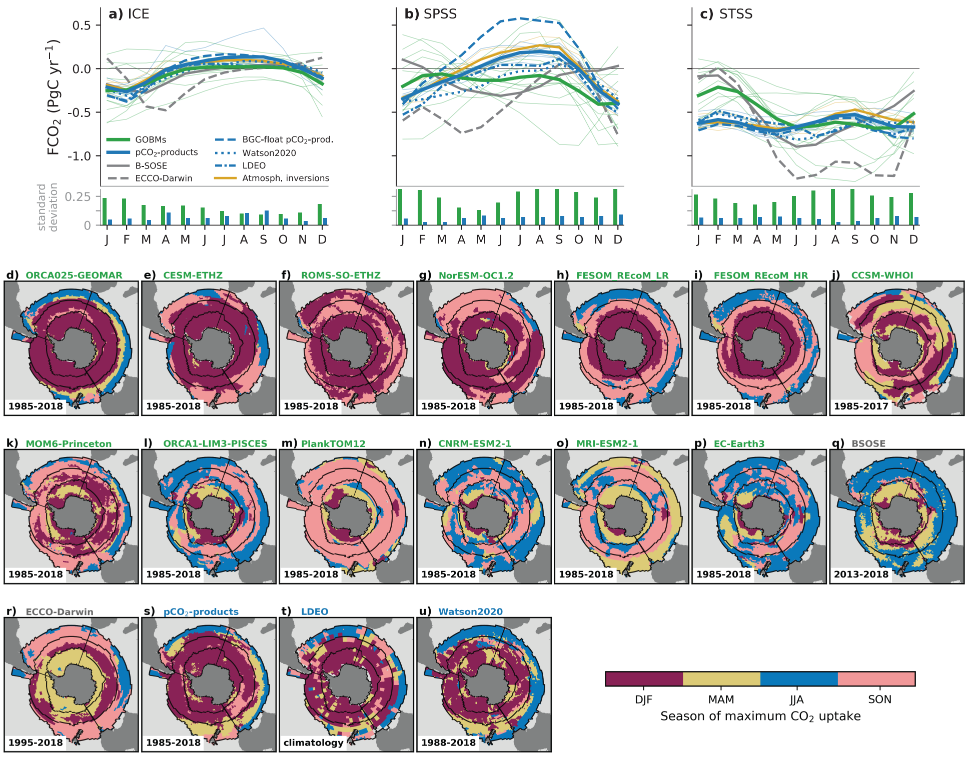

Figure 6. The seasonal cycle of air-sea CO_2 flux in the Southern Ocean separated by biomes for all data sets as indicated in the legend, a) subtropical seasonally stratified (STSS) biome, b) subpolar seasonally stratified (SPSS) biome, c) ice (ICE) biome. Thin green and blue lines depict individual GOBMs and pCO_2-products, and thick lines indicate their ensemble means. Note that the MPI model is excluded here. The ensemble standard deviation (1σ) is shown by the bars for each month. Panels (d-u) present the season of maximum CO_2 uptake per grid cell in the individual GOBMs, data-assimilated models and the ensemble mean of the pCO_2-products over the period indicated in the panels (varies by data set). See Figure S9 for the individual pCO_2-products (panel d-u equivalents) and Figure S10 for the seasonal cycle in all nine subregions (equivalent to panels a-c but further split into Atlantic, Pacific and Indian Ocean sectors).

biomes. Here, atmospheric inversions and pCO_2-products (including the BGC-float pCO_2 products), suggest the maximum CO_2 uptake to be in summer. In winter, the BGC-float pCO_2-products more than double the estimates of outgassing relative to the other pCO_2 products (Figure 6b). The GOBM ensemble average roughly agrees with this seasonal pattern, but simulates a reduced seasonal cycle amplitude (Figure 6b). The GOBM spread is large, not only in terms of magnitude but also phasing of the seasonal cycle in the SPSS (8 out of 13 GOBMs simulate the maximum uptake between November and January; Figure 6d-r). This illustrates how the transition between the different seasonal cycle regimes affects particularly the representation of the seasonality in the SPSS. In summary, most GOBMs and pCO_2-products agree on a summer peak in the ICE biome (but exceptions exist, Figure 6d-r), and a winter peak to the north of the Southern Ocean biomes. The largest discrepancy between data sets is where and how swift this transition occurs. While the use of static biomes adds to the discrepancies seen in the averaged seasonal cycles (Figure 6a-c), the disagreement between the phasing of individual GOBMs is likely a much larger contributor to these discrepancies (Figure 6d-p). We now turn to an investigation of the thermal and non-thermal effects on the seasonal cycle, which may help explain these discrepancies.

3.2.4 Thermal versus non-thermal effects on the seasonal cycle

The seasonal cycle of CO_2 fluxes in the Southern Ocean is a balancing act between competing thermal and non-thermal drivers (Mongwe et al., 2016, 2018; Prend et al., 2022). DIC drawdown by biological production leads to a summer maximum in CO_2 uptake, whereas upwelling and entrainment of DIC-rich water into the mixed layer in autumn and winter leads to a minimum in CO_2 uptake or even outgassing (Metzl et al., 2006; Mongwe et al., 2018). Seasonal variations in mixed layer temperature further affect the solubility of CO_2, with lower (higher) temperatures increasing (decreasing) solubility and thus promoting CO_2 uptake (outgassing) (Takahashi et al., 2002).

The thermal and non-thermal components of pCO_2 can be decomposed to determine the dominant driver on monthly timescales (Figure 7; Mongwe et al., 2018). Here, we do this by estimating the absolute difference of the rate of change of the thermal and non-thermal components (Figure 7; Eq. 3). The contribution of salinity and total alkalinity to seasonal pCO_2 changes are small in the Southern Ocean and compensate for each other on a seasonal scale (e.g., Sarmiento & Gruber, 2006; Lauderdale et al., 2016), thus we here consider the non-thermal component to be predominantly DIC-driven.

In general, the seasonal cycle phasing of the thermal component of the GOBMs agrees well with those of the pCO_2-products (Figure 7a-c). This should not come as a surprise, as GOBMs are forced by atmospheric reanalyses which assimilate observed SST (Doney et al., 2007). As a result, the thermal component of the pCO_2 seasonal cycle in the GOBMs (forced by reanalyses) compare much better to the thermal component derived from the pCO_2-products than fully coupled Earth System Models (Mongwe et al., 2016, 2018). The non-thermal contribution is thus the primary reason for the spread between GOBMs, and for the differences between GOBMs and pCO_2-products (Fig. 7a-c). Thus, we group GOBMs based on whether they are predominantly DIC or thermally driven across all three biomes (Fig. 7d-f, Table S2), which we term DIC-dominant or DIC-weak respectively.

In DIC-weak GOBMs, the strong underestimation of the non-thermal component causes these models to be too strongly temperature driven across the year (Figure 7). This then tends to shift the timing of uptake towards the colder months (when CO_2 solubility is largest), while the role of biologically driven uptake in spring and summer is suppressed in favor of warming driven outgassing. This effect is largely confined to the SPSS and to a lesser extent also the STSS, and can account for the mismatch in the seasonal cycle seen in some GOBMs. For example, in the SPSS, nearly all GOBMs and specif-

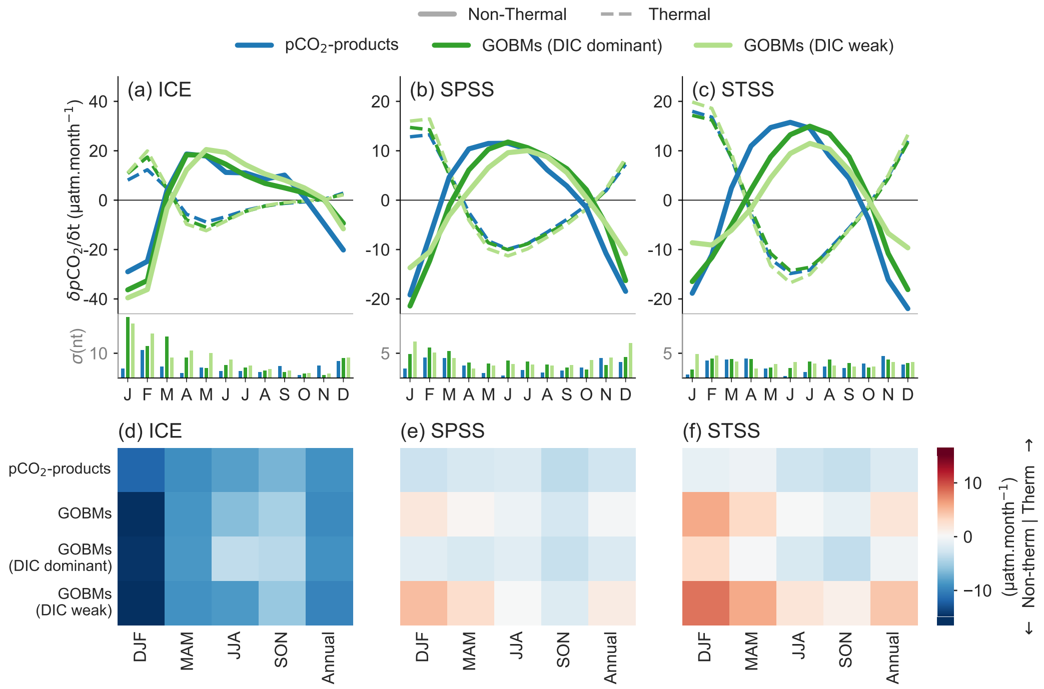

Figure 7. (a-c): Seasonal cycle of the rate of change of the thermal ($pCO_2^{T'}$, dashed lines) and non-thermal ($pCO_2^{nonT'}$, solid lines) components of ocean surface pCO_2 on monthly time scales given in μatm month^{-1} (Eq. 2). The bars on the bottom show standard deviations of the non-thermal component. Models have been grouped into DIC dominant/weak, where the DIC weak models have a thermal contribution >0 for the mean of the STSS and SPSS (shown in d-f; see Figure S11 for individual global and regional ocean biogeochemistry models, and Table S2 for the DIC dominant/weak model groups). (d-f): λpCO_2, the difference of the thermal and non-thermal (DIC) components of ocean surface pCO_2 as in Mongwe et al. (2018). When $\lambda pCO_2 > 0$ (red) indicates temperature dominance, and $\lambda pCO_2 < 0$ (blue) indicates that the non-thermal component (i.e., DIC) is dominant. The MPI model is excluded in this analysis.

ically all DIC-weak GOBMs have a shifted season of maximum uptake from summer to spring/winter, i.e., towards the colder months. (Fig. 6 and Table S2). In terms of the underlying mechanisms driving the too weak non-thermal component, we hypothesize that a lack of deep vertical mixing in winter leads to too little entrainment of DIC-rich deep waters, while simultaneously allowing for too early primary production (which may then shift the growing season earlier and reduce biologically driven summer uptake). Notably, the bias in pCO_2 is largest in summer (DJF), followed by autumn (MAM), and is about twice as large in the DIC-weak GOBMs than in the DIC-dominant GOBMs (Figure S13). This further supports the lesser importance of thermal processes in the STSS and SPSS regions evident in the pCO_2-products.

In the ICE biome GOBMs and pCO_2-products tend to agree much more closely in terms of their representation of the seasonal cycle (Fig. 6a). This is likely related to the strong role the seasonal advance and retreat of sea ice plays in air-sea CO_2 fluxes, both through its effect as a physical barrier, as well as through its effect on vertical mixing and light availability (thus impacting both physical and biological pathways of DIC into and out of the mixed layer, (Bakker et al., 2008; Shadwick et al., 2021; M. Yang et al., 2021)).

3.3 Temporal variability and trends in Southern Ocean air-sea CO_2 flux

We next inspect the temporal evolution of the air-sea CO_2 fluxes from 1985-2018 (Figure 8). In this annually-resolved perspective, we also discuss the mean fluxes for data sets that are not available for the full time-period. While the STSS was a net-sink region throughout the period, the SPSS and ICE have turned from neutral (around 0 PgC yr^{-1}) to net sink regions since 1985, based on GOBM and pCO_2-product ensemble mean estimates. This also holds for most individual GOBMs as only two of them simulate either the ICE or the SPSS biome to still be regions of outgassing at the end of the time series (CCSM-WHOI and EC-Earth3).

Acknowledging some agreement between GOBMs and pCO_2-based product ensemble means despite large spread across GOBMs (Figure 8 bars), substantial deviations among individual data sets appear. B-SOSE (2015-2018) suggests a 0.25 PgC yr^{-1} smaller uptake than the GOBM and pCO_2-product ensemble means for the entire Southern Ocean (Figure 8a). ECCO-Darwin has the largest flux estimate into the ocean in the SPSS and the entire Southern Ocean (1.30 PgC yr^{-1}, 1985-2018). Notably, the two data-assimilated models B-SOSE and ECCO-Darwin differ by a factor of 2 for the Southern Ocean wide estimate. In agreement with previous reports (Bushinsky et al., 2019), BGC-float pCO_2-products suggest Southern Ocean uptake to be 40% (0.4 PgC yr^{-1}) smaller than the pCO_2-products without BGC-float data (2015-2018). This discrepancy originates largely in the SPSS, where the BGC-float pCO_2-products estimate outgassing of 0.14 PgC yr^{-1}, and the ensemble mean of the SOCAT-only-based pCO_2-products estimate a CO_2 uptake of -0.13 PgC yr^{-1}. Smaller contributions to the deviation stem from the STSS and ICE biomes where BGC-float pCO_2-products report a smaller uptake by 0.14 PgC yr^{-1} when compared with the regular pCO_2-products. The Watson2020-product is generally close to the other pCO_2-products, with the exception of the SPSS where it suggests a flux of -0.18 PgC yr^{-1} (1985-2018), which is larger than any other pCO_2-product. The origin of the large SPSS difference in Watson2020 could, in part, be attributed to subtle differences in method choices in addition to different flux parameterisations (Watson et al., 2020). The atmospheric inversions produce a somewhat lower sink (-0.64 PgC yr^{-1}, average over three inversions 1985-2018), but are generally close to the pCO_2-products, as they mostly use surface pCO_2-products as a prior (Table 2 and Friedlingstein et al., 2022). There is also slightly higher interannual variability in the atmospheric inversion ensemble mean, but this is likely due to the small ensemble size.

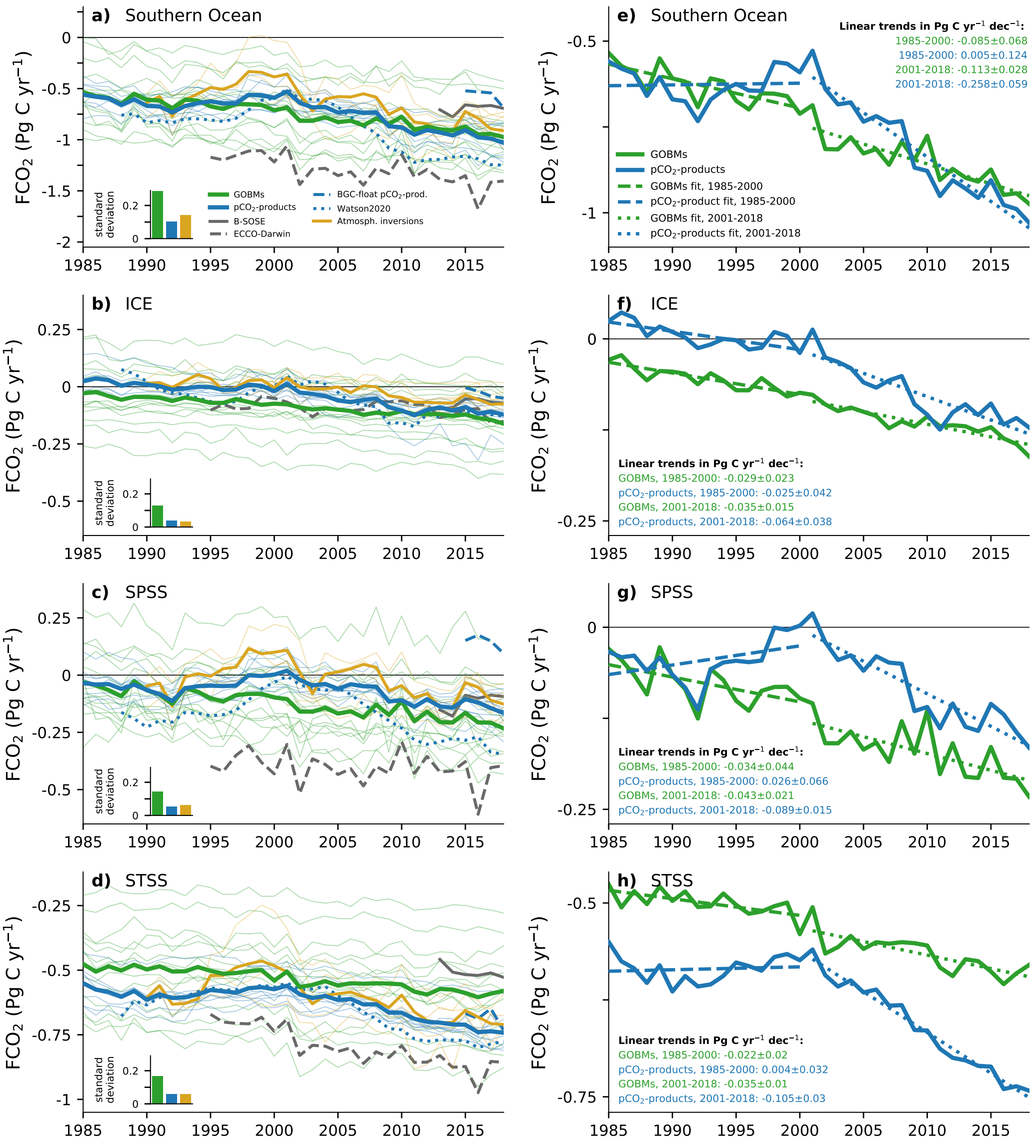

Figure 8. Temporal evolution of the Southern Ocean air-sea CO_2 flux for a) the entire Southern Ocean, and the b) subtropical seasonally stratified, c) subpolar seasonally stratified, and d) ice biomes. The ensemble standard deviation (1σ) averaged over the whole time series, is shown by the bars. Panels (e-h) are the same as panels (a-d) for the GOBM ensemble average and pCO_2-product ensemble average only, with linear trends between 1985-2000 and 2001-2018 as the dashed and dotted lines, respectively. The uncertainty range of the trend is calculated as one standard deviation of the trends across all GOBMs and pCO_2-products, respectively. Note the different y-axis scales. The separation into Atlantic, Pacific and Indian Ocean sectors is shown in Figure S12.

The temporal variability is quantified as the amplitude of 'interannual variability' (IAV). This is calculated as the standard deviation of the detrended time-series, as defined in Rödenbeck et al. (2015); Friedlingstein et al. (2022) which, in reality, captures both interannual and decadal variability components. Following this definition, the pCO_2-products have a larger interannual variability for the Southern Ocean wide integrated flux (0.09 PgC yr^{-1}, range 0.04 to 0.16 PgC yr^{-1}) compared to the GOBMs (0.06 PgC yr^{-1}, range 0.03 to 0.10 PgC yr^{-1}). Notably, the MPI-SOM-FFN pCO_2-product, which formed the basis of previous reports on Southern Ocean decadal variability (Landschützer et al., 2015), has the largest IAV of 0.16 PgC yr^{-1}, about 60% larger than the next largest pCO_2-product IAV. This is in line with previous studies that found that the MPI-SOM-FFN approach may overestimate Southern Ocean variability by 30% (Gloege et al., 2021) and the decadal trend 2000-2018 by 130% (Hauck et al., 2023). Within the Southern Ocean, the strongest IAV is found in the SPSS region (0.04 PgC yr^{-1} GOBMs, 0.05 PgC $yr^{-1}$$pCO_2$-products), followed by the STSS (0.02 PgC yr^{-1} GOBMs, 0.03 PgC yr^{-1} pCO_2-products) and ICE biome (0.02 PgC yr^{-1} for both data classes). Within the subpolar biome, the Indo-Pacific sector has a higher IAV (0.02 PgC yr^{-1}) than the Atlantic sector (0.01 PgC yr^{-1}). The large contribution to interannual variability in the SPSS may well be linked to the largest amplitude of the seasonal cycle of CO_2 flux (see section 3.2.3).

To assess the decadal-scale trends, we fit linear trends to the periods 1985-2000 and 2001-2018 (Figure 8e-h) with the year 2000 marking roughly the mid of the considered time period and the inflection point in global ocean CO_2 uptake (Gruber et al., 2023; Landschützer et al., 2016). The pCO_2-products suggest a stagnation of the flux in the STSS, and even a flux decrease in the SPSS prior to 2000. In contrast, GOBMs suggest a continued increase in the sink in the STSS and SPSS in the same period. In the ICE biome, GOBMs and pCO_2-products result in an increasing trend (Figure 8h). After 2000, pCO_2-products and GOBMs agree on a trend towards more CO_2 uptake, which is significantly different from zero in all biomes except for $pCO-2$-products in the ICE biome (see numbers in Figure 8e-h). However, they differ substantially in magnitude between GOBM and pCO_2-product ensemble means, particularly in the STSS (Figure 8f). The discrepancies in the magnitude of the trend act to decrease the gap between GOBM and pCO_2-product ensemble means in the SPSS and ICE biomes, but lead to the divergence in the flux estimate in the STSS.

On a sub-biome level (i.e., Atlantic, Indian, and Pacific sectors), all three sectors in the STSS were CO_2 sinks throughout the period and had weaker trends (less negative) before 2000 compared to the period after 2000 (Figure S12). In the SPSS, the Indian and Pacific sectors are characterized by intermittent outgassing and uptake patterns, in line with observations from BGC-floats (Prend et al., 2022). In the SPSS, only the Atlantic sector has a net uptake throughout the period, and the Indian Ocean sector shows the largest model spread of all three sectors (as in the STSS). In the ICE biome, a consistent quasi-linear evolution is apparent in all sectors. We further analyze divergence and drivers of trends in section 3.3.2.

3.3.1 Comparison with in-situ pCO_2

Here, we evaluate the accuracy of pCO_2 across data classes since pCO_2 is the dominant driver of air-sea CO_2 flux variability at a monthly scale (Landschützer et al., 2016). All data sets are compared with observations (monthly gridded SOCAT v2022 data set Sabine et al., 2013; Bakker et al., 2016, 2022). The RECCAP2 data sets are subsampled to match the SOCAT observations in time and space, meaning that we do not assess sampling biases, but rather the mismatch between the observed and estimated pCO2.

The comparison of the RECCAP2 GOBMs and pCO_2-products with gridded in-situ pCO_2 from SOCAT v2022 shows relatively good agreement (Figure 9a). The SOCAT pCO_2 data shows large interannual variability due to spatially and temporally vary-

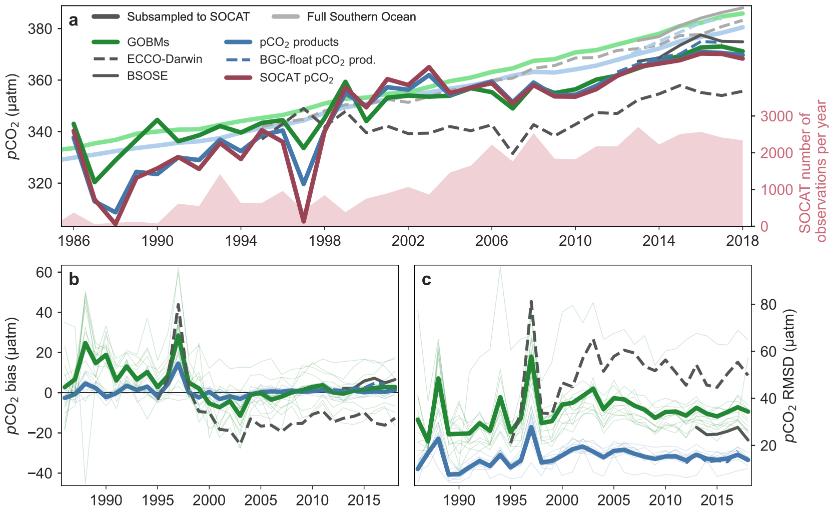

Figure 9. Comparison of surface mean pCO_2 for the whole Southern Ocean between global ocean biogeochemistry models (GOBMs) and pCO_2-products with in situ observations (gridded SOCAT v2022 data set Sabine et al., 2013). (a) Time-series of annually-averaged pCO_2 from GOBMs (green), data-assimilated models (grays), and pCO_2–products (blue). The darker shaded lines show the annual mean as calculated from the data sets subsampled to match the historic SOCAT sampling. The lighter shades show the annual mean calculated for the full coverage. The dark red line depicts the annual mean pCO_2 from SOCAT observations without interpolation. The assimilation products (ECCO-Darwin and B-SOSE) are kept separate as they have different time series lengths (shown by dashed and solid gray lines respectively). The light red area plot (right y-axis) shows the number of monthly by $1^\circ \times 1^\circ$ gridded SOCAT observations per year. (b) The bias of pCO_2 for all data classes (subsampled to match SOCAT observations, dark lines in a) relative to SOCAT pCO_2 observations (solid dark red line in a). (c) The root mean squared difference (RMSD) between SOCAT observations and estimates for all data classes. Bias and RMSD were calculated on a monthly by $1^\circ \times 1^\circ$ resolution, and the bias and RMSD were averaged to annual means afterwards. A plot of RMSE and bias for SPSS and STSS biomes and different seasons is presented in supplementary Figure S13.

ing sampling efforts from year to year, particularly prior to 2000 when samples are fewer and thus carry more weight (Figure 9a). For example, in 1997, SOCAT pCO_2 is anomalously low due to high sampling density in the Ross Sea during summer when primary production drives intense CO_2 drawdown (Arrigo & van Dijken, 2007). The pCO_2 products have a lower bias and a narrower spread than the GOBMs prior to 2000 ($1.7\pm4.3\mu$atm and $10.7\pm8.0\mu$atm respectively), with the bias and the spread decreasing after 2000 for both classes ($-0.3\pm2.6\mu$atm and $-0.9\pm3.9\mu$atm, Figure 9b). This comparison of simulated to observed pCO_2 at observation sites demonstrates that GOBMs are capable of reproducing SOCAT pCO_2 and its temporal evolution on large spatial and annual time-scales. Thus, for the period after 2000, the differences in CO_2 flux trend for the entire Southern Ocean between GOBMs and pCO_2-products (Figure 8) cannot be attributed to differences in pCO_2 in the regions where observations were taken. Instead, the differences arise primarily from areas where no pCO_2 observations exist, as also concluded in Hauck et al. (2020). The pCO_2 time-series calculated from the full coverage results in a lower pCO_2 value in the pCO_2-products than in the GOBMs (Figure 9a), which could explain the stronger CO_2 flux trend in the pCO_2-products (Figure 8). This discrepancy between pCO_2-products and GOBMs is larger in the last ten years (2009-2019: 5.8 μatm) than the previous decade (1999-2008: 2.8 μatm, Figure 9a). Nevertheless, the RMSD calculated from monthly mean data is higher in GOBMs than in pCO_2-products (Figure 9c). This is expected as the pCO_2-products are trained to fit the observations and further illustrates the GOBMs' deficiencies in simulating seasonal and spatial variability of the CO_2 uptake.

The assimilation model, ECCO-Darwin, has a negative bias after 2000 (-13.5 ± 3.0 μatm; Figure 4b), but this negative bias is not strongly reflected in the mean of the non-subsampled data, with the mean pCO_2 still being larger than that of the pCO_2-products, which do not underestimate the pCO_2 relative to SOCAT. This further emphasizes that sampling distribution may play an important role in the magnitude of the biases calculated in any model. The pCO_2 summer sampling bias in the Southern Ocean has long been recognised as a potential source of biases in pCO_2 estimates, particularly for the pCO_2-products that rely heavily on the in-situ data (Metzl et al., 2006; Gregor et al., 2017; Ritter et al., 2017; Djeutchouang et al., 2022). The SOCCOM project increased the number of winter samples with pH-enabled profiling floats (from 2014), suggesting stronger outgassing during winter than previously shown (Gray et al., 2018). In RECCAP2, the B-SOSE assimilation model and the BGC-float pCO_2-products both make use of this data (Verdy & Mazloff, 2017; Bushinsky et al., 2019). Both of these estimates overestimate pCO_2 relative to SOCAT pCO_2 highlighting the challenge in consolidating ship-based SOCAT and BGC-float data.

3.3.2 Climate versus CO_2 effects on trends in CO_2 flux

Our analysis so far has indicated that the GOBMs reproduce seasonal temperature effects on CO_2 flux reasonably well (Figure 7), and a larger uncertainty is associated with imprints of circulation and biological activity. Next, we inspect the zonal mean and spatial patterns of the CO_2 flux trend 1985-2018 (Figure 10). The pCO_2-products place the largest trend towards more CO_2 uptake in the entire ICE biome; however, data in this region is sparse and there is larger variability between pCO_2 products here (see also Figure 8). The pCO_2-products show a secondary peak in the STSS between about 40 to 45°S. The GOBMs in contrast have a large meridional gradient in the ICE biome with a peak in the trend between 60 and 65°S that is reduced in magnitude towards Antarctica. The secondary peak in the STSS is hardly apparent and also displaced southwards compared to the pCO_2-products. In addition, the pCO_2-products exhibit trends towards less CO_2 uptake in the Pacific and eastern Indian sector of the SPSS (Figure 10a-b). Although the difference in flux density between GOBMs and pCO_2-products is larger in the ICE biome, the discrepancy in the STSS contributes more to the total flux trend discrepancy due to the larger area of the STSS biome (Figure 8). The trend over 1985-2018

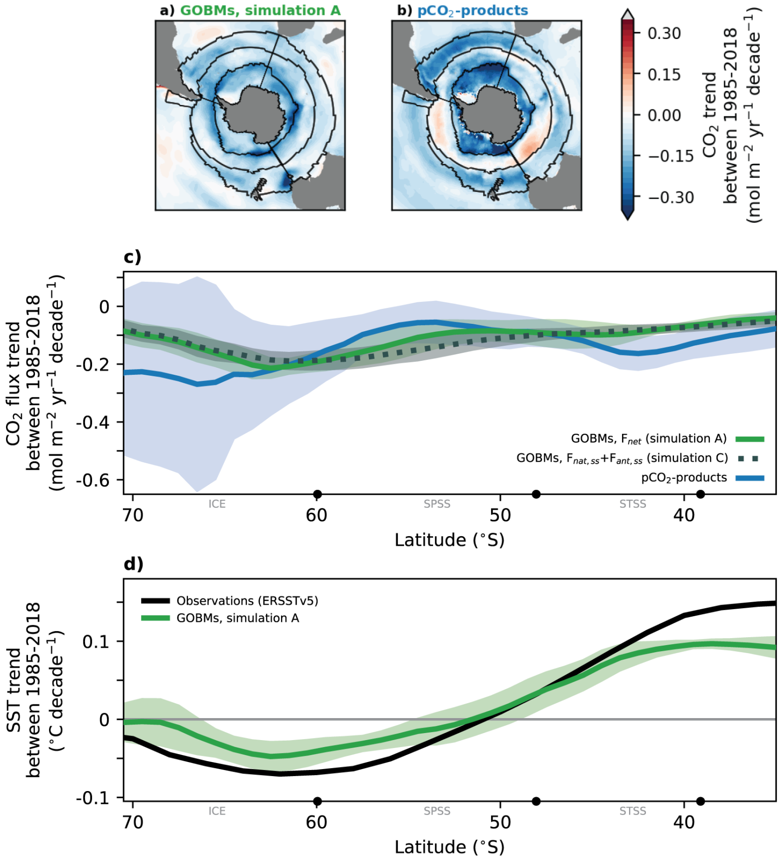

Figure 10. CO_2 flux trend between 1985 and 2018. (a-b) Spatial maps of the net CO_2 flux trend, for (a) the global ocean biogeochemistry models and (b) the pCO_2-products. (c) Zonal mean CO_2 flux trend 1985-2018 for the net CO_2 flux (blue: pCO_2-products, green: GOBMs) and the GOBM flux of $F_{nat,ss}$ and $F_{ant,ss}$, i.e., the flux as expected from increasing atmospheric CO_2 alone (green, dashed). (d) The sea surface temperature (SST) trend 1985-2018 in the GOBMs (green) and in the observational data set (black, NOAA Extended Reconstructed Sea Surface Temperature, ERSST, Version 5 (Huang et al., 2017)). Supplementary figures split this analysis in the periods 1985-2000 (Figure S14) and 2001-2018 (Figure S15). Individual GOBM trends for F_{net}, as well as $F_{nat,ss}$ plus $F_{ant,ss}$ and SST are shown in Figure S16.

includes some compensation between the trends over 1985-2000 and 2001-2018 (see Figures S14-S15). While the GOBMs show similar weak trends towards more uptake before and after 2000, the pCO_2-products show a trend towards less uptake in the earlier period 1985-2000 throughout the Southern Ocean except in the Weddell and Ross Seas. In the later period 2001-2018, the pCO_2 products estimate a much stronger trend towards more CO_2 uptake everywhere, as also shown in Figure 8. The CO_2 flux trends in the GOBMs are largely driven by increasing atmospheric CO_2 levels (simulation C in Figure 10c). However, the trend is reduced by climate change and variability throughout the SPSS and strengthened in the northern part of the ICE biome (compare simulations A that represents net FCO_2 and C that represents only steady state natural and anthropogenic fluxes, in Figure 10c). The effect of climate change and variability is substantially smaller than the uncertainty in the pCO_2-products. In line with GOBMs capturing the thermally-driven component of the pCO_2 seasonal cycle (Figure 8), we can also demonstrate that the GOBMs simulate sea surface temperature trends 1985-2018 rather well (Figure 10d). This is related to the choice of forcing the GOBMs with reanalysis data that itself depends on sea surface temperature observations (Doney et al., 2007). In contrast to fully coupled Earth System models in CMIP6 (Beadling et al., 2020), the suite of models used here capture the decadal trend pattern of warming along the northern flank of the Antarctic Circumpolar Current (ACC), and cooling in the south (Figure 10, Armour et al., 2016; F. Haumann et al., 2020). The lack of warming south of 50°S was previously related to the wind-driven upwelling of deep water that had not yet been exposed to anthropogenic warming and by northward heat transport (Armour et al., 2016). More recently, the cooling was suggested to be caused by increased freshwater export from the ice region, which increases stratification and thus reduces the upward heat flux from below by warm water masses (F. Haumann et al., 2020). While the GOBM ensemble mean captures the latitudinal structure of the SST trend well, it underestimates the magnitude of peak cooling at around 60°S as well as peak warming north of 40°S. Overall, however, the GOBM ensemble mean captures the latitudinal structure of the SST trend well. We can therefore not relate the discrepancies in the trend of the CO_2 flux to temperature biases. This leaves data sparsity as a reason for potential biases in the trend in the pCO_2-products, and biases in ocean circulation, sea ice and biology as possible reasons for biases in GOBMs.

3.4 Interior ocean storage of anthropogenic carbon

The focus of this section is the anthropogenic perturbation of dissolved inorganic carbon (DIC) in a subset of the GOBMs (see section 2.2.1), and in particular its accumulation rate over the period 1994 to 2007 (ΔC_{ant}), in comparison with the eMLR(C*) observational estimate (Gruber, Clement, et al., 2019) and the ocean inverse model OCIMv2021 (DeVries, 2022). The eMLR(C*) product uses a multiple linear regression approach to estimate ΔC_{ant} and captures both the influence of CO_2-driven and climate-driven change in sea-air CO_2 fluxes and transports, whereas OCIMv2021 captures only the CO_2-driven changes.

All data classes agree in having the largest ΔC_{ant} inventories within and to the north of the STSS biome (Figure 11), whose southern boundary approximately corresponds to the northern edge of the ACC. This pattern is related to the mechanisms by which C_{ant} is taken up at the surface and exported to depth (Mikaloff Fletcher et al., 2006; Morrison et al., 2022; Bopp et al., 2015). Subpolar upwelling exposes old C_{ant}-poor waters to elevated atmospheric CO_2 concentrations and this, combined with strong winds, drives a large influx of C_{ant} in the SPSS biome (Figure 12a-c). A small fraction of the C_{ant} moves southward and is exported within Antarctic Bottom Waters, while the largest fraction is transported northward within the upper cell of the meridional overturning circulation. C_{ant} air-sea fluxes remain elevated throughout the northward path, and are reinforced by the deep mixed layers in the regions where mode and intermediate waters are formed,

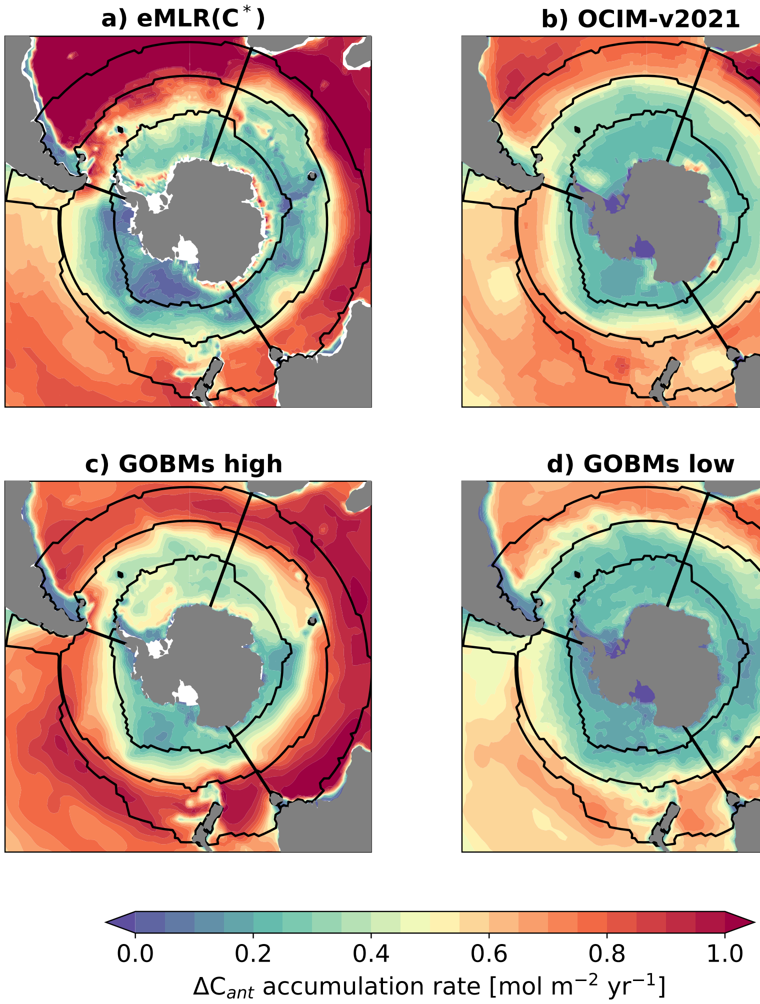

Figure 11. ΔC_{ant} yearly accumulation rate over the period 1994-2007 integrated until 3000 m depth in the observationally-constrained estimates a) eMLR(C*) (Gruber et al., 2019) and b) OCIM-v2021, in c) "GOBMs high" and in d) "GOBMs low" (individual GOBMs shown in Fig. S4). The robustness of the patterns has been tested as explained in Text S4 of the Supplement. Contours show the boundaries of the ICE, SPSS and STSS biomes. Values below 3000 m are not shown because of the low signal-to-uncertainty ratio in eMLR(C*).

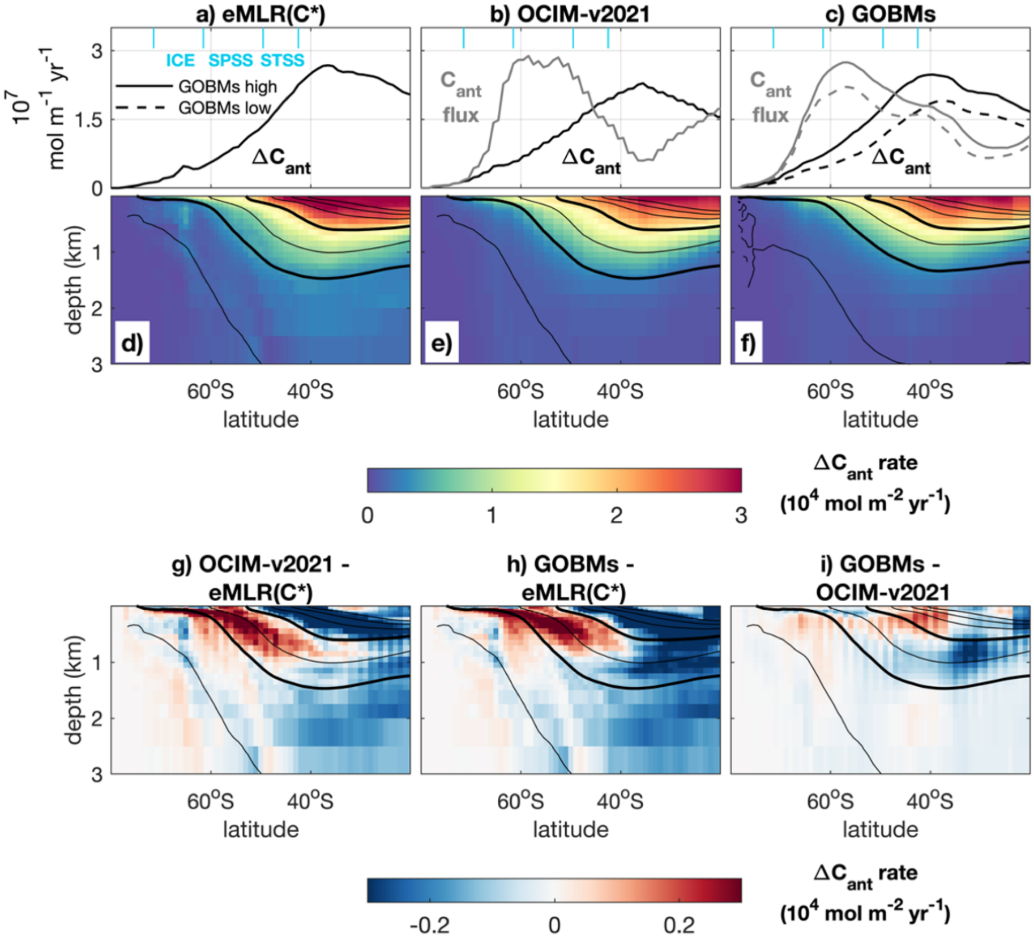

Figure 12. Zonal integrals of ΔC_{ant} yearly accumulation rate from 1994 to 2007 and of air-sea C_{ant} fluxes (positive downwards) averaged between 1994 and 2007 for a,d) eMLR(C*), b,e) OCIM-v2021 and c,f) GOBMs. a-c) (black line) ΔC_{ant} column inventory (0-3000 m) and (grey line) air-sea C_{ant} fluxes; for the GOBMs, the distinction is made between "GOBMs high" (full lines) and "GOBMs low" (dashed lines). g-i) Anomalies of ΔC_{ant} accumulation rates in g) OCIM-v2021 with respect to eMLR(C*), h) GOBMs with respect to eMLR(C*) and i) GOBMs with respect to OCIM-v2021. In all sections, contours show mean potential density (with a 0.03 kg m^{-3} spacing) referenced to the surface in World Ocean Atlas 2018 (Boyer et al., 2018), where thick lines indicate the 1026.9 kg m^{-3} and 1027.5 kg m^{-3} isopycnals. Anomalies of individual GOBMs shown in Fig. S18 (with respect to eMLR(C*) and Fig. S19 (with respect to OCIMv2021).

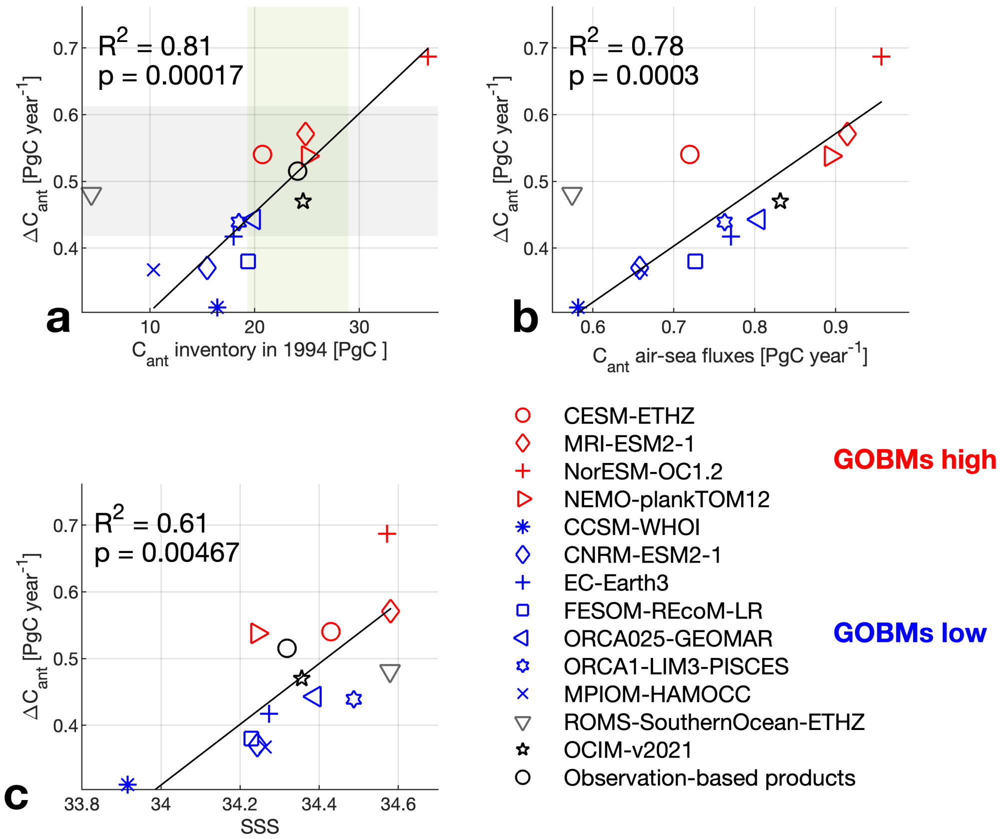

Figure 13. Scatter plots showing relationships between ΔC_{ant} accumulation rates between 1994 and 2007 (integrated to 3000 m) and different quantities namely a) the cumulative C_{ant} in 1994 integrated over the Southern Ocean, b) air-sea C_{ant} fluxes averaged between 1994 and 2007 and integrated over the Southern Ocean, c) sea surface salinity (SSS) horizontally averaged over the SPSS and STSS biomes (which show consistent SSS anomaly patterns, Fig. S17). Shown are a subset of the GOBMs (see 2.3), the OCIM-v2021 data-assimilated model, the observation-based cumulative C_{ant} until 1994 (C* method, Sabine et al., 2004) and the 1994-2007 ΔC_{ant} from (eMLR(C*) method, Gruber, Clement, et al., 2019), and SSS from EN4.2.1 (Good et al., 2013). Thin black lines show the linear fit of the data for the GOBMs only, with the explained variance (R^2) and the p-value indicated for each regression. The grey shading in a) indicates the 19% uncertainty levels around the mean of eMLR(C*) (Southern Hemisphere uncertainty estimate, based on Table 1, Gruber, Clement, et al., 2019) and the green shading the 20% uncertainty levels around the C*-based estimate of cumulative C_{ant} until 1994 (global uncertainty estimate Sabine et al., 2004; Matsumoto & Gruber, 2005). Models that have a ΔC_{ant} storage higher than the average of the two observationally-constrained data sets ("GOBMs high") are shown in red, whereas the models in which it is lower ("GOBMs low") are shown in blue. Because of its different spin-up procedure, ROMS-SouthernOcean-ETHZ is shown in the plots but has been excluded from the regression analysis. For OCIM-v2021, CNRM-ESM2-1 and MPIOM-HAMOCC the ΔC^{ss}_{ant} is shown, whereas in others the sum of steady state and non steady state is shown. As discussed in Text S2, ΔC^{ns}_{ant} accumulation rates are about 10-20% of the total ΔC_{ant}.

which results in a secondary peak at around 40°S in some GOBMs, diluted by the ensemble mean (Fig. 12c).

The effective transport of C_{ant} into the ocean interior relies on a number of physical processes, the dominant of which is the northward transport by the overturning circulation of the C_{ant} ventilated in the ocean interior by deep winter mixing (Frölicher et al., 2015; Morrison et al., 2022). The absorbed C_{ant} spreads northward along density surfaces within mode and intermediate waters (Figure 12d-f) and is circulated within and out of the Southern Ocean by the subtropical gyres (Frölicher et al., 2015; D. C. Jones et al., 2016; Waugh et al., 2019). As a result, the largest C_{ant} inventories are displaced to the north with respect to the maximum air-sea C_{ant} influx (Figure 12b,c). Another pathway by which the C_{ant} inventory can build up without a corresponding surface influx is by southward advection and subsequent subduction of high-C_{ant} Subtropical Waters (Iudicone et al., 2016; Morrison et al., 2022).

The observation-based product eMLR(C*) and the ocean inverse model OCIM-v2021 have similar ΔC_{ant} accumulation rates when integrated over the Southern Ocean for the period 1994 through 2007 (0.52 PgC yr^{-1} and 0.47 PgC yr^{-1}, respectively, Figure 13), but differ in their horizontal (Figure 11) and vertical (Figure 12) patterns. The eMLR(C*) exhibits particularly low ΔC_{ant} values at subpolar and high latitudes (Figure 12g), especially in the Pacific sector (Figure 11). The GOBMs multi-model-mean of ΔC_{ant} accumulation rates over the same 1994 through 2007 period and integrated within the Southern Ocean (Figure 13) is 0.46±0.11 PgC yr^{-1}, i.e., 7% lower than the mean of the two observational estimates considered here. 6 out of the 12 GOBMs fall within the 19% range of the observational eMLR(C*) uncertainty. Two thirds of all GOBMs (hereafter "GOBMs low") have lower than observed ΔC_{ant} accumulation rates (0.39±0.11 PgC yr^{-1}, about 20% lower than the observational estimates). The remaining GOBMs (hereafter "GOBMs high") have higher than observed ΔC_{ant} accumulation rates (0.58±0.07 PgC yr^{-1}, about 17% higher than the observational estimates). "GOBMs high" have a higher ΔC_{ant} storage than "GOBMs low" throughout the Southern Ocean (Figures 11c,d and 12c), higher C_{ant} air-sea fluxes (Figure 12c), higher sea surface salinity (SSS) in the SPSS and STSS biomes and mixed layer depths especially in the SPSS biome (Text S3, S4 and Figure S17). Along the zonal mean section, all GOBMs show a southward shift in ΔC_{ant} with respect to eMLR(C*) shown by a north-south dipole in the upper 1 km (Figure 12h), as similarly found in the comparison between OCIM-v2021 and eMLR(C*) (Figure 12g). With respect to OCIM-v2021, GOBMs show higher ΔC_{ant} above 1000 m depth and lower ΔC_{ant} beneath (Figure 12i). This could point to insufficient ventilation of C_{ant} in "GOBMs low" models (Figure S19), which represent the majority of the GOBMs. The amount of spread and the overall underestimate of ΔC_{ant} in the GOBMs is consistent with Earth System Models analyzed by Frölicher et al. (2015) and Terhaar et al. (2021), supporting the argument that biased ocean model dynamics and water mass properties rather than biases in the atmospheric forcing cause the C_{ant} underestimate (Terhaar et al., 2021; Bourgeois et al., 2022).

Integrated over the Southern Ocean, we find that the model spread in ΔC_{ant} accumulation rates from 1994 to 2007 can be largely explained (81% variance explained) by the spread in accumulated C_{ant} until 1994 (Figure 13), suggesting a coherent scaling between long-term and recent C_{ant} accumulation rates. The model spread in ΔC_{ant} accumulation rates is also related with the spread in C_{ant} air-sea fluxes averaged over 1994-2007 (78% variance explained). These results show that past long-term ΔC_{ant} accumulation rates are a better predictor for present ΔC_{ant} accumulation rate than present C_{ant} air-sea fluxes. The reason for this is that C_{ant} air-sea fluxes are linked to changes in C_{ant} storage through ocean transport, which may differ substantially between models (Frölicher et al., 2015; Terhaar et al., 2021; Bourgeois et al., 2022). This becomes obvious when considering the myriad of processes involved, including the strength of the overturning circulation, the strength of the subtropical gyres, the isopycnal stirring by

Table 3. Comparison of the Southern Ocean carbon sink estimate with the estimate presented in RECCAP1 (Lenton et al., 2013), which used a different definition of the Southern Ocean region (44-75°S) and covered a different period (1990-2009). GOBMs: Global Ocean Biogeochemistry Models. Reported numbers are means ± one standard deviation. Note for RECCAP1 the median of all models is reported.

Estimate	GOBMs	Observation-based
RECCAP2 1985-2018	-0.75 ± 0.28 PgC yr^{-1}	-0.73 ± 0.07 PgC yr^{-1}
RECCAP2 1985-2018 (44°-75°S)	-0.39 ± 0.24 PgC yr^{-1}	-0.30 ± 0.04 PgC yr^{-1}
RECCAP2 1990-2009 (44°-75°S)	-0.22 ± 0.25 PgC yr^{-1}	-0.14 ± 0.09 PgC yr^{-1}
RECCAP1 1990-2009 (44°-75°S)	-0.43 ± 0.38 PgC yr^{-1}	-0.27 ± 0.13 PgC yr^{-1}

mesoscale eddies, and localized subduction dynamics (Sallée et al., 2012; Morrison et al., 2022). The different way in which the GOBMs simulate these transport processes is possibly linked to the large model spread in ΔC_{ant} accumulation rates among GOBMs. Past studies have found that SSS affects the surface ocean density in the formation regions of mode and intermediate waters and could be used as a constraint of the C_{ant} air-sea fluxes, and thus of the C_{ant} storage within the recently-ventilated water masses (Terhaar et al., 2021). In this study and in Terhaar et al. (2023), we find that SSS explains a lower variance in the ΔC_{ant} accumulation rates (R^2=61%; Figure 13) and in the C_{ant} air-sea fluxes (R^2=57% Terhaar et al., 2023) with respect to the ESMs (R^2=0.74) analyzed by Terhaar et al. (2021). The relationship may be weaker due to the different suite of models used in the ESM and GOBM ensembles and remaining biases associated with incomplete spin-up (Terhaar et al., 2023).

4 Discussion

4.1 Summary and progress since RECCAP1

We provide an updated estimate of the Southern Ocean carbon sink (see Figure 1 for regional extent). The numbers we present (Table 3) are not directly comparable with the RECCAP1 estimate (Lenton et al., 2013) due to different region definitions (Figure 1) and periods (1990-2009 vs. 1985-2018). The RECCAP1 regional definition of the Southern Ocean (44-75°S) cut across and missed a large part of the strong CO_2 uptake north of the Subantarctic Front. Recalculating the RECCAP2 numbers for the RECCAP1 region would reduce the Southern Ocean CO_2 sink to 52% (GOBMs) or 41% (pCO_2-products) of its original value (Table 3). Adjusting RECCAP2 numbers for the 1990-2009 period would further reduce fluxes by about another 50%. Compared on equal footing (44°-75°S and 1990-2009), we find the Southern Ocean to be a weaker carbon sink in RECCAP2 compared to RECCAP1.

The observational and modeling communities have made substantial progress on quantifying and characterizing the Southern Ocean carbon sink since RECCAP1 (Lenton et al., 2013). The creation of the Surface Ocean CO_2 Atlas and its annual updates have marked a step-change by facilitating the development of statistical models (a.k.a. pCO_2-products). The large and diverse ensemble of pCO_2-products help to identify the robust features of the Southern Ocean carbon sink. The pCO_2-products have a relatively small spread compared to the global ocean biogeochemistry models in terms of mean and seasonal cycle, indicating that the uncertainty from differences in mapping methods is small. However, the spread in the trend estimates is in fact larger in the products than in the GOBMs (Figure 10). Further, the narrow spread in mean and seasonal cycle does not include the uncertainties due to sparse pCO_2 observations in the Southern Ocean, particularly in winter and before the 2000's (Ritter et al., 2017). In addition, pCO_2-products share the uncertainties associated with the bulk formulation of air-sea CO_2 exchange (R. H. Wanninkhof et al., 2009; Fay et al., 2021). While they do have their shortcomings, the pCO_2 products are an advance for constraining the Southern Ocean carbon sink compared to the atmospheric inversions that were used in RECCAP1 (Lenton et al., 2013). This is because the surface ocean pCO_2 observations provide a more direct constraint on the air-sea CO_2 flux than the relatively small atmospheric CO_2 signals over the ocean that form the basis of the atmospheric inversions.

The larger GOBM ensemble provides a more representative process-based estimate and the spread in GOBMs has been reduced since RECCAP1 (see Table 3 Lenton et al., 2013). The remaining spread is nevertheless large and points towards critical need for model development, where the largest sources of uncertainty stem from biological process description and circulation, which vary in importance depending on flux component (natural, anthropogenic, etc.), and spatio-temporal scale of interest. In terms of the anthropogenic component, the 12 GOBMs analyzed here have a 24% spread (standard deviation around the mean) in the C_{ant} accumulation rates, which is marginally larger than the $\sim$ 20% uncertainty associated with the observational estimates of ΔC_{ant} and C_{ant} (even though caution is warranted when directly comparing the uncertainty estimates, which are computed formally different across data classes; Gruber, Clement, et al., 2019; Sabine et al., 2004). Overall, the GOBM ensemble mean underestimates the observation-based estimates of the C_{ant} accumulation up to 1994 by 19% and the change between 1994-2007 by 7%. Admittedly, the GOBM ensemble analyzed here is relatively small, and the underestimation of C_{ant} and ΔC_{ant} is in the range of the uncertainty ranges of the observational estimates. We can nonetheless speculate that the detected underestimation is likely related to a combination of physical, chemical and methodological factors. First, our results point to too little or too shallow ventilation of mode and intermediate waters (Figure 12i), the causes of which can be related to insufficient vertical mixing or too sluggish northward export of the subducted waters (Morrison et al., 2022). However, while sea-surface salinity (SSS) was singled out as a strong predictor of C_{ant} air-sea fluxes in an ESM ensemble analyzed by (Terhaar et al., 2021), in our study and in (Terhaar et al., 2023), SSS was not found to be a clear constraint of the anthropogenic CO_2 uptake and its interior storage in the GOBMs. Rather, Terhaar et al. (2023) find that biases in the normalized surface Revelle factor could explain the underestimation of C_{ant} uptake. Finally, the relatively high pre-industrial CO_2 mixing ratios related to late starting dates in several GOBMs are likely causing an underestimation of the cumulative C_{ant} storage, which is especially large in the Southern Ocean (Terhaar et al., 2023). For the natural carbon fluxes, the difficulty in capturing the delicate balance between physical and biological processes is clearly manifested by the large model spread (Figure 3). In addition, the different spin-up procedures could play a role. Terhaar et al. (2023) indicate that the natural CO_2 flux component may be biased towards uptake that is too strong, possibly related to GOBMs not being in steady-state (Terhaar et al., 2023), which is particularly relevant in the Southern Ocean where old water masses resurface. While long preindustrial spin-ups would bring the GOBMs closer to steady-state and thus reduce drift, they may come at the cost of less realistic surface conditions and their response to climate change and variability (Séférian et al., 2016). Interestingly, the two data-assimilated GOBMs differ to a large extent, illustrating that dynamical processes in these models may still override information gained from assimilated observations.

The averages of the GOBM and pCO_2-product ensembles agree for many key estimates, showing progress over the past 10 years: the mean and spatial distribution of the sink is in good agreement (Figure 2), although discrepancies of the magnitude and, particularly, the trends still persist (Figures 8 and 10; see also Canadell et al., 2021). The fact that these ensemble means agree so well in many respects provides some confidence in the Southern Ocean CO_2 flux estimates because they are nearly independent. However, the agreement of GOBMs and pCO_2-products on the mean CO_2 flux is partly a result of compensation of regional and seasonal discrepancies (Figures 4, 5, 8). The agreement is also highly susceptible to the choice of river flux adjustment that either locates most outgassing of river-derived carbon in the Southern Ocean (Aumont et al., 2001) or in the tropical Atlantic (Lacroix et al., 2020). Reasons for the discrepancy between Aumont et al. (2001) and Lacroix et al. (2020) may be because of specific choices in nutrient and carbon input, lability of organic matter, resulting ocean model transport (see also the discussion in Terhaar et al., 2023). We here chose to use the river flux adjustment of Lacroix et al. (2020), scaled up to a global value of 0.65 PgC yr^{-1}, resulting in a small adjustment for the Southern Ocean of 0.04 PgC yr^{-1}. In contrast, the Southern Ocean (south of 20°S) adjustment based on Aumont et al. (2001) that is so far used in the Global Carbon Budget is higher by one order of magnitude (0.32 PgC yr^{-1}) and can explain the large mismatch in the mean flux (but not its trend) between GOBMs and pCO_2 products in the Southern Ocean in the Global Carbon Budget (Friedlingstein et al., 2022). The discrepancies in the trend cannot be explained by GOBM biases in warming trends as these are well reproduced (Figure 10). Similarly, the GOBM ensemble is not systematically biased towards formation of mode and intermediate waters that is too weak, in contrast to the ESMs, and an effect on the trend of the ocean carbon sink could not be evidenced (Terhaar et al., 2023). Further potential candidates for GOBM biases, which were not explored here, are stratification (Bourgeois et al., 2022), mixing, and mixed layer dynamics, which could also lead to excess carbon accumulation in the surface layer and thus may be the driver for the overestimation of the surface Revelle factor. In the pCO_2-products, the trend might be biased by data sparsity (Gloege et al., 2021; Hauck et al., 2023).

4.2 Seasonal cycle and thermal versus non-thermal drivers

As a community, we have a good understanding of the mechanisms that drive pCO_2 seasonality in the Southern Ocean (Lenton et al., 2013), but we do not fully understand their magnitudes, opposing or synergistic, in different seasons and regions (Mongwe et al., 2018). Part of this lack of understanding is due to a lack of observations throughout all seasons, though particularly acute during winter (Gray et al., 2018; Bushinsky et al., 2019; Sutton et al., 2021). Further, complex biological processes affecting pCO_2 in summer are more difficult to accurately describe in GOBMs (Mongwe et al., 2018).

While pCO_2 products require little to no understanding to reconstruct the seasonal cycle, they may still suffer from a lack of data (Ritter et al., 2017). This may be shown by the narrow ensemble spread of the pCO_2-products during winter (Figure 7d-f), which may result from poor sampling distribution. That being said, an observation system simulation experiment (OSSE) showed that the seasonal cycle in most of the Southern Ocean is in fact well captured by one pCO_2 product (Gloege et al., 2021). The narrower GOBM spread of the non-thermal pCO_2 component during winter may also suggest that wintertime processes (circulation) are less complex than summer (circulation and biology, Figure 7d-f).

The introduction of biogeochemical Argo floats since the mid 2010's has increased the number of winter observations (relative to the available ship-based observations), albeit inferred from pH and estimated total alkalinity and thus associated with a higher uncertainty (Williams et al., 2017). The machine learning approaches that include float-based observations result in stronger winter outgassing (Figure 4, Bushinsky et al., 2019). Direct pCO_2 measurements showed that the years used to train the machine learning model (2015-2018) may have had anomalously high pCO_2 (Sutton et al., 2021). However, if this is in fact the case, and not related to sampling locations, this may indicate much larger interannual variability in the Southern Ocean than the majority of the pCO_2-products currently estimate (Figure 8). Incorporating these data is thus potentially an important goal for pCO_2-products, but it has proven difficult to incorporate the float-based pCO_2 estimates further back in time than 2015, the start of the BGC-float record and account for their higher uncertainty (Bushinsky et al., 2019; Williams et al., 2017).

GOBMs also have a lower pCO_2 ensemble spread during winter compared with summer and agree on the spatial location of the winter flux minimum (Figure 4). Nevertheless, the range in magnitude is still more than twice as large as those of the pCO_2-products (Figure 7d-f). Since the thermal component is well captured in GOBMs (Figure 7d-e), the non-thermal physical drivers (i.e., circulation) determines the uncertainty observed in winter. In summer, GOBMs have difficulty capturing the delicate balance between biological and physical processes that leads to a large spread in model pCO_2 and fluxes (Mongwe et al., 2018). GOBMs may thus benefit from more process-based studies that further our understanding of pCO_2 drivers during summer, i.e., biological productivity, respiration, remineralization and sinking of organic carbon as part of the biological carbon pump.

4.3 Temporal variability of CO_2 fluxes

Our analysis reduces the previously reported discrepancy in variability of Southern Ocean air-sea CO_2 fluxes between data classes (GOBMs and pCO_2-product ensemble means, Gruber, Landschützer, & Lovenduski, 2019). We relate the growing agreement to the larger ensemble of pCO_2-products in our study, with the newer additions having a substantially lower variability than the two pCO_2-products (Jena-CarboScope and SOM-FFN) used by Gruber, Landschützer, and Lovenduski (2019). A recent study using the same RECCAP data base also concluded that there is agreement on the magnitude of interannual variability between GOBMs and pCO_2-products (Mayot et al., 2023).

The interannual to decadal variability of Southern Ocean air-sea CO_2 fluxes was discussed extensively in the literature, and was often related to variations in the Southern Annual Mode (SAM) (Le Quéré et al., 2007; Lovenduski et al., 2007; Lenton & Matear, 2007; Hauck et al., 2013; Nicholson et al., 2022; Mayot et al., 2023). Also, regional wind variability linked to the zonal wavenumber 3 was suggested as a driver of interannual CO_2 flux variability driving both the weakening in the 1990's and the strengthening in the 2000's (Landschützer et al., 2015; Keppler & Landschützer, 2019). The arguments of SAM or wave number 3 as dominant drivers of CO_2 flux interannual variability might not be fully independent from each other, as previously a wave number 3 like pattern was reported to describe MLD anomalies during positive SAM events (Sallée et al., 2010).

The fact that the maximum IAV of GOBMs is found in the SPSS Indo-Pacific sector (section 3.3, Figure S12) supports the argument of the above mentioned references that upwelling of carbon-rich deep water and related outgassing of natural carbon in response to a positive SAM and strengthening of westerly winds may be the dominant driver of interannual variability (DeVries et al., 2017). This is further supported by studies of atmospheric potential oxygen (APO), which can be used as a tracer of ocean-only processes from measurements of CO_2 and O_2 at atmospheric stations (Stephens et al., 1998). Nevison et al. (2020) showed that the interannual variations of APO seasonal minimum from stations in the Southern Hemisphere were strongly correlated with the SAM during years of positive phase. Further, they showed that GOBMs (as analyzed in this study) can capture the variability of CO_2 and APO fluxes driven by the SAM variations during the austral winter months. However, the study of Nevison et al. (2020) also illustrated that the SAM index variability cannot fully explain the changes in APO seasonal winter minima suggesting that other factors or modes of variability such as ENSO could impact the CO_2 and O_2 air-sea fluxes of the Southern Ocean as also previously suggested in an ocean modeling study (Verdy et al., 2007).

On top of the interannual variability, on which pCO_2 products and GOBMs seem to reach reasonable agreement, discrepancies in the CO_2 flux trend since 2000 have emerged

(Figure 8, Friedlingstein et al., 2022). These discrepancies highlight a major knowledge gap and urgently need to be resolved by critical analysis of potential biases in pCO_2-products as well as GOBMs (see section 4.1). While there is no evidence so far that adjustments of CO_2 fluxes based on model evaluation of interfrontal salinity and Revelle factor affect the trend (Terhaar et al., 2023), data sparsity tends to lead to an overestimation of decadal variability and trend in at least two of the pCO_2-products (Gloege et al., 2021; Hauck et al., 2023). Hence, both data classes need to be inspected for deficiencies.

4.4 Zonal asymmetry of the fluxes

While the primary spatial mode of variability in the Southern Ocean is from north to south, zonal variability in the dynamics, biogeochemistry, and carbon fluxes have been reported in the literature (Landschützer et al., 2015; Tamsitt et al., 2016; Rintoul, 2018; Prend et al., 2022). Similarly, we find substantial zonal asymmetry in both the mean states, and seasonal and interannual variability of the Southern Ocean CO_2 fluxes (Figures S10, S12); yet many of our results have been presented in a zonally-averaged perspective for the sake of brevity.

In this work, we find that the largest zonal asymmetries in the Southern Ocean mean air-sea CO_2 flux occur in the SPSS biome (Figure 4b-e, S12). Here, the Pacific and Indian sectors are larger sources (or weaker sinks) of CO_2 to the atmosphere than the Atlantic sector. This is consistent with the pCO_2-based products (Figure S12d-f). The float-based pCO_2-products amplify this winter outgassing dramatically. However, the GOBMs and the assimilative model ensemble averages do not show a coherent and convincing increase in outgassing in the Indian and Pacific relative to the Atlantic. The zonal asymmetry reported in the observation-based products is consistent with a recent BGC-float-based study that reported stronger outgassing in the Indian and Pacific sectors of the Southern Ocean (Prend et al., 2022). The authors attributed this dominance to stronger winter-time entrainment of deep waters to the surface in these regions. The zonal asymmetry is also apparent in the air-sea CO_2 fluxes decomposed into natural and anthropogenic contributions (Figure S7). Here, too, the SPSS is the region with the greatest asymmetry. In the Indian sector, the large natural outgassing fluxes of the ensemble mean are nearly perfectly opposed by the anthropogenic uptake.

4.5 Link large-scale synthesis to observational programs

The analysis presented here provides a synthesis of large-scale datasets with a focus on budgets, spatial and temporal patterns of fluxes and carbon accumulation, and a first-order assessment of large-scale processes (e.g., thermal versus non-thermal, anthropogenic vs natural carbon fluxes). In particular, it highlights spatio-temporal windows for which discrepancies between data classes are largest (e.g., magnitude of winter outgassing, delicate balance of physical versus biological processes in summer, magnitude of decadal trend of the Southern Ocean carbon sink). Importantly, this synthesis builds on contributions from many individual groups contributing repeat observations of surface and interior ocean biogeochemical properties from research vessels and ships of opportunity (e.g., Talley et al., 2016; Hoppema et al., 1998; van Heuven et al., 2014; Metzl et al., 1999; Pardo et al., 2017). The ship-based observations form the cornerstone for many of the data classes in this study: observation-based ocean interior estimates of CO_2 storage assess changes in deep ocean measurements of CO_2, the surface pCO_2 estimates use observations from ships of opportunity, and the GOBMs are evaluated against ocean interior observations. And while sampling biases and gaps in the ship-based measurements may be filled by autonomous platforms with lower accuracy (e.g., BGC-floats), they will always require crossover validation measurements from the high-accuracy shipboard measurements. This emphasizes that the ship-based observations need to continue into the future to characterize the evolution of the Southern Ocean carbon cycle. This will only become more important, once stabilization of atmospheric CO_2 will lead to a larger weight on ocean processes for control of air-sea fluxes relative to the current quasi-exponential growth rate of atmospheric CO_2.

Further, detailed regional process studies employing a wide range of methodologies across disciplines are also important to further our holistic understanding of the Southern Ocean carbon cycle and to improve the description of biogeochemistry and ecosystem dynamics in GOBMs, particularly in summer. One example for such an interdisciplinary field program is along the continental shelf west of the Antarctic Peninsula where shipboard observations indicate a strong, near-shore summer undersaturation of surface pCO_2 (Eveleth et al., 2017) and seasonal reduction in surface dissolved inorganic carbon (Hauri et al., 2015). The seasonal trends in the ocean CO_2 system on the shelf reflect a combination of biological net community production (Ducklow et al., 2018) and meltwater input diluting surface dissolved inorganic carbon and alkalinity (Hauri et al., 2015). Regional ocean biogeochemical models simulate similar onshore-offshore gradients in surface chlorophyll, biological productivity, dissolved inorganic carbon, and pCO_2 as well as the observed large interannual biophysical variability associated with year-to-year variations in seasonal sea-ice advance and retreat phenology (Schultz et al., 2021). Observed decadal trends for the region from the early 1990s to late 2010s indicate that reduced sea-ice extent associated with climate change drives an increase in upper ocean stability, phytoplankton biomass and biological dissolved inorganic carbon drawdown, resulting in a growing net downward air-sea CO_2 flux during summer (Brown et al., 2019). Recent year-round, autonomous mooring observations of pCO_2 and pH suggest a gradual increase in surface ocean pCO_2 and dissolved inorganic carbon over the fall and winter, with CO_2 outgassing during winter when pCO_2 is supersaturated largely blocked by sea-ice cover (Shadwick et al., 2021; M. Yang et al., 2021). Similar large-scale programs are needed in other parts of the Southern Ocean given its size and importance in the global carbon cycle. On-going research activities, also as part of the Southern Ocean Observing System (SOOS), e.g., in the Ross (Smith et al., 2021) and Weddell Seas (Arndt et al., 2022) have the potential of being extended.

5 Conclusions

Here, we present a schematic overview that summarizes the main characteristics of the Southern Ocean carbon cycle 1985-2018, as derived in this analysis and its supplementary material (Figure 14). In general, the sink strength for atmospheric CO_2 (net CO_2 flux, FCO_2) increases from South to North, but with important zonal asymmetry. The Atlantic and Indian Ocean sectors of the Subtropical Seasonally Stratified biome (STSS) are the regions that act as strongest sinks. In the Subpolar Seasonally Stratifed biome (SPSS), the Atlantic sector stands out as the only sector acting as an annual mean CO_2 sink. Also the seasonal cycle shows a distinct north-south gradient. In the ice-covered biome (ICE) the peak uptake occurs in summer and is driven by the seasonal cycle of dissolved inorganic carbon (DIC), i.e. by physical DIC transport and biological processes. In contrast, the dominant driver of the seasonal cycle of CO_2 uptake in the STSS is temperature, and thus the season of peak uptake occurs in winter. Trends in net CO_2 uptake derived from Global Ocean Biogeochemistry Models (GOBMs) and surface ocean pCO_2 observation based products (pCO_2-products) disagree in all biomes, but the discrepancy is strongest in the Pacific sector of the STSS. In terms of anthropogenic CO_2 (C_{ant}), the strongest uptake occurs in the SPSS. This is not visible in the map of net CO_2 flux, because the anthropogenic uptake manifests itself as a suppression of natural CO_2 outgassing. The largest anthropogenic carbon storage occurs in the STSS and northward.

Our analysis confirms the important role of the Southern Ocean in the global carbon cycle. We have highlighted key knowledge gaps that need to be closed through extended observation systems and augmented process descriptions in the dynamic models in order to further reduce uncertainties.

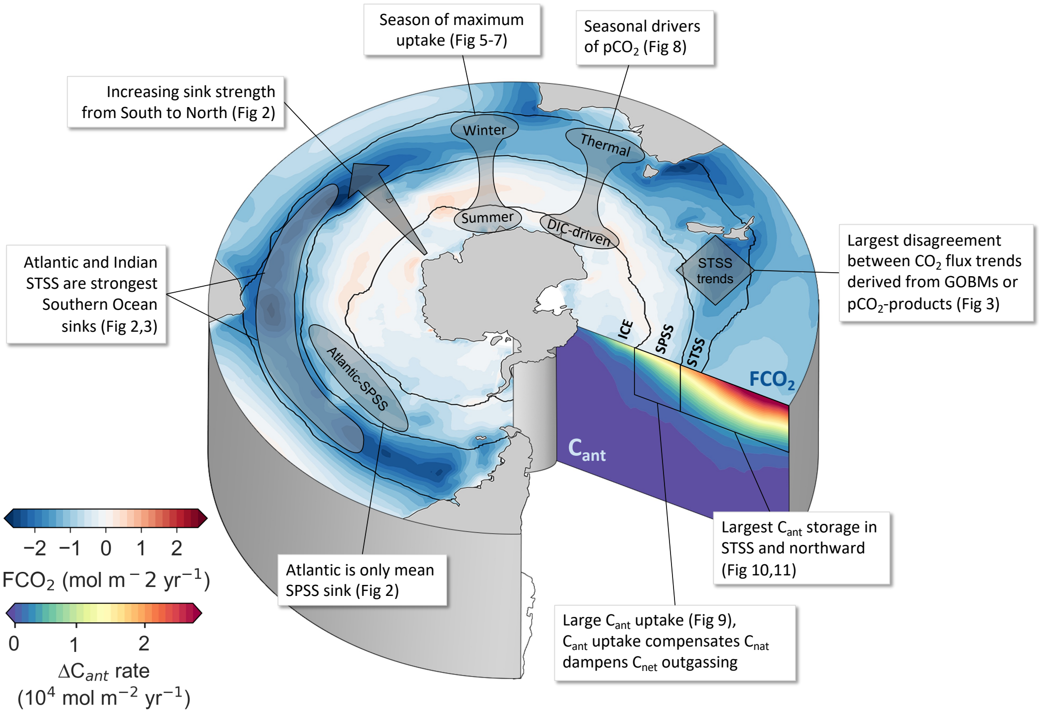

Figure 14. Main characteristics of the Southern Ocean carbon cycle 1985-2018. The surface ocean color shading depicts the net air-sea CO_2 flux (FCO_2) as the average of the ensemble means from pCO_2-products and Global Ocean Biogeochemistry Models (GOBMs). Blue color denotes a CO_2 flux into the ocean, and red color a flux out of the ocean. The zonal mean section shows the anthropogenic carbon (C_{ant}) accumulation in the ocean interior from GOBMs. ICE: ice-covered biome, SPSS: Subpolar Seasonally Stratified Biome, STSS; Subtopical Seasonally Stratified Biome.

Open Research Section

All RECCAP2 data is hosted on https://zenodo.org/. Link will be updated during the review process.

Acknowledgments

Acknowledgments will be added during the review.

References

Armour, K. C., Marshall, J., Scott, J. R., Donohoe, A., & Newsom, E. R. (2016). Southern Ocean warming delayed by circumpolar upwelling and equatorward transport. *Nature Geoscience*, *9*(7), 549–554. doi: 10.1038/ngeo2731

Arndt, S., Janout, M., Biddle, L., Campbell, E., & Thomalla, S. (2022). *The Weddell Sea and Dronning Maud Land (WSDML) Regional Working Group Virtual Science Workshop, 14–16 june 2022* (Tech. Rep.). Zenodo. Retrieved 2023-02-22, from `https://zenodo.org/record/6931424` doi: 10.5281/ZENODO.6931424

Arrigo, K. R., & van Dijken, G. L. (2007). Interannual variation in air-sea CO_2 flux in the Ross Sea, Antarctica: A model analysis. *Journal of Geophysical Research*, *112*(C3), C03020. doi: 10.1029/2006JC003492

Aumont, O., Ethé, C., Tagliabue, A., Bopp, L., & Gehlen, M. (2015). PISCES-v2: An ocean biogeochemical model for carbon and ecosystem studies. *Geoscientific Model Development*, *8*(8), 2465–2513. doi: 10.5194/gmd-8-2465-2015

Aumont, O., Orr, J. C., Monfray, P., Ludwig, W., Amiotte-Suchet, P., & Probst, J. L. (2001). Riverine-driven interhemispheric transport of carbon. *Global Biogeochemical Cycles*, *15*(2), 393–405. doi: 10.1029/1999GB001238

Ayers, J. M., & Strutton, P. G. (2013). Nutrient variability in Subantarctic Mode Waters forced by the Southern Annular Mode and ENSO. *Geophysical Research Letters*, *40*(13), 3419–3423. doi: 10.1002/grl.50638

Bakker, D., Alin, S. R., Becker, M., Bittig, H. C., Castaño-Primo, R., Feely, R. A., . . . Wilson, D. (2022). *Surface ocean CO_2 atlas database version 2022 (SOCATv2022), NCEI accession 0253659.* NOAA National Centers for Environmental Information. Retrieved from `https://doi.org/10.25921/1h9f-nb73`

Bakker, D., Hoppema, M., Schröder, M., Geibert, W., & Baar, H. J. W. D. (2008). A rapid transition from ice covered CO_2-rich waters to a biologically mediated CO_2 sink in the eastern Weddell Gyre. *Biogeosciences*, *5*, 1373–1386. doi: 10.5194/bg-5-1373-2008

Bakker, D., Pfeil, B., Landa, C. S., Metzl, N., O'Brien, K. M., Olsen, A., . . . Xu, S. (2016). A multi-decade record of high-quality CO_2 data in version 3 of the Surface Ocean CO_2 Atlas (SOCAT). *Earth System Science Data*, *8*(2), 383–413. doi: 10.5194/essd-8-383-2016

Beadling, R. L., Russell, J. L., Stouffer, R. J., Mazloff, M., Talley, L. D., Goodman, P. J., . . . Pandde, A. (2020). Representation of Southern Ocean Properties across Coupled Model Intercomparison Project Generations: CMIP3 to CMIP6. *Journal of Climate*, *33*(15), 6555–6581. doi: 10.1175/JCLI-D-19-0970.1

Berthet, S., Séférian, R., Bricaud, C., Chevallier, M., Voldoire, A., & Ethé, C. (2019). Evaluation of an Online Grid-Coarsening Algorithm in a Global Eddy-Admitting Ocean Biogeochemical Model. *Journal of Advances in Modeling Earth Systems*, *11*(6), 1759–1783. doi: 10.1029/2019MS001644

Bopp, L., Lévy, M., Resplandy, L., & Sallée, J. B. (2015). Pathways of anthropogenic carbon subduction in the global ocean. *Geophysical Research Letters*, *42*(15), 6416–6423. Retrieved from `http://doi.wiley.com/10.1002/2015GL065073` doi: 10.1002/2015GL065073

Bourgeois, T., Goris, N., Schwinger, J., & Tjiputra, J. F. (2022). Stratification constrains future heat and carbon uptake in the Southern Ocean between 30°S and 55°S. *Nature Communications*, *13*(1), 340. doi: 10.1038/s41467-022-27979-5

Boyer, T. P., Garcia, H. E., Locarnini, R. A., Zweng, M. M., Mishonov, A. V., Reagan, J. R., … Smolyar, I. V. (2018). *World Ocean Atlas 2018.* NOAA National Centers for Environmental Information. Retrieved from https://www.ncei.noaa.gov/archive/accession/NCEI-WOA18

Brown, M. S., Munro, D. R., Feehan, C. J., Sweeney, C., Ducklow, H. W., & Schofield, O. M. (2019). Enhanced oceanic CO_2 uptake along the rapidly changing West Antarctic Peninsula. *Nature Climate Change*, *9*(9), 678–683. Retrieved from http://dx.doi.org/10.1038/s41558-019-0552-3 doi: 10.1038/s41558-019-0552-3

Buitenhuis, E. T., Le Quéré, C., Bednaršek, N., & Schiebel, R. (2019). Large Contribution of Pteropods to Shallow $CaCO_3$ Export. *Global Biogeochemical Cycles*, *33*(3), 458–468. doi: 10.1029/2018GB006110

Bushinsky, S. M., Takeshita, Y., & Williams, N. L. (2019). Observing Changes in Ocean Carbonate Chemistry: Our Autonomous Future. *Current Climate Change Reports*. doi: 10.1007/s40641-019-00129-8

Caldeira, K., & Duffy, P. B. (2000). The Role of the Southern Ocean in Uptake and Storage of Anthropogenic Carbon Dioxide. *Science*, *287*(5453), 620–622. doi: 10.1126/science.287.5453.620

Campin, J.-m., Hill, C., Jones, H., & Marshall, J. (2011). Super-parameterization in ocean modeling : Application to deep convection. *Ocean Modelling*, *36*(1-2), 90–101. doi: 10.1016/j.ocemod.2010.10.003

Canadell, J., Monteiro, P., Costa, M., Cotrim da Cunha, L., Cox, P., Eliseev, A., … Zickfeld, K. (2021). Global Carbon and other Biogeochemical Cycles and Feedbacks. In V. Masson-Delmotte et al. (Eds.), *Climate Change 2021: The Physical Science Basis. Contribution of Working Group I to the Sixth Assessment Report of the Intergovernmental Panel on Climate Change* (pp. 673–816). Cambridge, United Kingdom: Cambridge University Press. doi: 10.1017/9781009157896.007

Carroll, D., Menemenlis, D., Adkins, J. F., Bowman, K. W., Brix, H., Dutkiewicz, S., … Zhang, H. (2020). The ECCO-Darwin Data-Assimilative Global Ocean Biogeochemistry Model: Estimates of Seasonal to Multidecadal Surface Ocean pCO2 and Air-Sea CO2 Flux. *Journal of Advances in Modeling Earth Systems*, *12*(10), 1–28. doi: 10.1029/2019MS001888

Carroll, D., Menemenlis, D., Dutkiewicz, S., Lauderdale, J. M., Adkins, J. F., Bowman, K. W., … Zhang, H. (2022). Attribution of Space-Time Variability in Global-Ocean Dissolved Inorganic Carbon. *Global Biogeochemical Cycles*, *36*(3), 1–24. doi: 10.1029/2021GB007162

Carter, B. R., Bittig, H. C., Fassbender, A. J., Sharp, J. D., Takeshita, Y., Xu, Y.-Y., … Barbero, L. (2021). New and updated global empirical seawater property estimation routines. *Limnol. Oceanogr.: Methods*, *19*, 785–809. doi: 10.1002/lom3.10461

Carter, B. R., Feely, R. A., Williams, N. L., Dickson, A. G., Fong, M. B., & Takeshita, Y. (2018). Updated methods for global locally interpolated estimation of alkalinity, pH, and nitrate. *Limnology and Oceanography: Methods*, *16*(2), 119–131. Retrieved from http://doi.wiley.com/10.1002/lom3.10232 doi: 10.1002/lom3.10232

Carter, B. R., Williams, N. L., Gray, A. R., & Feely, R. A. (2016). Locally interpolated alkalinity regression for global alkalinity estimation. *Limnology and Oceanography: Methods*, *14*(4), 268–277. doi: 10.1002/lom3.10087

Chau, T. T. T., Gehlen, M., & Chevallier, F. (2022). A seamless ensemble-based reconstruction of surface ocean pCO_2 and air-sea CO_2 fluxes over the global coastal and open oceans. *Biogeosciences*, *19*(4), 1087–1109. doi: 10.5194/bg-19-1087-2022

Chevallier, F., Fisher, M., Peylin, P., Serrar, S., Bousquet, P., Bréon, F. M., ... Ciais, P. (2005). Inferring CO_2 sources and sinks from satellite observations: Method and application to TOVS data. *Journal of Geophysical Research Atmospheres*, *110*(24), 1–13. doi: 10.1029/2005JD006390

Chien, C. T., Durgadoo, J. V., Ehlert, D., Frenger, I., Keller, D. P., Koeve, W., ... Oschlies, A. (2022). FOCI-MOPS v1 - integration of marine biogeochemistry within the Flexible Ocean and Climate Infrastructure version 1 (FOCI 1) Earth system model. *Geoscientific Model Development*, *15*(15), 5987–6024. doi: 10.5194/gmd-15-5987-2022

Clement, D., & Gruber, N. (2018). The eMLR(C*) Method to Determine Decadal Changes in the Global Ocean Storage of Anthropogenic CO_2. *Global Biogeochemical Cycles*. doi: 10.1002/2017GB005819

Crisp, D., Dolman, H., Tanhua, T., McKinley, G. A., Hauck, J., Bastos, A., ... Aich, V. (2022). How Well Do We Understand the Land-Ocean-Atmosphere Carbon Cycle? *Reviews of Geophysics*, *60*(2), 1–64. doi: 10.1029/2021RG000736

Denvil-Sommer, A., Gehlen, M., & Vrac, M. (2021). Observation system simulation experiments in the Atlantic Ocean for enhanced surface ocean pCO_2 reconstructions. *Ocean Science*, *17*(4), 1011–1030. doi: 10.5194/os-17-1011-2021

DeVries, T. (2014). The oceanic anthropogenic CO_2 sink: Storage, air-sea fluxes, and transports over the industrial era. *Global Biogeochemical Cycles*, *28*(7), 631–647. doi: 10.1002/2013GB004739

DeVries, T. (2022). The Ocean Carbon Cycle. *Annual Review of Environment and Resources*, *47*(1). doi: 10.1146/annurev-environ-120920-111307

DeVries, T., Holzer, M., & Primeau, F. (2017). Recent increase in oceanic carbon uptake driven by weaker upper-ocean overturning. *Nature*, *542*(7640), 215–218. doi: 10.1038/nature21068

DeVries, T., Yamamoto, K., Wanninkhof, R., Gruber, N., Hauck, J., Müller, J. D., ... others (2023). Magnitude, trends, and variability of the global ocean carbon sink from 1985-2018. *in review at Global Biogeochemical Cycles*.

Djeutchouang, L. M., Chang, N., Gregor, L., Vichi, M., & Monteiro, P. M. (2022). The sensitivity of pCO_2 reconstructions to sampling scales across a Southern Ocean sub-domain: a semi-idealized ocean sampling simulation approach. *Biogeosciences*, *19*(17), 4171–4195. doi: 10.5194/bg-19-4171-2022

Dlugokencky, E., Thoning, K., Lan, X., Tans, P., & Laboratory, N. G. M. (2021). *NOAA Greenhouse Gas Marine Boundary Layer Reference - CO_2*. NOAA GML. Retrieved from `https://gml.noaa.gov/ccgg/mbl/index.html` doi: https://doi.org/10.15138/DVNP-F961

Doney, S., Lima, I., Moore, J. K., Lindsay, K., Behrenfeld, M. J., Westberry, T. K., ... Takahashi, T. (2009). Skill metrics for confronting global upper ocean ecosystem-biogeochemistry models against field and remote sensing data. *Journal of Marine Systems*, *76*(1-2), 95–112. doi: 10.1016/j.jmarsys.2008.05.015

Doney, S., Yeager, S., Danabasoglu, G., Large, W. G., & McWilliams, J. C. (2007). Mechanisms governing interannual variability of upper-ocean temperature in a global ocean hindcast simulation. *Journal of Physical Oceanography*, *37*(7), 1918–1938. doi: 10.1175/JPO3089.1

Döscher, R., Acosta, M., Alessandri, A., Anthoni, P., Arsouze, T., Bergman, T., ... Zhang, Q. (2022). The EC-Earth3 Earth system model for the Coupled Model Intercomparison Project 6. *Geoscientific Model Development*, *15*(7), 2973–3020. doi: 10.5194/gmd-15-2973-2022

Drucker, R., & Riser, S. C. (2016). In situ phase-domain calibration of oxygen optodes on profiling floats. *Methods in Oceanography*, *17*, 296–318. doi: 10.1016/j.mio.2016.09.007

Ducklow, H. W., Stukel, M. R., Eveleth, R., Doney, S. C., Jickells, T., Schofield, O., ... Cassar, N. (2018). Spring-summer net community production, new production, particle export and related water column biogeochemical processes in the marginal sea ice zone of the Western Antarctic Peninsula 2012-2014. *Philosophical Transactions of the Royal Society A: Mathematical, Physical and Engineering Sciences*, *376*(2122). doi: 10.1098/rsta.2017.0177

Dutkiewicz, S., Follows, M. J., & Bragg, J. G. (2009). Modeling the coupling of ocean ecology and biogeochemistry. *Global Biogeochemical Cycles*, *23*(4), 1–15. doi: 10.1029/2008GB003405

Eddebbar, Y. A., Rodgers, K. B., Long, M. C., Subramanian, A. C., Xie, S.-P., & Keeling, R. F. (2019). El Niño–Like Physical and Biogeochemical Ocean Response to Tropical Eruptions. *Journal of Climate*, *32*(9), 2627–2649. doi: 10.1175/JCLI-D-18-0458.1

Eveleth, R., Cassar, N., Doney, S. C., Munro, D. R., & Sweeney, C. (2017). Biological and physical controls on O2/Ar, Ar and pCO2 variability at the Western Antarctic Peninsula and in the Drake Passage. *Deep-Sea Research Part II: Topical Studies in Oceanography*, *139*, 77–88. doi: 10.1016/j.dsr2.2016.05.002

Fay, A. R., Gregor, L., Landschützer, P., McKinley, G. A., Gruber, N., Gehlen, M., ... Zeng, J. (2021). SeaFlux: harmonization of air-sea CO_2 fluxes from surface pCO_2 data products using a standardized approach. *Earth System Science Data*, *13*(10), 4693–4710. doi: 10.5194/essd-13-4693-2021

Fay, A. R., & McKinley, G. A. (2014). Global open-ocean biomes: Mean and temporal variability. *Earth System Science Data*, *6*(2), 273–284. doi: 10.5194/essd-6-273-2014

Feng, L., Palmer, P. I., Parker, R. J., Deutscher, N. M., Feist, D. G., Kivi, R., ... Sussmann, R. (2016). Estimates of European uptake of CO_2 inferred from GOSAT XCO2 retrievals: Sensitivity to measurement bias inside and outside Europe. *Atmospheric Chemistry and Physics*, *16*(3), 1289–1302. doi: 10.5194/acp-16-1289-2016

Friedlingstein, P., O'Sullivan, M., Jones, M. W., Andrew, R. M., Gregor, L., Hauck, J., ... Zheng, B. (2022). Global Carbon Budget 2022. *Earth System Science Data*, *14*(11), 4811–4900. doi: 10.5194/essd-14-4811-2022

Frölicher, T. L., Sarmiento, J. L., Paynter, D. J., Dunne, J. P., Krasting, J. P., & Winton, M. (2015). Dominance of the Southern Ocean in anthropogenic carbon and heat uptake in CMIP5 models. *Journal of Climate*, *28*(2), 862–886. doi: 10.1175/JCLI-D-14-00117.1

Galbraith, E. D., Gnanadesikan, A., Dunne, J. P., & Hiscock, M. R. (2010). Regional impacts of iron-light colimitation in a global biogeochemical model. *Biogeosciences*, *7*(3), 1043–1064. doi: 10.5194/bg-7-1043-2010

Gloege, L., McKinley, G. A., Landschützer, P., Fay, A. R., Frölicher, T. L., Fyfe, J. C., ... Takano, Y. (2021). Quantifying Errors in Observationally Based Estimates of Ocean Carbon Sink Variability. *Global Biogeochemical Cycles*, *35*(4), 1–14. doi: 10.1029/2020GB006788

Gloege, L., Yan, M., Zheng, T., & McKinley, G. A. (2022). Improved Quantification of Ocean Carbon Uptake by Using Machine Learning to Merge Global Models and pCO_2 Data. *Journal of Advances in Modeling Earth Systems*, *14*(2), 1–19. doi: 10.1029/2021MS002620

Good, S. A., Martin, M. J., & Rayner, N. A. (2013). EN4: Quality controlled ocean temperature and salinity profiles and monthly objective analyses with uncertainty estimates. *Journal of Geophysical Research: Oceans*, *118*(12), 6704–6716. doi: 10.1002/2013JC009067

Gray, A. R., Johnson, K. S., Bushinsky, S. M., Riser, S. C., Russell, J. L., Talley, L. D., ... Sarmiento, J. L. (2018). Autonomous Biogeochemical Floats Detect Significant Carbon Dioxide Outgassing in the High-Latitude Southern Ocean. *Geophysical Research Letters*, *45*(17), 9049–9057. doi:

10.1029/2018GL078013

Gregor, L., & Gruber, N. (2021). OceanSODA-ETHZ: a global gridded data set of the surface ocean carbonate system for seasonal to decadal studies of ocean acidification. *Earth System Science Data*, *13*(2), 777–808. doi: 10.5194/essd-13-777-2021

Gregor, L., Kok, S., & Monteiro, P. M. S. (2017). Empirical methods for the estimation of Southern Ocean CO_2: support vector and random forest regression. *Biogeosciences*, *14*(23), 5551–5569. doi: 10.5194/bg-14-5551-2017

Gregor, L., Lebehot, A. D., Kok, S., & Scheel Monteiro, P. M. (2019). A comparative assessment of the uncertainties of global surface ocean CO_2 estimates using a machine-learning ensemble (CSIR-ML6 version 2019a) - have we hit the wall? *Geoscientific Model Development*, *12*(12), 5113–5136. doi: 10.5194/gmd-12-5113-2019

Gruber, N., Bakker, D. C. E., DeVries, T., Gregor, L., Hauck, J., Landschützer, P., . . . Müller, J. D. (2023). Trends and variability in the ocean carbon sink. *Nature Reviews Earth & Environment*, *4*(2), 119–134. Retrieved from https://doi.org/10.1038/s43017-022-00381-x doi: 10.1038/s43017-022-00381-x

Gruber, N., Clement, D., Carter, B. R., Feely, R. A., van Heuven, S., Hoppema, M., . . . Wanninkhof, R. (2019). The oceanic sink for anthropogenic co2 from 1994 to 2007. *Science*, *363*(6432), 1193-1199. Retrieved from https://www.science.org/doi/abs/10.1126/science.aau5153 doi: 10.1126/science.aau5153

Gruber, N., Gloor, M., Mikaloff Fletcher, S. E., Doney, S. C., Dutkiewicz, S., Follows, M. J., . . . Takahashi, T. (2009). Oceanic sources, sinks, and transport of atmospheric CO $_2$. *Global Biogeochemical Cycles*, *23*(1), n/a–n/a. doi: 10.1029/2008GB003349

Gruber, N., Landschützer, P., & Lovenduski, N. S. (2019). The Variable Southern Ocean Carbon Sink. *Annual Review of Marine Science*, *11*(1), 159–186. doi: 10.1146/annurev-marine-121916-063407

Gruber, N., Sarmiento, J. L., & Stocker, T. F. (1996). An improved method for detecting anthropogenic CO2 in the oceans. *Global Biogeochemical Cycles*, *10*(4), 809–837. Retrieved from http://doi.wiley.com/10.1029/96GB01608 doi: 10.1029/96GB01608

Hauck, J., Nissen, C., Landschützer, P., Rödenbeck, C., Bushinsky, S., & Olsen, A. (2023). Sparse observations induce large biases in estimates of the global ocean CO2 sink: an ocean model subsampling experiment. *Philosophical Transactions of the Royal Society A: Mathematical, Physical and Engineering Sciences*, *381*(2249). Retrieved from https://royalsocietypublishing.org/doi/10.1098/rsta.2022.0063 doi: 10.1098/rsta.2022.0063

Hauck, J., Völker, C., Wang, T., Hoppema, M., Losch, M., & Wolf-Gladrow, D. A. (2013). Seasonally different carbon flux changes in the Southern Ocean in response to the southern annular mode. *Global Biogeochemical Cycles*, *27*(4), 1236–1245. doi: 10.1002/2013GB004600

Hauck, J., Völker, C., Wolf-Gladrow, D. A., Laufkötter, C., Vogt, M., Aumont, O., . . . Totterdell, I. (2015). On the Southern Ocean CO_2 uptake and the role of the biological carbon pump in the 21st century. *Global Biogeochemical Cycles*, *29*(9), 1451–1470. doi: 10.1002/2015GB005140

Hauck, J., Zeising, M., Le Quéré, C., Gruber, N., Bakker, D. C. E., Bopp, L., . . . Séférian, R. (2020). Consistency and Challenges in the Ocean Carbon Sink Estimate for the Global Carbon Budget. *Frontiers in Marine Science*, *7*, 571720. doi: 10.3389/fmars.2020.571720

Haumann, A. (2016). *Southern ocean response to recent changes in surface freshwater fluxes* (Doctoral dissertation). doi: 10.3929/ETHZ-B-000166276

Haumann, F., Gruber, N., & Münnich, M. (2020). Sea-Ice Induced Southern Ocean

Subsurface Warming and Surface Cooling in a Warming Climate. *AGU Advances*, *1*(2). doi: 10.1029/2019av000132

Hauri, C., Doney, S. C., Takahashi, T., Erickson, M., Jiang, G., & Ducklow, H. (2015). Two decades of inorganic carbon dynamics along the West Antarctic Peninsula. *Biogeosciences*, *12*(22), 6761–6779. doi: 10.5194/bg-12-6761-2015

Holzer, M., & DeVries, T. (2022). Source-Labeled Anthropogenic Carbon Reveals a Large Shift of Preindustrial Carbon From the Ocean to the Atmosphere. *Global Biogeochemical Cycles*, *36*(10). doi: 10.1029/2022GB007405

Hoppema, M. (2004). Weddell Sea turned from source to sink for atmospheric CO_2 between pre-industrial time and present. *Global and Planetary Change*, *40*(3-4), 219–231. doi: 10.1016/j.gloplacha.2003.08.001

Hoppema, M., Bakker, K., van Heuven, S. M., van Ooijen, J. C., & de Baar, H. J. (2015). Distributions, trends and inter-annual variability of nutrients along a repeat section through the Weddell Sea (1996-2011). *Marine Chemistry*, *177*, 545–553. doi: 10.1016/j.marchem.2015.08.007

Hoppema, M., Fahrbach, E., Stoll, M. H., & de Baar, H. J. (1998). Increase of carbon dioxide in the bottom water of the Weddell Sea, Antarctica. *Marine Chemistry*, *59*(3-4), 201–210. doi: 10.1016/S0304-4203(97)00094-7

Huang, B., Thorne, P. W., Banzon, V. F., Boyer, T. P., Chepurin, G., Lawrimore, J. H., … Zhang, H.-M. (2017). *NOAA Extended Reconstructed Sea Surface Temperature (ERSST), Version 5.* NOAA National Centers for Environmental Information. doi: 10.7289/V5T72FNM

Iida, T., Odate, T., & Fukuchi, M. (2013). Long-Term Trends of Nutrients and Apparent Oxygen Utilization South of the Polar Front in Southern Ocean Intermediate Water from 1965 to 2008. *PLoS ONE*, *8*(8), e71766. doi: 10.1371/journal.pone.0071766

Iida, Y., Takatani, Y., Kojima, A., & Ishii, M. (2021). Global trends of ocean CO_2 sink and ocean acidification: an observation-based reconstruction of surface ocean inorganic carbon variables. *Journal of Oceanography*, *77*(2), 323–358. doi: 10.1007/s10872-020-00571-5

Ilyina, T., Six, K. D., Segschneider, J., Maier-Reimer, E., Li, H., & Núñez-Riboni, I. (2013). Global ocean biogeochemistry model HAMOCC: Model architecture and performance as component of the MPI-Earth system model in different CMIP5 experimental realizations. *Journal of Advances in Modeling Earth Systems*, *5*(2), 287–315. doi: 10.1029/2012MS000178

Ito, T., Woloszyn, M., & Mazloff, M. (2010). Anthropogenic carbon dioxide transport in the Southern Ocean driven by Ekman flow. *Nature*, *463*(7277), 80–83. doi: 10.1038/nature08687

Iudicone, D., Rodgers, K. B., Plancherel, Y., Aumont, O., Ito, T., Key, R. M., … Ishii, M. (2016). The formation of the ocean's anthropogenic carbon reservoir. *Scientific Reports*, *6*(1), 35473. doi: 10.1038/srep35473

Jacobs, S. S. (2004). Bottom water production and its links with the thermohaline circulation. *Antarctic Science*, *16*(4), 427–437. doi: 10.1017/S095410200400224X

Johnson, K. S., Plant, J. N., Coletti, L. J., Jannasch, H. W., Sakamoto, C. M., Riser, S. C., … Sarmiento, J. L. (2017). Biogeochemical sensor performance in the SOCCOM profiling float array. *Journal of Geophysical Research: Oceans*, *122*(8), 6416–6436. doi: 10.1002/2017JC012838

Jones, D. C., Meijers, A. J. S., Shuckburgh, E., Sallée, J.-B., Haynes, P., McAufield, E. K., & Mazloff, M. R. (2016). How does Subantarctic Mode Water ventilate the Southern Hemisphere subtropics? *Journal of Geophysical Research: Oceans*, *121*(9), 6558–6582. doi: 10.1002/2016JC011680

Jones, E., Bakker, D. C., Venables, H. J., & Hardman-Mountford, N. J. (2015). Seasonal cycle of CO_2 from the sea ice edge to island blooms in the Scotia Sea, Southern Ocean. *Marine Chemistry*, *177*, 490–500. doi: 10.1016/

j.marchem.2015.06.031

Jones, E., Bakker, D. C., Venables, H. J., & Watson, A. J. (2012). Dynamic seasonal cycling of inorganic carbon downstream of South Georgia, Southern Ocean. *Deep Sea Research Part II: Topical Studies in Oceanography*, *59-60*, 25–35. doi: 10.1016/j.dsr2.2011.08.001

Katavouta, A., & Williams, R. G. (2021). Ocean carbon cycle feedbacks in CMIP6 models: contributions from different basins. *Biogeosciences*, *18*(10), 3189–3218. doi: 10.5194/bg-18-3189-2021

Keppler, L., & Landschützer, P. (2019). Regional Wind Variability Modulates the Southern Ocean Carbon Sink. *Scientific Reports*, *9*(1), 7384. doi: 10.1038/s41598-019-43826-y

Kessler, A., & Tjiputra, J. (2016). The Southern Ocean as a constraint to reduce uncertainty in future ocean carbon sinks. *Earth System Dynamics*, *7*(2), 295–312. doi: 10.5194/esd-7-295-2016

Khatiwala, S., Primeau, F., & Hall, T. (2009). Reconstruction of the history of anthropogenic CO_2 concentrations in the ocean. *Nature*, *462*(7271), 346–349. doi: 10.1038/nature08526

Klatt, O., Fahrbach, E., Hoppema, M., & Rohardt, G. (2005). The transport of the weddell gyre across the prime meridian. *Deep Sea Research Part II: Topical Studies in Oceanography*, *52*(3), 513-528. Retrieved from `https://www.sciencedirect.com/science/article/pii/S0967064504003066` (Direct observations of oceanic flow: A tribute to Walter Zenk) doi: https://doi.org/10.1016/j.dsr2.2004.12.015

Kriest, I., & Oschlies, A. (2015). MOPS-1.0: Towards a model for the regulation of the global oceanic nitrogen budget by marine biogeochemical processes. *Geoscientific Model Development*, *8*(9), 2929–2957. doi: 10.5194/gmd-8-2929-2015

Lacroix, F., Ilyina, T., & Hartmann, J. (2020). Oceanic CO_2 outgassing and biological production hotspots induced by pre-industrial river loads of nutrients and carbon in a global modeling approach. *Biogeosciences*, *17*(1), 55–88. doi: 10.5194/bg-17-55-2020

Landschützer, P., Gruber, N., & Bakker, D. C. (2016). Decadal variations and trends of the global ocean carbon sink. *Global Biogeochemical Cycles*, *30*(10), 1396–1417. doi: 10.1002/2015GB005359

Landschützer, P., Gruber, N., & Bakker, D. C. E. (2020). *An observation-based global monthly gridded sea surface pCO_2 product from 1982 onward and its monthly climatology (NCEI Accession 0160558)* (Tech. Rep.). Retrieved from `https://www.ncei.noaa.gov/access/ocean-carbon-acidification-data-system/oceans/SPCO2{\_}1982{\_}present{\_}ETH{\_}SOM{\_}FFN.html`

Landschützer, P., Gruber, N., Bakker, D. C. E., & Schuster, U. (2014). Recent variability of the global ocean carbon sink. *Global Biogeochemical Cycles*, *28*(9), 927–949. doi: 10.1002/2014GB004853

Landschützer, P., Gruber, N., Haumann, F. A., Rödenbeck, C., Bakker, D. C. E., van Heuven, S., ... Wanninkhof, R. (2015). The reinvigoration of the Southern Ocean carbon sink. *Science*, *349*(6253), 1221–1224. doi: 10.1126/science.aab2620

Langlais, C. E., Lenton, A., Matear, R., Monselesan, D., Legresy, B., Cougnon, E., & Rintoul, S. (2017). Stationary Rossby waves dominate subduction of anthropogenic carbon in the Southern Ocean. *Scientific Reports*, *7*(1), 17076. doi: 10.1038/s41598-017-17292-3

Large, W. G., McWilliams, J. C., & Doney, S. C. (1994). Oceanic Vertical Mixing - a Review and a Model with a Nonlocal Boundary-Layer Parameterization. *Reviews of Geophysics*, *32*(94), 363–403. doi: 10.1029/94rg01872

Lauderdale, J. M., Dutkiewicz, S., Williams, R. G., & Follows, M. J. (2016). Quantifying the drivers of ocean-atmosphere CO_2 fluxes. *Global Biogeochemical Cy-*

cles, *30*(7), 983–999. doi: 10.1002/2016GB005400

Le Quéré, C., Andrew, R. M., Friedlingstein, P., Sitch, S., Hauck, J., Pongratz, J., . . . Zheng, B. (2018). Global Carbon Budget 2018. *Earth System Science Data*, *10*(4), 2141–2194. doi: 10.5194/essd-10-2141-2018

Le Quéré, C., Buitenhuis, E. T., Moriarty, R., Alvain, S., Aumont, O., Bopp, L., . . . Vallina, S. M. (2016). Role of zooplankton dynamics for Southern Ocean phytoplankton biomass and global biogeochemical cycles. *Biogeosciences*, *13*(14), 4111–4133. doi: 10.5194/bg-13-4111-2016

Le Quéré, C., Takahashi, T. T., Buitenhuis, E. T., Rödenbeck, C., & Sutherland, S. C. (2010). Impact of climate change and variability on the global oceanic sink of CO_2. *Global Biogeochemical Cycles*, *24*(4), 1–10. doi: 10.1029/2009GB003599

Lenton, A., & Matear, R. J. (2007). Role of the Southern Annular Mode (SAM) in Southern Ocean CO2 uptake. *Global Biogeochemical Cycles*, *21*(2), 1–17. doi: 10.1029/2006GB002714

Lenton, A., Tilbrook, B., Law, R. M., Bakker, D., Doney, S. C., Gruber, N., . . . Takahashi, T. (2013). Sea-air CO_2 fluxes in the Southern Ocean for the period 1990-2009. *Biogeosciences*, *10*(6), 4037–4054. doi: 10.5194/bg-10-4037-2013

Le Quéré, C., Rödenbeck, C., Buitenhuis, E. T., Conway, T. J., Langenfelds, R., Gomez, A., . . . Heimann, M. (2007). Saturation of the Southern Ocean CO_2 Sink Due to Recent Climate Change. *Science*, *316*, 1735–1738. doi: 10.1126/science.1136188

Liao, E., Resplandy, L., Liu, J., & Bowman, K. W. (2020). Amplification of the Ocean Carbon Sink During El Niños: Role of Poleward Ekman Transport and Influence on Atmospheric CO_2. *Global Biogeochemical Cycles*, *34*(9), 1–23. doi: 10.1029/2020GB006574

Lindsay, K., Bonan, G. B., Doney, S. C., Hoffman, F. M., Lawrence, D. M., Long, M. C., . . . Thornton, P. E. (2014). Preindustrial-control and twentieth-century carbon cycle experiments with the Earth system model CESM1(BGC). *Journal of Climate*, *27*(24), 8981–9005. doi: 10.1175/JCLI-D-12-00565.1

Liu, J., Baskaran, L., Bowman, K., Schimel, D., Anthony Bloom, A., Parazoo, C. N., . . . Wofsy, S. (2021). Carbon Monitoring System Flux Net Biosphere Exchange 2020 (CMS-Flux NBE 2020). *Earth System Science Data*, *13*(2), 299–330. doi: 10.5194/essd-13-299-2021

Long, M. C., Stephens, B. B., McKain, K., Sweeney, C., Keeling, R. F., Kort, E. A., . . . Wofsy, S. C. (2021). Strong Southern Ocean carbon uptake evident in airborne observations. *Science*, *374*(6572), 1275–1280. doi: 10.1126/science.abi4355

Lovenduski, N. S., Gruber, N., Doney, S. C., & Lima, I. D. (2007). Enhanced CO_2 outgassing in the Southern Ocean from a positive phase of the Southern Annular Mode. *Global Biogeochemical Cycles*, *21*(2), n/a–n/a. doi: 10.1029/2006GB002900

Madec, G., & the NEMO team. (2016). *NEMO reference manual 3_6_STABLE: "NEMO ocean engine" Note du Pôle de modélisation.* Paris, France: Institut Pierre-Simon Laplace (IPSL).

Marshall, J., & Speer, K. (2012). Closure of the meridional overturning circulation through Southern Ocean upwelling. *Nature Geoscience*, *5*(3), 171–180. doi: 10.1038/ngeo1391

Matsumoto, K., & Gruber, N. (2005). How accurate is the estimation of anthropogenic carbon in the ocean? An evaluation of the Δ C * method. *Global Biogeochemical Cycles*, *19*(3). Retrieved from `http://doi.wiley.com/10.1029/2004GB002397` doi: 10.1029/2004GB002397

Mauritsen, T., Bader, J., Becker, T., Behrens, J., Bittner, M., Brokopf, R., . . . Roeckner, E. (2019). Developments in the MPI-M Earth System Model version 1.2 (MPI-ESM1.2) and Its Response to Increasing CO_2. *Journal of Advances* *in Modeling Earth Systems*, *11*(4), 998–1038. doi: 10.1029/2018MS001400

Mayot, N., Le Quéré, C., Rödenbeck, C., Bernardello, R., Bopp, L., Djeutchouang, L. M., … Zeng, J. (2023). Climate-driven variability of the Southern Ocean CO 2 sink. *Philosophical Transactions of the Royal Society A: Mathematical, Physical and Engineering Sciences*, *381*(2249). Retrieved from `https://royalsocietypublishing.org/doi/10.1098/rsta.2022.0055` doi: 10.1098/rsta.2022.0055

McKinley, G. A., Fay, A. R., Eddebbar, Y. A., Gloege, L., & Lovenduski, N. S. (2020). External Forcing Explains Recent Decadal Variability of the Ocean Carbon Sink. *AGU Advances*, *1*(2). doi: 10.1029/2019AV000149

McNeil, B. I., & Matear, R. J. (2013). The non-steady state oceanic CO_2 signal: Its importance, magnitude and a novel way to detect it. *Biogeosciences*, *10*(4), 2219–2228. doi: 10.5194/bg-10-2219-2013

Metzl, N., Brunet, C., Jabaud-Jan, A., Poisson, A., & Schauer, B. (2006). Summer and winter air-sea CO_2 fluxes in the Southern Ocean. *Deep-Sea Research Part I: Oceanographic Research Papers*, *53*(9), 1548–1563. doi: 10.1016/j.dsr.2006.07.006

Metzl, N., Tilbrook, B., & Poisson, A. (1999). The annual fCO_2 cycle and the air-sea CO_2 flux in the sub-Antarctic Ocean. *Tellus B: Chemical and Physical Meteorology*, *51*(4), 849. doi: 10.3402/tellusb.v51i4.16495

Mikaloff Fletcher, S. E., Gruber, N., Jacobson, A. R., Doney, S. C., Dutkiewicz, S., Gerber, M., … Sarmiento, J. L. (2006). Inverse estimates of anthropogenic CO $_2$ uptake, transport, and storage by the ocean. *Global Biogeochemical Cycles*, *20*(2). doi: 10.1029/2005GB002530

Mikaloff Fletcher, S. E., Gruber, N., Jacobson, A. R., Gloor, M., Doney, S. C., Dutkiewicz, S., … Sarmiento, J. L. (2007). Inverse estimates of the oceanic sources and sinks of natural CO_2 and the implied oceanic carbon transport. *Global Biogeochemical Cycles*, *21*(1). doi: 10.1029/2006GB002751

Mongwe, N. P., Chang, N., & Monteiro, P. M. S. (2016). The seasonal cycle as a mode to diagnose biases in modelled CO_2 fluxes in the Southern Ocean. *Ocean Modelling*, *106*, 90–103. doi: 10.1016/j.ocemod.2016.09.006

Mongwe, N. P., Vichi, M., & Monteiro, P. M. S. (2018). The seasonal cycle of pCO_2 and CO_2 fluxes in the Southern Ocean: diagnosing anomalies in CMIP5 Earth system models. *Biogeosciences*, *15*(9), 2851–2872. doi: 10.5194/bg-15-2851-2018

Morrison, A. K., Waugh, D. W., Hogg, A. M., Jones, D. C., & Abernathey, R. P. (2022). Ventilation of the Southern Ocean Pycnocline. *Annual Review of Marine Science*, *14*(1), 405–430. doi: 10.1146/annurev-marine-010419-011012

Murnane, R. J., Sarmiento, J. L., & Le Quéré, C. (1999). Spatial distribution of air-sea CO_2 fluxes and the interhemispheric transport of carbon by the oceans. *Global Biogeochemical Cycles*, *13*(2), 287–305. doi: 10.1029/1998GB900009

Nevison, C. D., Munro, D. R., Lovenduski, N. S., Keeling, R. F., Manizza, M., Morgan, E. J., & Rödenbeck, C. (2020). Southern Annular Mode Influence on Wintertime Ventilation of the Southern Ocean Detected in Atmospheric O_2 and CO_2 Measurements. *Geophysical Research Letters*, *47*(4), 1–9. doi: 10.1029/2019GL085667

Nicholson, S. A., Whitt, D. B., Fer, I., du Plessis, M. D., Lebéhot, A. D., Swart, S., … Monteiro, P. M. (2022). Storms drive outgassing of CO_2 in the subpolar Southern Ocean. *Nature Communications*, *13*(1), 1–12. doi: 10.1038/s41467-021-27780-w

Nissen, C., Vogt, M., Münnich, M., Gruber, N., & Alexander Haumann, F. (2018). Factors controlling coccolithophore biogeography in the Southern Ocean. *Biogeosciences*, *15*(22), 6997–7024. doi: 10.5194/bg-15-6997-2018

Niwa, Y., Fujii, Y., Sawa, Y., Iida, Y., Ito, A., Satoh, M., … Saigusa, N. (2017). A 4D-Var inversion system based on the icosahedral grid model (NICAM-TM

4D-Var v1.0) - Part 2: Optimization scheme and identical twin experiment of atmospheric CO2 inversion. *Geoscientific Model Development*, *10*(6), 2201–2219. doi: 10.5194/gmd-10-2201-2017

Olsen, A., Key, R. M., van Heuven, S., Lauvset, S. K., Velo, A., Lin, X., ... Suzuki, T. (2016). The Global Ocean Data Analysis Project version 2 (GLODAPv2) - an internally consistent data product for the world ocean. *Earth System Science Data*, *8*(2), 297–323. doi: 10.5194/essd-8-297-2016

Orr, J. C., Maier-Reimer, E., Mikolajewicz, U., Monfray, P., Sarmiento, J. L., Toggweiler, J. R., ... Boutin, J. (2001). Estimates of anthropogenic carbon uptake from four three-dimensional global ocean models. *Global Biogeochemical Cycles*, *15*(1), 43–60. Retrieved from `http://doi.wiley.com/10.1029/2000GB001273` doi: 10.1029/2000GB001273

Orsi, A., Johnson, G., & Bullister, J. (1999). Circulation, mixing, and production of Antarctic Bottom Water. *Progress in Oceanography*, *43*(1), 55–109. doi: 10.1016/S0079-6611(99)00004-X

Panassa, E., Santana-Casiano, J. M., González-Dávila, M., Hoppema, M., van Heuven, S. M., Völker, C., ... Hauck, J. (2018). Variability of nutrients and carbon dioxide in the Antarctic Intermediate Water between 1990 and 2014. *Ocean Dynamics*, *68*(3), 295–308. doi: 10.1007/s10236-018-1131-2

Pardo, P. C., Tilbrook, B., Langlais, C., Trull, T. W., & Rintoul, S. R. (2017). Carbon uptake and biogeochemical change in the Southern Ocean, south of Tasmania. *Biogeosciences*, *14*(22), 5217–5237. doi: 10.5194/bg-14-5217-2017

Paulsen, H., Ilyina, T., Six, K. D., & Stemmler, I. (2017). Incorporating a prognostic representation of marine nitrogen fixers into the global ocean biogeochemical model HAMOCC. *Journal of Advances in Modeling Earth Systems*, *9*, 438–464. doi: 10.1002/2016MS000737.Received

Prend, C. J., Keerthi, M. G., Lévy, M., Aumont, O., Gille, S. T., & Talley, L. D. (2022). Sub-Seasonal Forcing Drives Year-To-Year Variations of Southern Ocean Primary Productivity. *Global Biogeochemical Cycles*, *36*(7), 1–15. doi: 10.1029/2022GB007329

Regnier, P. A., Resplandy, L., Najjar, R. G., & Ciais, P. (2022). The land-to-ocean loops of the global carbon cycle. *Nature 2022 603:7901*, *603*(7901), 401–410. doi: 10.1038/s41586-021-04339-9

Rintoul, S. R. (2018). The global influence of localized dynamics in the Southern Ocean. *Nature*, *558*(7709), 209–218. doi: 10.1038/s41586-018-0182-3

Riser, S. C., Swift, D., & Drucker, R. (2018). Profiling Floats in SOCCOM: Technical Capabilities for Studying the Southern Ocean. *Journal of Geophysical Research: Oceans*, *123*(6), 4055–4073. doi: 10.1002/2017JC013419

Ritter, R., Landschützer, P., Gruber, N., Fay, A. R., Iida, Y., Jones, S. D., ... Zeng, J. (2017). Observation-Based Trends of the Southern Ocean Carbon Sink. *Geophysical Research Letters*, *44*(24), 12,339–12,348. doi: 10.1002/2017GL074837

Rödenbeck, C., Bakker, D. C., Gruber, N., Iida, Y., Jacobson, A. R., Jones, S. D., ... Zeng, J. (2015). Data-based estimates of the ocean carbon sink variability - First results of the Surface Ocean pCO2 Mapping intercomparison (SOCOM). *Biogeosciences*, *12*(23), 7251–7278. doi: 10.5194/bg-12-7251-2015

Rödenbeck, C., Bakker, D. C., Metzl, N., Olsen, A., Sabine, C. L., Cassar, N., ... Heimann, M. (2014). Interannual sea–air CO_2 flux variability from an observation-driven ocean mixed-layer scheme. *Biogeosciences*, *11*(17), 4599–4613. doi: 10.5194/bg-11-4599-2014

Rödenbeck, C., Devries, T., Hauck, J., Le Quéré, C., & Keeling, R. F. (2022). Data-based estimates of interannual sea-air CO_2 flux variations 1957-2020 and their relation to environmental drivers. *Biogeosciences*, *19*(10), 2627–2652. doi: 10.5194/bg-19-2627-2022

Rödenbeck, C., Keeling, R. F., Bakker, D. C., Metzl, N., Olsen, A., Sabine, C. L., & Heimann, M. (2013). Global surface-ocean pCO_2 and sea-Air CO_2 flux variability from an observation-driven ocean mixed-layer scheme. *Ocean Science*, *9*(2), 193–216. doi: 10.5194/os-9-193-2013

Rödenbeck, C., Zaehle, S., Keeling, R., & Heimann, M. (2018). How does the terrestrial carbon exchange respond to inter-Annual climatic variations? A quantification based on atmospheric CO_2 data. *Biogeosciences*, *15*(8), 2481–2498. doi: 10.5194/bg-15-2481-2018

Russell, J. L., Dixon, K. W., Gnanadesikan, A., Stouffer, R. J., & Toggweiler, J. R. (2006). The Southern Hemisphere Westerlies in a Warming World: Propping Open the Door to the Deep Ocean. *Journal of Climate*, *19*(24), 6382–6390. doi: 10.1175/JCLI3984.1

Sabine, C. L., Feely, R. A., Gruber, N., Key, R. M., Lee, K., Bullister, J. L., ... Rios, A. F. (2004). The Oceanic Sink for Anthropogenic CO_2. *Science*, *305*(5682), 367–371. doi: 10.1126/science.1097403

Sabine, C. L., Hankin, S., Koyuk, H., Bakker, D. C., Pfeil, B., Olsen, A., ... Yoshikawa-Inoue, H. (2013). Surface Ocean CO_2 Atlas (SOCAT) gridded data products. *Earth System Science Data*, *5*(1), 145–153. doi: 10.5194/essd-5-145-2013

Sallée, J.-B., Speer, K., & Rintoul, S. R. (2010). Zonally asymmetric response of the Southern Ocean mixed-layer depth to the Southern Annular Mode. *Nature Geoscience*, *3*(4), 273–279. doi: 10.1038/ngeo812

Sallée, J.-B., Matear, R. J., Rintoul, S. R., & Lenton, A. (2012). Localized subduction of anthropogenic carbon dioxide in the Southern Hemisphere oceans. *Nature Geoscience*, *5*(8), 579–584. doi: 10.1038/ngeo1523

Sarmiento, J. L., & Gruber, N. (2006). *Ocean Biogeochemical Dynamics*. Princeton, NJ: Princeton University Press.

Sarmiento, J. L., Orr, J. C., & Siegenthaler, U. (1992). A perturbation simulation of CO 2 uptake in an ocean general circulation model. *Journal of Geophysical Research*, *97*(C3), 3621. Retrieved from `http://doi.wiley.com/10.1029/91JC02849` doi: 10.1029/91JC02849

Schourup-Kristensen, V., Sidorenko, D., Wolf-Gladrow, D. A., & Völker, C. (2014). A skill assessment of the biogeochemical model REcoM2 coupled to the finite element sea ice-ocean model (FESOM 1.3). *Geoscientific Model Development*, *7*(6), 2769–2802. doi: 10.5194/gmd-7-2769-2014

Schourup-Kristensen, V., Wekerle, C., Wolf-Gladrow, D. A., & Völker, C. (2018). Arctic Ocean biogeochemistry in the high resolution FESOM1.4-REcoM2 model. *Progress in Oceanography*, *168*(August), 65–81. doi: 10.1016/j.pocean.2018.09.006

Schultz, C., Doney, S. C., Hauck, J., Kavanaugh, M. T., & Schofield, O. (2021). Modeling Phytoplankton Blooms and Inorganic Carbon Responses to Sea-Ice Variability in the West Antarctic Peninsula. *Journal of Geophysical Research: Biogeosciences*, *126*(4), 1–21. doi: 10.1029/2020JG006227

Schwinger, J., Goris, N., Tjiputra, J. F., Kriest, I., Bentsen, M., Bethke, I., ... Heinze, C. (2016). Evaluation of NorESM-OC (versions 1 and 1.2), the ocean carbon-cycle stand-alone configuration of the Norwegian Earth System Model (NorESM1). *Geoscientific Model Development*, *9*(8), 2589–2622. doi: 10.5194/gmd-9-2589-2016

Séférian, R., Berthet, S., Yool, A., Palmiéri, J., Bopp, L., Tagliabue, A., ... Yamamoto, A. (2020). Tracking Improvement in Simulated Marine Biogeochemistry Between CMIP5 and CMIP6. *Current Climate Change Reports*, *6*(3), 95–119. doi: 10.1007/s40641-020-00160-0

Séférian, R., Gehlen, M., Bopp, L., Resplandy, L., Orr, J. C., Marti, O., ... Romanou, A. (2016). Inconsistent strategies to spin up models in CMIP5: Implications for ocean biogeochemical model performance assessment. *Geoscientific Model Development*, *9*(5), 1827–1851. doi: 10.5194/gmd-9-1827-2016

Séférian, R., Nabat, P., Michou, M., Saint-Martin, D., Voldoire, A., Colin, J., ...

Madec, G. (2019). Evaluation of CNRM Earth System Model, CNRM-ESM2-1: Role of Earth System Processes in Present-Day and Future Climate. *Journal of Advances in Modeling Earth Systems*, *11*(12), 4182–4227. doi: 10.1029/2019MS001791

Shadwick, E. H., De Meo, O. A., Schroeter, S., Arroyo, M. C., Martinson, D. G., & Ducklow, H. (2021). Sea Ice Suppression of CO_2 Outgassing in the West Antarctic Peninsula: Implications For The Evolving Southern Ocean Carbon Sink. *Geophysical Research Letters*, *48*(11), 1–10. doi: 10.1029/2020GL091835

Smith, W., Rivaro, P., Wang, Z., Larue, M., Heywood, K., Park, J., ... Kim, M. (2021). *Observational Activities in the Ross Sea: Current and Future National Contributions to SOOS - An Update* (Tech. Rep.). Retrieved 2023-02-22, from `https://zenodo.org/record/5762638` doi: 10.5281/ZENODO.5762638

Stammer, D., Wunsch, C., Giering, R., Eckert, C., Heimbach, P., Marotzke, J., ... Marshall, J. (2002). Global ocean circulation during 1992-1997, estimated from ocean observations and a general circulation model. *Journal of Geophysical Research: Oceans*, *107*(9). doi: 10.1029/2001jc000888

Stephens, B. B., Keeling, R. F., Heimann, M., Six, K. D., Murnane, R., & Caldeira, K. (1998). Testing global ocean carbon cycle models using measurements of atmospheric O_2 and CO_2 concentration. *Global Biogeochemical Cycles*, *12*(2), 213–230. doi: 10.1029/97GB03500

Stock, C. A., Dunne, J. P., Fan, S., Ginoux, P., John, J., Krasting, J. P., ... Zadeh, N. (2020). Ocean Biogeochemistry in GFDL's Earth System Model 4.1 and Its Response to Increasing Atmospheric CO2. *Journal of Advances in Modeling Earth Systems*, *12*(10). doi: 10.1029/2019MS002043

Sutton, A. J., Williams, N. L., & Tilbrook, B. (2021). Constraining Southern Ocean CO_2 Flux Uncertainty Using Uncrewed Surface Vehicle Observations. *Geophysical Research Letters*, *48*(3), 1–9. doi: 10.1029/2020GL091748

Takahashi, T., Olafsson, J., Goddard, J. G., Chipman, D. W., & Sutherland, S. C. (1993). Seasonal variation of CO_2 and nutrients in the high-latitude surface oceans: A comparative study. *Global Biogeochemical Cycles*, *7*(4), 843–878. doi: 10.1029/93GB02263

Takahashi, T., Sutherland, S. C., Sweeney, C., Poisson, A., Metzl, N., Tilbrook, B., ... Nojiri, Y. (2002). Global sea-air CO_2 flux based on climatological surface ocean pCO_2, and seasonal biological and temperature effects. *Deep-Sea Research Part II: Topical Studies in Oceanography*, *49*(9-10), 1601–1622. doi: 10.1016/S0967-0645(02)00003-6

Takahashi, T., Sutherland, S. C., Wanninkhof, R., Sweeney, C., Feely, R. A., Chipman, D. W., ... de Baar, H. J. (2009). Climatological mean and decadal change in surface ocean pCO_2, and net sea-air CO_2 flux over the global oceans. *Deep Sea Research Part II: Topical Studies in Oceanography*, *56*(8-10), 554–577. doi: 10.1016/j.dsr2.2008.12.009

Talley, L. (2013). Closure of the Global Overturning Circulation Through the Indian, Pacific, and Southern Oceans: Schematics and Transports. *Oceanography*, *26*(1), 80–97. doi: 10.5670/oceanog.2013.07

Talley, L., Feely, R., Sloyan, B., Wanninkhof, R., Baringer, M., Bullister, J., ... Zhang, J.-Z. (2016). Changes in Ocean Heat, Carbon Content, and Ventilation: A Review of the First Decade of GO-SHIP Global Repeat Hydrography. *Annual Review of Marine Science*, *8*(1), 185–215. doi: 10.1146/annurev-marine-052915-100829

Tamsitt, V., Talley, L. D., Mazloff, M. R., Cerovecki, I., Cerovečki, I., Tamsitt, V., ... Cerovečki, I. (2016). Zonal variations in the Southern Ocean heat budget. *Journal of Climate*, *29*(18), 6563–6579. doi: 10.1175/JCLI-D-15-0630.1

Terhaar, J., Frölicher, T. L., & Joos, F. (2021). Southern Ocean anthropogenic carbon sink constrained by sea surface salinity. *Science Advances*, *7*(18), eabd5964. doi: 10.1126/sciadv.abd5964

Terhaar, J., Frölicher, T. L., & Joos, F. (2022). Observation-constrained estimates of the global ocean carbon sink from Earth system models. *Biogeosciences*, *19*(18), 4431–4457. doi: 10.5194/bg-19-4431-2022

Terhaar, J., Goris, N., Müller, J. D., DeVries, T., Gruber, N., Hauck, J., ... Seferian, R. (2023). Assessment of global ocean biogeochemical models for ocean carbon sink estimates in RECCAP2 and recommendations for future studies. *submitted to Global Biogeochemical Cycles*.

Tohjima, Y., Mukai, H., MacHida, T., Hoshina, Y., & Nakaoka, S. I. (2019). Global carbon budgets estimated from atmospheric O_2:N_2 and CO_2 observations in the western Pacific region over a 15-year period. *Atmospheric Chemistry and Physics*, *19*(14), 9269–9285. doi: 10.5194/acp-19-9269-2019

Urakawa, L. S., Tsujino, H., Nakano, H., Sakamoto, K., Yamanaka, G., & Toyoda, T. (2020). The sensitivity of a depth-coordinate model to diapycnal mixing induced by practical implementations of the isopycnal tracer diffusion scheme. *Ocean Modelling*, *154*(August), 101693. doi: 10.1016/j.ocemod.2020.101693

van der Laan-Luijkx, I. T., van der Velde, I. R., van der Veen, E., Tsuruta, A., Stanislawska, K., Babenhauserheide, A., ... Peters, W. (2017). The CarbonTracker Data Assimilation Shell (CTDAS) v1.0: Implementation and global carbon balance 2001-2015. *Geoscientific Model Development*, *10*(7), 2785–2800. doi: 10.5194/gmd-10-2785-2017

van Heuven, S., Hoppema, M., Jones, E. M., & de Baar, H. J. (2014). Rapid invasion of anthropogenic CO2 into the deep circulation of the Weddell Gyre. *Philosophical Transactions of the Royal Society A: Mathematical, Physical and Engineering Sciences*, *372*(2019). doi: 10.1098/rsta.2013.0056

Verdy, A., Dutkiewicz, S., Follows, M. J., Marshall, J., & Czaja, A. (2007). Carbon dioxide and oxygen fluxes in the Southern Ocean: Mechanisms of interannual variability. *Global Biogeochemical Cycles*, *21*(2), 1–10. doi: 10.1029/2006GB002916

Verdy, A., & Mazloff, M. R. (2017). A data assimilating model for estimating Southern Ocean biogeochemistry. *Journal of Geophysical Research: Oceans*, *122*(9), 6968–6988. doi: 10.1002/2016JC012650

Wanninkhof, R. (1992). Relationship Between Wind Speed and Gas Exchange. *Journal of Geophysical Research, Oceans*, *97*(92), 7373–7382.

Wanninkhof, R. (2023). Impact predictor variables on magnitude, variability and trend of global air-sea CO_2 fluxes using an Extra Trees machine learning approach. *Global Biogeochemical Cycles*.

Wanninkhof, R., Asher, W. E., Weppernig, R., Chen, H., Schlosser, P., Langdon, C., & Sambrotto, R. (1993). Gas transfer experiment on Georges Bank using two volatile deliberate tracers. *Journal of Geophysical Research*, *98*(C11). doi: 10.1029/93jc01844

Wanninkhof, R. H. (2014). Relationship between wind speed and gas exchange over the ocean revisited. *Limnology and Oceanography: Methods*, *12*(JUN), 351–362. doi: 10.4319/lom.2014.12.351

Wanninkhof, R. H., Asher, W. E., Ho, D. T., Sweeney, C., & McGillis, W. R. (2009). Advances in Quantifying Air-Sea Gas Exchange and Environmental Forcing. *Annual Review of Marine Science*, *1*(1), 213–244. doi: 10.1146/annurev.marine.010908.163742

Wanninkhof, R. H., Park, G.-H. H., Takahashi, T. T., Sweeney, C., Feely, R. A., Nojiri, Y., ... Khatiwala, S. (2013). Global ocean carbon uptake: magnitude, variability and trends. *Biogeosciences*, *10*(3), 1983–2000. doi: 10.5194/bg-10-1983-2013

Watson, A. J., Schuster, U., Shutler, J. D., Holding, T., Ashton, I. G., Landschützer, P., ... Goddijn-Murphy, L. (2020). Revised estimates of ocean-atmosphere CO_2 flux are consistent with ocean carbon inventory. *Nature Communications*, *11*(1), 1–6. doi: 10.1038/s41467-020-18203-3

Waugh, D. W., Hall, T. M., Mcneil, B. I., Key, R., & Matear, R. J. (2006). Anthropogenic CO_2 in the oceans estimated using transit time distributions. *Tellus, Series B: Chemical and Physical Meteorology*, *58*(5), 376–389. doi: 10.1111/j.1600-0889.2006.00222.x

Waugh, D. W., Hogg, A. M., Spence, P., England, M. H., & Haine, T. W. (2019). Response of Southern Ocean ventilation to changes in midlatitude westerly winds. *Journal of Climate*, *32*(17), 5345–5361. doi: 10.1175/JCLI-D-19-0039.1

Williams, N. L., Juranek, L. W., Feely, R. A., Johnson, K. S., Sarmiento, J. L., Talley, L. D., ... Takeshita, Y. (2017). Calculating surface ocean pCO_2 from biogeochemical Argo floats equipped with pH: An uncertainty analysis. *Global Biogeochemical Cycles*, *31*(3), 591–604. doi: 10.1002/2016GB005541

Williams, N. L., Juranek, L. W., Johnson, K. S., Feely, R. A., Riser, S. C., Talley, L. D., ... Wanninkhof, R. (2016). Empirical algorithms to estimate water column pH in the Southern Ocean. *Geophysical Research Letters*, *43*, 3415-3422. doi: 10.1002/2016GL068539

Woolf, D. K., Land, P. E., Shutler, J. D., Goddijn-Murphy, L., & Donlon, C. J. (2016). On the calculation of air-sea fluxes of CO_2 in the presence of temperature and salinity gradients. *Journal of Geophysical Research: Oceans*, *121*(2), 1229–1248. doi: 10.1002/2015JC011427

Wright, R. M., Le Quéré, C., Buitenhuis, E., Pitois, S., & Gibbons, M. J. (2021). Role of jellyfish in the plankton ecosystem revealed using a global ocean biogeochemical model. *Biogeosciences*, *18*(4), 1291–1320. doi: 10.5194/bg-18-1291-2021

Wunsch, C., & Heimbach, P. (2013). *Dynamically and kinematically consistent global ocean circulation and ice state estimates* (2nd ed., Vol. 103). Elsevier Ltd. doi: 10.1016/B978-0-12-391851-2.00021-0

Yang, M., Smyth, T. J., Kitidis, V., Brown, I. J., Wohl, C., Yelland, M. J., & Bell, T. G. (2021). Natural variability in air-sea gas transfer efficiency of CO_2. *Scientific Reports*, *11*(1), 1–9. doi: 10.1038/s41598-021-92947-w

Yang, S., & Gruber, N. (2016). The anthropogenic perturbation of the marine nitrogen cycle by atmospheric deposition: Nitrogen cycle feedbacks and the 15N Haber-Bosch effect. *Global Biogeochemical Cycles*, *30*(10), 1418–1440. doi: 10.1002/2016GB005421

Zeng, J., Iida, Y., Matsunaga, T., & Shirai, T. (2022). Surface ocean CO_2 concentration and air-sea flux estimate by machine learning with modelled variable trends. *Frontiers in Marine Science*, *9*(September), 1–14. doi: 10.3389/fmars.2022.989233

The Southern Ocean carbon cycle 1985-2018: Mean, seasonal cycle, trends and storage

Judith Hauck[1], Luke Gregor[2],Cara Nissen[1,3], Lavinia Patara[4], Mark Hague[2], N. Precious Mongwe[5], Seth Bushinsky[6], Scott C. Doney[7], Nicolas Gruber[2], Corinne Le Quéré[8], Manfredi Manizza[9], Matthew Mazloff[9], Pedro M. S. Monteiro[5,10], Jens Terhaar[11,12,13]

[1]Alfred-Wegener-Institut, Helmholtz-Zentrum für Polar- und Meeresforschung, Bremerhaven, Germany
[2]Environmental Physics, Institute of Biogeochemistry and Pollutant Dynamics, ETH Zurich, Zürich, Switzerland
[3]Department of Atmospheric and Oceanic Sciences and Institute of Arctic and Alpine Research, University of Colorado, Boulder, Colorado, USA
[4]GEOMAR Helmholtz Centre for Ocean Research Kiel, Kiel, Germany
[5]Southern Ocean Carbon-Climate Observatory, CSIR, South Africa
[6]University of Hawai'i Mānoa
[7]Dept. of Environmental Sciences, University of Virginia, Charlottesville, VA, USA
[8]School of Environmental Sciences, University of East Anglia
[9]Scripps Institution of Oceanography, University of California - San Diego, La Jolla, CA
[10]School for Climate Studies, Stellenbosch University, South Africa
[11]Climate and Environmental Physics, Physics Institute, University of Bern, Switzerland
[12]Oeschger Centre for Climate Change Research, University of Bern, Switzerland
[13]Department of Marine Chemistry and Geochemistry, Woods Hole Oceanographic Institution, 360 Woods Hole Road, Woods Hole, 02543, Massachusetts, USA

Key Points:

- Ocean models and machine learning estimates agree on the mean Southern Ocean CO_2 sink, but the trend since 2000 differs by a factor of two.
- Compared with RECCAP1, the updated estimate for the Southern Ocean CO_2 uptake is 50% smaller.
- Large model spread in summer and winter indicates that sustained efforts are required to understand driving processes in all seasons.

Corresponding author: Judith Hauck, `judith.hauck@awi.de`

Abstract

We assess the Southern Ocean CO_2 uptake (1985-2018) using data sets gathered in the REgional Carbon Cycle Assessment and Processes Project phase 2 (RECCAP2). The Southern Ocean acted as a sink for CO_2 with close agreement between simulation results from global ocean biogeochemistry models (GOBMs, 0.75±0.28 PgC yr^{-1}) and pCO_2-observation-based products (0.73±0.07 PgC yr^{-1}). This sink is only half that reported by RECCAP1. The present-day net uptake is to first order a response to rising atmospheric CO_2, driving large amounts of anthropogenic CO_2 (C_{ant}) into the ocean, thereby overcompensating the loss of natural CO_2 to the atmosphere. An apparent knowledge gap is the increase of the sink since 2000, with pCO_2-products suggesting a growth that is more than twice as strong and uncertain as that of GOBMs (0.26±0.06 and 0.11± 0.03 Pg C yr−1 $decade^{-1}$ respectively). This is despite nearly identical pCO_2 trends in GOBMs and pCO_2-products when both products are compared only at the locations where pCO_2 was measured. Seasonal analyses revealed agreement in driving processes in winter with uncertainty in the magnitude of outgassing, whereas discrepancies are more fundamental in summer, when GOBMs exhibit difficulties in simulating the effects of the non-thermal processes of biology and mixing/circulation. Ocean interior accumulation of C_{ant} points to an underestimate of C_{ant} uptake and storage in GOBMs. Future work needs to link surface fluxes and interior ocean transport, build long overdue systematic observation networks and push towards better process understanding of drivers of the carbon cycle.

Plain Language Summary

The ocean takes up CO_2 from the atmosphere and thus slows climate change. The Southern Ocean has been long known to be an important region for ocean CO_2 uptake. Here, we bring together all available data sets that estimate the Southern Ocean CO_2 uptake, from models that simulate ocean circulation and physical and biological processes that affect the ocean carbon cycle, from surface ocean observation-based estimates, from atmospheric transport models that ingest atmospheric CO_2 observations, and from interior ocean biogeochemical observations. With these data sets, we find good agreement on the mean Southern Ocean CO_2 uptake 1985-2018, which is 50% smaller than previous estimates when recalculated for the time period and spatial extent used in the previous estimate. However, the estimates of the temporal change of the Southern Ocean CO_2 uptake differ by a factor of two and thus are not in agreement. We further highlight that knowledge gaps exist not only in winter when observations are typically rare, but equally in summer when biology plays a larger role, which is typically represented in a too simplistic fashion in the dynamic models.

1 Introduction

The Southern Ocean (Figure 1) is the primary conduit between the surface and the deep ocean (Talley, 2013; Morrison et al., 2022) making it a key region for the global carbon cycle and the climate system across time-scales from paleo to present day and into the future (Canadell et al., 2021). Firstly, water mass formation of Antarctic surface water occurs during large-scale upwelling of deep, old and carbon-rich water masses due to strong westerly winds (Russell et al., 2006; Marshall & Speer, 2012). Part of this water moves northwards by Ekman transport and contributes to the formation of Southern mode and intermediate waters (Ito et al., 2010; Sallée et al., 2012; Morrison et al., 2022) together with subtropical water masses (Iudicone et al., 2016). Another part moves southward and circulates in the large gyres of the Weddell and Ross Seas (Klatt et al., 2005). A fraction of these Antarctic surface waters densify on the Antarctic shelves through cooling and brine rejection during sea-ice formation on the Antarctic shelves to then flow down the Antarctic slope and form Antarctic Bottom Water (Orsi et al., 1999; Jacobs, 2004).

Historically, in pre-industrial times, the Southern Ocean was a net source of CO_2 to the atmosphere due to upwelling of carbon-rich deep waters (Mikaloff Fletcher et al., 2007). Importantly, the large-scale upwelling that drove the natural outgassing fluxes in the polar and subpolar Southern Ocean still occurs today. However, since industrialisation, increasing atmospheric levels of CO_2 have shifted the thermodynamic equilibrium of CO_2 partial pressure between the ocean and the atmosphere in the favor of the latter, thus overcompensating the natural outgassing(e.g., Hoppema, 2004). The contemporary net flux in the Southern Ocean can thus be understood as the sum of the outgassing of natural CO_2 and uptake of anthropogenic CO_2 (Gruber et al., 2009; Gruber, Landschützer, & Lovenduski, 2019). Importantly, the Southern Ocean has acted as the primary region of uptake for anthropogenic CO_2 in the industrialized era (Sarmiento et al., 1992; Orr et al., 2001; Caldeira & Duffy, 2000; Khatiwala et al., 2009; Frölicher et al., 2015; Mikaloff Fletcher et al., 2006), which is attributed to upwelling of old water masses (with low anthropogenic carbon) in a region of high wind speeds, as well as subsequent transport of excess carbon from the surface into the ocean interior through the formation of Subantarctic Mode and Antarctic Intermediate Water (Waugh et al., 2006; Mikaloff Fletcher et al., 2006; Bopp et al., 2015; Langlais et al., 2017; Sallée et al., 2012). In the absence of evidence of substantial changes in the biological carbon pump over the past decades, the role of biology for anthropogenic carbon uptake is thought to be small (Murnane et al., 1999; Holzer & DeVries, 2022). However, the biological carbon pump can have a strong imprint on the net fluxes during the summer when primary production draws down natural CO_2 at the surface (e.g., E. Jones et al., 2012, 2015).

While the general importance of the Southern Ocean for the ocean carbon sink is recognised, it is also the region with the largest uncertainty in the mean and trend of the sink (Hauck et al., 2020; Friedlingstein et al., 2022). This is partly because the observation-based estimates and model-based estimates measure different components of the ocean carbon sink, and assumptions on fluxes associated with river discharge need to made, which carry high uncertainty themselves (Aumont et al., 2001; Lacroix et al., 2020). Further, the decadal variability of the Southern Ocean and the underlying mechanisms thereof are a key contributor to the uncertainty and are a topic of continued discussion (Le Quéré et al., 2007; Landschützer et al., 2015; Gruber, Landschützer, & Lovenduski, 2019; Hauck et al., 2020; McKinley et al., 2020; Canadell et al., 2021). A stagnation in the growth of the Southern Ocean carbon sink in the 1990s is commonly attributed to a strengthening of the westerly winds and associated intensified upwelling of carbon- and nutrient-rich deep water (Le Quéré et al., 2007; Lovenduski et al., 2007; Hauck et al., 2013). Indeed, evidence for this stronger upwelling is indirectly observed by enhanced surface nutrient concentrations in all Southern Ocean basins (Hoppema et al., 2015; Panassa et al., 2018; T. Iida et al., 2013; Ayers & Strutton, 2013; Pardo et al., 2017). The early 2000's marked the start of the so-called reinvigoration of the Southern Ocean carbon sink (Landschützer et al., 2015). The strength of the reinvigoration is uncertain due to the observation-based products potentially overestimating the trends owing to data sparsity (Landschützer et al., 2015; Gloege et al., 2021; Hauck et al., 2023), while further analysis on the trends in the models is needed. Furthermore, the drivers of the reinvigoration are less well understood than for the stagnation, but it may be linked to changes in the atmospheric forcing (Gruber, Landschützer, & Lovenduski, 2019) and/or changes in the overturning circulation (DeVries et al., 2017). There is also evidence that both the stagnation and the reinvigoration are part of a global response to variations in atmospheric CO_2 growth rate, ocean temperature and circulation induced by the 1992 eruption of Mount Pinatubo (McKinley et al., 2020; Eddebbar et al., 2019).

The Southern Ocean carbon sink is projected to continue to play an important role in the future carbon cycle as shown by Earth System Model simulations (Hauck et al., 2015; Kessler & Tjiputra, 2016; Canadell et al., 2021; Terhaar et al., 2021). However, there are indications that system changes may occur, such as a shift to a larger proportion of the CO_2 uptake occurring in the polar Southern Ocean (Hauck et al., 2015), and a strong sensitivity of Southern Ocean carbon storage to physical ventilation and warming (Katavouta & Williams, 2021; Terhaar et al., 2021; Bourgeois et al., 2022).

In this study, we aim to synthesize and assess information on the Southern Ocean carbon sink over the period 1985 to 2018 in the framework of the REgional Carbon Cycle Assessment and Processes project, phase 2 (RECCAP2). This work builds on a previous assessment, RECCAP phase 1 (referred to as RECCAP1 for clarity), for the period 1990 to 2009 (Lenton et al., 2013). In RECCAP1, the Southern Ocean was defined as the ocean south of 44°S (building on earlier classification in the atmospheric inversion community), which, however, cut through the major anthropogenic CO_2 uptake region at the northern edge of the Southern Ocean. The assessment was based on five global ocean biogeochemical models, eleven atmospheric inversions, ten ocean inversions and a single pCO_2 observation-based data set, the climatology of Takahashi et al. (2009). RECCAP1 resulted in a best estimate of the net Southern Ocean CO_2 uptake (1990-2009) of 0.42 ± 0.07 PgC yr^{-1} based on all models (including inversions), with a surface pCO_2-based climatology (Takahashi et al., 2009) suggesting a lower number of 0.27 ± 0.13 PgC yr^{-1} Lenton et al. (2013). The interannual variability was estimated to be ±25% around this mean value. The largest proportion of the mean flux occurred in the region 44-58°S which spans large parts of the Subantarctic Zone and of the Polar Frontal Zone with similar contributions from the Atlantic, Pacific and Indian Ocean sectors. In the Antarctic Zone (south of 58°S), individual estimates did not agree on the sign of the net CO_2 flux.

A major advance since RECCAP1 is the release and continued updating of the Surface Ocean CO_2 Atlas (SOCAT Bakker et al., 2016), which currently provides 33.7 million quality-controlled and curated surface ocean pCO_2 measurements with an accuracy of <5 μatm in the 2022 release (Bakker et al., 2022). The release of SOCAT allowed for the development of the surface ocean pCO_2 observation-based products (pCO_2-products) that interpolate and extrapolate sparse ship-based observations from SOCAT to global coverage. Based on these maps of surface pCO_2, the air-sea CO_2 flux is then calculated using gas-exchange parameterizations and input data fields such as sea surface temperature and wind fields (R. H. Wanninkhof, 2014). Since RECCAP1, a diverse set of statistical and machine-learning approaches have been developed (e.g., Landschützer et al., 2014; Rödenbeck et al., 2014; Gregor et al., 2019; Chau et al., 2022). The pCO_2-products allowed for observation-based investigation of interannual and decadal variability. They confirmed the reported stagnation of the Southern Ocean carbon sink in the 1990s (Le Quéré et al., 2007), and identified the aforementioned reinvigoration in the 2000s (Landschützer et al., 2015; Ritter et al., 2017). However, these pCO_2-products have made the Southern Ocean's long-standing issue of sparse observations even more evident. Observation system simulation experiments (OSSEs) have shown that these methods are prone to regional and temporal biases (Denvil-Sommer et al., 2021) and some pCO_2-products may overestimate the decadal variability by 30% (Gloege et al., 2021). In fact, a recent study showed that the SOM-FFN pCO_2-product used in the reinvigoration study of Landschützer et al. (2015) overestimates the model-based decadal trend 2000-2018 by 130% in an ocean model subsampling experiment (Hauck et al., 2023). However, these OSSEs have also shown that augmenting ship-based observations with well-placed, high accuracy pCO_2 observations from autonomous platforms can reduce these biases (Denvil-Sommer et al., 2021; Djeutchouang et al., 2022; Hauck et al., 2023).

The gap in ship-based pCO_2 observations is slowly being addressed by a second major advance, that is autonomous measurement devices. Among these are pH-equipped biogeochemical Argo floats (BGC-floats) (Williams et al., 2016; Johnson et al., 2017). With this approach, float pH measurements are combined with multi-linear regression-derived alkalinity (Williams et al., 2016; Carter et al., 2016, 2018, 2021), to calculate estimates of pCO_2. Although uncertainties of the BGC-float based estimates of pCO_2 are, to date, higher (theoretical uncertainty of 11 μatm, Williams et al., 2017) than for direct pCO_2 measurements (2μatm, Bakker et al., 2016), some of these indirect pCO_2 estimates fill critical gaps in the sparsely sampled winter months. These novel data, either on their own (Gray et al., 2018) or as additional input for pCO_2-products (Bushinsky et al., 2019), reported a strong winter outgassing of CO_2 in the subpolar Southern Ocean for the years 2015 through 2017 that also led to a substantially smaller estimate of the annual Southern Ocean CO_2 uptake for these years. However, these larger-than-expected winter outgassing estimates were challenged by airborne flux estimates and direct pCO_2 measurements from a circumpolar navigation by an uncrewed sailing drone (Long et al., 2021; Sutton et al., 2021). The sailing drone observations were in agreement with ship-based pCO_2-product estimates throughout all seasons (Sutton et al., 2021). The authors attributed the discrepancy between BGC-floats and other estimates to either a bias of the float measurement devices or interannual variability. In support of the latter argument, the BGC-Argo-based air-sea CO_2 flux in the years 2017-2019 also did not reveal the strong winter outgassing signal of the years 2015 and 2016 (Sutton et al., 2021).

Another advance since RECCAP1 is that more global ocean biogeochemical models (GOBMs) have become available with improvements in resolution and physical and biogeochemical process representation (R. H. Wanninkhof et al., 2013; Friedlingstein et al., 2022). While the ability of the GOBMs to capture interannual variability of air-sea CO_2 fluxes (FCO_2) was questioned by the larger variability of pCO_2-product estimates (Le Quéré et al., 2018), the lower interannual variability of GOBMs now falls within the range of the larger ensemble of pCO_2-products (McKinley et al., 2020; Hauck et al., 2020). For the decadal variability of FCO_2, there is a moderate agreement between GOBMs and pCO_2-products on a stagnation of the sink in the 1990s and an increase of the sink in 2002-2011 but with a larger amplitude of the multi-year/decadal variability in the pCO_2-products (McKinley et al., 2020; Hauck et al., 2020; Gruber et al., 2023). Although the GOBMs compare reasonably well to global and Southern Ocean observations of surface ocean pCO_2 (Hauck et al., 2020), their estimates of the global ocean carbon sink remain below those of interior ocean anthropogenic carbon accumulation estimates from 1994 to 2007 (Gruber, Clement, et al., 2019), atmospheric inversions, observed O_2/N_2 ratios (Friedlingstein et al., 2022; Tohjima et al., 2019), and a similar underestimation was found in Earth System Models (Terhaar et al., 2022).

The final major advance in the last decade are regional and global data-assimilating global ocean biogeochemistry models (Verdy & Mazloff, 2017; Carroll et al., 2020). These models bring together the process-based knowledge from GOBMs, but use data assimilation schemes to minimize mismatches between simulated fields, and physical and biogeochemical observations.

Despite these recent advances in observations and models, the Southern Ocean is still the region with the largest discrepancy in mean CO_2 flux (although within the uncertainty of the fluxes associated with river discharge which are implicitly included in the observation-based estimates, but not in the models, see sections 2.2.1 and 2.3.1) and variability, as well as largest model spread (Friedlingstein et al., 2022; Canadell et al., 2021). In this study, we aim to quantify the Southern Ocean (following the RECCAP2 biome shown in Figure 1) surface CO_2 fluxes and interior storage of anthropogenic carbon over the period 1985-2018 from different classes of models and observations, and to identify knowledge gaps and ways forward.

This study is organized in the following way. In our methods, we describe the region (section 2.1), the datasets that we use throughout this synthesis (section 2.2), and how the data were processed (section 2.3). Our results contain first the estimates of the mean fluxes 1985-2018 and their decomposition into anthropogenic and natural fluxes, and atmospheric CO_2 versus climate effects (section 3.1). This is followed by an analysis of summer and winter fluxes and the full seasonal cycle, where we also decompose

pCO_2 into seasonal thermal and non-thermal contributions (section 3.2). We then analyse the regionally averaged temporal trends of CO_2 flux and also of pCO_2 in comparison with in situ pCO_2 observations, as well as atmospheric CO_2 and climate effects as drivers of the trends (section 3.3). In the final part of the results, the study then evaluates the GOBM simulation results with observation-based estimates of ocean interior storage of anthropogenic carbon in the Southern Ocean (section 3.4). The discussion first summarizes the results with a comparison of the RECCAP1 and RECCAP2 results (section 4.1). We also discuss the drivers of the seasonal cycle (section 4.2), the interannual and decadal variability (section 4.3), and the zonal asymmetry of the fluxes in the Southern Ocean (section 4.4). Lastly, we discuss how our study links with and can inform observational programs (section 4.5), before presenting a conceptual characterization of the Southern Ocean carbon cycle in the conclusions (section 5).

2 Methods

2.1 Regions

We use the RECCAP2 regions (DeVries, 2022) to define the Southern Ocean and its northern boundary (Figure 1). This definition of the Southern Ocean covers the subtropical seasonally stratified biome (STSS), the subpolar seasonally stratified biome (SPSS), and the ice biome (ICE) and is based on the global open ocean biome classification of Fay and McKinley (2014). This covers a larger area than the definition used in RECCAP1 (44-58°S, 58-75°S Lenton et al., 2013) and has the advantage that it does not cut through the subtropical region with its large CO_2 flux into the ocean. The northernmost extent of the Southern Ocean in this definition is 35°S. For parts of our analysis, we further separate the Atlantic, Indian, and Pacific Ocean sectors along longitudes of 20°E, 147°E, and 290°E (Figure 1).

2.2 Data sets

Here, we introduce data sets across four different data classes that are used for the assessment of the Southern Ocean CO_2 fluxes and storage, namely: ocean biogeochemistry models (14), surface pCO_2-based data-products (11), data assimilated and ocean inverse models (3), and atmospheric inversion models (6).

2.2.1 Ocean biogeochemistry models

We used 13 global ocean biogeochemistry models (GOBMs) and 1 regional ocean biogeochemistry model (Table 1). These models simulate ocean circulation and biogeochemical fluxes caused by physics (advection, mixing, gas-exchange) and by biological processes. They are forced with atmospheric fields from reanalysis products, e.g., by either heat and freshwater fluxes directly or by air temperature, wind speed, precipitation and humidity, which are converted to heat and freshwater fluxes using bulk formulae (see references in Table 1; Large et al., 1994). From these 14 models, eleven models are global ocean models with roughly 1°×1° resolution, and two global models (FESOM_REcoM_HR and ORCA025-GEOMAR) and the regional model (ROMS-SouthernOcean-ETHZ) are available in ca. 0.25°×0.25° resolution. Details of global model set-ups are given in (DeVries et al., 2023). The ROMS-based regional Southern Ocean model has a northern boundary at 24°S.

For the ocean-models listed above, up to four different simulations were provided (see also Table S1 and DeVries et al., 2023). These differ in whether atmospheric CO_2 and all other atmospheric forcing variables vary on interannual time scales, are repeated for a single year, or follow a multi-year climatology. In simulation A, the historical run, both atmospheric CO_2 and all other physical forcing variables vary on interannual time scales. In simulation B, the preindustrial control run, a repeated year or climatological

Table 1. Overview of data sets used in this paper. Sorted by data class, here: Global Ocean Biogeochemistry Models (GOBMs), Regional Ocean Biogeochemistry Model, and data assimilated models.

Data set	Time period	Specific information	Reference
Global Ocean Biogeochemistry Models		**Simulations**	
CCSM-WHOI	1985-2017	A, B, C, D	Doney et al. (2009)
CESM-ETHZ	1985-2018	A, B, C, D	Lindsay et al. (2014); S. Yang and Gruber (2016)
CNRM-ESM2-1	1985-2018	A, B, C, D	Séférian et al. (2019); Berthet et al. (2019); Séférian et al. (2020)
EC-Earth3	1985-2018	A, B, C, D	Döscher et al. (2022)
FESOM_REcoM_HR	1985-2018	A, B	Hauck et al. (2013); Schourup-Kristensen et al. (2014, 2018)
FESOM_REcoM_LR	1985-2018	A, B, C, D	Hauck et al. (2013); Schourup-Kristensen et al. (2014); Hauck et al. (2020)
MOM6-Princeton	1985-2018	A, B	Liao et al. (2020); Stock et al. (2020)
MPIOM-HAMOCC	1985-2018	A, B, C, D	Ilyina et al. (2013); Paulsen et al. (2017); Mauritsen et al. (2019)
MRI-ESM2-1	1985-2018	A, B, C, D	Urakawa et al. (2020)
NorESM-OC1.2	1985-2018	A, B, C, D	Schwinger et al. (2016)
ORCA025-GEOMAR	1985-2018	A, B, C, D	Madec and the NEMO team (2016); Kriest and Oschlies (2015); Chien et al. (2022)
ORCA1-LIM3-PISCES (IPSL-NEMO-PISCES)	1985-2018	A, B, C, D	Aumont et al. (2015)
PlankTOM12	1985-2018	A, B, C, D	Le Quéré et al. (2016); Buitenhuis et al. (2019); Wright et al. (2021)
Regional Ocean Biogeochemical Models		**Simulations**	
ROMS-SouthernOcean-ETHZ	1985-2018	A, B, D	A. Haumann (2016); Nissen et al. (2018)
Data-assimilated models			
B-SOSE	2013-2018		Verdy and Mazloff (2017)
ECCO-Darwin	1992-2017		Carroll et al. (2020, 2022)
OCIMv2021	1780-2018	A, B, C	DeVries (2022)

Table 2. Overview of data sets used in this paper (continued). Sorted by data class, here: pCO_2-products and atmospheric inversions. The atmospheric inversions were provided only since 1990.

Data set	Time period	Specific information	Reference
pCO_2-products			
AOML_EXTRAT	1998-2018		R. Wanninkhof (2023)
CMEMS-LSCE-FFNN	1985-2018		Chau et al. (2022)
CSIR-ML6	1985-2018		Gregor et al. (2019)
Jena-CarboScope (Mixed Layer Scheme)	1985-2018		Rödenbeck et al. (2013, 2022)
JMA-MLR	1985-2018		Y. Iida et al. (2021)
LDEO-HPD	1985-2018		Gloege et al. (2022)
NIES-ML3	1985-2018		Zeng et al. (2022)
OceanSODA-ETHZ	1985-2018		Gregor and Gruber (2021)
MPI-SOM-FFN	1985-2018		Landschützer et al. (2016, 2020)
Jena-CarboScope (SOCCOM)	2015-2018		Bushinsky et al. (2019) updated
MPI-SOM-FFN (SOCCOM)	2015-2018		Bushinsky et al. (2019) updated
Watson2020	1988-2018		Watson et al. (2020)
LDEO_climatology (Takahashi legacy)	climatology		Takahashi et al. (2009)
Atmospheric inversions		**Ocean prior**	
Jena CarboScope	1957-2020 (1990-2020)	CarboScope pCO_2-product	Rödenbeck et al. (2018)
CAMS	1979-2020 (1990-2020)	CMEMS-LSCE-FFNN pCO_2-product	Chevallier et al. (2005)
NISMON-CO2	1990-2020	JMA-MLR pCO_2-product	Niwa et al. (2017)
CarbonTrackerEurope (CTE)	2001-2020	CarboScope pCO_2-product	van der Laan-Luijkx et al. (2017)
UoE	2001-2020	Takahashi climatology	Feng et al. (2016)
CMS-Flux	2010-2020	MOM6 GOBM	Liu et al. (2021)

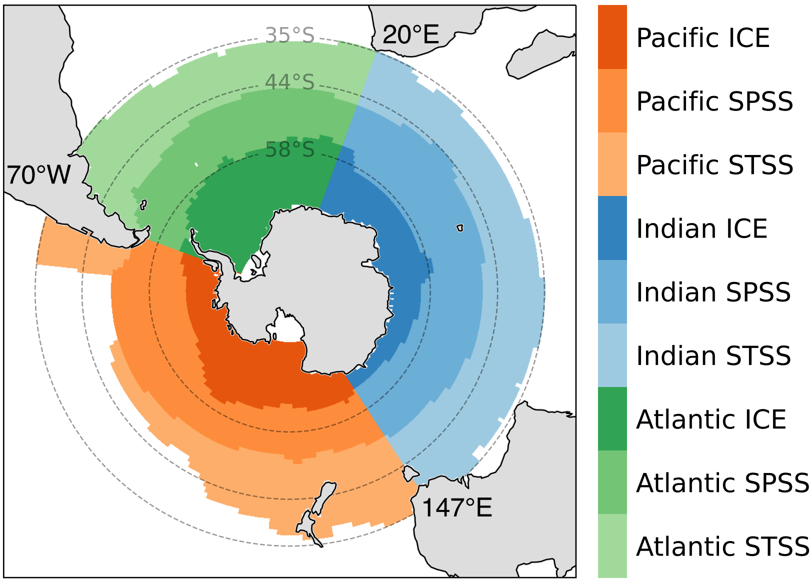

Figure 1. Study region. The Southern Ocean covers three biomes: The subtropical seasonally stratified (STSS), the subpolar seasonally stratified (SPSS), and the ice (ICE) biome. The biomes are defined following Fay and McKinley (2014). We further consider the Atlantic, Pacific, and Indian Ocean sectors separately in parts of the analysis. The dashed lines show the RECCAP2 Southern Ocean northernmost extent (35°S), the RECCAP1 Southern Ocean northernmost extent (44°S), and RECCAP1's boundary for the circumpolar region (58°S).

physical atmospheric forcing is used, and the atmospheric CO_2 levels are held constant at pre-industrial levels. In simulation C, the atmospheric CO_2 varies interannually and only the physical atmospheric forcing is climatological. In simulation D, the atmospheric CO_2 levels are held constant at pre-industrial levels, whereas the physical atmospheric forcing varies interannually. These simulations allow for the separation of the effects of the increase in atmospheric CO_2 and climate change and variability on air-sea CO_2 fluxes: the steady-state and non-steady state components of both natural and anthropogenic carbon. Here *anthropogenic* refers to the direct effect of increasing atmospheric CO_2 and *non-steady state* encompasses the effects of climate change and variability. For a detailed explanation, please see DeVries et al. (2023) and further explanation in Le Quéré et al. (2010); McNeil and Matear (2013); Hauck et al. (2020); Crisp et al. (2022); Gruber et al. (2023). Simulation A includes all components of the carbon fluxes. In the control simulation B, only the steady-state component of natural carbon is considered. In simulation C, only the steady-state components of both natural and anthropogenic carbon are accounted for. Lastly, in simulation D, only the steady state and non-steady state components of natural carbon are represented.

The majority of models do not account for the river-induced outgassing of carbon (DeVries et al., 2023; Terhaar et al., 2023), hence the air-sea CO_2 flux in simulation A corresponds to the S_{OCEAN} definition used in the Global Carbon Budget (Friedlingstein et al., 2022), which differs from pCO_2-product estimates by the river-induced term. Note that the river-induced term will be discussed in greater detail in section 4.1. In addition, simulation A may include a model bias (mean offset) and drift (temporally changing offset). We assess the model drift of the air-sea CO_2 flux by calculating the linear trend of the integrated CO_2 flux time series for the period 1985-2018 in simulation B for each model and each biome. The time series plots and the linear trends reported in Figure

8 are drift corrected by subtracting the trend from simulation B. We note that this drift-correction only marginally impacts the reported trends in the result section, as the trends in simulation B are small compared to the mean fluxes for all models (see supplementary material: Text S1 and Figure S1). In contrast to a global bias (any deviation of the global mean CO_2 flux from 0 in simulation B, see Hauck et al., 2020), the regional bias in the simulated flux cannot be assessed by the set of simulations as it cannot be separated from the natural steady-state air-sea CO_2 flux (Terhaar et al., 2023), which is non zero on a regional level.

We use the full suite of models in all analyses, with two exceptions. Firstly, we excluded the MPIOM-HAMOCC model in all seasonal analyses (Fig. 4-7) because its amplitude of the seasonal cycle is a factor 3-6 larger than in the other models in the three main Southern Ocean biomes (Figure S2), and including this outlier would skew the ensemble mean disproportionately. The exaggerated seasonal cycle in the MPIOM-HAMOCC model was found in earlier studies and is attributed to excessive net primary production in the Southern Ocean (Mongwe et al., 2018). Secondly, the decomposition into natural and anthropogenic CO_2 fluxes was not possible with GOBMs that only provided simulations A and B (MOM6-Princeton and FESOM-REcoM-HR). See section 2.3.4 for further restrictions on GOBM use and interpretation for the interior ocean anthropogenic carbon accumulation.

2.2.2 Surface pCO_2-based data-products

As a second data class, we use surface ocean pCO_2 observation-based data products (pCO_2-products) (Table 2, for more details see DeVries et al., 2023). These pCO_2-products extrapolate or interpolate sparse ship-based measurements of pCO_2 using statistical modeling approaches. All pCO_2-based data-products use SOCAT as the target dataset. The majority of pCO_2-products use similar gridded prediction datasets to fill the gaps, including sea surface temperature, sea surface salinity, mixed-layer depth, and chlorophyll-a estimates for the open ocean. We use 8 such pCO_2-products that all cover the full time-series 1985-2018 for the ensemble mean of pCO_2-products. AOML_EXTRAT covers a shorter period, and is thus not included in the ensemble mean 1985-2018, but is included in the ensemble mean 2015-2018. The largest methodological difference between the pCO_2-products stems from the algorithm choice. The majority of the methods use regression approaches (a.k.a. machine learning) such as artificial neural networks (e.g, MPI-SOM-FFN) and gradient boosted decision trees (e.g., CSIR-ML6) to capture the relationship between the ship-based measurements and the predictor variables. The Jena-CarboScope product includes a mechanistic understanding of mixing, entrainment, and fluxes of CO_2 into and out of the mixed layer (Rödenbeck et al., 2014). The HPD-LDEO method adjusts global ocean biogeochemistry model estimates of pCO_2 to be closer to observed ship-based measurements and is thus an observation-based posterior correction to the GOBM estimates (Gloege et al., 2022).

Further, two additional variants of MPI-SOM-FFN and Jena-CarboScope by Bushinsky et al. (2019, ship+float estimates are used here) include additional BGC-float-derived pCO_2 for the Southern Ocean (referred to as BGC-float pCO_2-products, 2015-2018). We also use the Watson2020 product, which is a neural network approach (based on MPI-SOM-FFN) but applies an adjustment to SOCAT pCO_2 that accounts for the difference between ship intake temperature and satellite sea surface temperature (Watson et al., 2020). The BGC-float pCO_2-products (2015-2018) and Watson2020 (1988-2018) are not included in the pCO_2-product ensemble averages, as they are based on fundamentally different pCO_2 values. We also use a monthly climatology product (LDEO-clim) that is centered on the year 2010 (Takahashi et al., 2009).The LDEO-clim product fills the gaps using a combination of inverse distance weighted interpolation and a diffusive-advective interpolation scheme (Takahashi et al., 2009). Note that this product is only used in representations of the seasonal cycle, and not for trend analyses. All these pCO_2-products estimate the bulk air-sea CO_2 flux with:

$$FCO_2 = K_0 \cdot k_w \cdot (\mathrm{pCO_2}^{\mathrm{sea}} - \mathrm{pCO_2}^{\mathrm{atm}}) \cdot (1 - \mathrm{ice}) \tag{1}$$

where K_0 is the solubility of CO_2 in seawater, k_w is the gas transfer velocity, $\mathrm{pCO}_2^{\mathrm{sea}}$ is the oceanic estimate of $\mathrm{pCO_2}$ from the $\mathrm{pCO_2}$-product, $\mathrm{pCO_2}$atm is the atmospheric $\mathrm{pCO_2}$, and ice is the sea-ice fraction, with the majority of the open ocean having a fraction of 0. Other than pCO_2^{sea}, k_w is the largest source of uncertainty in the calculation of bulk air-sea CO_2 fluxes R. H. Wanninkhof (2014); Fay et al. (2021). However, most of the $\mathrm{pCO_2}$-products use a quadratic formulation of k_w as described by R. Wanninkhof et al. (1993) meaning that the product spread is reduced due to similar choices – details are shown in Global chapter's Table S2 (DeVries et al., 2023). An exception is the Watson2020 product (Watson et al., 2020) that calculates air sea CO_2 fluxes using the formulation described in Woolf et al. (2016) where a cool and salty skin adjustment is applied.

2.2.3 Data-assimilated models

We use three data-assimilating models (Table 1). The Biogeochemical Southern Ocean State Estimate (B-SOSE Verdy & Mazloff, 2017) is an eddy-permitting 1/6-degree resolution data-assimilating model, which assimilates the data from Southern Ocean Carbon and Climate Observations and Modelling (SOCCOM) BGC-Argo floats as well as shipborne and other autonomous observations (i.e., GLODAP and SOCAT) over the period 2013-2018. In situ and satellite observations of the physical state are also assimilated. B-SOSE is based on the MIT general circulation model (MITgcm Campin et al., 2011) and uses software developed by the consortium for Estimating the Circulation and Climate of the Ocean (ECCO Stammer et al., 2002; Wunsch & Heimbach, 2013) to build on the SOSE physical model framework by adding the Nitrogen version of the Biogeochemistry with Light, Iron, Nutrients, and Gases (N-BLING; evolved from Galbraith et al., 2010) biogeochemical model. Consistency with the data is achieved by systematically adjusting the model initial conditions and the atmospheric state through the 4D-Var assimilation methodology. This B-SOSE assimilation methodology does not break the model biogeochemical or physical budgets. The budgets are closed, which allows one to understand signal attribution, though limits the control we have over the solution. For this reason B-SOSE is only consistent with the data on the timescales longer than approximately 90 days; the mesoscale eddies are reproduced statistically and not deterministically. Even with this assimilation methodology some seasonal biases still exist, and B-SOSE is still a work in progress.

The ECCO-Darwin data-assimilation model (Carroll et al., 2020) is based on a global ocean and sea ice configuration (about 1/3 degree) of the MIT general circulation model and is available from January 1992 to December 2017. Besides being global and covering a longer duration than B-SOSE, this product also uses a different biogeochemical model and assimilation technique. The ECCO circulation estimates used in this version are coupled online with the Darwin ecosystem model (Dutkiewicz et al., 2009), which represents the planktonic ecosystem dynamics coupled with biogeochemical cycles in the ocean. The R. Wanninkhof (1992) parameterization of gas transfer velocity is used and $\mathrm{pCO}_2^{\mathrm{atm}}$ is the National Oceanic and Atmospheric Administration Marine Boundary Layer Reference product (Dlugokencky et al., 2021). The biogeochemical observations used to evaluate and adjust ECCO-Darwin include (1) surface ocean fugacity ($\mathrm{fCO_2}$) from the monthly gridded Surface Ocean CO_2 Atlas (SOCATv5 Bakker et al., 2016), (2) GLODAPv2 ship-based profiles of NO_3, PO_4, SiO_2, O_2, dissolved inorganic carbon (DIC), and alkalinity (Olsen et al., 2016), and (3) BGC-Argo float profiles of NO_3 and O_2 (Drucker & Riser, 2016; Riser et al., 2018). To adjust the model's fit to the global biogeochemical observations, the Green's function approach is used to adjust biogeochemical initial conditions and model parameters.

OCIMv2021 is an inverse model that assimilates observations of temperature, salinity, CFCs and radiocarbon to achieve an estimate of the climatological mean ocean circulation (DeVries, 2022). This steady-state circulation model is used together with an abiotic carbon cycle model and atmospheric CO_2 forcing to simulate anthropogenic carbon uptake and its redistribution within the ocean. It uses a monthly time-step and simulates the period 1780 to 2018. No assimilation takes place during this period.

2.2.4 Atmospheric inversions

Six atmospheric inversions are available for our analysis (Table 2). Atmospheric inversions make use of the worldwide network of atmospheric CO_2 observations. They ingest a dataset of fossil fuel emissions, which are assumed to be well known, into an atmospheric transport model and then solve for the spatio-temporal distribution of land and ocean CO_2 fluxes while minimizing the mismatch with atmospheric CO_2 observations (Friedlingstein et al., 2022). Thus, the resulting land and ocean carbon fluxes are bound to the atmospheric CO_2 growth rate, but the estimated regional fluxes depend on the number of stations in the observational network. The inversions also start from prior estimates of land and ocean fluxes. For four inversion data sets that we use here, the ocean prior is taken from pCO_2 -products that are used in this analysis as well (Table 2). One inversion (UoE) uses the Takahashi climatology as a prior and one (CMS-Flux) an ocean biogeochemical model. The atmospheric inversions are thus not independent from the other data classes (Friedlingstein et al., 2022, their Table A4). The atmospheric inversion data were submitted for RECCAP in the same version as in the Global Carbon Budget 2021 (Friedlingstein et al., 2022), but only since 1990. The three inversions starting later (2001 or 2010) are only included in averages reported for 2015-2018 (Figures 4 and 5), and as individual lines in the time-series figure (Figure 8).

2.3 Processing

Throughout this study, we report the air-sea CO_2 exchange as the net flux (FCO_2), which is the sum of natural, anthropogenic and river-induced air-sea CO_2 flux (see e.g., DeVries et al., 2023; Hauck et al., 2020; Crisp et al., 2022). As the GOBMs vary widely in their choices on river carbon and nutrient input into the ocean and burial at the seafloor (see DeVries et al., 2023; Terhaar et al., 2023), an adjustment is applied to make all data classes comparable.

2.3.1 River flux adjustment

Globally, the majority of GOBMs produce a small imbalance of riverine carbon inflow and burial globally (<0.14 PgC yr^{-1}), which is smaller than the current best estimate of river-induced CO_2 ocean outgassing of 0.65 PgC yr^{-1} (Regnier et al., 2022). The imbalances are due to manifold choices and illustrate the lack of a closed land-ocean carbon loop in the GOBMs. As the GOBMs do not adequately account for the river discharge and its fate within the ocean, and thus for river-derived ocean CO_2 outgassing (Terhaar et al., 2023), we account for this outgassing by using the spatial patterns of river-induced air-sea CO_2 fluxes from Lacroix et al. (2020) that are scaled to the global value of 0.65 PgC yr^{-1} (Regnier et al., 2022). Southern Ocean outgassing from rivers amounts to 0.04 PgC yr^{-1}, i.e., around 6% of the global river flux. It is distributed over the Southern Ocean biomes as follows (positive outgassing): 0.00036 PgC yr^{-1} in the ICE biome, 0.053 PgC yr^{-1} (SPSS biome), -0.014 (STSS biome). The estimated riverine CO_2 fluxes were added to biome-integrated fluxes in simulation A for all GOBMs, so that these are comparable to the pCO_2-products. They are not added to spatial maps of CO_2 fluxes due to large uncertainties in the regional attribution by Lacroix et al. (2020). The riverine fluxes are one (ICE) to multiple (SPSS, STSS) orders of magnitude smaller than the mean fluxes quantified in this study. The uncertainty associated with the river flux adjustment is discussed in section 4.1.

2.3.2 Treatment of different area coverage

Air-sea CO_2 fluxes in all data classes were integrated over the area available for each GOBM, pCO_2-product etc., i.e., fluxes were not scaled to the same ocean area here. Relative to the ocean area in the RECCAP mask, the covered ocean areas in the GOBMs and data-assimilating models corresponds to 96.2-100% (minimum for CCSM-WHOI) and to 95.6-100% in the pCO_2-products (minimum for JMA-MLR). These differences mainly stem from the ICE biome. We assume that the discrepancy arising from differences in covered area are smaller than the uncertainty arising from any extrapolation to the same area.

2.3.3 pCO_2 decomposition

To separate temperature driven changes in pCO_2 from biological processes and mixing-driven entrainment, pCO_2 is decomposed into thermal and non-thermal components (Takahashi et al., 1993). The thermal component (pCO_2^T) is calculated as

$$pCO_2^T = \overline{pCO_2} \cdot e^{(0.0423 \cdot \Delta T)} \tag{2}$$

where $\overline{pCO_2}$ is the annual mean of pCO_2 and ΔT difference of the monthly mean temperature from the annual mean temperature. The non-thermal contribution (pCO_2^{nonT}) is estimated as the difference of the thermal contribution (pCO_2^T) from the monthly-averaged pCO_2. The first derivatives of these two components are subtracted from each other to create the pCO_2 seasonal driver metric, denoted as λpCO_2:

$$\lambda pCO_2 = \left| \frac{pCO_2^T}{\delta t} \right| - \left| \frac{pCO_2^{nonT}}{\delta t} \right| \tag{3}$$

Here, positive values indicate periods when the thermal component is a larger contributor to pCO_2, and negative values show where the DIC processes (non-thermal) play a dominant role in surface pCO_2 changes. We also denote the first derivatives as $pCO_2^{T'}$ and $pCO_2^{nonT'}$ for brevity.

2.3.4 Anthropogenic carbon inventories

Anthropogenic CO_2 (C_{ant}) is defined as the change in ocean dissolved inorganic carbon (DIC) since preindustrial times due to the direct effect of increasing CO_2 concentration in the atmosphere. It is computed as the DIC difference between experiments A and D. The accumulation of C_{ant} can be separated into a steady-state component (C_{ant}^{ss}, DIC difference between experiments C and B), that is influenced only by the increased atmospheric CO_2, and a non-steady-state component (C_{ant}^{ns}), which considers the effect of climate variability and change on C_{ant} (and which is maximally 10-20% of C_{ant}, Text S2 and Figures S3-S4). Here we focus mainly on the change in C_{ant} that has occurred over the period 1994-2007 (hereafter ΔC_{ant}), to correspond to the years covered by the eMLR(C*) observation-based estimate (Gruber, Clement, et al., 2019). The eMLR(C*) method (Clement & Gruber, 2018) uses ocean measurements of DIC from GLODAP2 (Olsen et al., 2016) over more than 30 years as the foundation to determine ΔC_{ant} between nominal years 1994 and 2007. The method has been shown to be accurate at global and basin scales, but is more uncertain at sub-basin scales and should not be used below 3000 m depth. The (2 sigma) uncertainty of the eMLR(C*) product is estimated to be around 19% for the Southern Hemisphere (Gruber, Clement, et al., 2019). The eMLR(C*) method differs fundamentally from past indirect or model-based methods used to estimate C_{ant} accumulated since pre-industrial times (Gruber et al., 1996; Sabine et al., 2004; Waugh et al., 2006; DeVries, 2014). Of these, we used the 1800-1994 cumulative C_{ant}

estimate based on (Sabine et al., 2004), which is characterized by an uncertainty of about 20% globally (Sabine et al., 2004; Matsumoto & Gruber, 2005). In terms of GOBMs, we used all those listed in Table 1, with the exception of FESOM-REcoM-HR and MOM6-Princeton who provided only experiments A and B. For most GOBMs, we analyze C_{ant}^{tot}, to allow for a more accurate comparison with the observation-based data set (eMLR(C*)). However, for MPIOM-HAMOCC and CNRM-ESM2-1 it was only possible to compute C_{ant}^{ss}, because of physical forcing inconsistencies between experiments A and D. We believe that the advantage of including all GOBMs in the analysis outweighs the disadvantages of having an incoherent definition of C_{ant} among GOBMs. It should be noted that the spin-up procedure of ROMS-SouthernOcean-ETHZ, which uses atmospheric CO_2 from 1969 to 1978 (for a ten year spin-up of the biogeochemical component), makes it suitable only for the analysis of ΔC_{ant} between 1994 and 2007, and not of cumulative C_{ant} until 1994 nor of air-sea C_{ant} fluxes in specific years. As explained in the RECCAP2 model evaluation chapter (Terhaar et al., 2023), all GOBMs are forced with a very similar atmospheric CO_2 mixing ratio (xCO_2) over the historical period. However, the atmospheric xCO_2 in the pre-industrial control simulations across the GOBM ensemble varies between 278 ppm and 287.4 ppm, leading to an underestimate of the C_{ant} storage for those models with a late starting date (Terhaar et al., 2023).

3 Results

3.1 Mean air-sea CO_2 fluxes 1985-2018

We start with a comparison of the average air-sea CO_2 flux in the two data classes (GOBMs, pCO_2-products) that cover the full period 1985-2018. We exclude data classes with fewer products for the sake of robustness, and show the comparison between all data classes in sections 3.2 and 3.3. The mean net Southern Ocean air-sea CO_2 flux 1985-2018 by the GOBM ensemble is -0.75± 0.28 PgC yr^{-1} and -0.73 ±0.07 PgC yr^{-1} (flux into the ocean) for the pCO_2-product ensemble mean (Figure 2a). While both ensemble means result in an almost identical ocean uptake of CO_2, the GOBM ensemble spread is four times larger.

All Southern Ocean regions are sinks of CO_2 based on the ensemble averages of the GOBMs and pCO_2-products (Figure 2). The subtropical seasonally stratified biome (STSS), which is a subduction area with deep winter mixed layer depth and intermediate chlorophyll concentration (Fay & McKinley, 2014), is the largest sink according to all data sets (GOBMs: -0.53±-0.17 PgC yr^{-1}, pCO_2-based products:-0.62±0.06 PgC yr $^{-1}$, Figure 2a). Second is the subpolar seasonally stratified biome (SPSS) (GOBMs: -0.13± 0.14 PgC yr^{-1}, pCO_2-products: -0.07± 0.02 PgC yr^{-1}), which is characterized by upwelling of old water, rich in natural carbon but with low anthropogenic carbon content. The upwelled water is also rich in nutrients, and thus a region with important biological activity. Note that three GOBMs simulate the SPSS to be a source of CO_2 to the atmosphere. The marginal sea ice (ICE) biome is the weakest CO_2 sink (GOBMs: -0.09±0.13 PgC yr^{-1}; pCO_2-products: -0.05±0.02 PgC yr^{-1}) due to sea ice acting as a lid that prevents carbon outgassing in winter, and is the smallest of all three biomes covering an area of about 60% the size of STSS or SPSS (Fay & McKinley, 2014). Four individual models suggest that the ICE biome is a weak outgassing region, but no other data set supports this.

In a zonal mean view (Figure 2b), the smallest uptake occurs between 62 and 55°S and the largest uptake around 40°S. However, the amplitude differs between data classes, with the pCO_2-products having a larger difference between minima and maxima (1.96 mol C m^{-2} yr^{-1}), than the GOBM ensemble mean (1.19 mol C m^{-2} yr^{-1}). Some of the individual GOBMs deviate from this pattern (see supplementary figure S5a for zonal means of individual models).

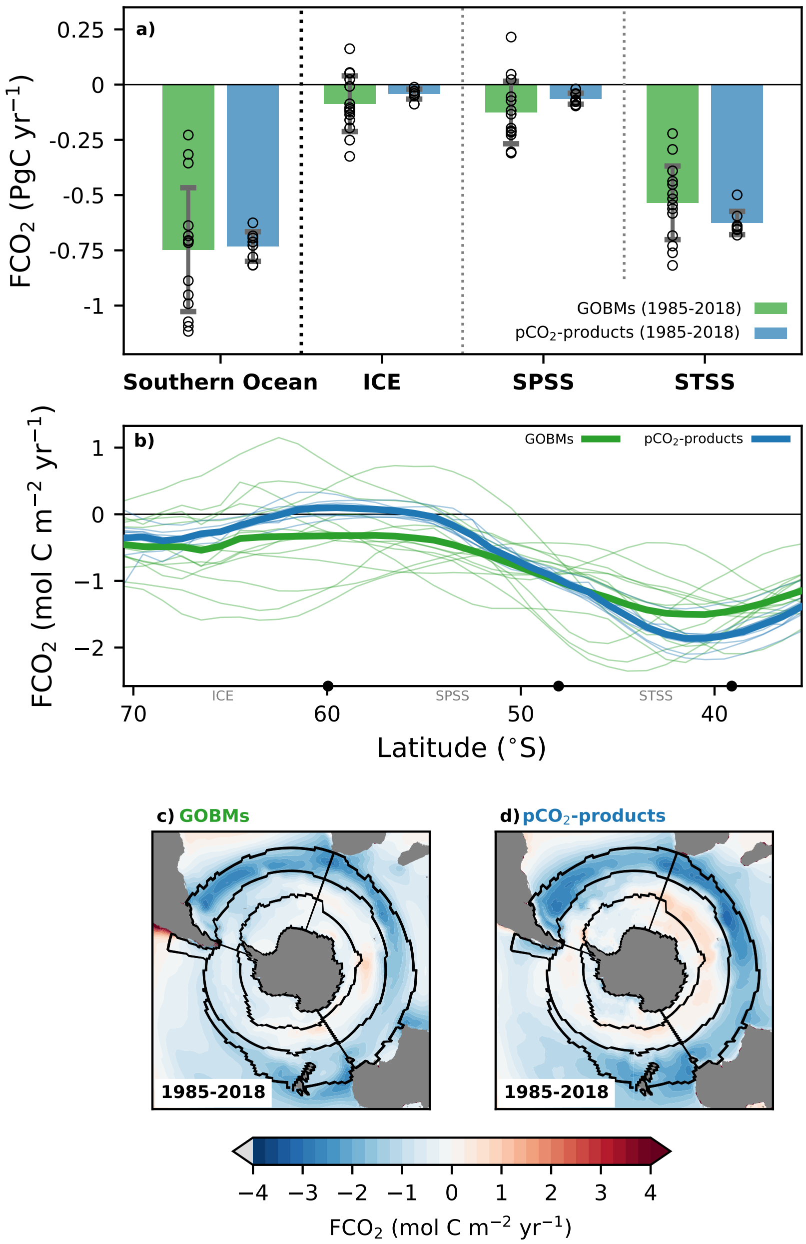

Figure 2. Temporal average of the Southern Ocean CO_2 net flux (FCO_2). A positive flux denotes outgassing from ocean to atmosphere. The temporal average is calculated over the period 1985 to 2018 for the global ocean biogeochemistry models (GOBMs) and pCO_2-products (Table 1). (a) The green and blue bar plots show the ensemble mean of the GOBMs and pCO_2-based data-products, and open circles indicate the individual GOBMs and pCO_2-products. The ensemble standard deviation (1σ) is shown by the error bars. The river flux adjustment added to the GOBMs is small (0.04 PgC yr^{-1}), its distribution over the biomes is described in section 2.3.1. (b) zonal mean flux density of the different data sets. Thick green and blue lines show the ensemble means, and thin green and blue lines show the individual GOBMs and pCO_2-products. Approximate boundaries for biomes are marked with black points on the x-axis. (c-d) maps of spatial distribution of net CO_2 flux for ensemble means of GOBMs, and pCO_2-products.

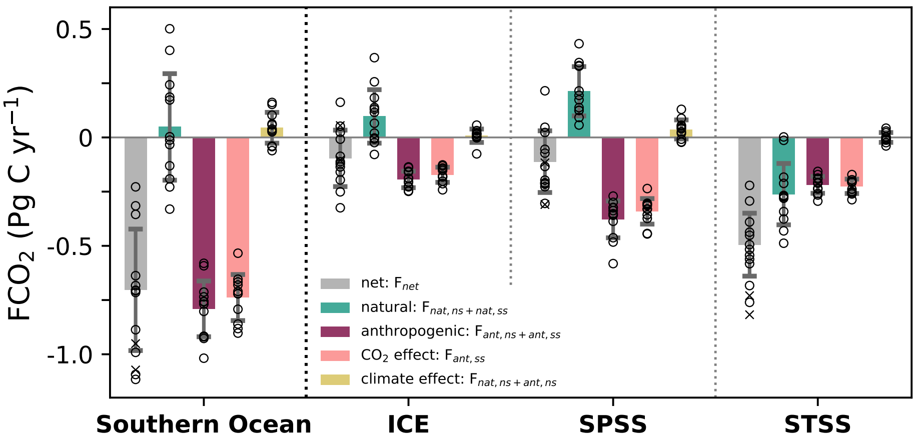

Figure 3. Decomposition of the modeled net air-sea CO_2 flux 1985-2018 into natural and anthropogenic CO_2 fluxes; as well as into CO_2 and climate effects. See method section 2.2.1 for explanation on this decomposition. The separation into natural and anthropogenic CO_2 fluxes is not possible for FESOM-REcoM-HR and MOM6-Princeton models as only simulations A and B are available. These models are only shown as crosses for net FCO_2 but not used for averaging. Hence, separation within this figure is coherent, but the net FCO_2 is slightly different from the net FCO_2 in Figure 2.

Regionally, significant differences emerge between the Atlantic, Indian and Pacific sectors of the Southern Ocean (Figure 2c-d). Within the STSS, large CO_2 fluxes into the ocean occur in the Atlantic and Indian sector across all data classes (Figure 2b-c, mean flux density: -1.93 mol C m^{-2} yr^{-1} and -2.05 mol C m^{-2} yr^{-1} for GOBMs and pCO_2-products, respectively, in the Atlantic sector, -1.44 mol C m^{-2} yr^{-1} and -1.89 mol C m^{-2} yr^{-1} in the Indian sector, and -1.22 mol C m^{-2} yr^{-1} and -1.54 mol C m^{-2} yr^{-1} in the Pacific sector). CO_2 outgassing locations differ across the data classes. In the GOBM ensemble mean, the outgassing is mainly confined to the Indian sector of the SPSS, whereas it is more widely spread in the pCO_2-product ensemble mean covering the Pacific and Indian Ocean sectors of the SPSS and the Indian sector in the ICE biome. The smooth appearance of the outgassing signal in the GOBM and pCO_2-product ensemble means may be partly attributable to averaging over multiple data sets and months and years.

3.1.1 Decomposition into anthropogenic and natural carbon fluxes and climate versus atmospheric CO_2 effects on the mean CO_2 flux

With the aid of the additional model simulations, we can decompose the net Southern Ocean air-sea CO_2 flux into natural and anthropogenic components, and separate the indirect effects of physical climate change and the direct geochemical effect of increasing atmospheric CO_2 mixing ratios. The GOBM ensemble mean indicates that the *natural* Southern Ocean carbon cycle without anthropogenic perturbation would be a small CO_2 source to the atmosphere of 0.05 PgC yr^{-1}, although with a large model spread as indicated by the standard deviation of 0.25 PgC yr^{-1} (Figure 3). In fact, six GOBMs simulate negative natural CO_2 fluxes, i.e., into the ocean, and six GOBMs simulate positive natural fluxes, i.e., out of the ocean. This also illustrates that the GOBM spread of net fluxes (standard deviation: 0.28 PgC yr^{-1}) is, to the first order, dominated by the model differences of natural fluxes (standard deviation: 0.25 PgC yr^{-1}), which may contain artifacts from model biases and drift (Terhaar et al., 2023). The spread of anthropogenic fluxes is smaller (0.13 PgC yr^{-1}). The small *natural* outgassing signal in the ensemble mean is a balance of natural CO_2 uptake in the STSS (-0.26±0.14 PgC yr^{-1}) and outgassing in the SPSS (0.21±0.11 PgC yr^{-1}) and ICE (0.10± 0.12 PgC yr^{-1}) biomes. This is in qualitative agreement with the patterns of natural CO_2 fluxes by Mikaloff Fletcher et al. (2007).

The *anthropogenic* perturbation (-0.79±0.13 PgC yr^{-1}) has turned the SPSS and ICE biomes, and possibly the entire Southern Ocean, from source to sink. The large anthropogenic flux contribution in the SPSS (-0.38±0.08 PgC yr^{-1}) suppresses the natural CO_2 outgassing flux. The STSS is a sink for both natural and anthropogenic flux components. The *direct effect of increasing atmospheric CO_2* enhances the Southern Ocean sink by -0.74±0.11 PgC yr^{-1} and is the largest signal in the anthropogenic perturbation. A smaller component stems from the climate change effect on this steady state CO_2-induced flux (Figure S6). The direct CO_2 effect is largest in the SPSS (-0.34±0.06 PgC yr^{-1}) where old water masses reach the surface that are undersaturated in anthropogenic carbon, followed by the STSS and ICE biomes (-0.23±0.03 PgC yr^{-1} and -0.17±0.03 PgC yr^{-1}). In the upwelling regions, the primary effect of rising atmospheric CO_2 is thus to suppress the outgassing of natural carbon.

The *effect of physical climate change and variability*, i.e., warming and changes in wind speed patterns and strength that provoke changes in circulation (Le Quéré et al., 2007; Lovenduski et al., 2007; Hauck et al., 2013), reduces the CO_2 flux into the ocean (+0.04±0.07 PgC yr^{-1}), but is overall small in comparison to the direct CO_2 effect. This climate change induced outgassing stems nearly entirely from the SPSS (+0.04±0.04 PgC yr^{-1}), with the largest contribution from the Indian sector followed by the Pacific (Figure S7). Thus, the climate change effect amplifies the natural CO_2 outgassing, which is also the largest in the Indian and Pacific sectors of the SPSS. The climate effect is a combination of climate effects on natural and anthropogenic CO_2 fluxes, which partly oppose each other (Figure S6).

3.2 The seasonal cycle of air-sea CO_2 fluxes in the Southern Ocean

We now shift our focus to seasonal fluxes by separating fluxes into separate winter (Figure 4) and summer (Figure 5) mean CO_2 fluxes. For this, we examine the period 2015-2018, for which all data sets are available (see Figure S8 for an annual mean figure for 2015-2018).

3.2.1 Winter

In winter, all but two data sets (one GOBM and BGC-float pCO_2-products) agree that the Southern Ocean is a sink of CO_2 (GOBMs: -0.83±0.40 PgC yr^{-1}, pCO_2 products: -0.48±0.08 PgC yr^{-1}; Figure 4a). The general pattern of strong uptake towards the north and a reduction towards the south is common to all data classes, though exceptions for individual GOBMs do exist (Figure 4a,b). Expounding on this, the strong uptake in the STSS is shown by all data sets, but further south the coherence disintegrates. Within the SPSS, there is considerable variation in position and magnitude of maximum outgassing with some GOBMs being a sink along the entire zonal mean (Figure 4a,b). Towards the southern reaches of the ICE biome, fluxes are more coherent as they are constrained by sea-ice cover in winter (Figure 4b). For the zonal means of individual GOBMs, see Figure S5.

The divergence between data class average flux estimates for the Southern Ocean are explained nearly entirely by differences in the SPSS (GOBMs: -0.15±0.32 PgC yr^{-1} and pCO_2 products: 0.15±0.09 PgC yr^{-1}, in Figure 4a). Note also that the spread of the individual GOBMs is the largest in the SPSS (0.32 PgC yr^{-1}), although it is also substantial in the other biomes (STSS: 0.29 PgC yr^{-1}, ICE: 0.13 PgC yr^{-1}) (Figure 5a).

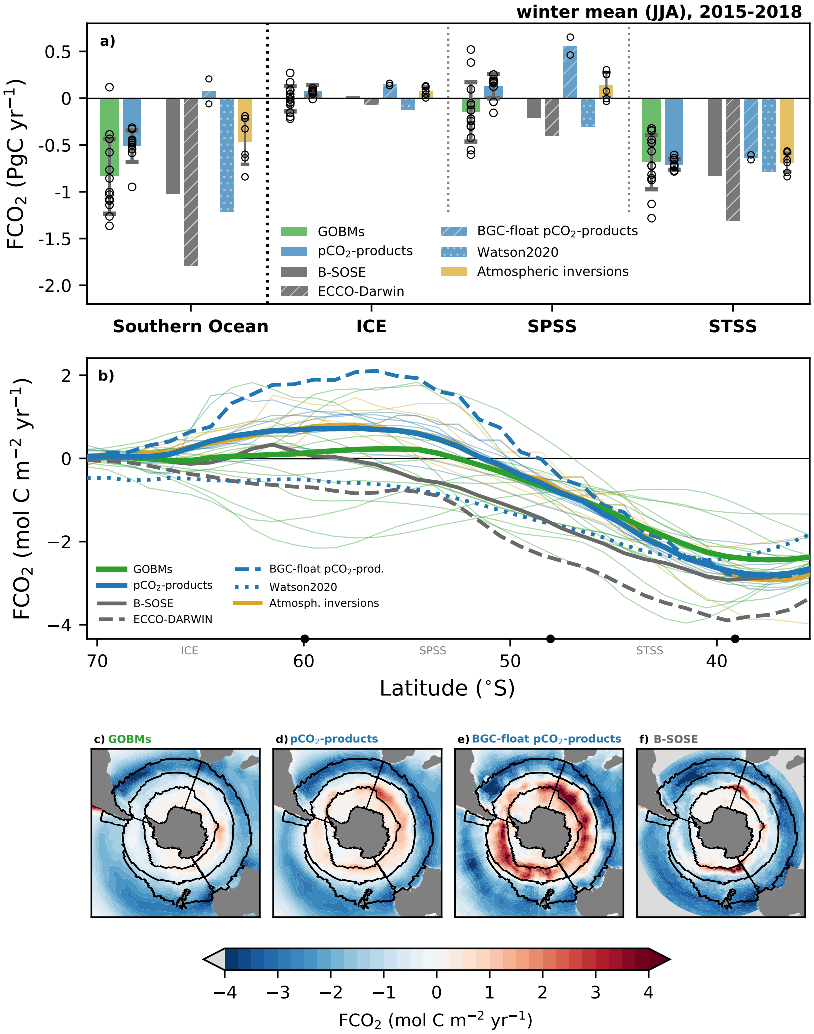

Figure 4. Average winter (June-August) air-sea CO_2 fluxes (FCO_2) in the period 2015-2018, (a) averaged over biomes, (b) zonal mean flux density, (c-f) maps of flux density. Same as Figure 2, but including also data sets with shorter coverage, and a map of the CO_2 flux from the BGC-float pCO_2-products (panel e), and B-SOSE (f), and hence focussing on the period 2015-2018 for all data sets for comparability. Note that the MPI model is excluded here. The zonal mean of individual models are presented in Figure S5c.

The SPSS is also where we see the largest impact of the inclusion of floats in the BGC-float pCO_2-products (Figure 4d,e), with the mean outgassing flux more than doubling that of the regular pCO_2-product ensemble.

The zonal differences and features of fluxes between data classes are also most distinct in the SPSS (Figures 4c-f). In short, the Atlantic sector of the SPSS has the lowest flux (weak source or even sink), while the Indian and Pacific sectors dominate the outgassing. The data-assimilated model B-SOSE has stronger localized outgassing compared with the other data classes but bear in mind that B-SOSE is only one data sets (Figure 4f), while the other data classes (Figures 4c-e) represent up to 13, thus potentially averaging out local signals. The outgassing hotspot at the boundary between the Atlantic and Indian sectors of the SPSS can also be recognized in the pCO_2-products (Figure 4d). The second hotspot in the western Pacific SPSS is not distinguishable in the other data sets.

3.2.2 Summer

In summer, GOBMs, pCO_2-products and inversions largely show CO_2 uptake within the three Southern Ocean biomes, and outgassing north of the STSS (Figure 5a-b). In contrast to winter, the GOBM ensemble mean for summer 2015-2018 (-1.04$\pm$0.77 PgC yr^{-1}) underestimates the CO_2 uptake relative to the pCO_2-product ensemble mean (-1.46$\pm$0.18 PgC yr^{-1}, Figure 5a). This also holds true for the data-assimilated models, where B-SOSE even simulates outgassing in the SPSS (Figure 5a,b,f). Otherwise, the data-assimilated models, B-SOSE and ECCO-Darwin, deviate substantially from the other data classes. The differences between pCO_2-products with and without BGC-float data are hardly apparent in summer (Figure 5a, compared to 4a). This could be due to a smaller discrepancy between float and ship-data in summer, and/or a dominance of SOCAT data in summer for the ship+float estimate. For context, for the period 2015 through 2018, BGC-float data account for up to 70% of winter pCO_2 monthly by 1°×1° measurements in the Southern Ocean (SOCAT + floats), while in summer the floats represent only 20% (Bakker et al., 2016; Bushinsky et al., 2019).

While the STSS was a region of coherence between data classes in winter (Figure 4), it is the main source of the discrepancy between the GOBM and pCO_2-product ensemble means in summer (GOBMs: -0.40$\pm$0.28 PgC yr^{-1}, pCO_2-products: -0.73$\pm$0.08 PgC yr^{-1}). The discrepancy is comparatively smaller in the SPSS (GOBMs: -0.33$\pm$0.34 PgC yr^{-1}, pCO_2-products: -0.42$\pm$0.06 PgC yr^{-1}). We note that CO_2 fluxes for both GOBMs and pCO_2-products show less variation from ICE to STSS in summer compared to winter (Figure 4b vs 5b, respectively). There is, nevertheless, an offset with lower GOBM CO_2 uptake than in pCO_2-products north of 55°S, and vice versa to the south. Also, the GOBM spread in the represented magnitude of the fluxes is large. In absolute terms, the GOBM ensemble spread of fluxes in summer (from -2.03 to +0.28 PgC yr^{-1}) is larger than in winter (from -1.36 to 0.12 PgC yr^{-1}) or than the spread in the annual mean (from -1.30 to -0.38 PgC yr^{-1}; see Figure S5b for zonal means of individual GOBMs). This mirrors the difficulty in representing the balance between physical and biological processes in summer, which is further assessed in the next two sections 3.2.3 and 3.2.4.

3.2.3 The full seasonal cycle

We diagnose distinctly different seasonal cycles in the three biomes. The ICE biome has a rather clear maximum uptake in summer in the GOBM and pCO_2-product ensemble means, as well as most individual data sets (Figure 6a). In the STSS, the pCO_2-products suggest a weak seasonal cycle with a maximum uptake in autumn (Figure 6c), while the majority of GOBMs simulate a maximum CO_2 uptake in winter and a substantially smaller flux in summer. The largest disagreement occurs in the SPSS, where the seasonal cycle transitions from winter outgassing in the ICE biome to summer outgassing in the STSS

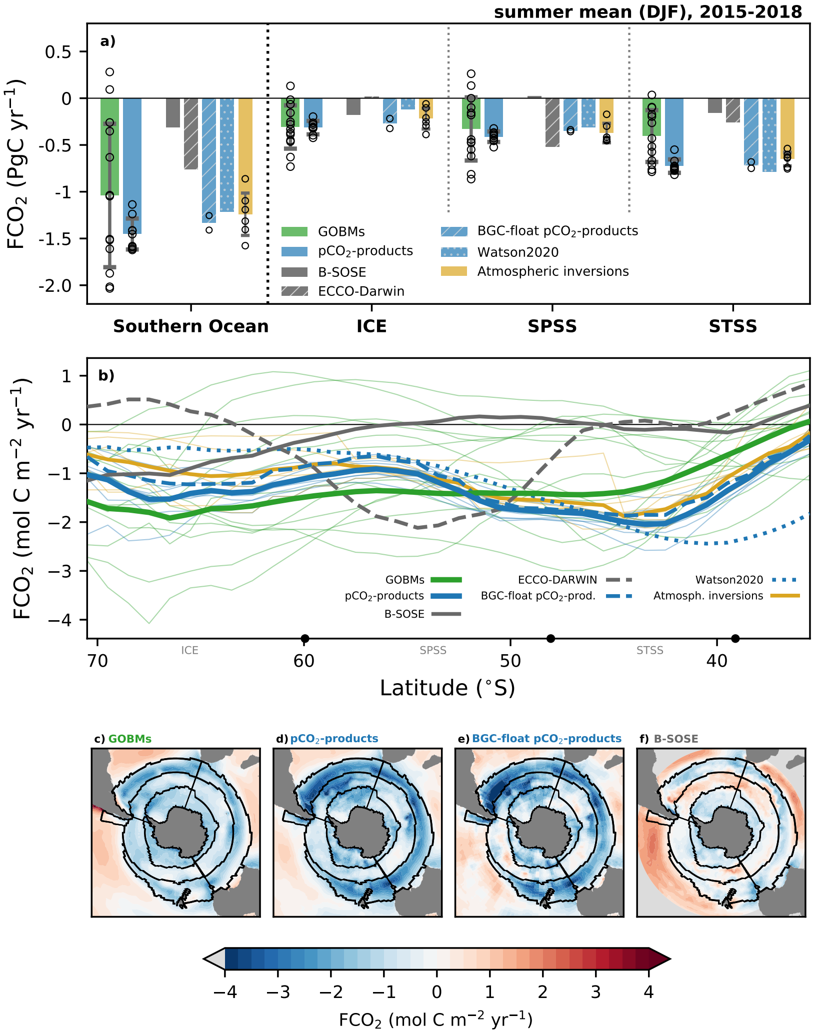

Figure 5. Average summer (December-February) air-sea CO_2 fluxes (FCO_2) in the period 2015-2018. Same as Figure 4, but for summer. The zonal mean of individual models are presented in Figure S5b.

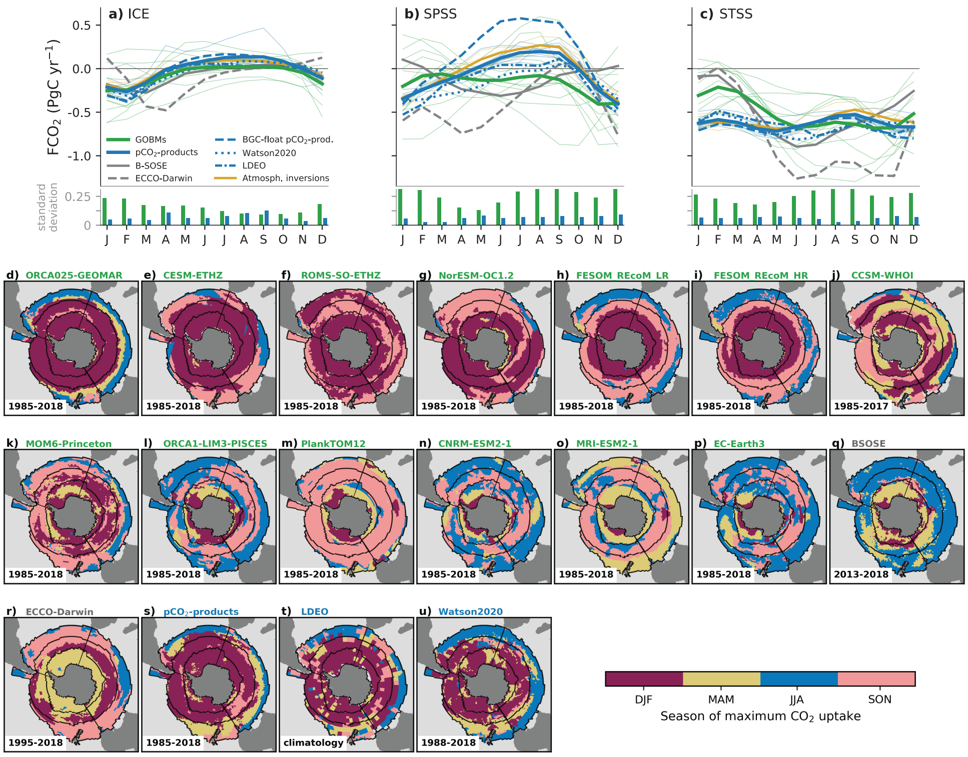

Figure 6. The seasonal cycle of air-sea CO_2 flux in the Southern Ocean separated by biomes for all data sets as indicated in the legend, a) subtropical seasonally stratified (STSS) biome, b) subpolar seasonally stratified (SPSS) biome, c) ice (ICE) biome. Thin green and blue lines depict individual GOBMs and pCO_2-products, and thick lines indicate their ensemble means. Note that the MPI model is excluded here. The ensemble standard deviation (1σ) is shown by the bars for each month. Panels (d-u) present the season of maximum CO_2 uptake per grid cell in the individual GOBMs, data-assimilated models and the ensemble mean of the pCO_2-products over the period indicated in the panels (varies by data set). See Figure S9 for the individual pCO_2-products (panel d-u equivalents) and Figure S10 for the seasonal cycle in all nine subregions (equivalent to panels a-c but further split into Atlantic, Pacific and Indian Ocean sectors).

biomes. Here, atmospheric inversions and pCO_2-products (including the BGC-float pCO_2 products), suggest the maximum CO_2 uptake to be in summer. In winter, the BGC-float pCO_2-products more than double the estimates of outgassing relative to the other pCO_2 products (Figure 6b). The GOBM ensemble average roughly agrees with this seasonal pattern, but simulates a reduced seasonal cycle amplitude (Figure 6b). The GOBM spread is large, not only in terms of magnitude but also phasing of the seasonal cycle in the SPSS (8 out of 13 GOBMs simulate the maximum uptake between November and January; Figure 6d-r). This illustrates how the transition between the different seasonal cycle regimes affects particularly the representation of the seasonality in the SPSS. In summary, most GOBMs and pCO_2-products agree on a summer peak in the ICE biome (but exceptions exist, Figure 6d-r), and a winter peak to the north of the Southern Ocean biomes. The largest discrepancy between data sets is where and how swift this transition occurs. While the use of static biomes adds to the discrepancies seen in the averaged seasonal cycles (Figure 6a-c), the disagreement between the phasing of individual GOBMs is likely a much larger contributor to these discrepancies (Figure 6d-p). We now turn to an investigation of the thermal and non-thermal effects on the seasonal cycle, which may help explain these discrepancies.

3.2.4 Thermal versus non-thermal effects on the seasonal cycle

The seasonal cycle of CO_2 fluxes in the Southern Ocean is a balancing act between competing thermal and non-thermal drivers (Mongwe et al., 2016, 2018; Prend et al., 2022). DIC drawdown by biological production leads to a summer maximum in CO_2 uptake, whereas upwelling and entrainment of DIC-rich water into the mixed layer in autumn and winter leads to a minimum in CO_2 uptake or even outgassing (Metzl et al., 2006; Mongwe et al., 2018). Seasonal variations in mixed layer temperature further affect the solubility of CO_2, with lower (higher) temperatures increasing (decreasing) solubility and thus promoting CO_2 uptake (outgassing) (Takahashi et al., 2002).

The thermal and non-thermal components of pCO_2 can be decomposed to determine the dominant driver on monthly timescales (Figure 7; Mongwe et al., 2018). Here, we do this by estimating the absolute difference of the rate of change of the thermal and non-thermal components (Figure 7; Eq. 3). The contribution of salinity and total alkalinity to seasonal pCO_2 changes are small in the Southern Ocean and compensate for each other on a seasonal scale (e.g., Sarmiento & Gruber, 2006; Lauderdale et al., 2016), thus we here consider the non-thermal component to be predominantly DIC-driven.

In general, the seasonal cycle phasing of the thermal component of the GOBMs agrees well with those of the pCO_2-products (Figure 7a-c). This should not come as a surprise, as GOBMs are forced by atmospheric reanalyses which assimilate observed SST (Doney et al., 2007). As a result, the thermal component of the pCO_2 seasonal cycle in the GOBMs (forced by reanalyses) compare much better to the thermal component derived from the pCO_2-products than fully coupled Earth System Models (Mongwe et al., 2016, 2018). The non-thermal contribution is thus the primary reason for the spread between GOBMs, and for the differences between GOBMs and pCO_2-products (Fig. 7a-c). Thus, we group GOBMs based on whether they are predominantly DIC or thermally driven across all three biomes (Fig. 7d-f, Table S2), which we term DIC-dominant or DIC-weak respectively.

In DIC-weak GOBMs, the strong underestimation of the non-thermal component causes these models to be too strongly temperature driven across the year (Figure 7). This then tends to shift the timing of uptake towards the colder months (when CO_2 solubility is largest), while the role of biologically driven uptake in spring and summer is suppressed in favor of warming driven outgassing. This effect is largely confined to the SPSS and to a lesser extent also the STSS, and can account for the mismatch in the seasonal cycle seen in some GOBMs. For example, in the SPSS, nearly all GOBMs and specif-

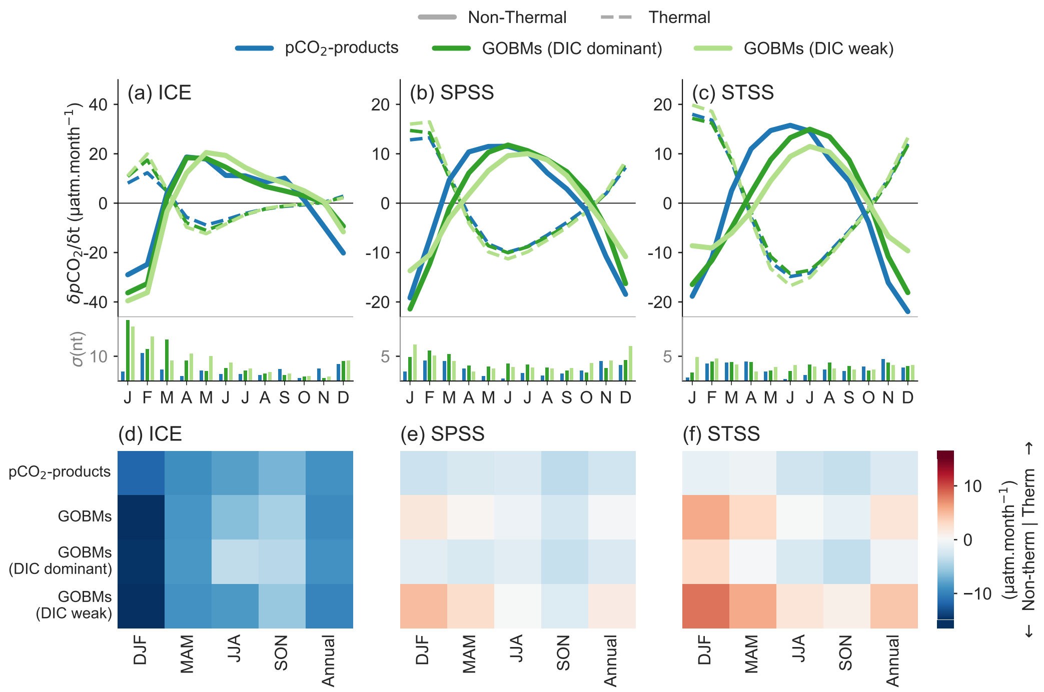

Figure 7. (a-c): Seasonal cycle of the rate of change of the thermal ($pCO_2^{T'}$, dashed lines) and non-thermal ($pCO_2^{nonT'}$, solid lines) components of ocean surface pCO_2 on monthly time scales given in μatm month^{-1} (Eq. 2). The bars on the bottom show standard deviations of the non-thermal component. Models have been grouped into DIC dominant/weak, where the DIC weak models have a thermal contribution >0 for the mean of the STSS and SPSS (shown in d-f; see Figure S11 for individual global and regional ocean biogeochemistry models, and Table S2 for the DIC dominant/weak model groups). (d-f): λpCO_2, the difference of the thermal and non-thermal (DIC) components of ocean surface pCO_2 as in Mongwe et al. (2018). When $\lambda pCO_2 > 0$ (red) indicates temperature dominance, and $\lambda pCO_2 < 0$ (blue) indicates that the non-thermal component (i.e., DIC) is dominant. The MPI model is excluded in this analysis.

ically all DIC-weak GOBMs have a shifted season of maximum uptake from summer to spring/winter, i.e., towards the colder months. (Fig. 6 and Table S2). In terms of the underlying mechanisms driving the too weak non-thermal component, we hypothesize that a lack of deep vertical mixing in winter leads to too little entrainment of DIC-rich deep waters, while simultaneously allowing for too early primary production (which may then shift the growing season earlier and reduce biologically driven summer uptake). Notably, the bias in pCO_2 is largest in summer (DJF), followed by autumn (MAM), and is about twice as large in the DIC-weak GOBMs than in the DIC-dominant GOBMs (Figure S13). This further supports the lesser importance of thermal processes in the STSS and SPSS regions evident in the pCO_2-products.

In the ICE biome GOBMs and pCO_2-products tend to agree much more closely in terms of their representation of the seasonal cycle (Fig. 6a). This is likely related to the strong role the seasonal advance and retreat of sea ice plays in air-sea CO_2 fluxes, both through its effect as a physical barrier, as well as through its effect on vertical mixing and light availability (thus impacting both physical and biological pathways of DIC into and out of the mixed layer, (Bakker et al., 2008; Shadwick et al., 2021; M. Yang et al., 2021)).

3.3 Temporal variability and trends in Southern Ocean air-sea CO_2 flux

We next inspect the temporal evolution of the air-sea CO_2 fluxes from 1985-2018 (Figure 8). In this annually-resolved perspective, we also discuss the mean fluxes for data sets that are not available for the full time-period. While the STSS was a net-sink region throughout the period, the SPSS and ICE have turned from neutral (around 0 PgC yr^{-1}) to net sink regions since 1985, based on GOBM and pCO_2-product ensemble mean estimates. This also holds for most individual GOBMs as only two of them simulate either the ICE or the SPSS biome to still be regions of outgassing at the end of the time series (CCSM-WHOI and EC-Earth3).

Acknowledging some agreement between GOBMs and pCO_2-based product ensemble means despite large spread across GOBMs (Figure 8 bars), substantial deviations among individual data sets appear. B-SOSE (2015-2018) suggests a 0.25 PgC yr^{-1} smaller uptake than the GOBM and pCO_2-product ensemble means for the entire Southern Ocean (Figure 8a). ECCO-Darwin has the largest flux estimate into the ocean in the SPSS and the entire Southern Ocean (1.30 PgC yr^{-1}, 1985-2018). Notably, the two data-assimilated models B-SOSE and ECCO-Darwin differ by a factor of 2 for the Southern Ocean wide estimate. In agreement with previous reports (Bushinsky et al., 2019), BGC-float pCO_2-products suggest Southern Ocean uptake to be 40% (0.4 PgC yr^{-1}) smaller than the pCO_2-products without BGC-float data (2015-2018). This discrepancy originates largely in the SPSS, where the BGC-float pCO_2-products estimate outgassing of 0.14 PgC yr^{-1}, and the ensemble mean of the SOCAT-only-based pCO_2-products estimate a CO_2 uptake of -0.13 PgC yr^{-1}. Smaller contributions to the deviation stem from the STSS and ICE biomes where BGC-float pCO_2-products report a smaller uptake by 0.14 PgC yr^{-1} when compared with the regular pCO_2-products. The Watson2020-product is generally close to the other pCO_2-products, with the exception of the SPSS where it suggests a flux of -0.18 PgC yr^{-1} (1985-2018), which is larger than any other pCO_2-product. The origin of the large SPSS difference in Watson2020 could, in part, be attributed to subtle differences in method choices in addition to different flux parameterisations (Watson et al., 2020). The atmospheric inversions produce a somewhat lower sink (-0.64 PgC yr^{-1}, average over three inversions 1985-2018), but are generally close to the pCO_2-products, as they mostly use surface pCO_2-products as a prior (Table 2 and Friedlingstein et al., 2022). There is also slightly higher interannual variability in the atmospheric inversion ensemble mean, but this is likely due to the small ensemble size.

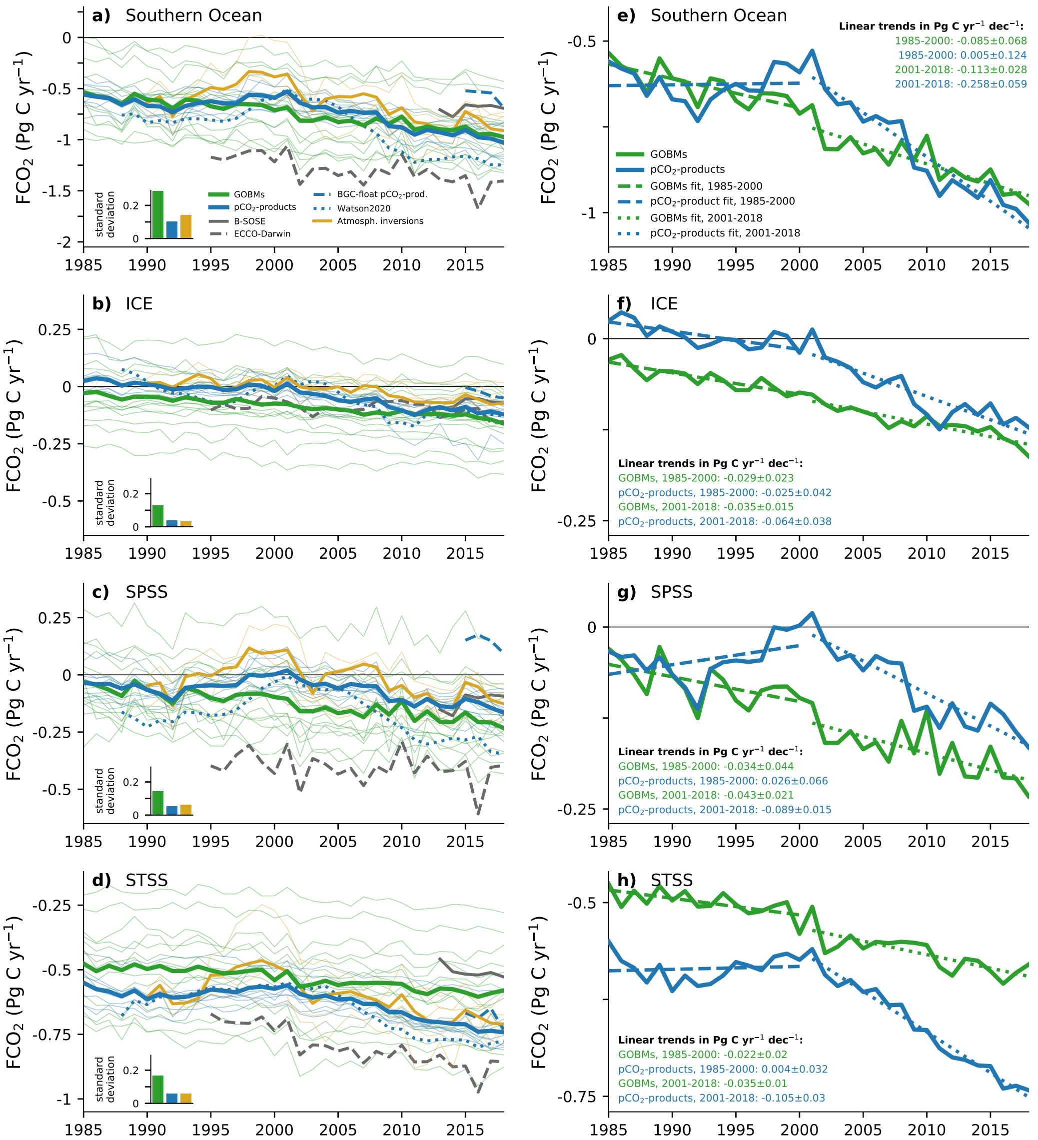

Figure 8. Temporal evolution of the Southern Ocean air-sea CO_2 flux for a) the entire Southern Ocean, and the b) subtropical seasonally stratified, c) subpolar seasonally stratified, and d) ice biomes. The ensemble standard deviation (1σ) averaged over the whole time series, is shown by the bars. Panels (e-h) are the same as panels (a-d) for the GOBM ensemble average and pCO_2-product ensemble average only, with linear trends between 1985-2000 and 2001-2018 as the dashed and dotted lines, respectively. The uncertainty range of the trend is calculated as one standard deviation of the trends across all GOBMs and pCO_2-products, respectively. Note the different y-axis scales. The separation into Atlantic, Pacific and Indian Ocean sectors is shown in Figure S12.

The temporal variability is quantified as the amplitude of 'interannual variability' (IAV). This is calculated as the standard deviation of the detrended time-series, as defined in Rödenbeck et al. (2015); Friedlingstein et al. (2022) which, in reality, captures both interannual and decadal variability components. Following this definition, the pCO_2-products have a larger interannual variability for the Southern Ocean wide integrated flux (0.09 PgC yr^{-1}, range 0.04 to 0.16 PgC yr^{-1}) compared to the GOBMs (0.06 PgC yr^{-1}, range 0.03 to 0.10 PgC yr^{-1}). Notably, the MPI-SOM-FFN pCO_2-product, which formed the basis of previous reports on Southern Ocean decadal variability (Landschützer et al., 2015), has the largest IAV of 0.16 PgC yr^{-1}, about 60% larger than the next largest pCO_2-product IAV. This is in line with previous studies that found that the MPI-SOM-FFN approach may overestimate Southern Ocean variability by 30% (Gloege et al., 2021) and the decadal trend 2000-2018 by 130% (Hauck et al., 2023). Within the Southern Ocean, the strongest IAV is found in the SPSS region (0.04 PgC yr^{-1} GOBMs, 0.05 PgC $yr^{-1}$$pCO_2$-products), followed by the STSS (0.02 PgC yr^{-1} GOBMs, 0.03 PgC yr^{-1} pCO_2-products) and ICE biome (0.02 PgC yr^{-1} for both data classes). Within the subpolar biome, the Indo-Pacific sector has a higher IAV (0.02 PgC yr^{-1}) than the Atlantic sector (0.01 PgC yr^{-1}). The large contribution to interannual variability in the SPSS may well be linked to the largest amplitude of the seasonal cycle of CO_2 flux (see section 3.2.3).

To assess the decadal-scale trends, we fit linear trends to the periods 1985-2000 and 2001-2018 (Figure 8e-h) with the year 2000 marking roughly the mid of the considered time period and the inflection point in global ocean CO_2 uptake (Gruber et al., 2023; Landschützer et al., 2016). The pCO_2-products suggest a stagnation of the flux in the STSS, and even a flux decrease in the SPSS prior to 2000. In contrast, GOBMs suggest a continued increase in the sink in the STSS and SPSS in the same period. In the ICE biome, GOBMs and pCO_2-products result in an increasing trend (Figure 8h). After 2000, pCO_2-products and GOBMs agree on a trend towards more CO_2 uptake, which is significantly different from zero in all biomes except for $pCO-2$-products in the ICE biome (see numbers in Figure 8e-h). However, they differ substantially in magnitude between GOBM and pCO_2-product ensemble means, particularly in the STSS (Figure 8f). The discrepancies in the magnitude of the trend act to decrease the gap between GOBM and pCO_2-product ensemble means in the SPSS and ICE biomes, but lead to the divergence in the flux estimate in the STSS.

On a sub-biome level (i.e., Atlantic, Indian, and Pacific sectors), all three sectors in the STSS were CO_2 sinks throughout the period and had weaker trends (less negative) before 2000 compared to the period after 2000 (Figure S12). In the SPSS, the Indian and Pacific sectors are characterized by intermittent outgassing and uptake patterns, in line with observations from BGC-floats (Prend et al., 2022). In the SPSS, only the Atlantic sector has a net uptake throughout the period, and the Indian Ocean sector shows the largest model spread of all three sectors (as in the STSS). In the ICE biome, a consistent quasi-linear evolution is apparent in all sectors. We further analyze divergence and drivers of trends in section 3.3.2.

3.3.1 Comparison with in-situ pCO_2

Here, we evaluate the accuracy of pCO_2 across data classes since pCO_2 is the dominant driver of air-sea CO_2 flux variability at a monthly scale (Landschützer et al., 2016). All data sets are compared with observations (monthly gridded SOCAT v2022 data set Sabine et al., 2013; Bakker et al., 2016, 2022). The RECCAP2 data sets are subsampled to match the SOCAT observations in time and space, meaning that we do not assess sampling biases, but rather the mismatch between the observed and estimated pCO2.

The comparison of the RECCAP2 GOBMs and pCO_2-products with gridded in-situ pCO_2 from SOCAT v2022 shows relatively good agreement (Figure 9a). The SOCAT pCO_2 data shows large interannual variability due to spatially and temporally vary-

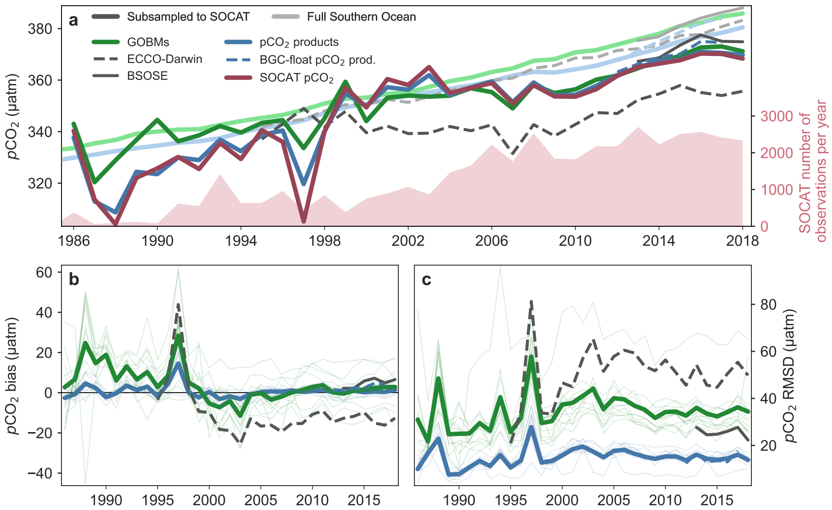

Figure 9. Comparison of surface mean pCO_2 for the whole Southern Ocean between global ocean biogeochemistry models (GOBMs) and pCO_2-products with in situ observations (gridded SOCAT v2022 data set Sabine et al., 2013). (a) Time-series of annually-averaged pCO_2 from GOBMs (green), data-assimilated models (grays), and pCO_2–products (blue). The darker shaded lines show the annual mean as calculated from the data sets subsampled to match the historic SOCAT sampling. The lighter shades show the annual mean calculated for the full coverage. The dark red line depicts the annual mean pCO_2 from SOCAT observations without interpolation. The assimilation products (ECCO-Darwin and B-SOSE) are kept separate as they have different time series lengths (shown by dashed and solid gray lines respectively). The light red area plot (right y-axis) shows the number of monthly by $1^\circ \times 1^\circ$ gridded SOCAT observations per year. (b) The bias of pCO_2 for all data classes (subsampled to match SOCAT observations, dark lines in a) relative to SOCAT pCO_2 observations (solid dark red line in a). (c) The root mean squared difference (RMSD) between SOCAT observations and estimates for all data classes. Bias and RMSD were calculated on a monthly by $1^\circ \times 1^\circ$ resolution, and the bias and RMSD were averaged to annual means afterwards. A plot of RMSE and bias for SPSS and STSS biomes and different seasons is presented in supplementary Figure S13.

ing sampling efforts from year to year, particularly prior to 2000 when samples are fewer and thus carry more weight (Figure 9a). For example, in 1997, SOCAT pCO_2 is anomalously low due to high sampling density in the Ross Sea during summer when primary production drives intense CO_2 drawdown (Arrigo & van Dijken, 2007). The pCO_2 products have a lower bias and a narrower spread than the GOBMs prior to 2000 (1.7±4.3μatm and 10.7±8.0μatm respectively), with the bias and the spread decreasing after 2000 for both classes (-0.3±2.6μatm and -0.9±3.9μatm, Figure 9b). This comparison of simulated to observed pCO_2 at observation sites demonstrates that GOBMs are capable of reproducing SOCAT pCO_2 and its temporal evolution on large spatial and annual time-scales. Thus, for the period after 2000, the differences in CO_2 flux trend for the entire Southern Ocean between GOBMs and pCO_2-products (Figure 8) cannot be attributed to differences in pCO_2 in the regions where observations were taken. Instead, the differences arise primarily from areas where no pCO_2 observations exist, as also concluded in Hauck et al. (2020). The pCO_2 time-series calculated from the full coverage results in a lower pCO_2 value in the pCO_2-products than in the GOBMs (Figure 9a), which could explain the stronger CO_2 flux trend in the pCO_2-products (Figure 8). This discrepancy between pCO_2-products and GOBMs is larger in the last ten years (2009-2019: 5.8 μatm) than the previous decade (1999-2008: 2.8 μatm, Figure 9a). Nevertheless, the RMSD calculated from monthly mean data is higher in GOBMs than in pCO_2-products (Figure 9c). This is expected as the pCO_2-products are trained to fit the observations and further illustrates the GOBMs' deficiencies in simulating seasonal and spatial variability of the CO_2 uptake.

The assimilation model, ECCO-Darwin, has a negative bias after 2000 (-13.5±3.0 μatm; Figure 4b), but this negative bias is not strongly reflected in the mean of the non-subsampled data, with the mean pCO_2 still being larger than that of the pCO_2-products, which do not underestimate the pCO_2 relative to SOCAT. This further emphasizes that sampling distribution may play an important role in the magnitude of the biases calculated in any model. The pCO_2 summer sampling bias in the Southern Ocean has long been recognised as a potential source of biases in pCO_2 estimates, particularly for the pCO_2-products that rely heavily on the in-situ data (Metzl et al., 2006; Gregor et al., 2017; Ritter et al., 2017; Djeutchouang et al., 2022). The SOCCOM project increased the number of winter samples with pH-enabled profiling floats (from 2014), suggesting stronger outgassing during winter than previously shown (Gray et al., 2018). In RECCAP2, the B-SOSE assimilation model and the BGC-float pCO_2-products both make use of this data (Verdy & Mazloff, 2017; Bushinsky et al., 2019). Both of these estimates overestimate pCO_2 relative to SOCAT pCO_2 highlighting the challenge in consolidating ship-based SOCAT and BGC-float data.

3.3.2 Climate versus CO_2 effects on trends in CO_2 flux

Our analysis so far has indicated that the GOBMs reproduce seasonal temperature effects on CO_2 flux reasonably well (Figure 7), and a larger uncertainty is associated with imprints of circulation and biological activity. Next, we inspect the zonal mean and spatial patterns of the CO_2 flux trend 1985-2018 (Figure 10). The pCO_2-products place the largest trend towards more CO_2 uptake in the entire ICE biome; however, data in this region is sparse and there is larger variability between pCO_2 products here (see also Figure 8). The pCO_2-products show a secondary peak in the STSS between about 40 to 45°S. The GOBMs in contrast have a large meridional gradient in the ICE biome with a peak in the trend between 60 and 65°S that is reduced in magnitude towards Antarctica. The secondary peak in the STSS is hardly apparent and also displaced southwards compared to the pCO_2-products. In addition, the pCO_2-products exhibit trends towards less CO_2 uptake in the Pacific and eastern Indian sector of the SPSS (Figure 10a-b). Although the difference in flux density between GOBMs and pCO_2-products is larger in the ICE biome, the discrepancy in the STSS contributes more to the total flux trend discrepancy due to the larger area of the STSS biome (Figure 8). The trend over 1985-2018

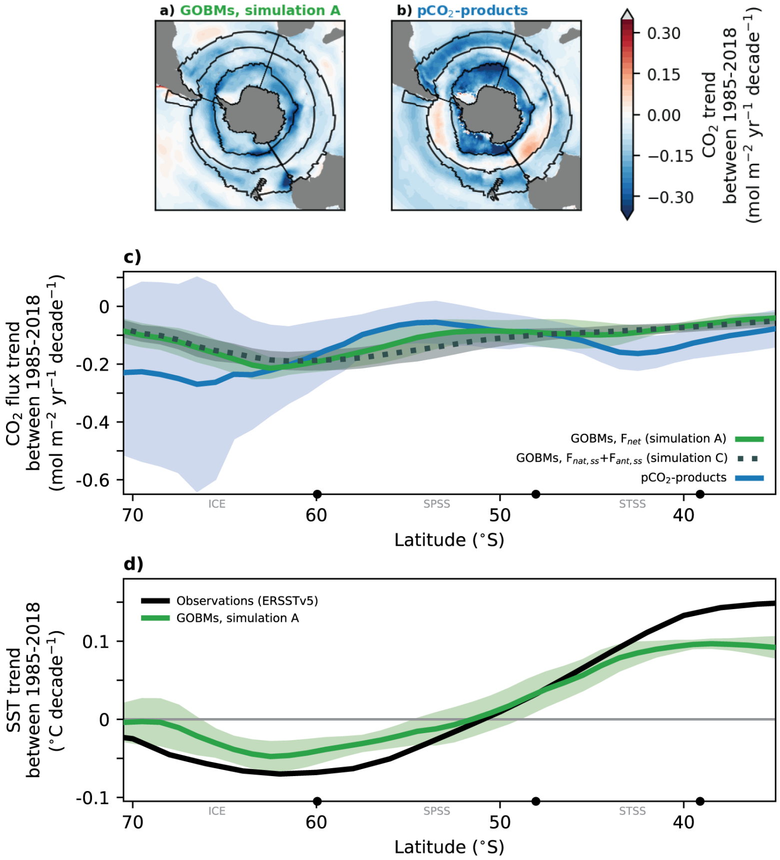

Figure 10. CO_2 flux trend between 1985 and 2018. (a-b) Spatial maps of the net CO_2 flux trend, for (a) the global ocean biogeochemistry models and (b) the pCO_2-products. (c) Zonal mean CO_2 flux trend 1985-2018 for the net CO_2 flux (blue: pCO_2-products, green: GOBMs) and the GOBM flux of $F_{nat,ss}$ and $F_{ant,ss}$, i.e., the flux as expected from increasing atmospheric CO_2 alone (green, dashed). (d) The sea surface temperature (SST) trend 1985-2018 in the GOBMs (green) and in the observational data set (black, NOAA Extended Reconstructed Sea Surface Temperature, ERSST, Version 5 (Huang et al., 2017)). Supplementary figures split this analysis in the periods 1985-2000 (Figure S14) and 2001-2018 (Figure S15). Individual GOBM trends for F_{net}, as well as $F_{nat,ss}$ plus $F_{ant,ss}$ and SST are shown in Figure S16.

includes some compensation between the trends over 1985-2000 and 2001-2018 (see Figures S14-S15). While the GOBMs show similar weak trends towards more uptake before and after 2000, the pCO_2-products show a trend towards less uptake in the earlier period 1985-2000 throughout the Southern Ocean except in the Weddell and Ross Seas. In the later period 2001-2018, the pCO_2 products estimate a much stronger trend towards more CO_2 uptake everywhere, as also shown in Figure 8. The CO_2 flux trends in the GOBMs are largely driven by increasing atmospheric CO_2 levels (simulation C in Figure 10c). However, the trend is reduced by climate change and variability throughout the SPSS and strengthened in the northern part of the ICE biome (compare simulations A that represents net FCO_2 and C that represents only steady state natural and anthropogenic fluxes, in Figure 10c). The effect of climate change and variability is substantially smaller than the uncertainty in the pCO_2-products. In line with GOBMs capturing the thermally-driven component of the pCO_2 seasonal cycle (Figure 8), we can also demonstrate that the GOBMs simulate sea surface temperature trends 1985-2018 rather well (Figure 10d). This is related to the choice of forcing the GOBMs with reanalysis data that itself depends on sea surface temperature observations (Doney et al., 2007). In contrast to fully coupled Earth System models in CMIP6 (Beadling et al., 2020), the suite of models used here capture the decadal trend pattern of warming along the northern flank of the Antarctic Circumpolar Current (ACC), and cooling in the south (Figure 10, Armour et al., 2016; F. Haumann et al., 2020). The lack of warming south of 50°S was previously related to the wind-driven upwelling of deep water that had not yet been exposed to anthropogenic warming and by northward heat transport (Armour et al., 2016). More recently, the cooling was suggested to be caused by increased freshwater export from the ice region, which increases stratification and thus reduces the upward heat flux from below by warm water masses (F. Haumann et al., 2020). While the GOBM ensemble mean captures the latitudinal structure of the SST trend well, it underestimates the magnitude of peak cooling at around 60°S as well as peak warming north of 40°S. Overall, however, the GOBM ensemble mean captures the latitudinal structure of the SST trend well. We can therefore not relate the discrepancies in the trend of the CO_2 flux to temperature biases. This leaves data sparsity as a reason for potential biases in the trend in the pCO_2-products, and biases in ocean circulation, sea ice and biology as possible reasons for biases in GOBMs.

3.4 Interior ocean storage of anthropogenic carbon

The focus of this section is the anthropogenic perturbation of dissolved inorganic carbon (DIC) in a subset of the GOBMs (see section 2.2.1), and in particular its accumulation rate over the period 1994 to 2007 (ΔC_{ant}), in comparison with the eMLR(C*) observational estimate (Gruber, Clement, et al., 2019) and the ocean inverse model OCIMv2021 (DeVries, 2022). The eMLR(C*) product uses a multiple linear regression approach to estimate ΔC_{ant} and captures both the influence of CO_2-driven and climate-driven change in sea-air CO_2 fluxes and transports, whereas OCIMv2021 captures only the CO_2-driven changes.

All data classes agree in having the largest ΔC_{ant} inventories within and to the north of the STSS biome (Figure 11), whose southern boundary approximately corresponds to the northern edge of the ACC. This pattern is related to the mechanisms by which C_{ant} is taken up at the surface and exported to depth (Mikaloff Fletcher et al., 2006; Morrison et al., 2022; Bopp et al., 2015). Subpolar upwelling exposes old C_{ant}-poor waters to elevated atmospheric CO_2 concentrations and this, combined with strong winds, drives a large influx of C_{ant} in the SPSS biome (Figure 12a-c). A small fraction of the C_{ant} moves southward and is exported within Antarctic Bottom Waters, while the largest fraction is transported northward within the upper cell of the meridional overturning circulation. C_{ant} air-sea fluxes remain elevated throughout the northward path, and are reinforced by the deep mixed layers in the regions where mode and intermediate waters are formed,

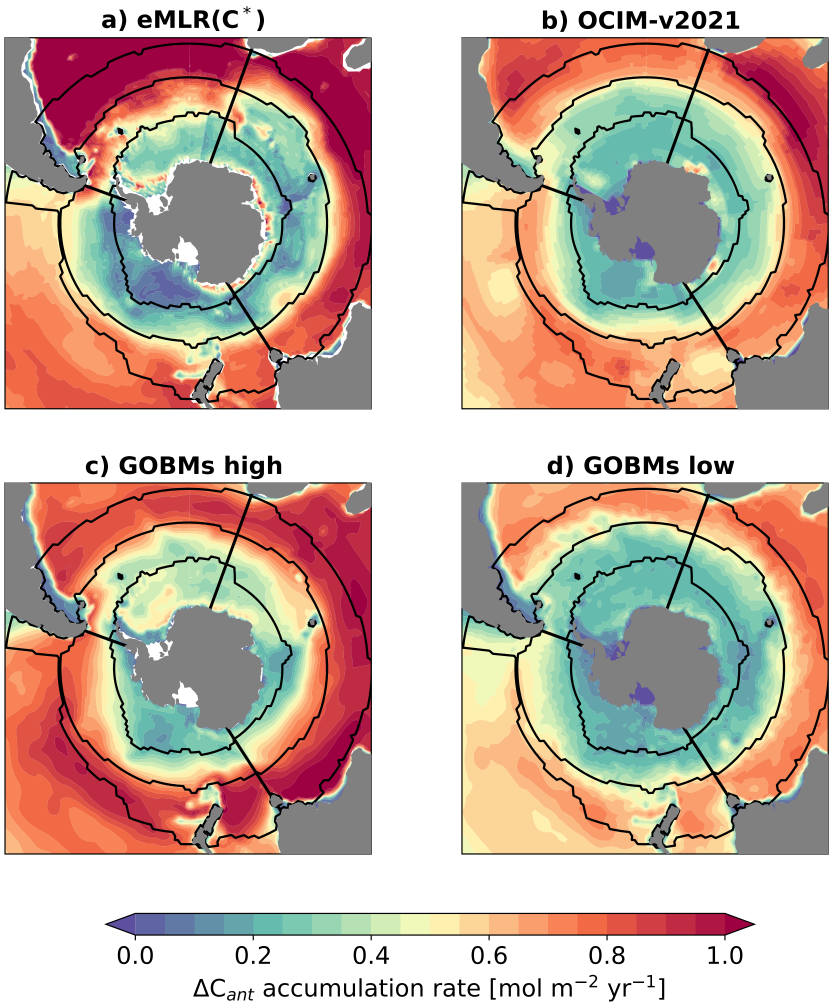

Figure 11. ΔC_{ant} yearly accumulation rate over the period 1994-2007 integrated until 3000 m depth in the observationally-constrained estimates a) eMLR(C*) (Gruber et al., 2019) and b) OCIM-v2021, in c) "GOBMs high" and in d) "GOBMs low" (individual GOBMs shown in Fig. S4). The robustness of the patterns has been tested as explained in Text S4 of the Supplement. Contours show the boundaries of the ICE, SPSS and STSS biomes. Values below 3000 m are not shown because of the low signal-to-uncertainty ratio in eMLR(C*).

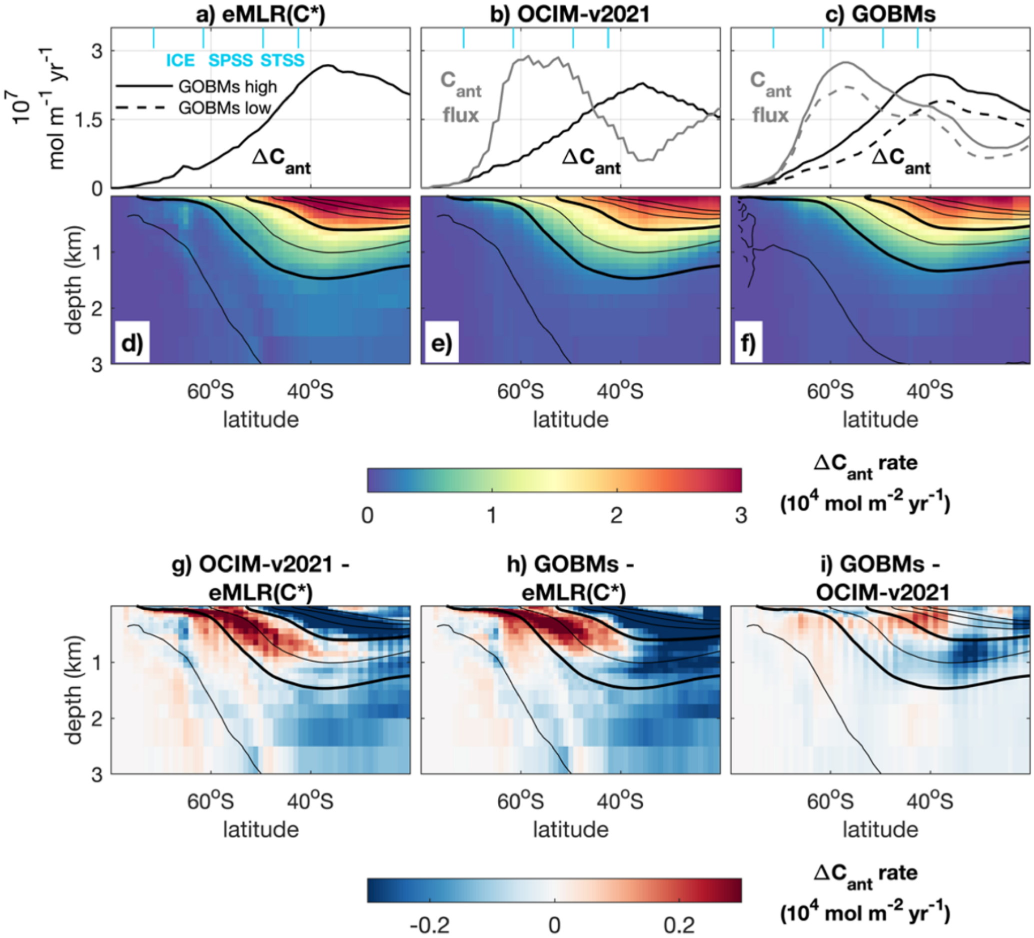

Figure 12. Zonal integrals of ΔC_{ant} yearly accumulation rate from 1994 to 2007 and of air-sea C_{ant} fluxes (positive downwards) averaged between 1994 and 2007 for a,d) eMLR(C*), b,e) OCIM-v2021 and c,f) GOBMs. a-c) (black line) ΔC_{ant} column inventory (0-3000 m) and (grey line) air-sea C_{ant} fluxes; for the GOBMs, the distinction is made between "GOBMs high" (full lines) and "GOBMs low" (dashed lines). g-i) Anomalies of ΔC_{ant} accumulation rates in g) OCIM-v2021 with respect to eMLR(C*), h) GOBMs with respect to eMLR(C*) and i) GOBMs with respect to OCIM-v2021. In all sections, contours show mean potential density (with a 0.03 kg m^{-3} spacing) referenced to the surface in World Ocean Atlas 2018 (Boyer et al., 2018), where thick lines indicate the 1026.9 kg m^{-3} and 1027.5 kg m^{-3} isopycnals. Anomalies of individual GOBMs shown in Fig. S18 (with respect to eMLR(C*)) and Fig. S19 (with respect to OCIMv2021).

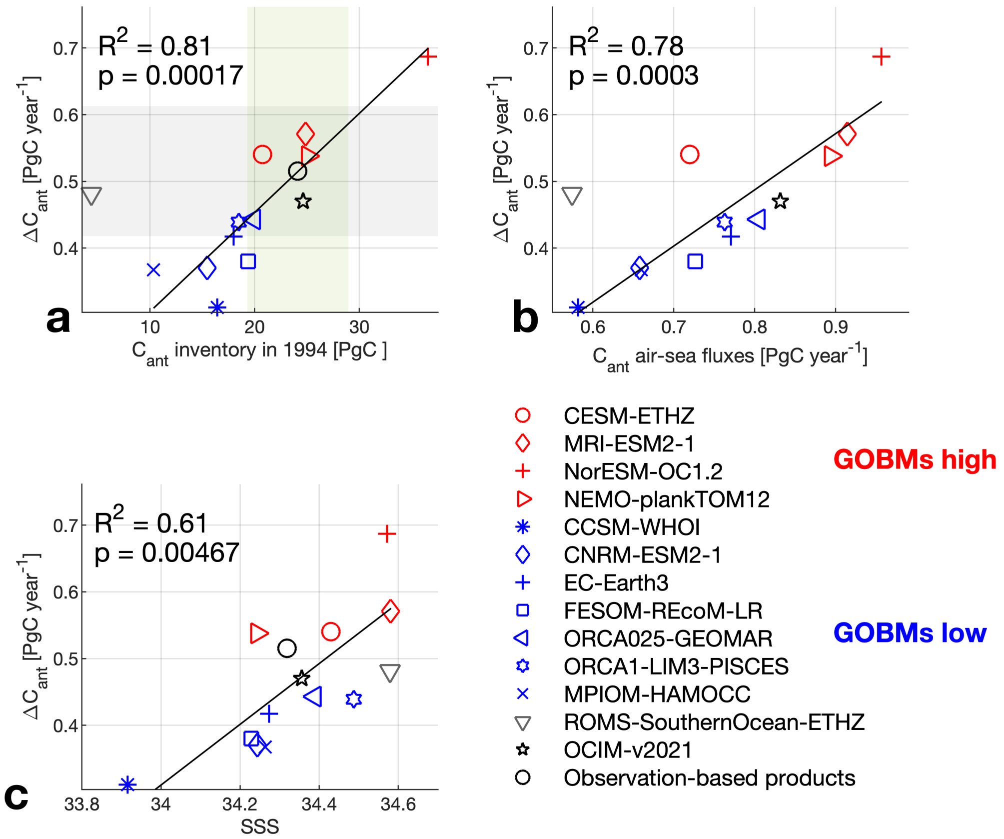

Figure 13. Scatter plots showing relationships between ΔC_{ant} accumulation rates between 1994 and 2007 (integrated to 3000 m) and different quantities namely a) the cumulative C_{ant} in 1994 integrated over the Southern Ocean, b) air-sea C_{ant} fluxes averaged between 1994 and 2007 and integrated over the Southern Ocean, c) sea surface salinity (SSS) horizontally averaged over the SPSS and STSS biomes (which show consistent SSS anomaly patterns, Fig. S17). Shown are a subset of the GOBMs (see 2.3), the OCIM-v2021 data-assimilated model, the observation-based cumulative C_{ant} until 1994 (C* method, Sabine et al., 2004) and the 1994-2007 ΔC_{ant} from (eMLR(C*) method, Gruber, Clement, et al., 2019), and SSS from EN4.2.1 (Good et al., 2013). Thin black lines show the linear fit of the data for the GOBMs only, with the explained variance (R^2) and the p-value indicated for each regression. The grey shading in a) indicates the 19% uncertainty levels around the mean of eMLR(C*) (Southern Hemisphere uncertainty estimate, based on Table 1, Gruber, Clement, et al., 2019) and the green shading the 20% uncertainty levels around the C*-based estimate of cumulative C_{ant} until 1994 (global uncertainty estimate Sabine et al., 2004; Matsumoto & Gruber, 2005). Models that have a ΔC_{ant} storage higher than the average of the two observationally-constrained data sets ("GOBMs high") are shown in red, whereas the models in which it is lower ("GOBMs low") are shown in blue. Because of its different spin-up procedure, ROMS-SouthernOcean-ETHZ is shown in the plots but has been excluded from the regression analysis. For OCIM-v2021, CNRM-ESM2-1 and MPIOM-HAMOCC the ΔC^{ss}_{ant} is shown, whereas in others the sum of steady state and non steady state is shown. As discussed in Text S2, ΔC^{ns}_{ant} accumulation rates are about 10-20% of the total ΔC_{ant}.

which results in a secondary peak at around 40°S in some GOBMs, diluted by the ensemble mean (Fig. 12c).

The effective transport of C_{ant} into the ocean interior relies on a number of physical processes, the dominant of which is the northward transport by the overturning circulation of the C_{ant} ventilated in the ocean interior by deep winter mixing (Frölicher et al., 2015; Morrison et al., 2022). The absorbed C_{ant} spreads northward along density surfaces within mode and intermediate waters (Figure 12d-f) and is circulated within and out of the Southern Ocean by the subtropical gyres (Frölicher et al., 2015; D. C. Jones et al., 2016; Waugh et al., 2019). As a result, the largest C_{ant} inventories are displaced to the north with respect to the maximum air-sea C_{ant} influx (Figure 12b,c). Another pathway by which the C_{ant} inventory can build up without a corresponding surface influx is by southward advection and subsequent subduction of high-C_{ant} Subtropical Waters (Iudicone et al., 2016; Morrison et al., 2022).

The observation-based product eMLR(C*) and the ocean inverse model OCIM-v2021 have similar ΔC_{ant} accumulation rates when integrated over the Southern Ocean for the period 1994 through 2007 (0.52 PgC yr^{-1} and 0.47 PgC yr^{-1}, respectively, Figure 13), but differ in their horizontal (Figure 11) and vertical (Figure 12) patterns. The eMLR(C*) exhibits particularly low ΔC_{ant} values at subpolar and high latitudes (Figure 12g), especially in the Pacific sector (Figure 11). The GOBMs multi-model-mean of ΔC_{ant} accumulation rates over the same 1994 through 2007 period and integrated within the Southern Ocean (Figure 13) is 0.46±0.11 PgC yr^{-1}, i.e., 7% lower than the mean of the two observational estimates considered here. 6 out of the 12 GOBMs fall within the 19% range of the observational eMLR(C*) uncertainty. Two thirds of all GOBMs (hereafter "GOBMs low") have lower than observed ΔC_{ant} accumulation rates (0.39±0.11 PgC yr^{-1}, about 20% lower than the observational estimates). The remaining GOBMs (hereafter "GOBMs high") have higher than observed ΔC_{ant} accumulation rates (0.58±0.07 PgC yr^{-1}, about 17% higher than the observational estimates). "GOBMs high" have a higher ΔC_{ant} storage than "GOBMs low" throughout the Southern Ocean (Figures 11c,d and 12c), higher C_{ant} air-sea fluxes (Figure 12c), higher sea surface salinity (SSS) in the SPSS and STSS biomes and mixed layer depths especially in the SPSS biome (Text S3, S4 and Figure S17). Along the zonal mean section, all GOBMs show a southward shift in ΔC_{ant} with respect to eMLR(C*) shown by a north-south dipole in the upper 1 km (Figure 12h), as similarly found in the comparison between OCIM-v2021 and eMLR(C*) (Figure 12g). With respect to OCIM-v2021, GOBMs show higher ΔC_{ant} above 1000 m depth and lower ΔC_{ant} beneath (Figure 12i). This could point to insufficient ventilation of C_{ant} in "GOBMs low" models (Figure S19), which represent the majority of the GOBMs. The amount of spread and the overall underestimate of ΔC_{ant} in the GOBMs is consistent with Earth System Models analyzed by Frölicher et al. (2015) and Terhaar et al. (2021), supporting the argument that biased ocean model dynamics and water mass properties rather than biases in the atmospheric forcing cause the C_{ant} underestimate (Terhaar et al., 2021; Bourgeois et al., 2022).

Integrated over the Southern Ocean, we find that the model spread in ΔC_{ant} accumulation rates from 1994 to 2007 can be largely explained (81% variance explained) by the spread in accumulated C_{ant} until 1994 (Figure 13), suggesting a coherent scaling between long-term and recent C_{ant} accumulation rates. The model spread in ΔC_{ant} accumulation rates is also related with the spread in C_{ant} air-sea fluxes averaged over 1994-2007 (78% variance explained). These results show that past long-term ΔC_{ant} accumulation rates are a better predictor for present ΔC_{ant} accumulation rate than present C_{ant} air-sea fluxes. The reason for this is that C_{ant} air-sea fluxes are linked to changes in C_{ant} storage through ocean transport, which may differ substantially between models (Frölicher et al., 2015; Terhaar et al., 2021; Bourgeois et al., 2022). This becomes obvious when considering the myriad of processes involved, including the strength of the overturning circulation, the strength of the subtropical gyres, the isopycnal stirring by

Table 3. Comparison of the Southern Ocean carbon sink estimate with the estimate presented in RECCAP1 (Lenton et al., 2013), which used a different definition of the Southern Ocean region (44-75°S) and covered a different period (1990-2009). GOBMs: Global Ocean Biogeochemistry Models. Reported numbers are means ± one standard deviation. Note for RECCAP1 the median of all models is reported.

Estimate	GOBMs	Observation-based
RECCAP2 1985-2018	-0.75 ± 0.28 PgC yr^{-1}	-0.73 ± 0.07 PgC yr^{-1}
RECCAP2 1985-2018 (44°-75°S)	-0.39 ± 0.24 PgC yr^{-1}	-0.30 ± 0.04 PgC yr^{-1}
RECCAP2 1990-2009 (44°-75°S)	-0.22 ± 0.25 PgC yr^{-1}	-0.14 ± 0.09 PgC yr^{-1}
RECCAP1 1990-2009 (44°-75°S)	-0.43 ± 0.38 PgC yr^{-1}	-0.27 ± 0.13 PgC yr^{-1}

mesoscale eddies, and localized subduction dynamics (Sallée et al., 2012; Morrison et al., 2022). The different way in which the GOBMs simulate these transport processes is possibly linked to the large model spread in ΔC_{ant} accumulation rates among GOBMs. Past studies have found that SSS affects the surface ocean density in the formation regions of mode and intermediate waters and could be used as a constraint of the C_{ant} air-sea fluxes, and thus of the C_{ant} storage within the recently-ventilated water masses (Terhaar et al., 2021). In this study and in Terhaar et al. (2023), we find that SSS explains a lower variance in the ΔC_{ant} accumulation rates (R^2=61%; Figure 13) and in the C_{ant} air-sea fluxes (R^2=57% Terhaar et al., 2023) with respect to the ESMs (R^2=0.74) analyzed by Terhaar et al. (2021). The relationship may be weaker due to the different suite of models used in the ESM and GOBM ensembles and remaining biases associated with incomplete spin-up (Terhaar et al., 2023).

4 Discussion

4.1 Summary and progress since RECCAP1

We provide an updated estimate of the Southern Ocean carbon sink (see Figure 1 for regional extent). The numbers we present (Table 3) are not directly comparable with the RECCAP1 estimate (Lenton et al., 2013) due to different region definitions (Figure 1) and periods (1990-2009 vs. 1985-2018). The RECCAP1 regional definition of the Southern Ocean (44-75°S) cut across and missed a large part of the strong CO_2 uptake north of the Subantarctic Front. Recalculating the RECCAP2 numbers for the RECCAP1 region would reduce the Southern Ocean CO_2 sink to 52% (GOBMs) or 41% (pCO_2-products) of its original value (Table 3). Adjusting RECCAP2 numbers for the 1990-2009 period would further reduce fluxes by about another 50%. Compared on equal footing (44°-75°S and 1990-2009), we find the Southern Ocean to be a weaker carbon sink in RECCAP2 compared to RECCAP1.

The observational and modeling communities have made substantial progress on quantifying and characterizing the Southern Ocean carbon sink since RECCAP1 (Lenton et al., 2013). The creation of the Surface Ocean CO_2 Atlas and its annual updates have marked a step-change by facilitating the development of statistical models (a.k.a. pCO_2-products). The large and diverse ensemble of pCO_2-products help to identify the robust features of the Southern Ocean carbon sink. The pCO_2-products have a relatively small spread compared to the global ocean biogeochemistry models in terms of mean and seasonal cycle, indicating that the uncertainty from differences in mapping methods is small. However, the spread in the trend estimates is in fact larger in the products than in the GOBMs (Figure 10). Further, the narrow spread in mean and seasonal cycle does not include the uncertainties due to sparse pCO_2 observations in the Southern Ocean, particularly in winter and before the 2000's (Ritter et al., 2017). In addition, pCO_2-products share the uncertainties associated with the bulk formulation of air-sea CO_2 exchange (R. H. Wanninkhof et al., 2009; Fay et al., 2021). While they do have their shortcomings, the pCO_2 products are an advance for constraining the Southern Ocean carbon sink compared to the atmospheric inversions that were used in RECCAP1 (Lenton et al., 2013). This is because the surface ocean pCO_2 observations provide a more direct constraint on the air-sea CO_2 flux than the relatively small atmospheric CO_2 signals over the ocean that form the basis of the atmospheric inversions.

The larger GOBM ensemble provides a more representative process-based estimate and the spread in GOBMs has been reduced since RECCAP1 (see Table 3 Lenton et al., 2013). The remaining spread is nevertheless large and points towards critical need for model development, where the largest sources of uncertainty stem from biological process description and circulation, which vary in importance depending on flux component (natural, anthropogenic, etc.), and spatio-temporal scale of interest. In terms of the anthropogenic component, the 12 GOBMs analyzed here have a 24% spread (standard deviation around the mean) in the C_{ant} accumulation rates, which is marginally larger than the $\sim$ 20% uncertainty associated with the observational estimates of ΔC_{ant} and C_{ant} (even though caution is warranted when directly comparing the uncertainty estimates, which are computed formally different across data classes; Gruber, Clement, et al., 2019; Sabine et al., 2004). Overall, the GOBM ensemble mean underestimates the observation-based estimates of the C_{ant} accumulation up to 1994 by 19% and the change between 1994-2007 by 7%. Admittedly, the GOBM ensemble analyzed here is relatively small, and the underestimation of C_{ant} and ΔC_{ant} is in the range of the uncertainty ranges of the observational estimates. We can nonetheless speculate that the detected underestimation is likely related to a combination of physical, chemical and methodological factors. First, our results point to too little or too shallow ventilation of mode and intermediate waters (Figure 12i), the causes of which can be related to insufficient vertical mixing or too sluggish northward export of the subducted waters (Morrison et al., 2022). However, while sea-surface salinity (SSS) was singled out as a strong predictor of C_{ant} air-sea fluxes in an ESM ensemble analyzed by (Terhaar et al., 2021), in our study and in (Terhaar et al., 2023), SSS was not found to be a clear constraint of the anthropogenic CO_2 uptake and its interior storage in the GOBMs. Rather, Terhaar et al. (2023) find that biases in the normalized surface Revelle factor could explain the underestimation of C_{ant} uptake. Finally, the relatively high pre-industrial CO_2 mixing ratios related to late starting dates in several GOBMs are likely causing an underestimation of the cumulative C_{ant} storage, which is especially large in the Southern Ocean (Terhaar et al., 2023). For the natural carbon fluxes, the difficulty in capturing the delicate balance between physical and biological processes is clearly manifested by the large model spread (Figure 3). In addition, the different spin-up procedures could play a role. Terhaar et al. (2023) indicate that the natural CO_2 flux component may be biased towards uptake that is too strong, possibly related to GOBMs not being in steady-state (Terhaar et al., 2023), which is particularly relevant in the Southern Ocean where old water masses resurface. While long preindustrial spin-ups would bring the GOBMs closer to steady-state and thus reduce drift, they may come at the cost of less realistic surface conditions and their response to climate change and variability (Séférian et al., 2016). Interestingly, the two data-assimilated GOBMs differ to a large extent, illustrating that dynamical processes in these models may still override information gained from assimilated observations.

The averages of the GOBM and pCO_2-product ensembles agree for many key estimates, showing progress over the past 10 years: the mean and spatial distribution of the sink is in good agreement (Figure 2), although discrepancies of the magnitude and, particularly, the trends still persist (Figures 8 and 10; see also Canadell et al., 2021). The fact that these ensemble means agree so well in many respects provides some confidence in the Southern Ocean CO_2 flux estimates because they are nearly independent. However, the agreement of GOBMs and pCO_2-products on the mean CO_2 flux is partly a result of compensation of regional and seasonal discrepancies (Figures 4, 5, 8). The agreement is also highly susceptible to the choice of river flux adjustment that either locates most outgassing of river-derived carbon in the Southern Ocean (Aumont et al., 2001) or in the tropical Atlantic (Lacroix et al., 2020). Reasons for the discrepancy between Aumont et al. (2001) and Lacroix et al. (2020) may be because of specific choices in nutrient and carbon input, lability of organic matter, resulting ocean model transport (see also the discussion in Terhaar et al., 2023). We here chose to use the river flux adjustment of Lacroix et al. (2020), scaled up to a global value of 0.65 PgC yr^{-1}, resulting in a small adjustment for the Southern Ocean of 0.04 PgC yr^{-1}. In contrast, the Southern Ocean (south of 20°S) adjustment based on Aumont et al. (2001) that is so far used in the Global Carbon Budget is higher by one order of magnitude (0.32 PgC yr^{-1}) and can explain the large mismatch in the mean flux (but not its trend) between GOBMs and pCO_2 products in the Southern Ocean in the Global Carbon Budget (Friedlingstein et al., 2022). The discrepancies in the trend cannot be explained by GOBM biases in warming trends as these are well reproduced (Figure 10). Similarly, the GOBM ensemble is not systematically biased towards formation of mode and intermediate waters that is too weak, in contrast to the ESMs, and an effect on the trend of the ocean carbon sink could not be evidenced (Terhaar et al., 2023). Further potential candidates for GOBM biases, which were not explored here, are stratification (Bourgeois et al., 2022), mixing, and mixed layer dynamics, which could also lead to excess carbon accumulation in the surface layer and thus may be the driver for the overestimation of the surface Revelle factor. In the pCO_2-products, the trend might be biased by data sparsity (Gloege et al., 2021; Hauck et al., 2023).

4.2 Seasonal cycle and thermal versus non-thermal drivers

As a community, we have a good understanding of the mechanisms that drive pCO_2 seasonality in the Southern Ocean (Lenton et al., 2013), but we do not fully understand their magnitudes, opposing or synergistic, in different seasons and regions (Mongwe et al., 2018). Part of this lack of understanding is due to a lack of observations throughout all seasons, though particularly acute during winter (Gray et al., 2018; Bushinsky et al., 2019; Sutton et al., 2021). Further, complex biological processes affecting pCO_2 in summer are more difficult to accurately describe in GOBMs (Mongwe et al., 2018).

While pCO_2 products require little to no understanding to reconstruct the seasonal cycle, they may still suffer from a lack of data (Ritter et al., 2017). This may be shown by the narrow ensemble spread of the pCO_2-products during winter (Figure 7d-f), which may result from poor sampling distribution. That being said, an observation system simulation experiment (OSSE) showed that the seasonal cycle in most of the Southern Ocean is in fact well captured by one pCO_2 product (Gloege et al., 2021). The narrower GOBM spread of the non-thermal pCO_2 component during winter may also suggest that wintertime processes (circulation) are less complex than summer (circulation and biology, Figure 7d-f).

The introduction of biogeochemical Argo floats since the mid 2010's has increased the number of winter observations (relative to the available ship-based observations), albeit inferred from pH and estimated total alkalinity and thus associated with a higher uncertainty (Williams et al., 2017). The machine learning approaches that include float-based observations result in stronger winter outgassing (Figure 4, Bushinsky et al., 2019). Direct pCO_2 measurements showed that the years used to train the machine learning model (2015-2018) may have had anomalously high pCO_2 (Sutton et al., 2021). However, if this is in fact the case, and not related to sampling locations, this may indicate much larger interannual variability in the Southern Ocean than the majority of the pCO_2-products currently estimate (Figure 8). Incorporating these data is thus potentially an important goal for pCO_2-products, but it has proven difficult to incorporate the float-based pCO_2 estimates further back in time than 2015, the start of the BGC-float record and account for their higher uncertainty (Bushinsky et al., 2019; Williams et al., 2017).

GOBMs also have a lower pCO_2 ensemble spread during winter compared with summer and agree on the spatial location of the winter flux minimum (Figure 4). Nevertheless, the range in magnitude is still more than twice as large as those of the pCO_2-products (Figure 7d-f). Since the thermal component is well captured in GOBMs (Figure 7d-e), the non-thermal physical drivers (i.e., circulation) determines the uncertainty observed in winter. In summer, GOBMs have difficulty capturing the delicate balance between biological and physical processes that leads to a large spread in model pCO_2 and fluxes (Mongwe et al., 2018). GOBMs may thus benefit from more process-based studies that further our understanding of pCO_2 drivers during summer, i.e., biological productivity, respiration, remineralization and sinking of organic carbon as part of the biological carbon pump.

4.3 Temporal variability of CO_2 fluxes

Our analysis reduces the previously reported discrepancy in variability of Southern Ocean air-sea CO_2 fluxes between data classes (GOBMs and pCO_2-product ensemble means, Gruber, Landschützer, & Lovenduski, 2019). We relate the growing agreement to the larger ensemble of pCO_2-products in our study, with the newer additions having a substantially lower variability than the two pCO_2-products (Jena-CarboScope and SOM-FFN) used by Gruber, Landschützer, and Lovenduski (2019). A recent study using the same RECCAP data base also concluded that there is agreement on the magnitude of interannual variability between GOBMs and pCO_2-products (Mayot et al., 2023).

The interannual to decadal variability of Southern Ocean air-sea CO_2 fluxes was discussed extensively in the literature, and was often related to variations in the Southern Annual Mode (SAM) (Le Quéré et al., 2007; Lovenduski et al., 2007; Lenton & Matear, 2007; Hauck et al., 2013; Nicholson et al., 2022; Mayot et al., 2023). Also, regional wind variability linked to the zonal wavenumber 3 was suggested as a driver of interannual CO_2 flux variability driving both the weakening in the 1990's and the strengthening in the 2000's (Landschützer et al., 2015; Keppler & Landschützer, 2019). The arguments of SAM or wave number 3 as dominant drivers of CO_2 flux interannual variability might not be fully independent from each other, as previously a wave number 3 like pattern was reported to describe MLD anomalies during positive SAM events (Sallée et al., 2010).

The fact that the maximum IAV of GOBMs is found in the SPSS Indo-Pacific sector (section 3.3, Figure S12) supports the argument of the above mentioned references that upwelling of carbon-rich deep water and related outgassing of natural carbon in response to a positive SAM and strengthening of westerly winds may be the dominant driver of interannual variability (DeVries et al., 2017). This is further supported by studies of atmospheric potential oxygen (APO), which can be used as a tracer of ocean-only processes from measurements of CO_2 and O_2 at atmospheric stations (Stephens et al., 1998). Nevison et al. (2020) showed that the interannual variations of APO seasonal minimum from stations in the Southern Hemisphere were strongly correlated with the SAM during years of positive phase. Further, they showed that GOBMs (as analyzed in this study) can capture the variability of CO_2 and APO fluxes driven by the SAM variations during the austral winter months. However, the study of Nevison et al. (2020) also illustrated that the SAM index variability cannot fully explain the changes in APO seasonal winter minima suggesting that other factors or modes of variability such as ENSO could impact the CO_2 and O_2 air-sea fluxes of the Southern Ocean as also previously suggested in an ocean modeling study (Verdy et al., 2007).

On top of the interannual variability, on which pCO_2 products and GOBMs seem to reach reasonable agreement, discrepancies in the CO_2 flux trend since 2000 have emerged

(Figure 8, Friedlingstein et al., 2022). These discrepancies highlight a major knowledge gap and urgently need to be resolved by critical analysis of potential biases in pCO_2-products as well as GOBMs (see section 4.1). While there is no evidence so far that adjustments of CO_2 fluxes based on model evaluation of interfrontal salinity and Revelle factor affect the trend (Terhaar et al., 2023), data sparsity tends to lead to an overestimation of decadal variability and trend in at least two of the pCO_2-products (Gloege et al., 2021; Hauck et al., 2023). Hence, both data classes need to be inspected for deficiencies.

4.4 Zonal asymmetry of the fluxes

While the primary spatial mode of variability in the Southern Ocean is from north to south, zonal variability in the dynamics, biogeochemistry, and carbon fluxes have been reported in the literature (Landschützer et al., 2015; Tamsitt et al., 2016; Rintoul, 2018; Prend et al., 2022). Similarly, we find substantial zonal asymmetry in both the mean states, and seasonal and interannual variability of the Southern Ocean CO_2 fluxes (Figures S10, S12); yet many of our results have been presented in a zonally-averaged perspective for the sake of brevity.

In this work, we find that the largest zonal asymmetries in the Southern Ocean mean air-sea CO_2 flux occur in the SPSS biome (Figure 4b-e, S12). Here, the Pacific and Indian sectors are larger sources (or weaker sinks) of CO_2 to the atmosphere than the Atlantic sector. This is consistent with the pCO_2-based products (Figure S12d-f). The float-based pCO_2-products amplify this winter outgassing dramatically. However, the GOBMs and the assimilative model ensemble averages do not show a coherent and convincing increase in outgassing in the Indian and Pacific relative to the Atlantic. The zonal asymmetry reported in the observation-based products is consistent with a recent BGC-float-based study that reported stronger outgassing in the Indian and Pacific sectors of the Southern Ocean (Prend et al., 2022). The authors attributed this dominance to stronger winter-time entrainment of deep waters to the surface in these regions. The zonal asymmetry is also apparent in the air-sea CO_2 fluxes decomposed into natural and anthropogenic contributions (Figure S7). Here, too, the SPSS is the region with the greatest asymmetry. In the Indian sector, the large natural outgassing fluxes of the ensemble mean are nearly perfectly opposed by the anthropogenic uptake.

4.5 Link large-scale synthesis to observational programs

The analysis presented here provides a synthesis of large-scale datasets with a focus on budgets, spatial and temporal patterns of fluxes and carbon accumulation, and a first-order assessment of large-scale processes (e.g., thermal versus non-thermal, anthropogenic vs natural carbon fluxes). In particular, it highlights spatio-temporal windows for which discrepancies between data classes are largest (e.g., magnitude of winter outgassing, delicate balance of physical versus biological processes in summer, magnitude of decadal trend of the Southern Ocean carbon sink). Importantly, this synthesis builds on contributions from many individual groups contributing repeat observations of surface and interior ocean biogeochemical properties from research vessels and ships of opportunity (e.g., Talley et al., 2016; Hoppema et al., 1998; van Heuven et al., 2014; Metzl et al., 1999; Pardo et al., 2017). The ship-based observations form the cornerstone for many of the data classes in this study: observation-based ocean interior estimates of CO_2 storage assess changes in deep ocean measurements of CO_2, the surface pCO_2 estimates use observations from ships of opportunity, and the GOBMs are evaluated against ocean interior observations. And while sampling biases and gaps in the ship-based measurements may be filled by autonomous platforms with lower accuracy (e.g., BGC-floats), they will always require crossover validation measurements from the high-accuracy shipboard measurements. This emphasizes that the ship-based observations need to continue into the future to characterize the evolution of the Southern Ocean carbon cycle. This will only become more important, once stabilization of atmospheric CO_2 will lead to a larger weight on ocean processes for control of air-sea fluxes relative to the current quasi-exponential growth rate of atmospheric CO_2.

Further, detailed regional process studies employing a wide range of methodologies across disciplines are also important to further our holistic understanding of the Southern Ocean carbon cycle and to improve the description of biogeochemistry and ecosystem dynamics in GOBMs, particularly in summer. One example for such an interdisciplinary field program is along the continental shelf west of the Antarctic Peninsula where shipboard observations indicate a strong, near-shore summer undersaturation of surface pCO_2 (Eveleth et al., 2017) and seasonal reduction in surface dissolved inorganic carbon (Hauri et al., 2015). The seasonal trends in the ocean CO_2 system on the shelf reflect a combination of biological net community production (Ducklow et al., 2018) and meltwater input diluting surface dissolved inorganic carbon and alkalinity (Hauri et al., 2015). Regional ocean biogeochemical models simulate similar onshore-offshore gradients in surface chlorophyll, biological productivity, dissolved inorganic carbon, and pCO_2 as well as the observed large interannual biophysical variability associated with year-to-year variations in seasonal sea-ice advance and retreat phenology (Schultz et al., 2021). Observed decadal trends for the region from the early 1990s to late 2010s indicate that reduced sea-ice extent associated with climate change drives an increase in upper ocean stability, phytoplankton biomass and biological dissolved inorganic carbon drawdown, resulting in a growing net downward air-sea CO_2 flux during summer (Brown et al., 2019). Recent year-round, autonomous mooring observations of pCO_2 and pH suggest a gradual increase in surface ocean pCO_2 and dissolved inorganic carbon over the fall and winter, with CO_2 outgassing during winter when pCO_2 is supersaturated largely blocked by sea-ice cover (Shadwick et al., 2021; M. Yang et al., 2021). Similar large-scale programs are needed in other parts of the Southern Ocean given its size and importance in the global carbon cycle. On-going research activities, also as part of the Southern Ocean Observing System (SOOS), e.g., in the Ross (Smith et al., 2021) and Weddell Seas (Arndt et al., 2022) have the potential of being extended.

5 Conclusions

Here, we present a schematic overview that summarizes the main characteristics of the Southern Ocean carbon cycle 1985-2018, as derived in this analysis and its supplementary material (Figure 14). In general, the sink strength for atmospheric CO_2 (net CO_2 flux, FCO_2) increases from South to North, but with important zonal asymmetry. The Atlantic and Indian Ocean sectors of the Subtropical Seasonally Stratified biome (STSS) are the regions that act as strongest sinks. In the Subpolar Seasonally Stratifed biome (SPSS), the Atlantic sector stands out as the only sector acting as an annual mean CO_2 sink. Also the seasonal cycle shows a distinct north-south gradient. In the ice-covered biome (ICE) the peak uptake occurs in summer and is driven by the seasonal cycle of dissolved inorganic carbon (DIC), i.e. by physical DIC transport and biological processes. In contrast, the dominant driver of the seasonal cycle of CO_2 uptake in the STSS is temperature, and thus the season of peak uptake occurs in winter. Trends in net CO_2 uptake derived from Global Ocean Biogeochemistry Models (GOBMs) and surface ocean pCO_2 observation based products (pCO_2-products) disagree in all biomes, but the discrepancy is strongest in the Pacific sector of the STSS. In terms of anthropogenic CO_2 (C_{ant}), the strongest uptake occurs in the SPSS. This is not visible in the map of net CO_2 flux, because the anthropogenic uptake manifests itself as a suppression of natural CO_2 outgassing. The largest anthropogenic carbon storage occurs in the STSS and northward.

Our analysis confirms the important role of the Southern Ocean in the global carbon cycle. We have highlighted key knowledge gaps that need to be closed through extended observation systems and augmented process descriptions in the dynamic models in order to further reduce uncertainties.

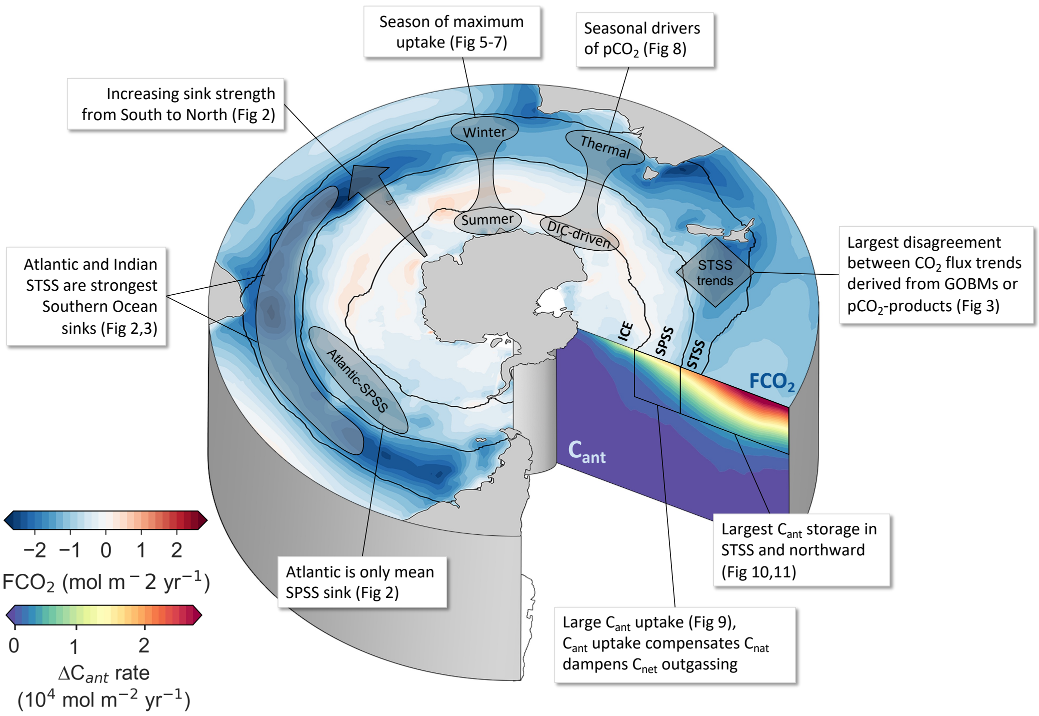

Figure 14. Main characteristics of the Southern Ocean carbon cycle 1985-2018. The surface ocean color shading depicts the net air-sea CO_2 flux (FCO_2) as the average of the ensemble means from pCO_2-products and Global Ocean Biogeochemistry Models (GOBMs). Blue color denotes a CO_2 flux into the ocean, and red color a flux out of the ocean. The zonal mean section shows the anthropogenic carbon (C_{ant}) accumulation in the ocean interior from GOBMs. ICE: ice-covered biome, SPSS: Subpolar Seasonally Stratified Biome, STSS; Subtopical Seasonally Stratified Biome.

Open Research Section

All RECCAP2 data is hosted on https://zenodo.org/. Link will be updated during the review process.

Acknowledgments

Acknowledgments will be added during the review.

References

Armour, K. C., Marshall, J., Scott, J. R., Donohoe, A., & Newsom, E. R. (2016). Southern Ocean warming delayed by circumpolar upwelling and equatorward transport. *Nature Geoscience*, *9*(7), 549–554. doi: 10.1038/ngeo2731

Arndt, S., Janout, M., Biddle, L., Campbell, E., & Thomalla, S. (2022). *The Weddell Sea and Dronning Maud Land (WSDML) Regional Working Group Virtual Science Workshop, 14–16 june 2022* (Tech. Rep.). Zenodo. Retrieved 2023-02-22, from `https://zenodo.org/record/6931424` doi: 10.5281/ZENODO.6931424

Arrigo, K. R., & van Dijken, G. L. (2007). Interannual variation in air-sea CO_2 flux in the Ross Sea, Antarctica: A model analysis. *Journal of Geophysical Research*, *112*(C3), C03020. doi: 10.1029/2006JC003492

Aumont, O., Ethé, C., Tagliabue, A., Bopp, L., & Gehlen, M. (2015). PISCES-v2: An ocean biogeochemical model for carbon and ecosystem studies. *Geoscientific Model Development*, *8*(8), 2465–2513. doi: 10.5194/gmd-8-2465-2015

Aumont, O., Orr, J. C., Monfray, P., Ludwig, W., Amiotte-Suchet, P., & Probst, J. L. (2001). Riverine-driven interhemispheric transport of carbon. *Global Biogeochemical Cycles*, *15*(2), 393–405. doi: 10.1029/1999GB001238

Ayers, J. M., & Strutton, P. G. (2013). Nutrient variability in Subantarctic Mode Waters forced by the Southern Annular Mode and ENSO. *Geophysical Research Letters*, *40*(13), 3419–3423. doi: 10.1002/grl.50638

Bakker, D., Alin, S. R., Becker, M., Bittig, H. C., Castaño-Primo, R., Feely, R. A., … Wilson, D. (2022). *Surface ocean CO_2 atlas database version 2022 (SOCATv2022), NCEI accession 0253659.* NOAA National Centers for Environmental Information. Retrieved from `https://doi.org/10.25921/1h9f-nb73`

Bakker, D., Hoppema, M., Schröder, M., Geibert, W., & Baar, H. J. W. D. (2008). A rapid transition from ice covered CO_2-rich waters to a biologically mediated CO_2 sink in the eastern Weddell Gyre. *Biogeosciences*, *5*, 1373–1386. doi: 10.5194/bg-5-1373-2008

Bakker, D., Pfeil, B., Landa, C. S., Metzl, N., O'Brien, K. M., Olsen, A., … Xu, S. (2016). A multi-decade record of high-quality CO_2 data in version 3 of the Surface Ocean CO_2 Atlas (SOCAT). *Earth System Science Data*, *8*(2), 383–413. doi: 10.5194/essd-8-383-2016

Beadling, R. L., Russell, J. L., Stouffer, R. J., Mazloff, M., Talley, L. D., Goodman, P. J., … Pandde, A. (2020). Representation of Southern Ocean Properties across Coupled Model Intercomparison Project Generations: CMIP3 to CMIP6. *Journal of Climate*, *33*(15), 6555–6581. doi: 10.1175/JCLI-D-19-0970.1

Berthet, S., Séférian, R., Bricaud, C., Chevallier, M., Voldoire, A., & Ethé, C. (2019). Evaluation of an Online Grid-Coarsening Algorithm in a Global Eddy-Admitting Ocean Biogeochemical Model. *Journal of Advances in Modeling Earth Systems*, *11*(6), 1759–1783. doi: 10.1029/2019MS001644

Bopp, L., Lévy, M., Resplandy, L., & Sallée, J. B. (2015). Pathways of anthropogenic carbon subduction in the global ocean. *Geophysical Research Letters*, *42*(15), 6416–6423. Retrieved from `http://doi.wiley.com/10.1002/2015GL065073` doi: 10.1002/2015GL065073

Bourgeois, T., Goris, N., Schwinger, J., & Tjiputra, J. F. (2022). Stratification constrains future heat and carbon uptake in the Southern Ocean between 30°S and 55°S. *Nature Communications*, *13*(1), 340. doi: 10.1038/s41467-022-27979-5

Boyer, T. P., Garcia, H. E., Locarnini, R. A., Zweng, M. M., Mishonov, A. V., Reagan, J. R., … Smolyar, I. V. (2018). *World Ocean Atlas 2018.* NOAA National Centers for Environmental Information. Retrieved from https://www.ncei.noaa.gov/archive/accession/NCEI-WOA18

Brown, M. S., Munro, D. R., Feehan, C. J., Sweeney, C., Ducklow, H. W., & Schofield, O. M. (2019). Enhanced oceanic CO_2 uptake along the rapidly changing West Antarctic Peninsula. *Nature Climate Change*, *9*(9), 678–683. Retrieved from http://dx.doi.org/10.1038/s41558-019-0552-3 doi: 10.1038/s41558-019-0552-3

Buitenhuis, E. T., Le Quéré, C., Bednaršek, N., & Schiebel, R. (2019). Large Contribution of Pteropods to Shallow $CaCO_3$ Export. *Global Biogeochemical Cycles*, *33*(3), 458–468. doi: 10.1029/2018GB006110

Bushinsky, S. M., Takeshita, Y., & Williams, N. L. (2019). Observing Changes in Ocean Carbonate Chemistry: Our Autonomous Future. *Current Climate Change Reports*. doi: 10.1007/s40641-019-00129-8

Caldeira, K., & Duffy, P. B. (2000). The Role of the Southern Ocean in Uptake and Storage of Anthropogenic Carbon Dioxide. *Science*, *287*(5453), 620–622. doi: 10.1126/science.287.5453.620

Campin, J.-m., Hill, C., Jones, H., & Marshall, J. (2011). Super-parameterization in ocean modeling : Application to deep convection. *Ocean Modelling*, *36*(1-2), 90–101. doi: 10.1016/j.ocemod.2010.10.003

Canadell, J., Monteiro, P., Costa, M., Cotrim da Cunha, L., Cox, P., Eliseev, A., … Zickfeld, K. (2021). Global Carbon and other Biogeochemical Cycles and Feedbacks. In V. Masson-Delmotte et al. (Eds.), *Climate Change 2021: The Physical Science Basis. Contribution of Working Group I to the Sixth Assessment Report of the Intergovernmental Panel on Climate Change* (pp. 673–816). Cambridge, United Kingdom: Cambridge University Press. doi: 10.1017/9781009157896.007

Carroll, D., Menemenlis, D., Adkins, J. F., Bowman, K. W., Brix, H., Dutkiewicz, S., … Zhang, H. (2020). The ECCO-Darwin Data-Assimilative Global Ocean Biogeochemistry Model: Estimates of Seasonal to Multidecadal Surface Ocean pCO2 and Air-Sea CO2 Flux. *Journal of Advances in Modeling Earth Systems*, *12*(10), 1–28. doi: 10.1029/2019MS001888

Carroll, D., Menemenlis, D., Dutkiewicz, S., Lauderdale, J. M., Adkins, J. F., Bowman, K. W., … Zhang, H. (2022). Attribution of Space-Time Variability in Global-Ocean Dissolved Inorganic Carbon. *Global Biogeochemical Cycles*, *36*(3), 1–24. doi: 10.1029/2021GB007162

Carter, B. R., Bittig, H. C., Fassbender, A. J., Sharp, J. D., Takeshita, Y., Xu, Y.-Y., … Barbero, L. (2021). New and updated global empirical seawater property estimation routines. *Limnol. Oceanogr.: Methods*, *19*, 785–809. doi: 10.1002/lom3.10461

Carter, B. R., Feely, R. A., Williams, N. L., Dickson, A. G., Fong, M. B., & Takeshita, Y. (2018). Updated methods for global locally interpolated estimation of alkalinity, pH, and nitrate. *Limnology and Oceanography: Methods*, *16*(2), 119–131. Retrieved from http://doi.wiley.com/10.1002/lom3.10232 doi: 10.1002/lom3.10232

Carter, B. R., Williams, N. L., Gray, A. R., & Feely, R. A. (2016). Locally interpolated alkalinity regression for global alkalinity estimation. *Limnology and Oceanography: Methods*, *14*(4), 268–277. doi: 10.1002/lom3.10087

Chau, T. T. T., Gehlen, M., & Chevallier, F. (2022). A seamless ensemble-based reconstruction of surface ocean pCO_2 and air-sea CO_2 fluxes over the global coastal and open oceans. *Biogeosciences*, *19*(4), 1087–1109. doi: 10.5194/bg-19-1087-2022

Chevallier, F., Fisher, M., Peylin, P., Serrar, S., Bousquet, P., Bréon, F. M., ... Ciais, P. (2005). Inferring CO_2 sources and sinks from satellite observations: Method and application to TOVS data. *Journal of Geophysical Research Atmospheres*, *110*(24), 1–13. doi: 10.1029/2005JD006390

Chien, C. T., Durgadoo, J. V., Ehlert, D., Frenger, I., Keller, D. P., Koeve, W., ... Oschlies, A. (2022). FOCI-MOPS v1 - integration of marine biogeochemistry within the Flexible Ocean and Climate Infrastructure version 1 (FOCI 1) Earth system model. *Geoscientific Model Development*, *15*(15), 5987–6024. doi: 10.5194/gmd-15-5987-2022

Clement, D., & Gruber, N. (2018). The eMLR(C*) Method to Determine Decadal Changes in the Global Ocean Storage of Anthropogenic CO_2. *Global Biogeochemical Cycles*. doi: 10.1002/2017GB005819

Crisp, D., Dolman, H., Tanhua, T., McKinley, G. A., Hauck, J., Bastos, A., ... Aich, V. (2022). How Well Do We Understand the Land-Ocean-Atmosphere Carbon Cycle? *Reviews of Geophysics*, *60*(2), 1–64. doi: 10.1029/2021RG000736

Denvil-Sommer, A., Gehlen, M., & Vrac, M. (2021). Observation system simulation experiments in the Atlantic Ocean for enhanced surface ocean pCO_2 reconstructions. *Ocean Science*, *17*(4), 1011–1030. doi: 10.5194/os-17-1011-2021

DeVries, T. (2014). The oceanic anthropogenic CO_2 sink: Storage, air-sea fluxes, and transports over the industrial era. *Global Biogeochemical Cycles*, *28*(7), 631–647. doi: 10.1002/2013GB004739

DeVries, T. (2022). The Ocean Carbon Cycle. *Annual Review of Environment and Resources*, *47*(1). doi: 10.1146/annurev-environ-120920-111307

DeVries, T., Holzer, M., & Primeau, F. (2017). Recent increase in oceanic carbon uptake driven by weaker upper-ocean overturning. *Nature*, *542*(7640), 215–218. doi: 10.1038/nature21068

DeVries, T., Yamamoto, K., Wanninkhof, R., Gruber, N., Hauck, J., Müller, J. D., ... others (2023). Magnitude, trends, and variability of the global ocean carbon sink from 1985-2018. *in review at Global Biogeochemical Cycles*.

Djeutchouang, L. M., Chang, N., Gregor, L., Vichi, M., & Monteiro, P. M. (2022). The sensitivity of pCO_2 reconstructions to sampling scales across a Southern Ocean sub-domain: a semi-idealized ocean sampling simulation approach. *Biogeosciences*, *19*(17), 4171–4195. doi: 10.5194/bg-19-4171-2022

Dlugokencky, E., Thoning, K., Lan, X., Tans, P., & Laboratory, N. G. M. (2021). *NOAA Greenhouse Gas Marine Boundary Layer Reference - CO_2*. NOAA GML. Retrieved from `https://gml.noaa.gov/ccgg/mbl/index.html` doi: https://doi.org/10.15138/DVNP-F961

Doney, S., Lima, I., Moore, J. K., Lindsay, K., Behrenfeld, M. J., Westberry, T. K., ... Takahashi, T. (2009). Skill metrics for confronting global upper ocean ecosystem-biogeochemistry models against field and remote sensing data. *Journal of Marine Systems*, *76*(1-2), 95–112. doi: 10.1016/j.jmarsys.2008.05.015

Doney, S., Yeager, S., Danabasoglu, G., Large, W. G., & McWilliams, J. C. (2007). Mechanisms governing interannual variability of upper-ocean temperature in a global ocean hindcast simulation. *Journal of Physical Oceanography*, *37*(7), 1918–1938. doi: 10.1175/JPO3089.1

Döscher, R., Acosta, M., Alessandri, A., Anthoni, P., Arsouze, T., Bergman, T., ... Zhang, Q. (2022). The EC-Earth3 Earth system model for the Coupled Model Intercomparison Project 6. *Geoscientific Model Development*, *15*(7), 2973–3020. doi: 10.5194/gmd-15-2973-2022

Drucker, R., & Riser, S. C. (2016). In situ phase-domain calibration of oxygen optodes on profiling floats. *Methods in Oceanography*, *17*, 296–318. doi: 10.1016/j.mio.2016.09.007

Ducklow, H. W., Stukel, M. R., Eveleth, R., Doney, S. C., Jickells, T., Schofield, O., … Cassar, N. (2018). Spring-summer net community production, new production, particle export and related water column biogeochemical processes in the marginal sea ice zone of the Western Antarctic Peninsula 2012-2014. *Philosophical Transactions of the Royal Society A: Mathematical, Physical and Engineering Sciences*, *376*(2122). doi: 10.1098/rsta.2017.0177

Dutkiewicz, S., Follows, M. J., & Bragg, J. G. (2009). Modeling the coupling of ocean ecology and biogeochemistry. *Global Biogeochemical Cycles*, *23*(4), 1–15. doi: 10.1029/2008GB003405

Eddebbar, Y. A., Rodgers, K. B., Long, M. C., Subramanian, A. C., Xie, S.-P., & Keeling, R. F. (2019). El Niño–Like Physical and Biogeochemical Ocean Response to Tropical Eruptions. *Journal of Climate*, *32*(9), 2627–2649. doi: 10.1175/JCLI-D-18-0458.1

Eveleth, R., Cassar, N., Doney, S. C., Munro, D. R., & Sweeney, C. (2017). Biological and physical controls on O2/Ar, Ar and pCO2 variability at the Western Antarctic Peninsula and in the Drake Passage. *Deep-Sea Research Part II: Topical Studies in Oceanography*, *139*, 77–88. doi: 10.1016/j.dsr2.2016.05.002

Fay, A. R., Gregor, L., Landschützer, P., McKinley, G. A., Gruber, N., Gehlen, M., … Zeng, J. (2021). SeaFlux: harmonization of air-sea CO_2 fluxes from surface pCO_2 data products using a standardized approach. *Earth System Science Data*, *13*(10), 4693–4710. doi: 10.5194/essd-13-4693-2021

Fay, A. R., & McKinley, G. A. (2014). Global open-ocean biomes: Mean and temporal variability. *Earth System Science Data*, *6*(2), 273–284. doi: 10.5194/essd-6-273-2014

Feng, L., Palmer, P. I., Parker, R. J., Deutscher, N. M., Feist, D. G., Kivi, R., … Sussmann, R. (2016). Estimates of European uptake of CO_2 inferred from GOSAT XCO2 retrievals: Sensitivity to measurement bias inside and outside Europe. *Atmospheric Chemistry and Physics*, *16*(3), 1289–1302. doi: 10.5194/acp-16-1289-2016

Friedlingstein, P., O'Sullivan, M., Jones, M. W., Andrew, R. M., Gregor, L., Hauck, J., … Zheng, B. (2022). Global Carbon Budget 2022. *Earth System Science Data*, *14*(11), 4811–4900. doi: 10.5194/essd-14-4811-2022

Frölicher, T. L., Sarmiento, J. L., Paynter, D. J., Dunne, J. P., Krasting, J. P., & Winton, M. (2015). Dominance of the Southern Ocean in anthropogenic carbon and heat uptake in CMIP5 models. *Journal of Climate*, *28*(2), 862–886. doi: 10.1175/JCLI-D-14-00117.1

Galbraith, E. D., Gnanadesikan, A., Dunne, J. P., & Hiscock, M. R. (2010). Regional impacts of iron-light colimitation in a global biogeochemical model. *Biogeosciences*, *7*(3), 1043–1064. doi: 10.5194/bg-7-1043-2010

Gloege, L., McKinley, G. A., Landschützer, P., Fay, A. R., Frölicher, T. L., Fyfe, J. C., … Takano, Y. (2021). Quantifying Errors in Observationally Based Estimates of Ocean Carbon Sink Variability. *Global Biogeochemical Cycles*, *35*(4), 1–14. doi: 10.1029/2020GB006788

Gloege, L., Yan, M., Zheng, T., & McKinley, G. A. (2022). Improved Quantification of Ocean Carbon Uptake by Using Machine Learning to Merge Global Models and pCO_2 Data. *Journal of Advances in Modeling Earth Systems*, *14*(2), 1–19. doi: 10.1029/2021MS002620

Good, S. A., Martin, M. J., & Rayner, N. A. (2013). EN4: Quality controlled ocean temperature and salinity profiles and monthly objective analyses with uncertainty estimates. *Journal of Geophysical Research: Oceans*, *118*(12), 6704–6716. doi: 10.1002/2013JC009067

Gray, A. R., Johnson, K. S., Bushinsky, S. M., Riser, S. C., Russell, J. L., Talley, L. D., … Sarmiento, J. L. (2018). Autonomous Biogeochemical Floats Detect Significant Carbon Dioxide Outgassing in the High-Latitude Southern Ocean. *Geophysical Research Letters*, *45*(17), 9049–9057. doi:

10.1029/2018GL078013
Gregor, L., & Gruber, N. (2021). OceanSODA-ETHZ: a global gridded data set of the surface ocean carbonate system for seasonal to decadal studies of ocean acidification. *Earth System Science Data*, *13*(2), 777–808. doi: 10.5194/essd-13-777-2021
Gregor, L., Kok, S., & Monteiro, P. M. S. (2017). Empirical methods for the estimation of Southern Ocean CO_2: support vector and random forest regression. *Biogeosciences*, *14*(23), 5551–5569. doi: 10.5194/bg-14-5551-2017
Gregor, L., Lebehot, A. D., Kok, S., & Scheel Monteiro, P. M. (2019). A comparative assessment of the uncertainties of global surface ocean CO_2 estimates using a machine-learning ensemble (CSIR-ML6 version 2019a) - have we hit the wall? *Geoscientific Model Development*, *12*(12), 5113–5136. doi: 10.5194/gmd-12-5113-2019
Gruber, N., Bakker, D. C. E., DeVries, T., Gregor, L., Hauck, J., Landschützer, P., ... Müller, J. D. (2023). Trends and variability in the ocean carbon sink. *Nature Reviews Earth & Environment*, *4*(2), 119–134. Retrieved from `https://doi.org/10.1038/s43017-022-00381-x` doi: 10.1038/s43017-022-00381-x
Gruber, N., Clement, D., Carter, B. R., Feely, R. A., van Heuven, S., Hoppema, M., ... Wanninkhof, R. (2019). The oceanic sink for anthropogenic co2 from 1994 to 2007. *Science*, *363*(6432), 1193-1199. Retrieved from `https://www.science.org/doi/abs/10.1126/science.aau5153` doi: 10.1126/science.aau5153
Gruber, N., Gloor, M., Mikaloff Fletcher, S. E., Doney, S. C., Dutkiewicz, S., Follows, M. J., ... Takahashi, T. (2009). Oceanic sources, sinks, and transport of atmospheric CO $_2$. *Global Biogeochemical Cycles*, *23*(1), n/a–n/a. doi: 10.1029/2008GB003349
Gruber, N., Landschützer, P., & Lovenduski, N. S. (2019). The Variable Southern Ocean Carbon Sink. *Annual Review of Marine Science*, *11*(1), 159–186. doi: 10.1146/annurev-marine-121916-063407
Gruber, N., Sarmiento, J. L., & Stocker, T. F. (1996). An improved method for detecting anthropogenic CO2 in the oceans. *Global Biogeochemical Cycles*, *10*(4), 809–837. Retrieved from `http://doi.wiley.com/10.1029/96GB01608` doi: 10.1029/96GB01608
Hauck, J., Nissen, C., Landschützer, P., Rödenbeck, C., Bushinsky, S., & Olsen, A. (2023). Sparse observations induce large biases in estimates of the global ocean CO2 sink: an ocean model subsampling experiment. *Philosophical Transactions of the Royal Society A: Mathematical, Physical and Engineering Sciences*, *381*(2249). Retrieved from `https://royalsocietypublishing.org/doi/10.1098/rsta.2022.0063` doi: 10.1098/rsta.2022.0063
Hauck, J., Völker, C., Wang, T., Hoppema, M., Losch, M., & Wolf-Gladrow, D. A. (2013). Seasonally different carbon flux changes in the Southern Ocean in response to the southern annular mode. *Global Biogeochemical Cycles*, *27*(4), 1236–1245. doi: 10.1002/2013GB004600
Hauck, J., Völker, C., Wolf-Gladrow, D. A., Laufkötter, C., Vogt, M., Aumont, O., ... Totterdell, I. (2015). On the Southern Ocean CO_2 uptake and the role of the biological carbon pump in the 21st century. *Global Biogeochemical Cycles*, *29*(9), 1451–1470. doi: 10.1002/2015GB005140
Hauck, J., Zeising, M., Le Quéré, C., Gruber, N., Bakker, D. C. E., Bopp, L., ... Séférian, R. (2020). Consistency and Challenges in the Ocean Carbon Sink Estimate for the Global Carbon Budget. *Frontiers in Marine Science*, *7*, 571720. doi: 10.3389/fmars.2020.571720
Haumann, A. (2016). *Southern ocean response to recent changes in surface freshwater fluxes* (Doctoral dissertation). doi: 10.3929/ETHZ-B-000166276
Haumann, F., Gruber, N., & Münnich, M. (2020). Sea-Ice Induced Southern Ocean

Subsurface Warming and Surface Cooling in a Warming Climate. *AGU Advances*, *1*(2). doi: 10.1029/2019av000132

Hauri, C., Doney, S. C., Takahashi, T., Erickson, M., Jiang, G., & Ducklow, H. (2015). Two decades of inorganic carbon dynamics along the West Antarctic Peninsula. *Biogeosciences*, *12*(22), 6761–6779. doi: 10.5194/bg-12-6761-2015

Holzer, M., & DeVries, T. (2022). Source-Labeled Anthropogenic Carbon Reveals a Large Shift of Preindustrial Carbon From the Ocean to the Atmosphere. *Global Biogeochemical Cycles*, *36*(10). doi: 10.1029/2022GB007405

Hoppema, M. (2004). Weddell Sea turned from source to sink for atmospheric CO_2 between pre-industrial time and present. *Global and Planetary Change*, *40*(3-4), 219–231. doi: 10.1016/j.gloplacha.2003.08.001

Hoppema, M., Bakker, K., van Heuven, S. M., van Ooijen, J. C., & de Baar, H. J. (2015). Distributions, trends and inter-annual variability of nutrients along a repeat section through the Weddell Sea (1996-2011). *Marine Chemistry*, *177*, 545–553. doi: 10.1016/j.marchem.2015.08.007

Hoppema, M., Fahrbach, E., Stoll, M. H., & de Baar, H. J. (1998). Increase of carbon dioxide in the bottom water of the Weddell Sea, Antarctica. *Marine Chemistry*, *59*(3-4), 201–210. doi: 10.1016/S0304-4203(97)00094-7

Huang, B., Thorne, P. W., Banzon, V. F., Boyer, T. P., Chepurin, G., Lawrimore, J. H., … Zhang, H.-M. (2017). *NOAA Extended Reconstructed Sea Surface Temperature (ERSST), Version 5.* NOAA National Centers for Environmental Information. doi: 10.7289/V5T72FNM

Iida, T., Odate, T., & Fukuchi, M. (2013). Long-Term Trends of Nutrients and Apparent Oxygen Utilization South of the Polar Front in Southern Ocean Intermediate Water from 1965 to 2008. *PLoS ONE*, *8*(8), e71766. doi: 10.1371/journal.pone.0071766

Iida, Y., Takatani, Y., Kojima, A., & Ishii, M. (2021). Global trends of ocean CO_2 sink and ocean acidification: an observation-based reconstruction of surface ocean inorganic carbon variables. *Journal of Oceanography*, *77*(2), 323–358. doi: 10.1007/s10872-020-00571-5

Ilyina, T., Six, K. D., Segschneider, J., Maier-Reimer, E., Li, H., & Núñez-Riboni, I. (2013). Global ocean biogeochemistry model HAMOCC: Model architecture and performance as component of the MPI-Earth system model in different CMIP5 experimental realizations. *Journal of Advances in Modeling Earth Systems*, *5*(2), 287–315. doi: 10.1029/2012MS000178

Ito, T., Woloszyn, M., & Mazloff, M. (2010). Anthropogenic carbon dioxide transport in the Southern Ocean driven by Ekman flow. *Nature*, *463*(7277), 80–83. doi: 10.1038/nature08687

Iudicone, D., Rodgers, K. B., Plancherel, Y., Aumont, O., Ito, T., Key, R. M., … Ishii, M. (2016). The formation of the ocean's anthropogenic carbon reservoir. *Scientific Reports*, *6*(1), 35473. doi: 10.1038/srep35473

Jacobs, S. S. (2004). Bottom water production and its links with the thermohaline circulation. *Antarctic Science*, *16*(4), 427–437. doi: 10.1017/S095410200400224X

Johnson, K. S., Plant, J. N., Coletti, L. J., Jannasch, H. W., Sakamoto, C. M., Riser, S. C., … Sarmiento, J. L. (2017). Biogeochemical sensor performance in the SOCCOM profiling float array. *Journal of Geophysical Research: Oceans*, *122*(8), 6416–6436. doi: 10.1002/2017JC012838

Jones, D. C., Meijers, A. J. S., Shuckburgh, E., Sallée, J.-B., Haynes, P., McAufield, E. K., & Mazloff, M. R. (2016). How does Subantarctic Mode Water ventilate the Southern Hemisphere subtropics? *Journal of Geophysical Research: Oceans*, *121*(9), 6558–6582. doi: 10.1002/2016JC011680

Jones, E., Bakker, D. C., Venables, H. J., & Hardman-Mountford, N. J. (2015). Seasonal cycle of CO_2 from the sea ice edge to island blooms in the Scotia Sea, Southern Ocean. *Marine Chemistry*, *177*, 490–500. doi: 10.1016/

j.marchem.2015.06.031
Jones, E., Bakker, D. C., Venables, H. J., & Watson, A. J. (2012). Dynamic seasonal cycling of inorganic carbon downstream of South Georgia, Southern Ocean. *Deep Sea Research Part II: Topical Studies in Oceanography*, *59-60*, 25–35. doi: 10.1016/j.dsr2.2011.08.001
Katavouta, A., & Williams, R. G. (2021). Ocean carbon cycle feedbacks in CMIP6 models: contributions from different basins. *Biogeosciences*, *18*(10), 3189–3218. doi: 10.5194/bg-18-3189-2021
Keppler, L., & Landschützer, P. (2019). Regional Wind Variability Modulates the Southern Ocean Carbon Sink. *Scientific Reports*, *9*(1), 7384. doi: 10.1038/s41598-019-43826-y
Kessler, A., & Tjiputra, J. (2016). The Southern Ocean as a constraint to reduce uncertainty in future ocean carbon sinks. *Earth System Dynamics*, *7*(2), 295–312. doi: 10.5194/esd-7-295-2016
Khatiwala, S., Primeau, F., & Hall, T. (2009). Reconstruction of the history of anthropogenic CO_2 concentrations in the ocean. *Nature*, *462*(7271), 346–349. doi: 10.1038/nature08526
Klatt, O., Fahrbach, E., Hoppema, M., & Rohardt, G. (2005). The transport of the weddell gyre across the prime meridian. *Deep Sea Research Part II: Topical Studies in Oceanography*, *52*(3), 513-528. Retrieved from `https://www.sciencedirect.com/science/article/pii/S0967064504003066` (Direct observations of oceanic flow: A tribute to Walter Zenk) doi: https://doi.org/10.1016/j.dsr2.2004.12.015
Kriest, I., & Oschlies, A. (2015). MOPS-1.0: Towards a model for the regulation of the global oceanic nitrogen budget by marine biogeochemical processes. *Geoscientific Model Development*, *8*(9), 2929–2957. doi: 10.5194/gmd-8-2929-2015
Lacroix, F., Ilyina, T., & Hartmann, J. (2020). Oceanic CO_2 outgassing and biological production hotspots induced by pre-industrial river loads of nutrients and carbon in a global modeling approach. *Biogeosciences*, *17*(1), 55–88. doi: 10.5194/bg-17-55-2020
Landschützer, P., Gruber, N., & Bakker, D. C. (2016). Decadal variations and trends of the global ocean carbon sink. *Global Biogeochemical Cycles*, *30*(10), 1396–1417. doi: 10.1002/2015GB005359
Landschützer, P., Gruber, N., & Bakker, D. C. E. (2020). *An observation-based global monthly gridded sea surface pCO_2 product from 1982 onward and its monthly climatology (NCEI Accession 0160558)* (Tech. Rep.). Retrieved from `https://www.ncei.noaa.gov/access/ocean-carbon-acidification-data-system/oceans/SPCO2{\_}1982{\_}present{\_}ETH{\_}SOM{\_}FFN.html`
Landschützer, P., Gruber, N., Bakker, D. C. E., & Schuster, U. (2014). Recent variability of the global ocean carbon sink. *Global Biogeochemical Cycles*, *28*(9), 927–949. doi: 10.1002/2014GB004853
Landschützer, P., Gruber, N., Haumann, F. A., Rödenbeck, C., Bakker, D. C. E., van Heuven, S., ... Wanninkhof, R. (2015). The reinvigoration of the Southern Ocean carbon sink. *Science*, *349*(6253), 1221–1224. doi: 10.1126/science.aab2620
Langlais, C. E., Lenton, A., Matear, R., Monselesan, D., Legresy, B., Cougnon, E., & Rintoul, S. (2017). Stationary Rossby waves dominate subduction of anthropogenic carbon in the Southern Ocean. *Scientific Reports*, *7*(1), 17076. doi: 10.1038/s41598-017-17292-3
Large, W. G., McWilliams, J. C., & Doney, S. C. (1994). Oceanic Vertical Mixing - a Review and a Model with a Nonlocal Boundary-Layer Parameterization. *Reviews of Geophysics*, *32*(94), 363–403. doi: 10.1029/94rg01872
Lauderdale, J. M., Dutkiewicz, S., Williams, R. G., & Follows, M. J. (2016). Quantifying the drivers of ocean-atmosphere CO_2 fluxes. *Global Biogeochemical Cy-*

cles, *30*(7), 983–999. doi: 10.1002/2016GB005400
Le Quéré, C., Andrew, R. M., Friedlingstein, P., Sitch, S., Hauck, J., Pongratz, J., … Zheng, B. (2018). Global Carbon Budget 2018. *Earth System Science Data*, *10*(4), 2141–2194. doi: 10.5194/essd-10-2141-2018
Le Quéré, C., Buitenhuis, E. T., Moriarty, R., Alvain, S., Aumont, O., Bopp, L., … Vallina, S. M. (2016). Role of zooplankton dynamics for Southern Ocean phytoplankton biomass and global biogeochemical cycles. *Biogeosciences*, *13*(14), 4111–4133. doi: 10.5194/bg-13-4111-2016
Le Quéré, C., Takahashi, T. T., Buitenhuis, E. T., Rödenbeck, C., & Sutherland, S. C. (2010). Impact of climate change and variability on the global oceanic sink of CO_2. *Global Biogeochemical Cycles*, *24*(4), 1–10. doi: 10.1029/2009GB003599
Lenton, A., & Matear, R. J. (2007). Role of the Southern Annular Mode (SAM) in Southern Ocean CO2 uptake. *Global Biogeochemical Cycles*, *21*(2), 1–17. doi: 10.1029/2006GB002714
Lenton, A., Tilbrook, B., Law, R. M., Bakker, D., Doney, S. C., Gruber, N., … Takahashi, T. (2013). Sea-air CO_2 fluxes in the Southern Ocean for the period 1990-2009. *Biogeosciences*, *10*(6), 4037–4054. doi: 10.5194/bg-10-4037-2013
Le Quéré, C., Rödenbeck, C., Buitenhuis, E. T., Conway, T. J., Langenfelds, R., Gomez, A., … Heimann, M. (2007). Saturation of the Southern Ocean CO_2 Sink Due to Recent Climate Change. *Science*, *316*, 1735–1738. doi: 10.1126/science.1136188
Liao, E., Resplandy, L., Liu, J., & Bowman, K. W. (2020). Amplification of the Ocean Carbon Sink During El Niños: Role of Poleward Ekman Transport and Influence on Atmospheric CO_2. *Global Biogeochemical Cycles*, *34*(9), 1–23. doi: 10.1029/2020GB006574
Lindsay, K., Bonan, G. B., Doney, S. C., Hoffman, F. M., Lawrence, D. M., Long, M. C., … Thornton, P. E. (2014). Preindustrial-control and twentieth-century carbon cycle experiments with the Earth system model CESM1(BGC). *Journal of Climate*, *27*(24), 8981–9005. doi: 10.1175/JCLI-D-12-00565.1
Liu, J., Baskaran, L., Bowman, K., Schimel, D., Anthony Bloom, A., Parazoo, C. N., … Wofsy, S. (2021). Carbon Monitoring System Flux Net Biosphere Exchange 2020 (CMS-Flux NBE 2020). *Earth System Science Data*, *13*(2), 299–330. doi: 10.5194/essd-13-299-2021
Long, M. C., Stephens, B. B., McKain, K., Sweeney, C., Keeling, R. F., Kort, E. A., … Wofsy, S. C. (2021). Strong Southern Ocean carbon uptake evident in airborne observations. *Science*, *374*(6572), 1275–1280. doi: 10.1126/science.abi4355
Lovenduski, N. S., Gruber, N., Doney, S. C., & Lima, I. D. (2007). Enhanced CO_2 outgassing in the Southern Ocean from a positive phase of the Southern Annular Mode. *Global Biogeochemical Cycles*, *21*(2), n/a–n/a. doi: 10.1029/2006GB002900
Madec, G., & the NEMO team. (2016). *NEMO reference manual 3_6_STABLE: "NEMO ocean engine" Note du Pôle de modélisation.* Paris, France: Institut Pierre-Simon Laplace (IPSL).
Marshall, J., & Speer, K. (2012). Closure of the meridional overturning circulation through Southern Ocean upwelling. *Nature Geoscience*, *5*(3), 171–180. doi: 10.1038/ngeo1391
Matsumoto, K., & Gruber, N. (2005). How accurate is the estimation of anthropogenic carbon in the ocean? An evaluation of the Δ C * method. *Global Biogeochemical Cycles*, *19*(3). Retrieved from `http://doi.wiley.com/10.1029/2004GB002397` doi: 10.1029/2004GB002397
Mauritsen, T., Bader, J., Becker, T., Behrens, J., Bittner, M., Brokopf, R., … Roeckner, E. (2019). Developments in the MPI-M Earth System Model version 1.2 (MPI-ESM1.2) and Its Response to Increasing CO_2. *Journal of Advances*

in Modeling Earth Systems, *11*(4), 998–1038. doi: 10.1029/2018MS001400

Mayot, N., Le Quéré, C., Rödenbeck, C., Bernardello, R., Bopp, L., Djeutchouang, L. M., … Zeng, J. (2023). Climate-driven variability of the Southern Ocean CO 2 sink. *Philosophical Transactions of the Royal Society A: Mathematical, Physical and Engineering Sciences*, *381*(2249). Retrieved from `https://royalsocietypublishing.org/doi/10.1098/rsta.2022.0055` doi: 10.1098/rsta.2022.0055

McKinley, G. A., Fay, A. R., Eddebbar, Y. A., Gloege, L., & Lovenduski, N. S. (2020). External Forcing Explains Recent Decadal Variability of the Ocean Carbon Sink. *AGU Advances*, *1*(2). doi: 10.1029/2019AV000149

McNeil, B. I., & Matear, R. J. (2013). The non-steady state oceanic CO_2 signal: Its importance, magnitude and a novel way to detect it. *Biogeosciences*, *10*(4), 2219–2228. doi: 10.5194/bg-10-2219-2013

Metzl, N., Brunet, C., Jabaud-Jan, A., Poisson, A., & Schauer, B. (2006). Summer and winter air-sea CO_2 fluxes in the Southern Ocean. *Deep-Sea Research Part I: Oceanographic Research Papers*, *53*(9), 1548–1563. doi: 10.1016/j.dsr.2006.07.006

Metzl, N., Tilbrook, B., & Poisson, A. (1999). The annual fCO_2 cycle and the air-sea CO_2 flux in the sub-Antarctic Ocean. *Tellus B: Chemical and Physical Meteorology*, *51*(4), 849. doi: 10.3402/tellusb.v51i4.16495

Mikaloff Fletcher, S. E., Gruber, N., Jacobson, A. R., Doney, S. C., Dutkiewicz, S., Gerber, M., … Sarmiento, J. L. (2006). Inverse estimates of anthropogenic CO $_2$ uptake, transport, and storage by the ocean. *Global Biogeochemical Cycles*, *20*(2). doi: 10.1029/2005GB002530

Mikaloff Fletcher, S. E., Gruber, N., Jacobson, A. R., Gloor, M., Doney, S. C., Dutkiewicz, S., … Sarmiento, J. L. (2007). Inverse estimates of the oceanic sources and sinks of natural CO_2 and the implied oceanic carbon transport. *Global Biogeochemical Cycles*, *21*(1). doi: 10.1029/2006GB002751

Mongwe, N. P., Chang, N., & Monteiro, P. M. S. (2016). The seasonal cycle as a mode to diagnose biases in modelled CO_2 fluxes in the Southern Ocean. *Ocean Modelling*, *106*, 90–103. doi: 10.1016/j.ocemod.2016.09.006

Mongwe, N. P., Vichi, M., & Monteiro, P. M. S. (2018). The seasonal cycle of pCO_2 and CO_2 fluxes in the Southern Ocean: diagnosing anomalies in CMIP5 Earth system models. *Biogeosciences*, *15*(9), 2851–2872. doi: 10.5194/bg-15-2851-2018

Morrison, A. K., Waugh, D. W., Hogg, A. M., Jones, D. C., & Abernathey, R. P. (2022). Ventilation of the Southern Ocean Pycnocline. *Annual Review of Marine Science*, *14*(1), 405–430. doi: 10.1146/annurev-marine-010419-011012

Murnane, R. J., Sarmiento, J. L., & Le Quéré, C. (1999). Spatial distribution of air-sea CO_2 fluxes and the interhemispheric transport of carbon by the oceans. *Global Biogeochemical Cycles*, *13*(2), 287–305. doi: 10.1029/1998GB900009

Nevison, C. D., Munro, D. R., Lovenduski, N. S., Keeling, R. F., Manizza, M., Morgan, E. J., & Rödenbeck, C. (2020). Southern Annular Mode Influence on Wintertime Ventilation of the Southern Ocean Detected in Atmospheric O_2 and CO_2 Measurements. *Geophysical Research Letters*, *47*(4), 1–9. doi: 10.1029/2019GL085667

Nicholson, S. A., Whitt, D. B., Fer, I., du Plessis, M. D., Lebéhot, A. D., Swart, S., … Monteiro, P. M. (2022). Storms drive outgassing of CO_2 in the subpolar Southern Ocean. *Nature Communications*, *13*(1), 1–12. doi: 10.1038/s41467-021-27780-w

Nissen, C., Vogt, M., Münnich, M., Gruber, N., & Alexander Haumann, F. (2018). Factors controlling coccolithophore biogeography in the Southern Ocean. *Biogeosciences*, *15*(22), 6997–7024. doi: 10.5194/bg-15-6997-2018

Niwa, Y., Fujii, Y., Sawa, Y., Iida, Y., Ito, A., Satoh, M., … Saigusa, N. (2017). A 4D-Var inversion system based on the icosahedral grid model (NICAM-TM

4D-Var v1.0) - Part 2: Optimization scheme and identical twin experiment of atmospheric CO2 inversion. *Geoscientific Model Development*, *10*(6), 2201–2219. doi: 10.5194/gmd-10-2201-2017

Olsen, A., Key, R. M., van Heuven, S., Lauvset, S. K., Velo, A., Lin, X., ... Suzuki, T. (2016). The Global Ocean Data Analysis Project version 2 (GLODAPv2) - an internally consistent data product for the world ocean. *Earth System Science Data*, *8*(2), 297–323. doi: 10.5194/essd-8-297-2016

Orr, J. C., Maier-Reimer, E., Mikolajewicz, U., Monfray, P., Sarmiento, J. L., Toggweiler, J. R., ... Boutin, J. (2001). Estimates of anthropogenic carbon uptake from four three-dimensional global ocean models. *Global Biogeochemical Cycles*, *15*(1), 43–60. Retrieved from `http://doi.wiley.com/10.1029/2000GB001273` doi: 10.1029/2000GB001273

Orsi, A., Johnson, G., & Bullister, J. (1999). Circulation, mixing, and production of Antarctic Bottom Water. *Progress in Oceanography*, *43*(1), 55–109. doi: 10.1016/S0079-6611(99)00004-X

Panassa, E., Santana-Casiano, J. M., González-Dávila, M., Hoppema, M., van Heuven, S. M., Völker, C., ... Hauck, J. (2018). Variability of nutrients and carbon dioxide in the Antarctic Intermediate Water between 1990 and 2014. *Ocean Dynamics*, *68*(3), 295–308. doi: 10.1007/s10236-018-1131-2

Pardo, P. C., Tilbrook, B., Langlais, C., Trull, T. W., & Rintoul, S. R. (2017). Carbon uptake and biogeochemical change in the Southern Ocean, south of Tasmania. *Biogeosciences*, *14*(22), 5217–5237. doi: 10.5194/bg-14-5217-2017

Paulsen, H., Ilyina, T., Six, K. D., & Stemmler, I. (2017). Incorporating a prognostic representation of marine nitrogen fixers into the global ocean biogeochemical model HAMOCC. *Journal of Advances in Modeling Earth Systems*, *9*, 438–464. doi: 10.1002/2016MS000737.Received

Prend, C. J., Keerthi, M. G., Lévy, M., Aumont, O., Gille, S. T., & Talley, L. D. (2022). Sub-Seasonal Forcing Drives Year-To-Year Variations of Southern Ocean Primary Productivity. *Global Biogeochemical Cycles*, *36*(7), 1–15. doi: 10.1029/2022GB007329

Regnier, P. A., Resplandy, L., Najjar, R. G., & Ciais, P. (2022). The land-to-ocean loops of the global carbon cycle. *Nature 2022 603:7901*, *603*(7901), 401–410. doi: 10.1038/s41586-021-04339-9

Rintoul, S. R. (2018). The global influence of localized dynamics in the Southern Ocean. *Nature*, *558*(7709), 209–218. doi: 10.1038/s41586-018-0182-3

Riser, S. C., Swift, D., & Drucker, R. (2018). Profiling Floats in SOCCOM: Technical Capabilities for Studying the Southern Ocean. *Journal of Geophysical Research: Oceans*, *123*(6), 4055–4073. doi: 10.1002/2017JC013419

Ritter, R., Landschützer, P., Gruber, N., Fay, A. R., Iida, Y., Jones, S. D., ... Zeng, J. (2017). Observation-Based Trends of the Southern Ocean Carbon Sink. *Geophysical Research Letters*, *44*(24), 12,339–12,348. doi: 10.1002/2017GL074837

Rödenbeck, C., Bakker, D. C., Gruber, N., Iida, Y., Jacobson, A. R., Jones, S. D., ... Zeng, J. (2015). Data-based estimates of the ocean carbon sink variability - First results of the Surface Ocean pCO2 Mapping intercomparison (SOCOM). *Biogeosciences*, *12*(23), 7251–7278. doi: 10.5194/bg-12-7251-2015

Rödenbeck, C., Bakker, D. C., Metzl, N., Olsen, A., Sabine, C. L., Cassar, N., ... Heimann, M. (2014). Interannual sea–air CO_2 flux variability from an observation-driven ocean mixed-layer scheme. *Biogeosciences*, *11*(17), 4599–4613. doi: 10.5194/bg-11-4599-2014

Rödenbeck, C., Devries, T., Hauck, J., Le Quéré, C., & Keeling, R. F. (2022). Data-based estimates of interannual sea-air CO_2 flux variations 1957-2020 and their relation to environmental drivers. *Biogeosciences*, *19*(10), 2627–2652. doi: 10.5194/bg-19-2627-2022

Rödenbeck, C., Keeling, R. F., Bakker, D. C., Metzl, N., Olsen, A., Sabine, C. L., & Heimann, M. (2013). Global surface-ocean pCO_2 and sea-Air CO_2 flux variability from an observation-driven ocean mixed-layer scheme. *Ocean Science*, *9*(2), 193–216. doi: 10.5194/os-9-193-2013

Rödenbeck, C., Zaehle, S., Keeling, R., & Heimann, M. (2018). How does the terrestrial carbon exchange respond to inter-Annual climatic variations? A quantification based on atmospheric CO_2 data. *Biogeosciences*, *15*(8), 2481–2498. doi: 10.5194/bg-15-2481-2018

Russell, J. L., Dixon, K. W., Gnanadesikan, A., Stouffer, R. J., & Toggweiler, J. R. (2006). The Southern Hemisphere Westerlies in a Warming World: Propping Open the Door to the Deep Ocean. *Journal of Climate*, *19*(24), 6382–6390. doi: 10.1175/JCLI3984.1

Sabine, C. L., Feely, R. A., Gruber, N., Key, R. M., Lee, K., Bullister, J. L., ... Rios, A. F. (2004). The Oceanic Sink for Anthropogenic CO_2. *Science*, *305*(5682), 367–371. doi: 10.1126/science.1097403

Sabine, C. L., Hankin, S., Koyuk, H., Bakker, D. C., Pfeil, B., Olsen, A., ... Yoshikawa-Inoue, H. (2013). Surface Ocean CO_2 Atlas (SOCAT) gridded data products. *Earth System Science Data*, *5*(1), 145–153. doi: 10.5194/essd-5-145-2013

Sallée, J.-B., Speer, K., & Rintoul, S. R. (2010). Zonally asymmetric response of the Southern Ocean mixed-layer depth to the Southern Annular Mode. *Nature Geoscience*, *3*(4), 273–279. doi: 10.1038/ngeo812

Sallée, J.-B., Matear, R. J., Rintoul, S. R., & Lenton, A. (2012). Localized subduction of anthropogenic carbon dioxide in the Southern Hemisphere oceans. *Nature Geoscience*, *5*(8), 579–584. doi: 10.1038/ngeo1523

Sarmiento, J. L., & Gruber, N. (2006). *Ocean Biogeochemical Dynamics.* Princeton, NJ: Princeton University Press.

Sarmiento, J. L., Orr, J. C., & Siegenthaler, U. (1992). A perturbation simulation of CO 2 uptake in an ocean general circulation model. *Journal of Geophysical Research*, *97*(C3), 3621. Retrieved from `http://doi.wiley.com/10.1029/91JC02849` doi: 10.1029/91JC02849

Schourup-Kristensen, V., Sidorenko, D., Wolf-Gladrow, D. A., & Völker, C. (2014). A skill assessment of the biogeochemical model REcoM2 coupled to the finite element sea ice-ocean model (FESOM 1.3). *Geoscientific Model Development*, *7*(6), 2769–2802. doi: 10.5194/gmd-7-2769-2014

Schourup-Kristensen, V., Wekerle, C., Wolf-Gladrow, D. A., & Völker, C. (2018). Arctic Ocean biogeochemistry in the high resolution FESOM1.4-REcoM2 model. *Progress in Oceanography*, *168*(August), 65–81. doi: 10.1016/j.pocean.2018.09.006

Schultz, C., Doney, S. C., Hauck, J., Kavanaugh, M. T., & Schofield, O. (2021). Modeling Phytoplankton Blooms and Inorganic Carbon Responses to Sea-Ice Variability in the West Antarctic Peninsula. *Journal of Geophysical Research: Biogeosciences*, *126*(4), 1–21. doi: 10.1029/2020JG006227

Schwinger, J., Goris, N., Tjiputra, J. F., Kriest, I., Bentsen, M., Bethke, I., ... Heinze, C. (2016). Evaluation of NorESM-OC (versions 1 and 1.2), the ocean carbon-cycle stand-alone configuration of the Norwegian Earth System Model (NorESM1). *Geoscientific Model Development*, *9*(8), 2589–2622. doi: 10.5194/gmd-9-2589-2016

Séférian, R., Berthet, S., Yool, A., Palmiéri, J., Bopp, L., Tagliabue, A., ... Yamamoto, A. (2020). Tracking Improvement in Simulated Marine Biogeochemistry Between CMIP5 and CMIP6. *Current Climate Change Reports*, *6*(3), 95–119. doi: 10.1007/s40641-020-00160-0

Séférian, R., Gehlen, M., Bopp, L., Resplandy, L., Orr, J. C., Marti, O., ... Romanou, A. (2016). Inconsistent strategies to spin up models in CMIP5: Implications for ocean biogeochemical model performance assessment. *Geoscientific Model Development*, *9*(5), 1827–1851. doi: 10.5194/gmd-9-1827-2016

Séférian, R., Nabat, P., Michou, M., Saint-Martin, D., Voldoire, A., Colin, J., ...

Madec, G. (2019). Evaluation of CNRM Earth System Model, CNRM-ESM2-1: Role of Earth System Processes in Present-Day and Future Climate. *Journal of Advances in Modeling Earth Systems*, *11*(12), 4182–4227. doi: 10.1029/2019MS001791

Shadwick, E. H., De Meo, O. A., Schroeter, S., Arroyo, M. C., Martinson, D. G., & Ducklow, H. (2021). Sea Ice Suppression of CO_2 Outgassing in the West Antarctic Peninsula: Implications For The Evolving Southern Ocean Carbon Sink. *Geophysical Research Letters*, *48*(11), 1–10. doi: 10.1029/2020GL091835

Smith, W., Rivaro, P., Wang, Z., Larue, M., Heywood, K., Park, J., ... Kim, M. (2021). *Observational Activities in the Ross Sea: Current and Future National Contributions to SOOS - An Update* (Tech. Rep.). Retrieved 2023-02-22, from `https://zenodo.org/record/5762638` doi: 10.5281/ZENODO.5762638

Stammer, D., Wunsch, C., Giering, R., Eckert, C., Heimbach, P., Marotzke, J., ... Marshall, J. (2002). Global ocean circulation during 1992-1997, estimated from ocean observations and a general circulation model. *Journal of Geophysical Research: Oceans*, *107*(9). doi: 10.1029/2001jc000888

Stephens, B. B., Keeling, R. F., Heimann, M., Six, K. D., Murnane, R., & Caldeira, K. (1998). Testing global ocean carbon cycle models using measurements of atmospheric O_2 and CO_2 concentration. *Global Biogeochemical Cycles*, *12*(2), 213–230. doi: 10.1029/97GB03500

Stock, C. A., Dunne, J. P., Fan, S., Ginoux, P., John, J., Krasting, J. P., ... Zadeh, N. (2020). Ocean Biogeochemistry in GFDL's Earth System Model 4.1 and Its Response to Increasing Atmospheric CO2. *Journal of Advances in Modeling Earth Systems*, *12*(10). doi: 10.1029/2019MS002043

Sutton, A. J., Williams, N. L., & Tilbrook, B. (2021). Constraining Southern Ocean CO_2 Flux Uncertainty Using Uncrewed Surface Vehicle Observations. *Geophysical Research Letters*, *48*(3), 1–9. doi: 10.1029/2020GL091748

Takahashi, T., Olafsson, J., Goddard, J. G., Chipman, D. W., & Sutherland, S. C. (1993). Seasonal variation of CO_2 and nutrients in the high-latitude surface oceans: A comparative study. *Global Biogeochemical Cycles*, *7*(4), 843–878. doi: 10.1029/93GB02263

Takahashi, T., Sutherland, S. C., Sweeney, C., Poisson, A., Metzl, N., Tilbrook, B., ... Nojiri, Y. (2002). Global sea-air CO_2 flux based on climatological surface ocean pCO_2, and seasonal biological and temperature effects. *Deep-Sea Research Part II: Topical Studies in Oceanography*, *49*(9-10), 1601–1622. doi: 10.1016/S0967-0645(02)00003-6

Takahashi, T., Sutherland, S. C., Wanninkhof, R., Sweeney, C., Feely, R. A., Chipman, D. W., ... de Baar, H. J. (2009). Climatological mean and decadal change in surface ocean pCO_2, and net sea-air CO_2 flux over the global oceans. *Deep Sea Research Part II: Topical Studies in Oceanography*, *56*(8-10), 554–577. doi: 10.1016/j.dsr2.2008.12.009

Talley, L. (2013). Closure of the Global Overturning Circulation Through the Indian, Pacific, and Southern Oceans: Schematics and Transports. *Oceanography*, *26*(1), 80–97. doi: 10.5670/oceanog.2013.07

Talley, L., Feely, R., Sloyan, B., Wanninkhof, R., Baringer, M., Bullister, J., ... Zhang, J.-Z. (2016). Changes in Ocean Heat, Carbon Content, and Ventilation: A Review of the First Decade of GO-SHIP Global Repeat Hydrography. *Annual Review of Marine Science*, *8*(1), 185–215. doi: 10.1146/annurev-marine-052915-100829

Tamsitt, V., Talley, L. D., Mazloff, M. R., Cerovecki, I., Cerovečki, I., Tamsitt, V., ... Cerovečki, I. (2016). Zonal variations in the Southern Ocean heat budget. *Journal of Climate*, *29*(18), 6563–6579. doi: 10.1175/JCLI-D-15-0630.1

Terhaar, J., Frölicher, T. L., & Joos, F. (2021). Southern Ocean anthropogenic carbon sink constrained by sea surface salinity. *Science Advances*, *7*(18), eabd5964. doi: 10.1126/sciadv.abd5964

Terhaar, J., Frölicher, T. L., & Joos, F. (2022). Observation-constrained estimates of the global ocean carbon sink from Earth system models. *Biogeosciences*, *19*(18), 4431–4457. doi: 10.5194/bg-19-4431-2022

Terhaar, J., Goris, N., Müller, J. D., DeVries, T., Gruber, N., Hauck, J., ... Seferian, R. (2023). Assessment of global ocean biogeochemical models for ocean carbon sink estimates in RECCAP2 and recommendations for future studies. *submitted to Global Biogeochemical Cycles*.

Tohjima, Y., Mukai, H., MacHida, T., Hoshina, Y., & Nakaoka, S. I. (2019). Global carbon budgets estimated from atmospheric O_2:N_2 and CO_2 observations in the western Pacific region over a 15-year period. *Atmospheric Chemistry and Physics*, *19*(14), 9269–9285. doi: 10.5194/acp-19-9269-2019

Urakawa, L. S., Tsujino, H., Nakano, H., Sakamoto, K., Yamanaka, G., & Toyoda, T. (2020). The sensitivity of a depth-coordinate model to diapycnal mixing induced by practical implementations of the isopycnal tracer diffusion scheme. *Ocean Modelling*, *154*(August), 101693. doi: 10.1016/j.ocemod.2020.101693

van der Laan-Luijkx, I. T., van der Velde, I. R., van der Veen, E., Tsuruta, A., Stanislawska, K., Babenhauserheide, A., ... Peters, W. (2017). The CarbonTracker Data Assimilation Shell (CTDAS) v1.0: Implementation and global carbon balance 2001-2015. *Geoscientific Model Development*, *10*(7), 2785–2800. doi: 10.5194/gmd-10-2785-2017

van Heuven, S., Hoppema, M., Jones, E. M., & de Baar, H. J. (2014). Rapid invasion of anthropogenic CO2 into the deep circulation of the Weddell Gyre. *Philosophical Transactions of the Royal Society A: Mathematical, Physical and Engineering Sciences*, *372*(2019). doi: 10.1098/rsta.2013.0056

Verdy, A., Dutkiewicz, S., Follows, M. J., Marshall, J., & Czaja, A. (2007). Carbon dioxide and oxygen fluxes in the Southern Ocean: Mechanisms of interannual variability. *Global Biogeochemical Cycles*, *21*(2), 1–10. doi: 10.1029/2006GB002916

Verdy, A., & Mazloff, M. R. (2017). A data assimilating model for estimating Southern Ocean biogeochemistry. *Journal of Geophysical Research: Oceans*, *122*(9), 6968–6988. doi: 10.1002/2016JC012650

Wanninkhof, R. (1992). Relationship Between Wind Speed and Gas Exchange. *Journal of Geophysical Research, Oceans*, *97*(92), 7373–7382.

Wanninkhof, R. (2023). Impact predictor variables on magnitude, variability and trend of global air-sea CO_2 fluxes using an Extra Trees machine learning approach. *Global Biogeochemical Cycles*.

Wanninkhof, R., Asher, W. E., Weppernig, R., Chen, H., Schlosser, P., Langdon, C., & Sambrotto, R. (1993). Gas transfer experiment on Georges Bank using two volatile deliberate tracers. *Journal of Geophysical Research*, *98*(C11). doi: 10.1029/93jc01844

Wanninkhof, R. H. (2014). Relationship between wind speed and gas exchange over the ocean revisited. *Limnology and Oceanography: Methods*, *12*(JUN), 351–362. doi: 10.4319/lom.2014.12.351

Wanninkhof, R. H., Asher, W. E., Ho, D. T., Sweeney, C., & McGillis, W. R. (2009). Advances in Quantifying Air-Sea Gas Exchange and Environmental Forcing. *Annual Review of Marine Science*, *1*(1), 213–244. doi: 10.1146/annurev.marine.010908.163742

Wanninkhof, R. H., Park, G.-H. H., Takahashi, T. T., Sweeney, C., Feely, R. A., Nojiri, Y., ... Khatiwala, S. (2013). Global ocean carbon uptake: magnitude, variability and trends. *Biogeosciences*, *10*(3), 1983–2000. doi: 10.5194/bg-10-1983-2013

Watson, A. J., Schuster, U., Shutler, J. D., Holding, T., Ashton, I. G., Landschützer, P., ... Goddijn-Murphy, L. (2020). Revised estimates of ocean-atmosphere CO_2 flux are consistent with ocean carbon inventory. *Nature Communications*, *11*(1), 1–6. doi: 10.1038/s41467-020-18203-3

Waugh, D. W., Hall, T. M., Mcneil, B. I., Key, R., & Matear, R. J. (2006). Anthropogenic CO_2 in the oceans estimated using transit time distributions. *Tellus, Series B: Chemical and Physical Meteorology*, *58*(5), 376–389. doi: 10.1111/j.1600-0889.2006.00222.x

Waugh, D. W., Hogg, A. M., Spence, P., England, M. H., & Haine, T. W. (2019). Response of Southern Ocean ventilation to changes in midlatitude westerly winds. *Journal of Climate*, *32*(17), 5345–5361. doi: 10.1175/JCLI-D-19-0039.1

Williams, N. L., Juranek, L. W., Feely, R. A., Johnson, K. S., Sarmiento, J. L., Talley, L. D., ... Takeshita, Y. (2017). Calculating surface ocean pCO_2 from biogeochemical Argo floats equipped with pH: An uncertainty analysis. *Global Biogeochemical Cycles*, *31*(3), 591–604. doi: 10.1002/2016GB005541

Williams, N. L., Juranek, L. W., Johnson, K. S., Feely, R. A., Riser, S. C., Talley, L. D., ... Wanninkhof, R. (2016). Empirical algorithms to estimate water column pH in the Southern Ocean. *Geophysical Research Letters*, *43*, 3415-3422. doi: 10.1002/2016GL068539

Woolf, D. K., Land, P. E., Shutler, J. D., Goddijn-Murphy, L., & Donlon, C. J. (2016). On the calculation of air-sea fluxes of CO_2 in the presence of temperature and salinity gradients. *Journal of Geophysical Research: Oceans*, *121*(2), 1229–1248. doi: 10.1002/2015JC011427

Wright, R. M., Le Quéré, C., Buitenhuis, E., Pitois, S., & Gibbons, M. J. (2021). Role of jellyfish in the plankton ecosystem revealed using a global ocean biogeochemical model. *Biogeosciences*, *18*(4), 1291–1320. doi: 10.5194/bg-18-1291-2021

Wunsch, C., & Heimbach, P. (2013). *Dynamically and kinematically consistent global ocean circulation and ice state estimates* (2nd ed., Vol. 103). Elsevier Ltd. doi: 10.1016/B978-0-12-391851-2.00021-0

Yang, M., Smyth, T. J., Kitidis, V., Brown, I. J., Wohl, C., Yelland, M. J., & Bell, T. G. (2021). Natural variability in air-sea gas transfer efficiency of CO_2. *Scientific Reports*, *11*(1), 1–9. doi: 10.1038/s41598-021-92947-w

Yang, S., & Gruber, N. (2016). The anthropogenic perturbation of the marine nitrogen cycle by atmospheric deposition: Nitrogen cycle feedbacks and the 15N Haber-Bosch effect. *Global Biogeochemical Cycles*, *30*(10), 1418–1440. doi: 10.1002/2016GB005421

Zeng, J., Iida, Y., Matsunaga, T., & Shirai, T. (2022). Surface ocean CO_2 concentration and air-sea flux estimate by machine learning with modelled variable trends. *Frontiers in Marine Science*, *9*(September), 1–14. doi: 10.3389/fmars.2022.989233

Global Biogeochemical Cycles

Supporting Information for

The Southern Ocean carbon cycle 1985-2018: mean, seasonal cycle, trends and storage

Judith Hauck, Luke Gregor, Cara Nissen, Lavinia Patara, Mark Hague, N. Precious Mongwe, Seth Bushinsky, Scott C. Doney, Nicolas Gruber, Corinne Le Quere, Manfredi Manizza, Matthew Mazloff, Pedro M. S. Monteiro, Jens Terhaar

See main text for affiliations.

Contents of this file

Introduction

- The supplementary material contains additional information and analysis. In particular, we present additional analysis, resolved to show results of individual data sets and further separation into Atlantic, Pacific and Indian Ocean sectors of the Southern Ocean.

Text S1. Linear CO_2 flux trends in the control simulation

In the whole Southern Ocean, the linear trend in simulation B (Figure S1) is smaller than 10 TgC yr^{-1} decade^{-1} for 10 out of the 14 models; larger than 10 TgC yr^{-1} decade^{-1} for the other four (maximum 55 TgC yr^{-1} decade^{-1}). Overall, the trend in simulation B is thus small compared to the mean fluxes in simulation A.

Text S2. Non steady state component of ΔC_{ant} accumulation rates

In Figures 11-13 we show the steady state ΔC_{ant} for OCIMv2021 and two GOBMs (CNRM, and MPIOM-HAMOCC), since it is the only one available, whereas the total ΔC_{ant} (i.e. the sum of the steady state and non-steady components) is shown for the other data sets. This warrants a closer inspection at the non-steady ΔC_{ant} (Fig. S3) in relation to the steady ΔC_{ant}. Indeed, total ΔC_{ant} accumulation rates between 1994-1007 patterns may be affected by decadal changes in ocean circulation occurring over that period, which would affect its non-steady component (but not its steady component). As it can be seen from Fig. S3, ΔC_{ant}^{ns} is around 10-20% of the total ΔC_{ant} (Fig. S4). The spatial patterns of ΔC_{ant}^{ns} are quite diverse among GOBMs (despite having an overall tendency towards increased ΔC_{ant} uptake in the Weddell Sea), which is surprising considering that GOBMs are forced by similar atmospheric reanalysis products. It can be concluded that other factors, such as model internal variability and the individual strategy to perform a steady-state simulation, play a role in driving ΔC_{ant}^{ns}.

Text S3. Computation of annual MLD diagnostic

Given its important role in ventilating the deep ocean (Morrison et al., 2022), we include here an assessment of mixed layer depth (MLD) across different GOBMs. In addition to the user-defined fixed-threshold September MLD provided by all of GOBMs, we additionally computed MLDs based on the interior temperature and salinity values using a variable density threshold method (Holte et al., 2017). Because, following the RECCAP-2 protocol, most GOBMs provided only annually-averaged temperature and salinity values, we call this diagnostic an annual MLD diagnostic. Monthly means would have been the preferred choice, considering the large seasonal variations in the upper ocean temperature and salinity, but this diagnostic has the advantage of being computed uniformly across all GOBMs and of using a variable density threshold, which has been shown to provide a more realistic picture especially at high latitudes (Holte et al., 2017). 3D monthly fields were only available for two hindcast models (NEMO-PlankTOM12 and CCSM-WHOI) and for the observed World Ocean Atlas 2018 (WOA18 climatology). An analysis of the impact of using annual means instead of monthly means of temperature and salinity, shows an underestimation of annual MLD diagnostic with respect to the monthly MLD diagnostic of around 45%-50% but no significant differences in spatial patterns.

Text S4. Composite analysis of "GOBMs high" and "GOBMs low"

To gain a better understanding of the factors driving the inter-model spread in ΔC_{ant} accumulation rates, we analyzed composites for GOBMs overestimating (hereafter "GOBMs high", Figure 11c) and underestimating (hereafter "GOBMs low", Figure 11d) ΔC_{ant} with respect to the average of the two observationally-constrained estimates. A consistent pattern of higher ΔC_{ant} accumulation rates in the "GOBMs high" with respect to "GOBMs low" emerges (Fig. 11c,d, Figure S4). Composite anomalies with respect to the multi-model-mean of different physical variables (Fig. S17) can help interpret the drivers of the different ΔC_{ant} accumulation rates in "GOBMs high" and "GOBMs low". "GOBMs high" consistently show positive anomalies of C_{ant} air-sea fluxes throughout the Southern Ocean (except for some areas around Antarctica), associated with higher-than-average sea surface salinity (SSS) and deeper mixing in the STSS and SPSS biomes. Mixing anomalies are distributed more uniformly when using the annual MLD diagnostic (Text S3) than when using the user-defined September MLD. The clear dependence of

C_{ant} air-sea fluxes on SSS in the STSS and SPSS biomes is in line with Terhaar et al. (2021) and with results from the Evaluation Chapter of RECCAP-2 (Terhaar et al., 2023) where a tight relationship is found between C_{ant} air-sea fluxes and SSS averaged between the Polar Front (approximately the southern edge of the SPSS biome) and the Subtropical Front (approximately the northern edge of the STSS biome). Interestingly, "GOBMs high" models have lower-than-average SSS in the ICE biome, possibly because of thicker sea ice (Fig. S17), which impedes the formation of polynyas and associated brine rejection. By construction, the anomalies of "GOBMs low" provide a specular picture with respect to "GOBMs high".

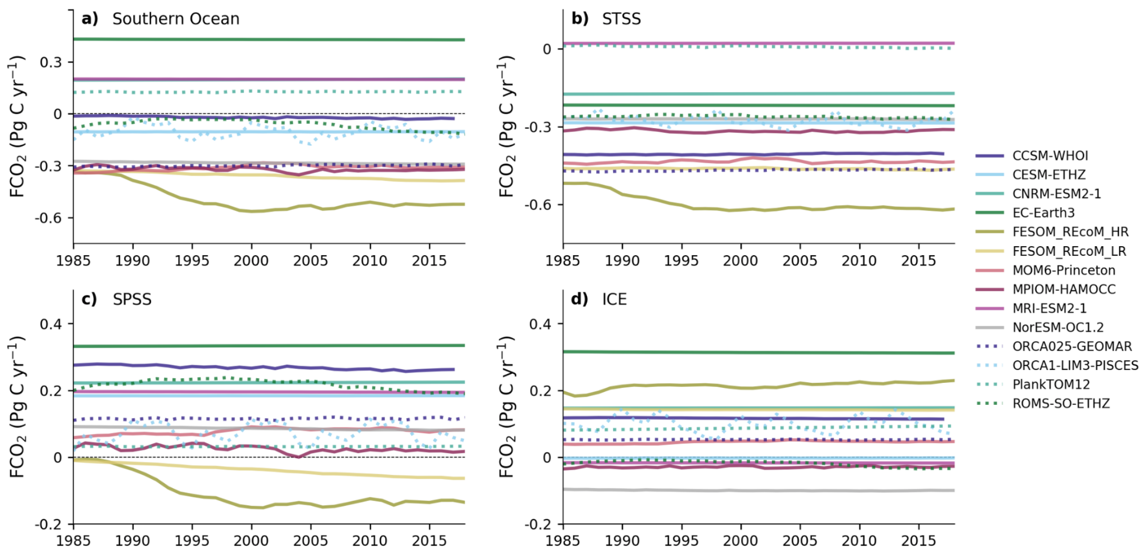

Figure S1. CO_2 flux in simulation B (control) for each individual GOBM for the (a) Southern Ocean, (b) STSS, (c) SPSS, and (d) ICE biomes.

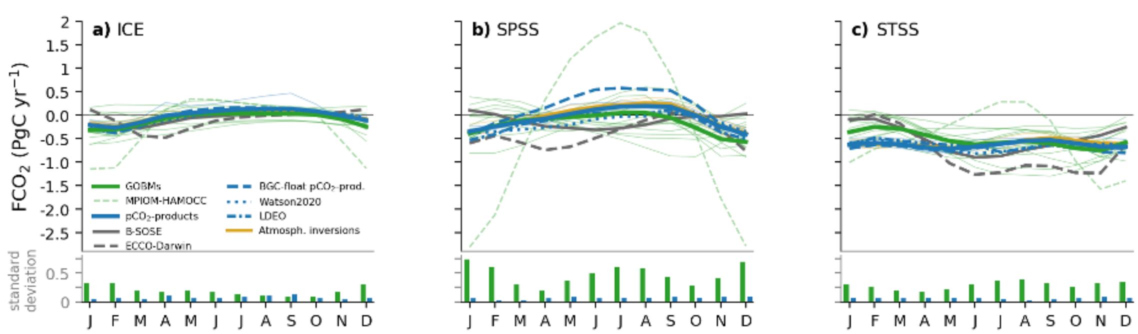

Figure S2. Same as Figure 6a-c, but with MPIOM-HAMOCC included. Note the different y-axes scales compared to Figure 6.

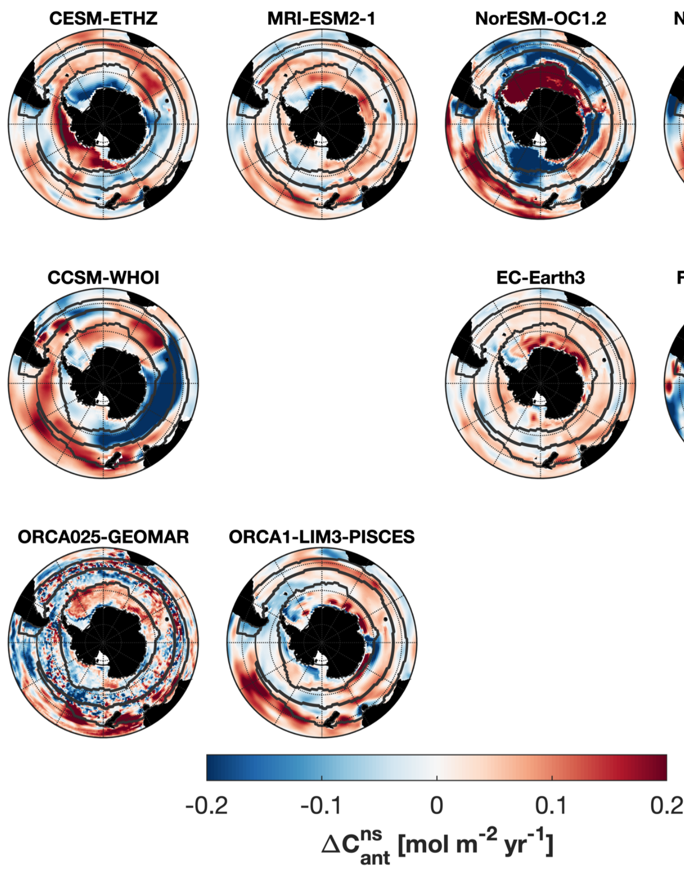

Figure S3. Non-steady state anthropogenic carbon (ΔC_{ant}^{ns}) accumulation rates over the period 1994-2007. Shown are only models where this decomposition is possible.

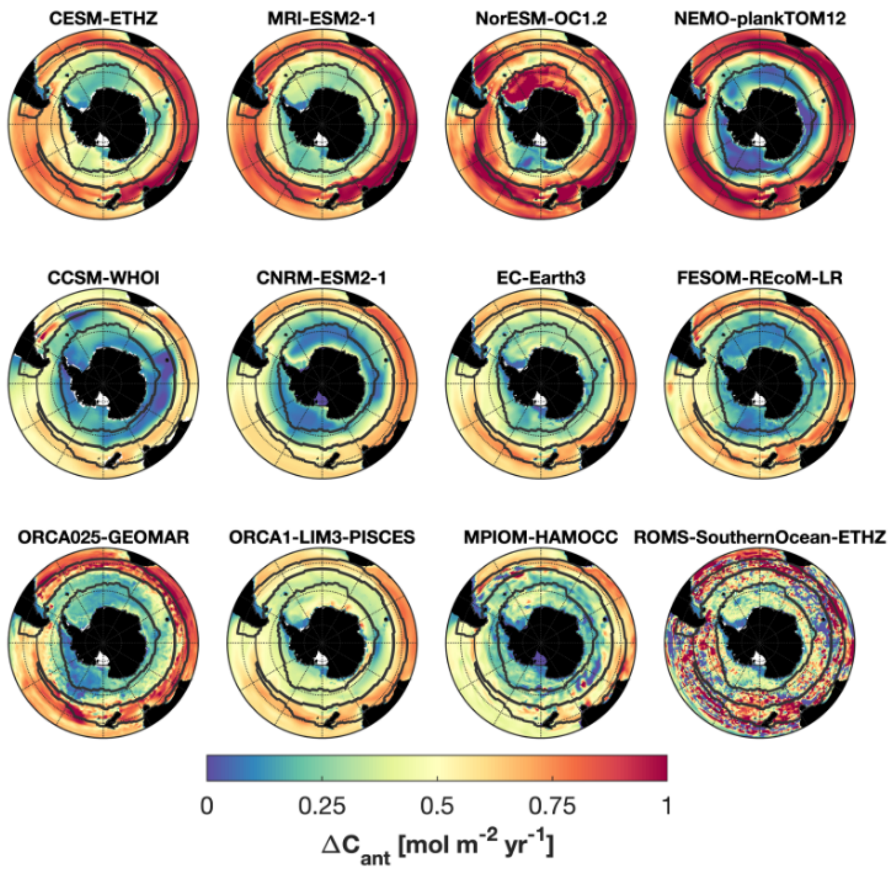

Figure S4. ΔC_{ant} accumulation rate from 1994 to 2007 integrated to 3000 m depth for individual models. ΔC_{ant}^{tot} is shown for "GOBMs high" models CESM-ETHZ, MRI-ESM2-1, NorESM-OC1.2, and NEMO-PlankTOM12 (top row), for "GOBMs low" models CCSM-WHOI, CNRM-ESM2-1, EC-Earth3, FESOM_REcoM_LR, ORCA025-GEOMAR, ORCA1-LIM3-PISCES, and MPIOM-HAMOCC and for the regional model ROMS-SouthernOcean-ETHZ (middle and bottom rows). ΔC_{ant}^{ss} is shown for MPIOM-HAMOCC and CNRM-ESM2-1 (as justified in the main text and Text S2). Biome boundaries are shown as contours.

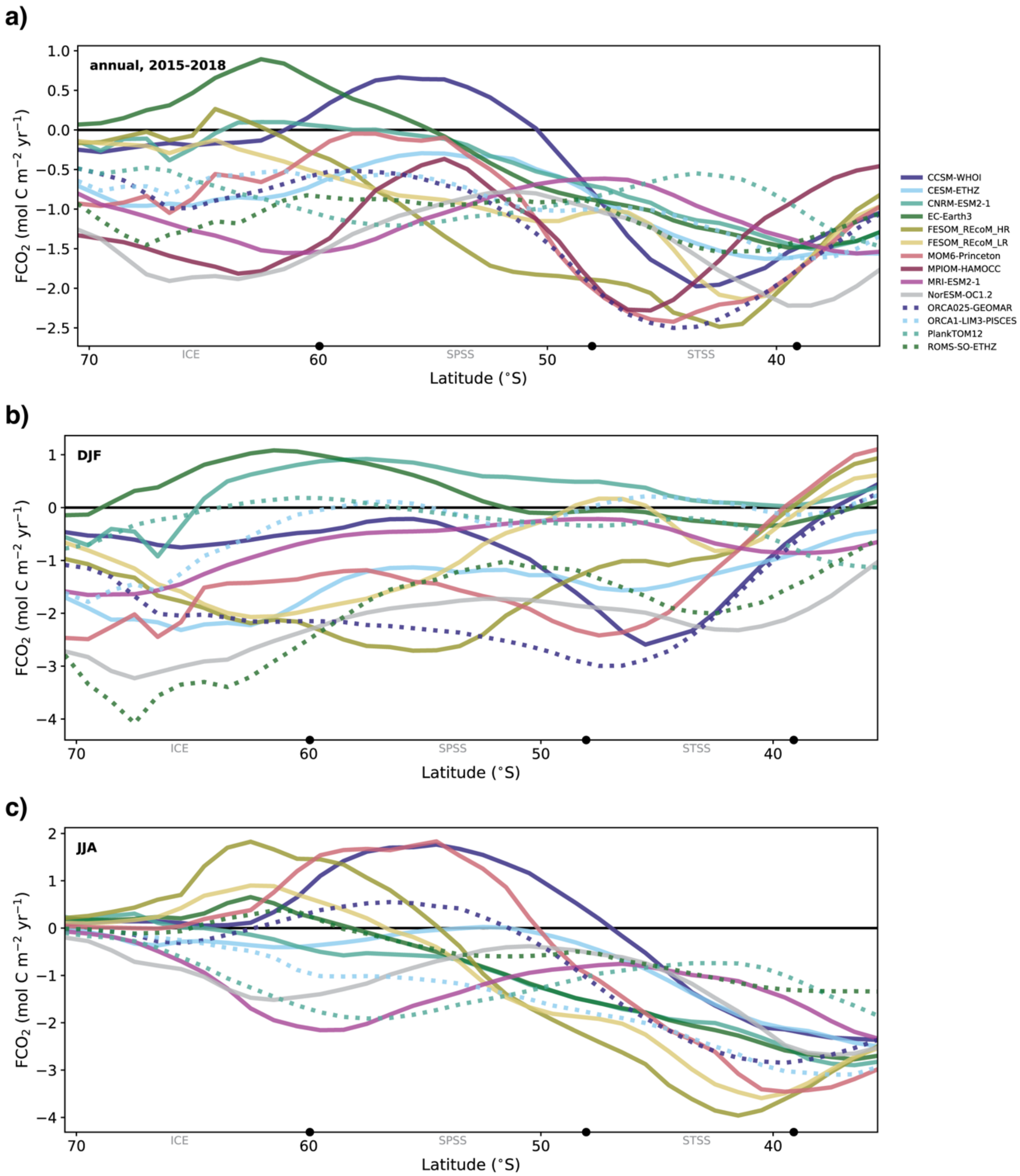

Figure S5: Zonal mean of flux density for individual GOBMs in the period 2015-2018. We show the (a) annual, (b) summer, and (c) winter zonal averages. The black markers on the x-axes show the mean location of the biome boundaries with the names of the biomes shown in gray. The MPIOM-HAMOCC model is excluded in panels b and c because of an overly strong seasonal amplitude.

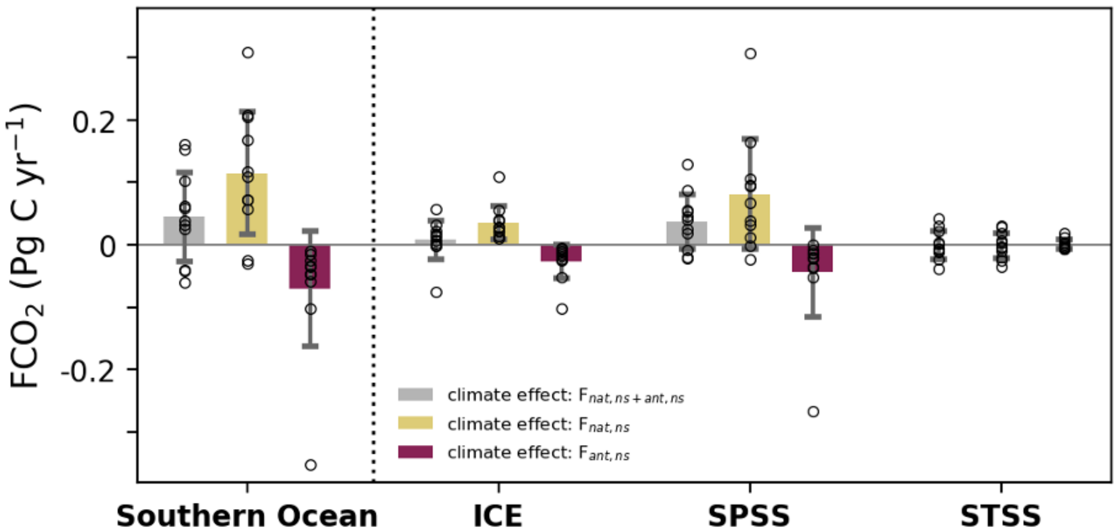

Figure S6: Same as Figure 3, but separating the total climate effect on CO_2 fluxes (gray) into the climate effect on natural (yellow) and anthropogenic (dark red) CO_2 fluxes. The climate effects on natural and anthropogenic CO_2 fluxes partly compensate each other.

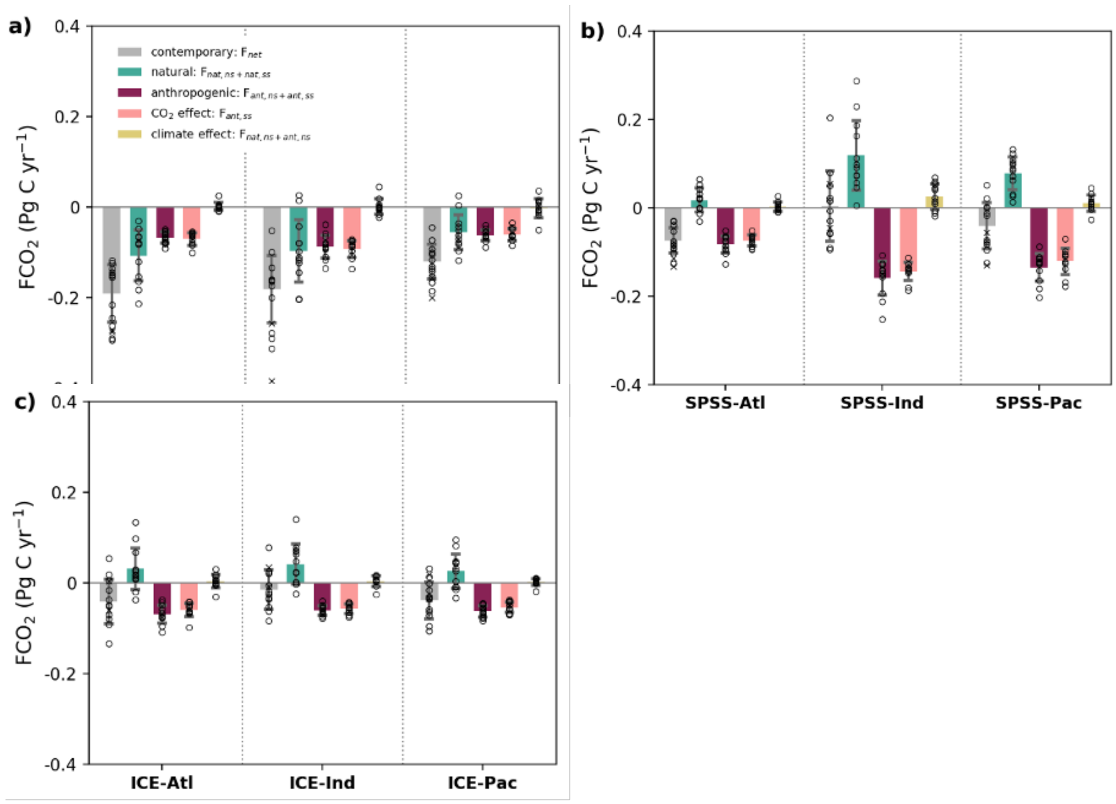

Figure S7: Same as Figure 3, but further split into Atlantic, Pacific and Indian Ocean sectors. The sub-biome-scale natural–anthropogenic decomposition of the air-sea CO_2 fluxes from the Global Ocean Biogeochemical Models in the Southern Ocean for the (a) Subtropical Seasonally Stratified, (b) Subpolar Seasonally Stratified, and (c) ICE biomes. The bars show the model ensemble mean, the circles show the individual models, and the error bars represent one standard deviation around the mean.

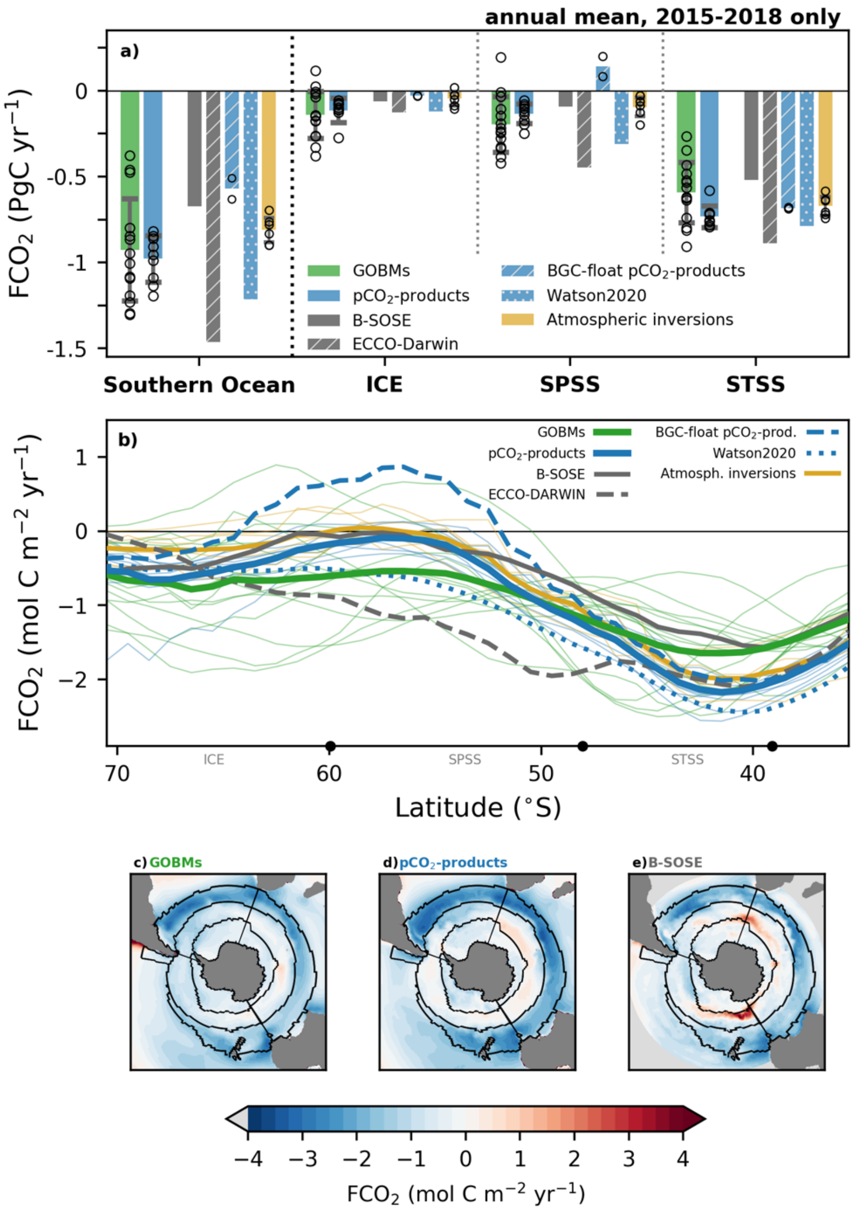

Figure S8. Temporal average of the contemporary Southern Ocean CO_2 flux (FCO_2) 2015-2018. A positive flux denotes outgassing from ocean to atmosphere. GOBMs: global ocean biogeochemistry models. (a) The green and blue bar plots show the ensemble mean of the GOBMs and pCO_2-products, and open circles indicate the individual GOBMs and pCO_2- products. The ensemble standard deviation (1σ) is shown by the error bars. The other bars show other individual estimates as indicated in the legend (see also methods), (b-d) maps of spatial distribution of net CO_2 flux for ensemble means of GOBMs, pCO_2- products and of the data-assimilated regional model B-SOSE. (e) zonal mean flux of the different data sets. Thick green and blue lines show the ensemble means, and thin green and blue lines show the individual GOBMs and p CO_2-products. Other colors as in panel a. Approximate boundaries for biomes are marked with black points on the x axis.

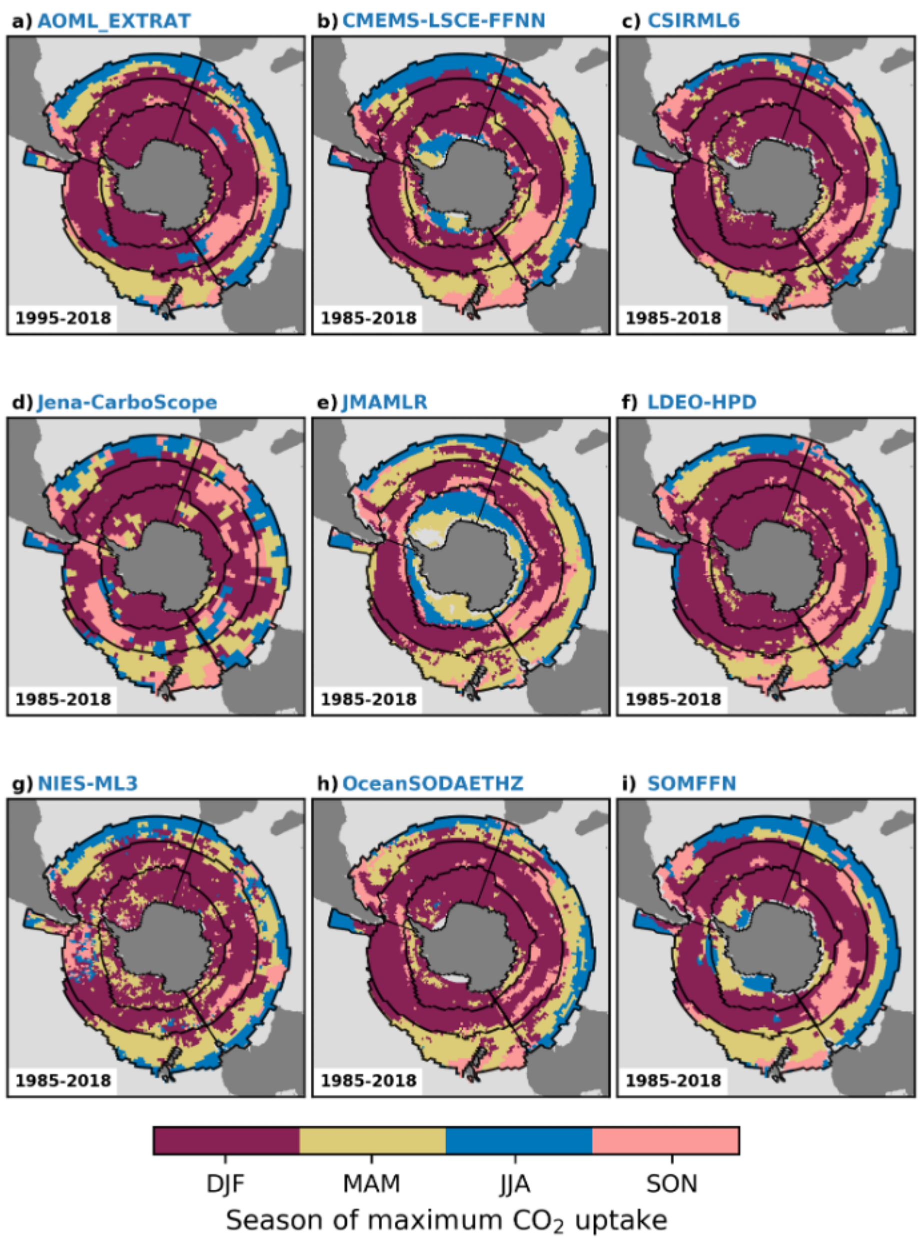

Figure S9: The season of maximum CO_2 uptake per grid cell for the pCO_2-products over the period indicated in the panels.

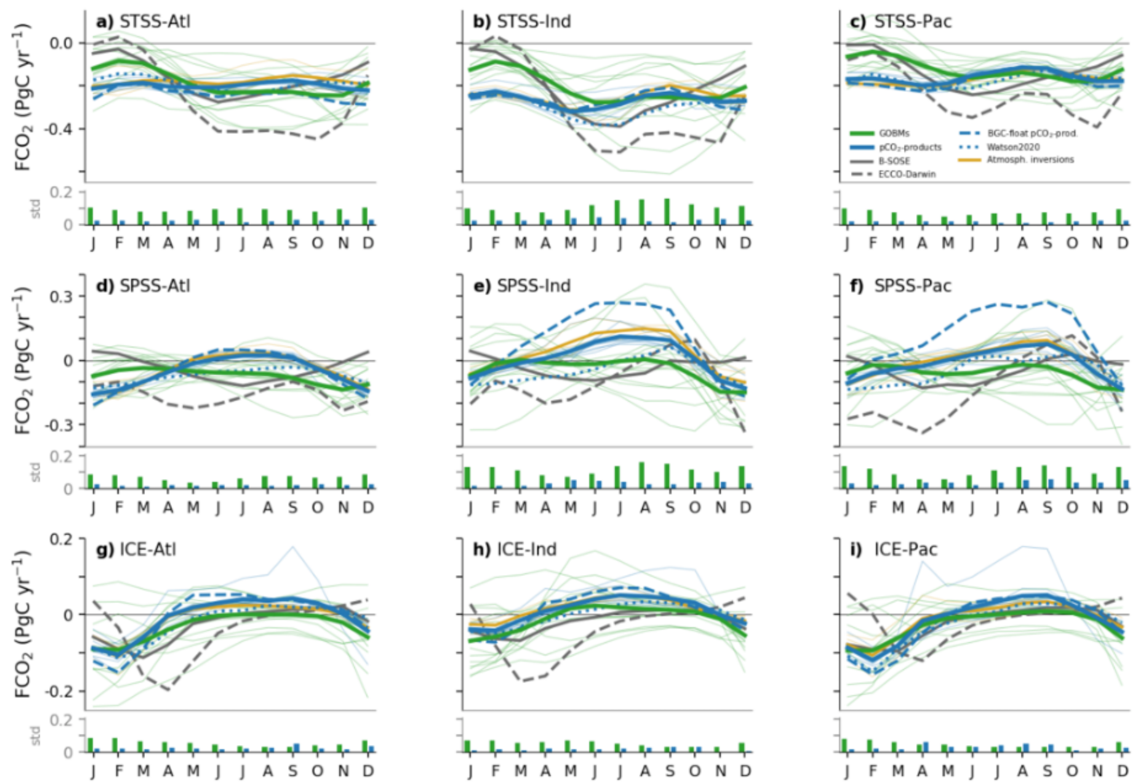

Figure S10: Seasonal cycle monthly climatology of FCO2 for the nine subregions of the Southern Ocean (see Figure 1). The top, middle and bottom rows show the STSS, SPSS and ICE biomes respectively, while the left, center and right columns represent the Atlantic, Indian, and Pacific sectors of each biome respectively. The standard deviation of the GOBMs (solid green) and pCO_2-products (solid blue) are shown in the narrow lower panels of each subplot. Data has not been centered to a specific year, and each dataset has the start and end years as noted in Table 1.

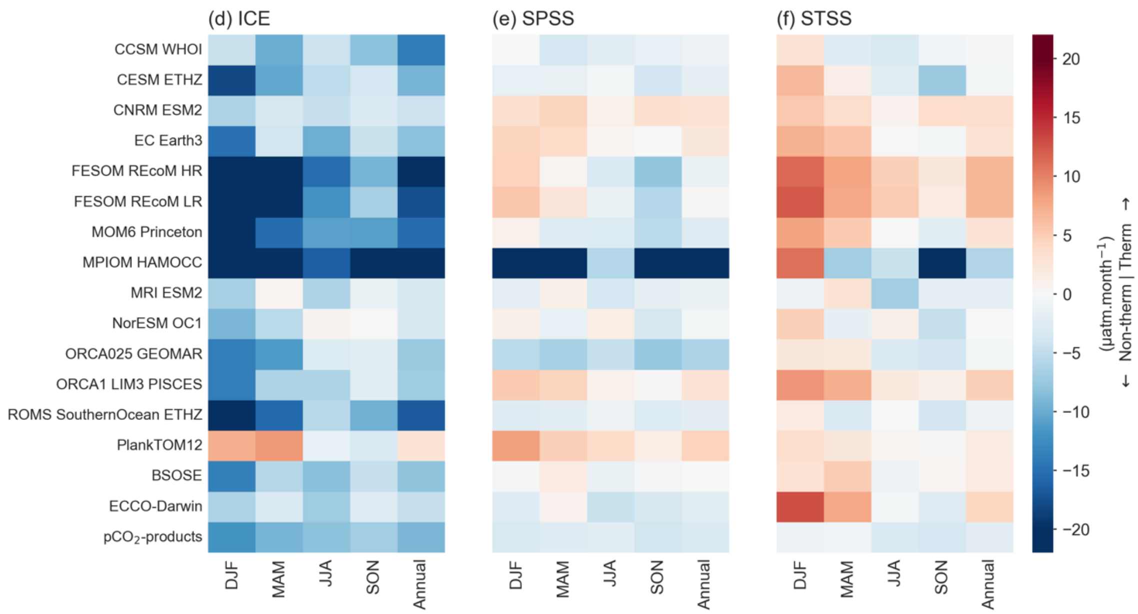

Figure S11: Same as Figure 7d-f, but showing all individual global and regional ocean biogeochemistry models and data assimilating models.

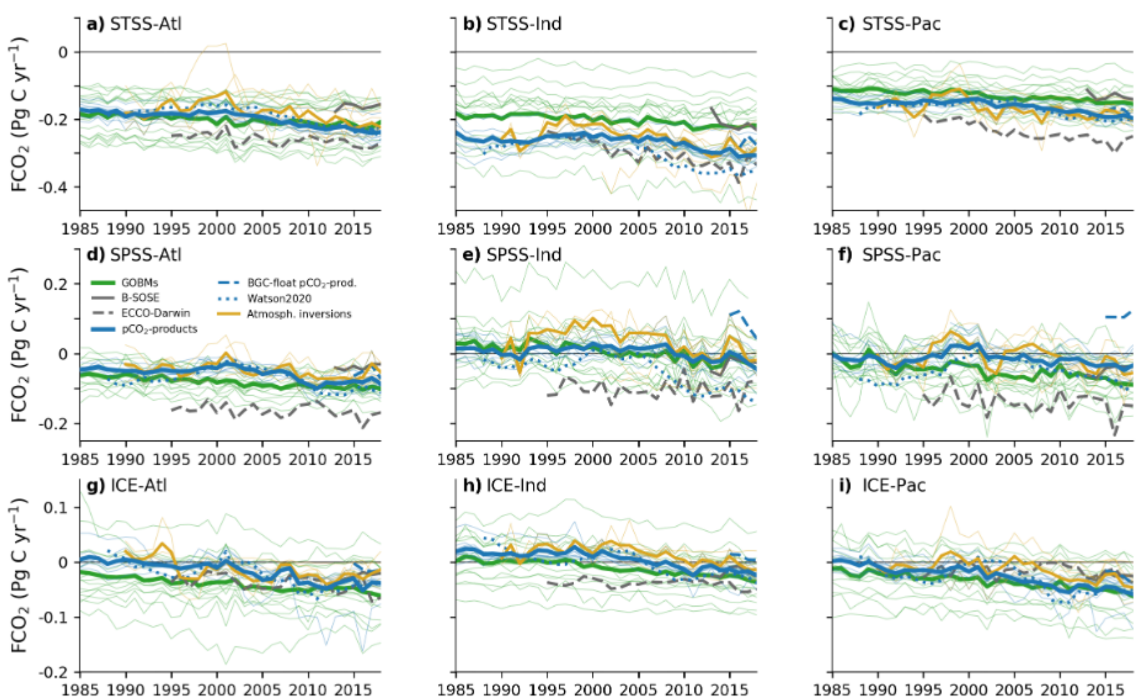

Figure S12: Same as Figure 8b-d, but further split into Atlantic, Pacific and Indian Ocean sectors of the biomes.

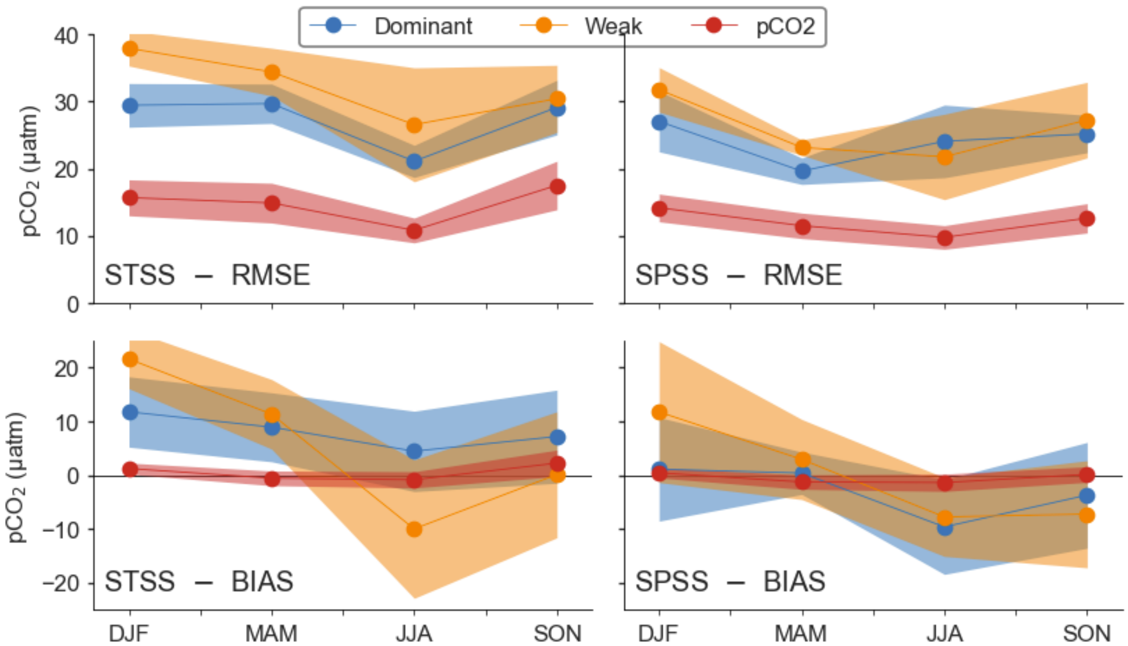

Figure S13: Comparison of surface ocean pCO_2 from DIC-dominant (blue), DIC-weak (yellow) global and regional ocean biogeochemistry models (see Table S1) and pCO_2-products (blue) to pCO2 from gridded SOCAT v2022 data set (see also Figure 9 for full Southern Ocean analysis, and section 3.3.1). Here, we calculate bias and RMSE for all observations for a given season and region. The bias is the sum of the residuals while the RMSE is the square root of the sum of the squared residuals.

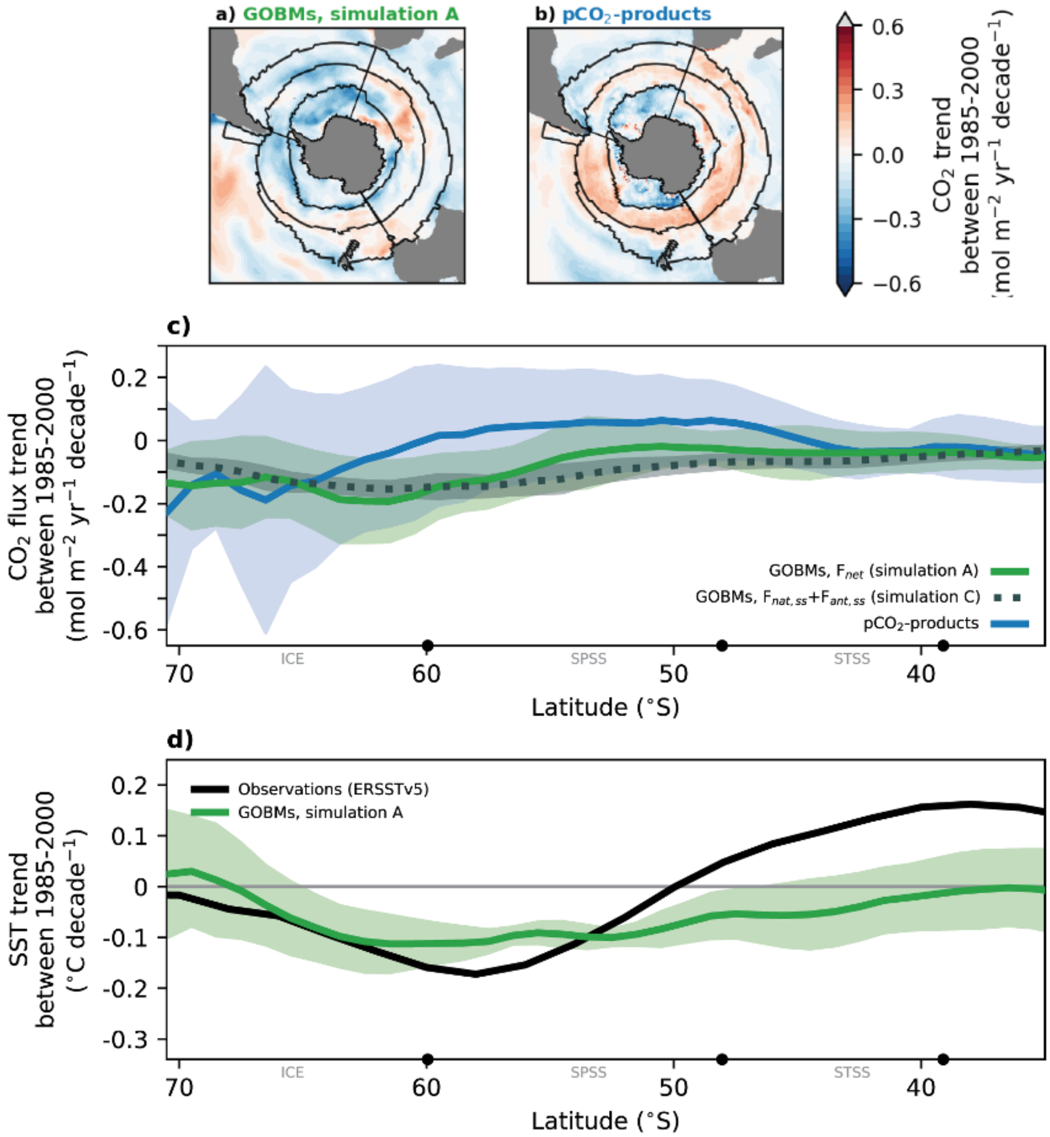

Figure S14: Same as Figure 10, but CO_2 flux trend shown here for the period 1985 to 2000. Note different scales than in Figure 10.

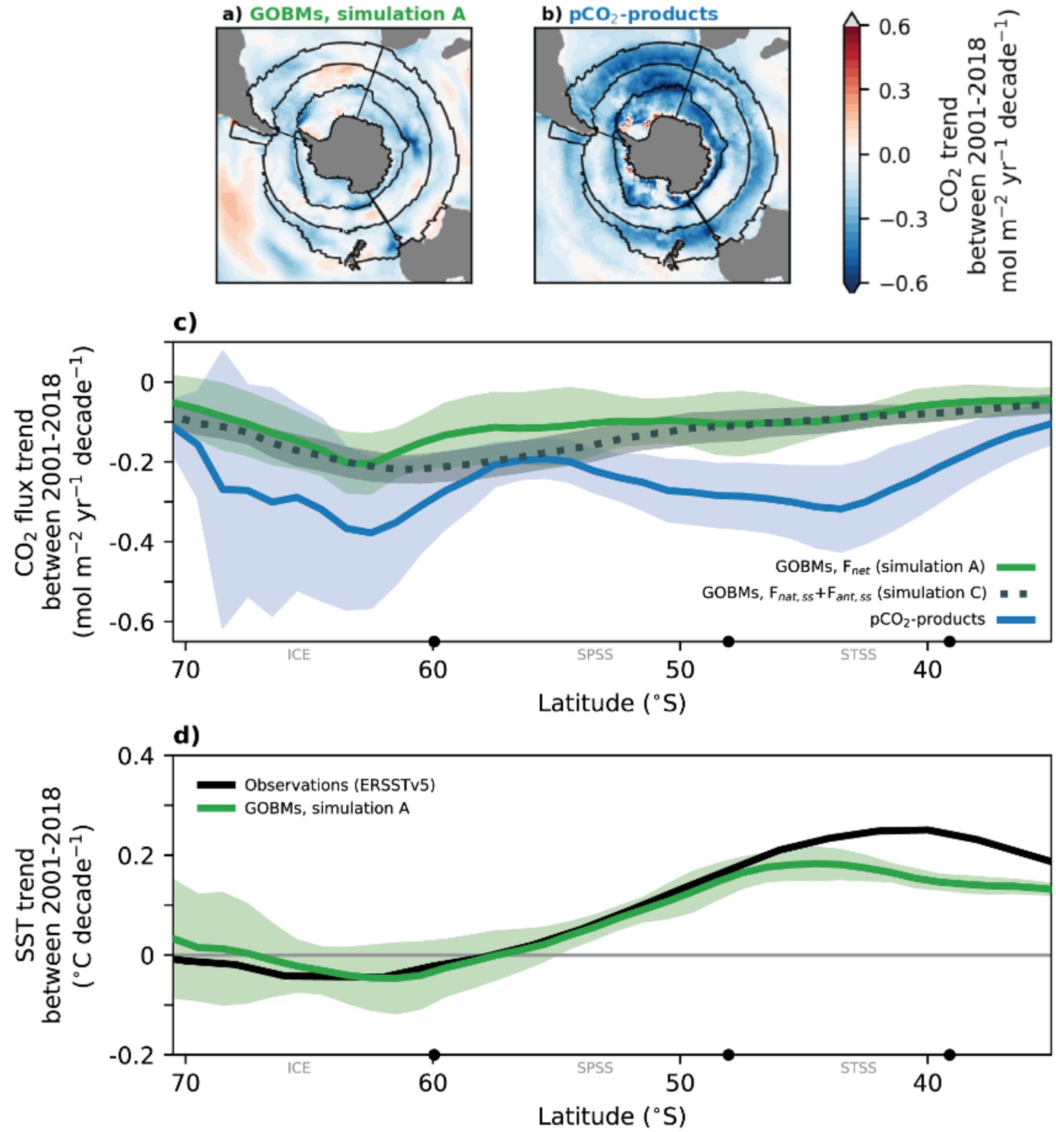

Figure S15: Same as Figure 10, but CO_2 flux trend shown here for the period 2001 to 2018. Note different scales than in Figure 10.

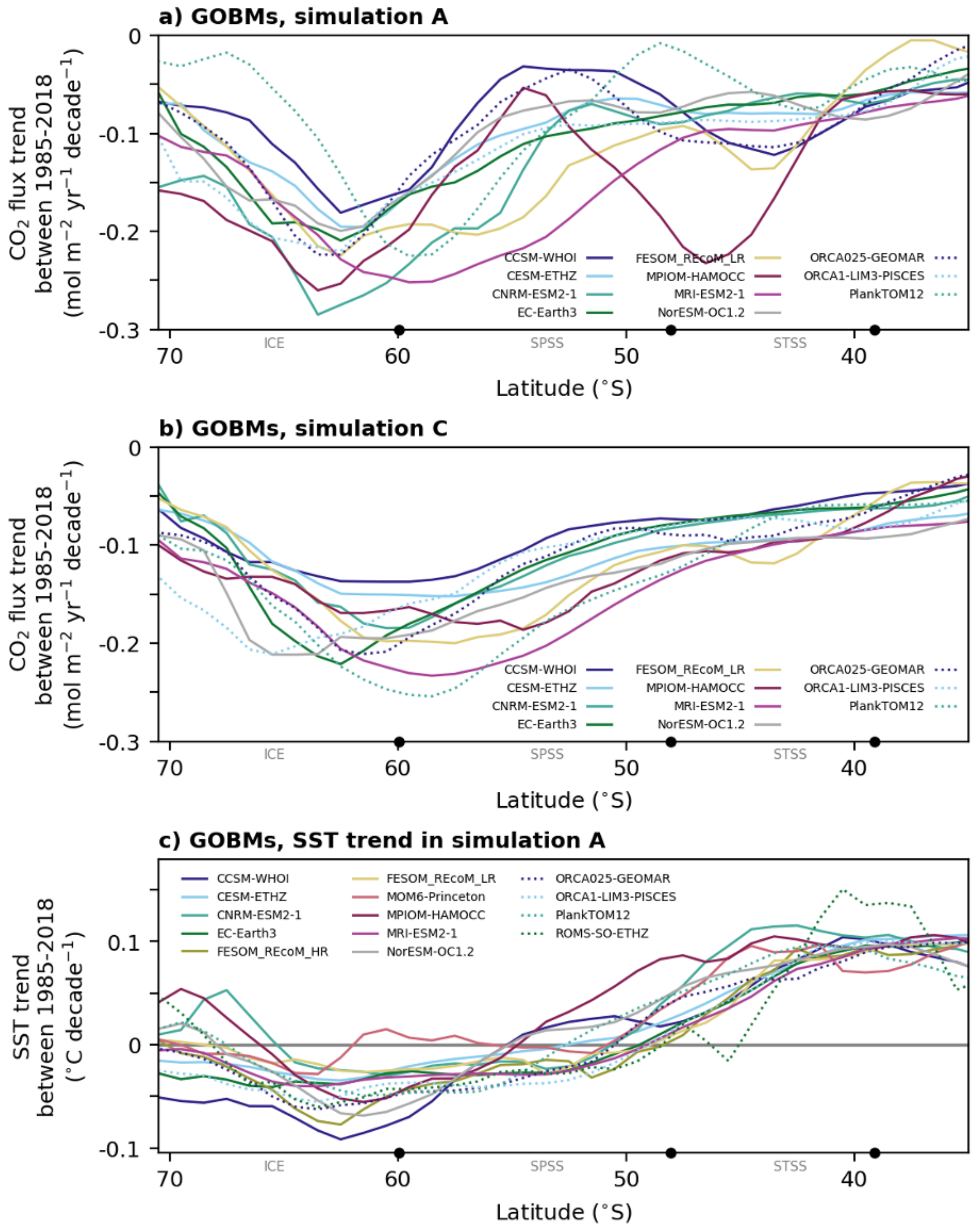

Figure S16: CO_2 flux and temperature trends1985-2018 for individual models. (a) Net CO_2 flux trend from simulation A, (b) Steady state CO_2 flux trend ($F_{nat,ss}$ and $F_{ant,ss}$) from simulation, (c) sea surface temperature (SST) trend in simulation A.

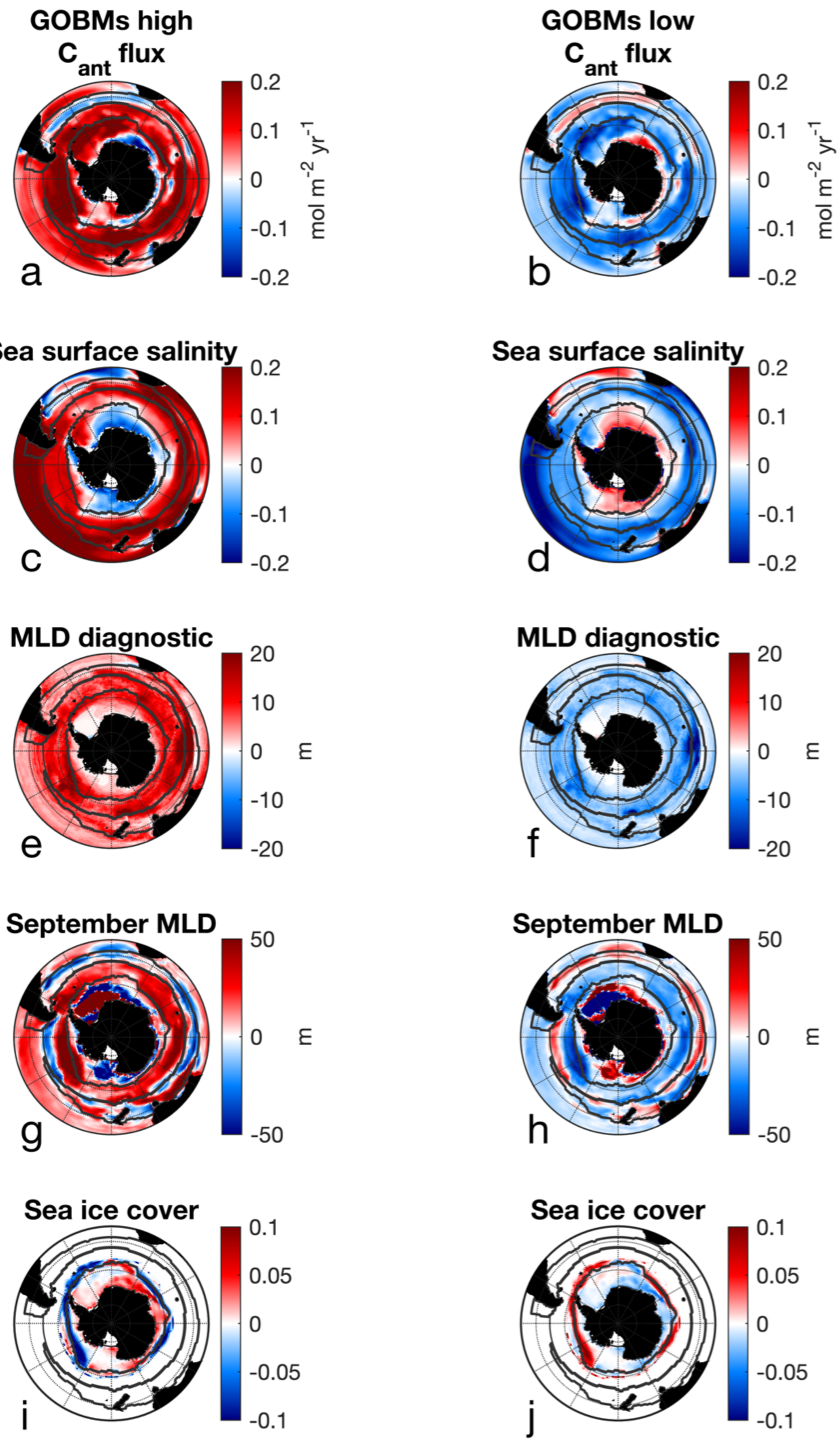

Figure S17: Composite anomalies averaged over years 1994-1007 of a,b) C_{ant} flux, c,d) sea surface salinity, e,f) MLD annual diagnostic using variable density threshold, g,h) user-defined September MLD with fixed density threshold, and i,j) sea ice concentration for models with ΔC_{ant} higher ("GOBMs high", left column) and lower ("GOBMs low", right column) than the average of the observation-based products eMLRC* and OCIM-v2021.

Shown are anomalies with respect to the multi-model-mean of these nine models. The "GOBMs high" models are CESM-ETHZ, MRI-ESM-1, NorESM-OC1.2, and NEMO-PlankTOM12. The "GOBMs low" models are: CCSM-WHOI, CNRM-ESM2-1, EC-Earth3, FESOM-REcoM-LR, ORCA025-GEOMAR, ORCA1-LIM3-PISCES and MPIOM-HAMOCC. CNRM-ESM2 was excluded from the composite analysis because it shows areas of negative ΔC_{ant} ; ROMS-SouthernOcean-ETHZ was also excluded because it has a different spin-up procedure with respect to other models (see Methods Section). The robustness of the patterns has been tested by removing in turn one model from the list. The patterns are retained even when the two models at the higher end (NorESM-OC1.2) and lower end (CCSM-WHOI) are removed from the composites. By construction, the sum of anomaly patterns in GOBMs high and GOBMs low is zero (in other words, the patterns are specular with respect to the multi model mean).

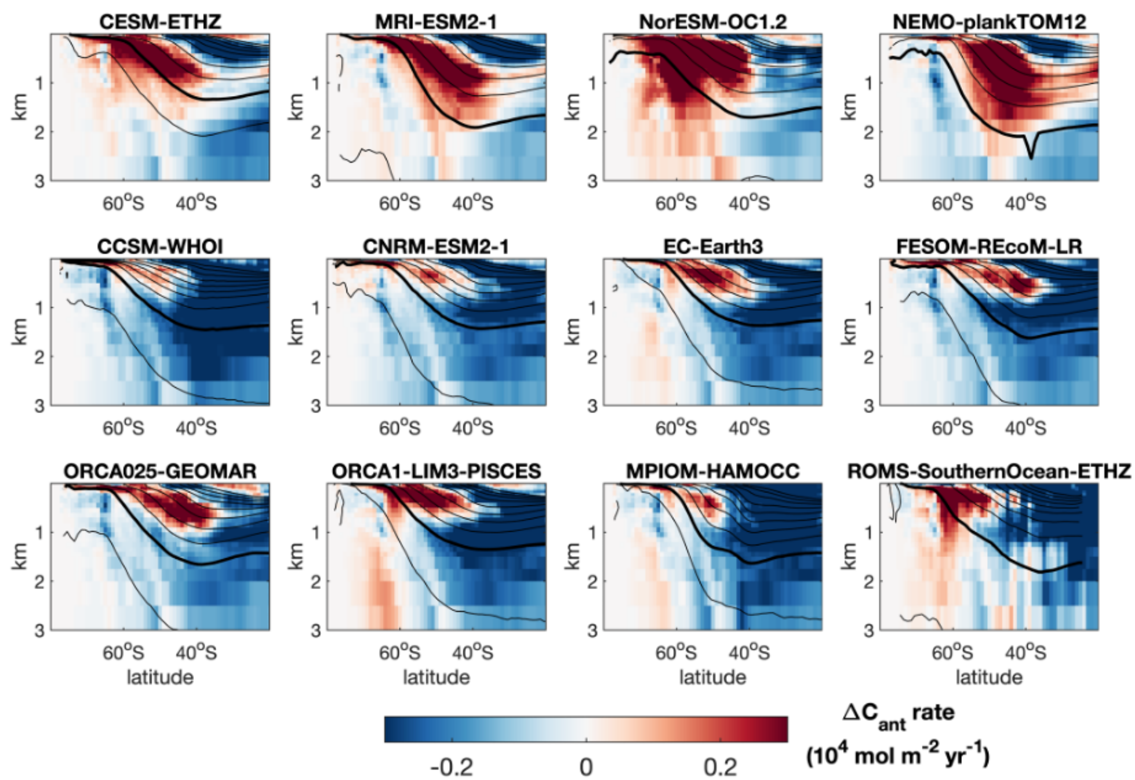

Figure S18: Anomalies, computed with respect to eMLR(C*), of ΔC_{ant} accumulation rates for the "GOBMs high" (top row) , for "GOBMs low" and for the regional model ROMS-SouthernOcean-ETHZ (middle and bottom rows). Contours show, for each model, the zonally-averaged potential density for the period 1994-2007 (with a 0.02 kg m^{-3} spacing), where the thick contour indicates the 1027.6 kg m^{-3} isopycnal.

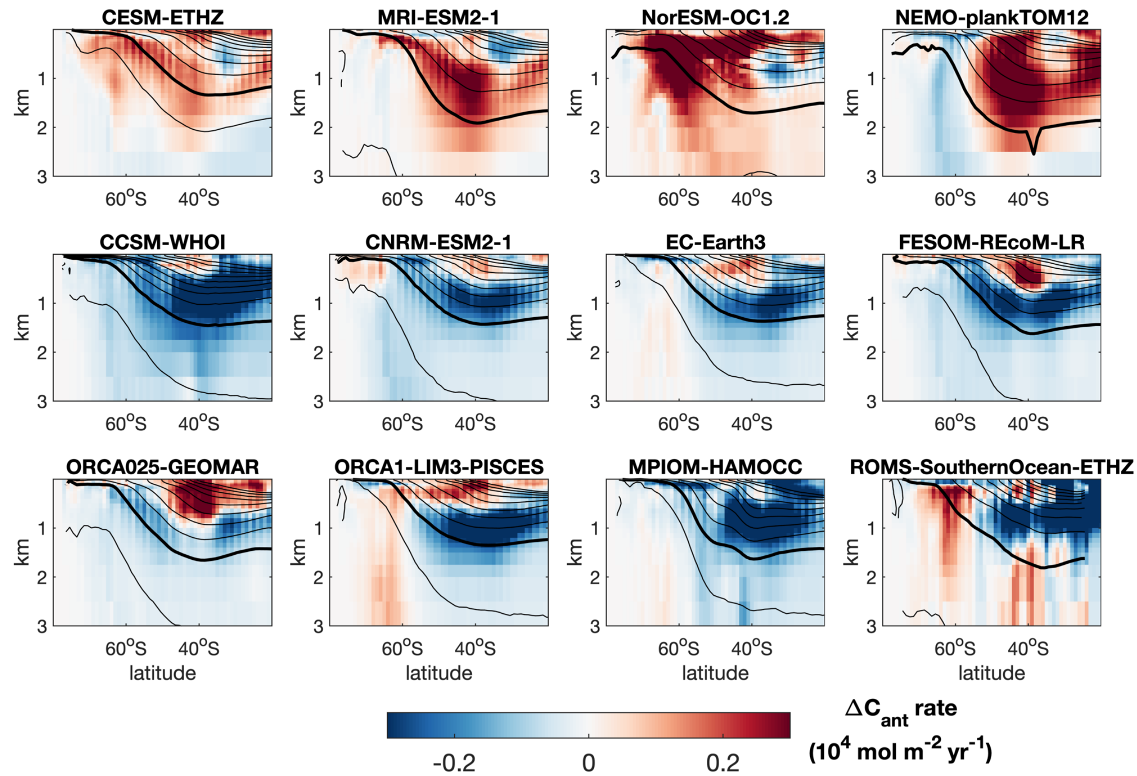

Figure S19: Anomalies, computed with respect to OCIM-v2021, of ΔC_{ant} accumulation rates for the "GOBMs high" (top row) , for "GOBMs low" and for the regional model ROMS-SouthernOcean-ETHZ (middle and bottom rows). Contours show, for each model, the zonally-averaged potential density for the period 1994-2007 (with a 0.02 kg m^{-3} spacing), where the thick contour indicates the 1027.6 kg m^{-3} isopycnal.

Table S1. Illustration of the Global Ocean Biogeochemistry Models (GOBMs) simulations A to D. Simulation A and C are forced with interannual varying atmospheric CO_2 as in historical observations, and simulations B and D are forced with constant (preindustrial atmospheric CO_2. Climate forcing varies interannually in simulations A and D, and a repeated single year or multi-year climatology is used in simulations B and C. F_{net}: net air-sea CO_2 flux. Flux components: C_{ant}: anthropogenic carbon, C_{nat}: natural carbon, ss: steady state, ns: non steady state. See main text for explanation.

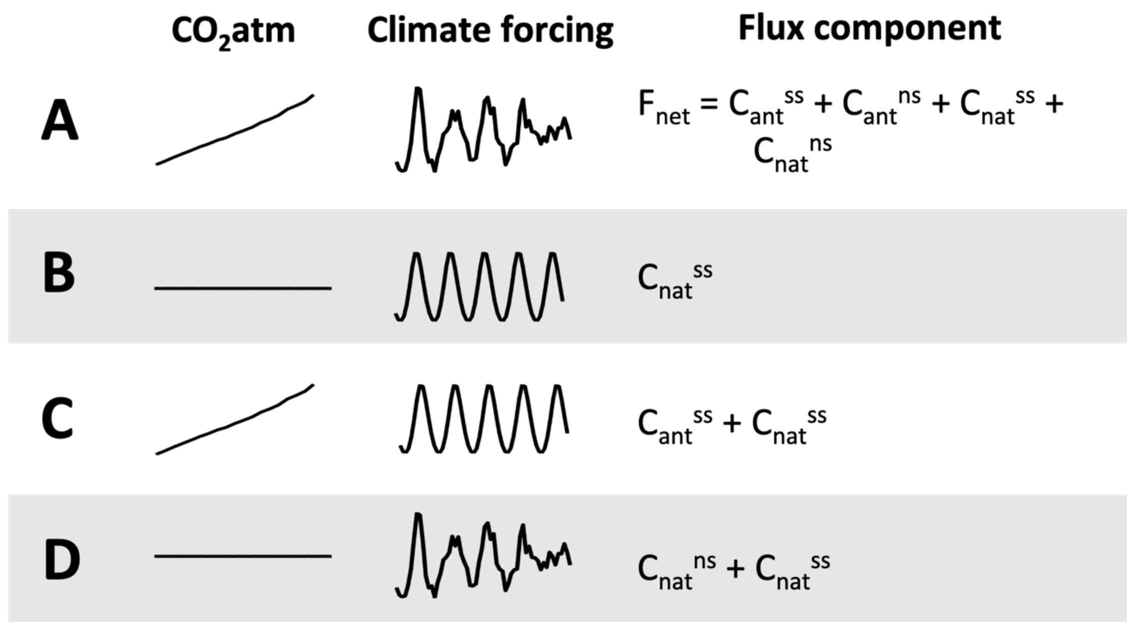

Table S2. Refers to the classification of models in Figure 7 into those that have a strong or weak DIC seasonal cycle contribution to pCO_2. We refer to these as DIC dominant or DIC weak rather than thermal or non-thermal as the thermal contribution is relatively similar for all models as the RECCAP2 models use atmospheric forcing, resulting in well-constrained temperature contributions.

	Global and regional ocean biogeochemistry models
DIC dominant	CCSM WHOI, CESM ETHZ, MRI-ESM2, NorESM-OC1, ORCA025-GEOMAR, ROMS-SouthernOcean-ETHZ
DIC weak	CNRM-ESM2, EC-Earth3, FESOM-REcoM-HR, FESOM-REcoM-LR, MOM6-Princeton, ORCA1-LIM3-PISCES, PlankTOM12